# On-belt Tomosynthesis:

# 3D Imaging of Baggage for Security Inspection

Selina Kolokytha

Supervisors:

Prof Robert Speller

Prof Stuart Robson

September 2015


Thesis submitted for the degree of

*Doctor of Philosophy*

(Ph.D.)

*For Μιμη and Peta-Joanne*

# Declaration of authorship

I, Selina Kolokytha, confirm that the work presented in this thesis is my own. Where information has been derived from other sources, I confirm that this has been indicated in the thesis.

Signed

Date *14/09/2015*

# Abstract

This thesis describes the design, testing and evaluation of 'On-belt Tomosynthesis' (ObT): a cost-effective baggage screening system based on limited angle digital x-ray tomosynthesis and close-range photogrammetry. It is designed to be retrofitted to existing airport conveyor-belt systems and to overcome the limitations of current systems creating a pseudo-3D imaging system by combining x-ray and optical imaging to form digital tomograms.

The ObT design and set-up consists of a configuration of two x-ray sources illuminating 12 strip detectors around a conveyor belt curve forming an 180° arc. Investigating the acquired ObT x-ray images' noise sources and distortions, improvements were demonstrated using developed image correction methods. An increase of 45% in image uniformity was shown as a result, in the post-correction images.

Simulation image reconstruction of objects with lower attenuation coefficients showed the potential of ObT to clearly distinguish between them. Reconstruction of real data showed that objects of bigger attenuation differences (copper versus perspex, rather than air versus perspex) could be observed better.

The main conclusion from the reconstruction results was that the current imaging method needed further refinements, regarding the geometry registration and the image reconstruction. The simulation results confirmed that advancing the experimental method could produce better results than the ones which can currently be achieved.

For the current state of ObT, a standard deviation of ±2 mm in (a) the source coordinates, and ±2° in (b) the detector angles does not affect the image reconstruction results. Therefore, a low-cost single camera coordination and tracking solution was developed to replace the previously used manual measurements. Results obtained by the developed solution showed that the necessary prerequisites for the ObT image reconstruction could be addressed. The resulting standard deviation was of an average of 0.4 mm and 1° degree for (a) and (b) respectively.

# Acknowledgements

I have been blessed to have had support from so many people throughout this journey; a humbling experience. I am sincerely grateful to every single one of you - a feeling I hope I have successfully conveyed in action, besides in words.

My profound appreciation goes to my supervisors who's input was invaluable: Prof Robert Speller, for your priceless guidance and aid in all scientific and personal aspects throughout my studies; Prof Stuart Robson, for your remarkable contributions along the course of this work, especially your patience in teaching me a new science and your continuous caring and moral uplifting.

I would like to greatly thank Dr Deeph Chana and Dr Jan Boehm for the very stimulating and enriching Viva discussion, as well as the time and attention they dedicated in reading my thesis and suggesting profitable improvements.

My deepest gratitude goes to my colleagues, friends and family for their precious support and encouragement, and I wish to acknowledge funding from EPSRC. I was privileged to have collaborated with Dr Caroline Reid, Dr Elena Vescovo and Dr Magdalena Szafraniec and I am greatly thankful their valuable input to ObT. Profound acknowledgment goes to Dr Marta M. Betcke for her extremely generous help with computer simulation and reconstruction software - your input was outstanding. Prof. Mark Shortis, Dr Tasos Konstatinidis, (Dr) Nick Calvert I am incredibly grateful for your scientific contributions. To my reviewers, especially Dr Paul Burke, my deepest gratitude. Ireneos, Ana-Monica, Yi, Rob, Reem, Chiaki, Dagmar, George, Dan, Nik, Christos, Natasa, Thanasis, Katherine, Alex and **Pierre** I am lucky to have friends like you. Sarah, thank you for everything. Evi $\sigma\varepsilon\ \varepsilon\upsilon\chi\alpha\rho\iota\sigma\tau\omega$. To my extended family, Beasley, Wilson, Prowse, Boneli, Lykoudi, Boord, Kolokytha, I am blessed to have you. My accomplishments are sourced in my inspirational parents' love and energy.

Thank you to everyone in England, Greece, and beyond, who was a part of this enriching journey.

May your futures be blessed.

# Contents

# List of Abbreviations

1D,2D,3D One-, Two-, Three-Dimensional

6DOF six Degrees Of Freedom

A Amperes

BA Bundle Adjustment

BD Block Diagram

CCD Charge-Coupled Device

CNR Contrast to Noise Ratio

CNR Contrast-to-Noise Ratio

COR Centre Of Rotation

CT Computed Tomography

DAQ Data Acquisition

DSLR Digital Single Lens Reflex

ESF Edge Spread Function

ESF Edge Spread Function

FOV Field Of View

FP Front Panel

FS Focal Spot

FWHM Full Width at Half Maximum

GOF Goodness Of Fit

g grams

Hz Hertz

LED Light Emitting Diode

LED Light-Emitting Diode

LSE Least Squares Estimate

LSF Line Spread Function

LSF Line Spread Function

m meters

MTF Modulation Transfer Function

n/a not applicable

NASA National Aeronautics and Space Administration

NNPS Normalised Noise Power Spectrum

NPS Noise Power Spectrum

ObT On-belt Tomosynthesis

RMSE/RMS Root Mean Squared Error

ROI Region Of Interest

SAA Shift-And-Add

SCT Single Camera Tracker

SSE Sum of Squares Due to Error

TP Test Piece

UCL University College London

VI Virtual Instrument

VMS Vision Measurement System software

VMS Vision Measurement System

VOI Volume Of Interest

V Volts

W Watt

# List of Tables

# List of Figures

# Chapter 1

# Introduction

***The precondition to freedom is security.*** [1]

## 1.1 Security Screening

Within the grand scheme of security, aviation security, and specifically the protection of airports and aircrafts from terrorism and smuggling, has undergone significant development in recent years. This study specifically focuses on baggage inspection: the technology used for the detection of explosives and illicit materials, with the purpose of prohibiting the illegal movement of goods and dangerous items, in accordance with local legislative requirements[Singh and Singh, 2003, ECORYS, 2009]. In addition, aviation activity, in terms of annual commercial flights, is reportedly growing at a rate of 3-5% per year [Kölle et al., 2011, ATAG, 2014]. During 2014, a record total of 37.4 million commercial flights worldwide, carrying over 3 billion passengers was reported [ATAG, 2014]. Figure 1.1 shows a graphical representation of the increase in the annual total of commercial flight passengers from 1967 to 2014. Clearly, the demand for security in movement of passengers' accompanying baggage is enormous and growing [Wells and Bradley, 2012, IATA, 2013].

For aviation security, a turning point in the level of required screening was the bombing of Pan Am flight 103 on 21/12/1988 where plastic explosives were used. Until then, security screening was based on solely detecting weapons that could be used by terrorists to hi-jack an aircraft, hence, security requirements only demanded the ability to detect guns and ammunition [Speller, 2001]. Therefore, devices used prior to this were designed to detect materials with high atomic numbers (Z), such as metals. The importance of aviation security increased further in 2009-2010 with the Northwest Airlines Flight 253 failed onboard plastic explosives detonation attempt [Sharp, 2010], and the collective cargo plane bombing plot [Burns, 2010, Spiegel, 2010]. Detection

[1] Dinh [2001], ICA [2012]

technology needed to become broader as well as more refined. It could no longer be based on high-Z materials, but needed to incorporate the selective detection of materials, such as plastic, with lower Z values. Besides the specific materials and their densities, explosive devices are also characterised by the presence of wires and detonator devices. The quantity of plastic high explosive that must be detected to prevent the bringing down of an aircraft is thought to be less than 1kg, which until PanAm-103 was thought to be between 1-5 kg [Speller, 2001]. A vast range of methods have been developed and implemented in aviation security for detecting such materials [Singh and Singh, 2003]. These checks are performed on passengers themselves, their carry-on baggage, their check-in baggage, and on cargo containers [Singh and Singh, 2003]. Therefore different problems are presented in each case, which need to be tackled appropriately. This study focuses on security screening of check-in baggage. The methods developed for detecting illicit materials, involve radiation-based security systems. Neutrons (subatomic particles) and X-rays (electromagnetic waves) are the most commonly used techniques in inspection systems. X-ray based systems are preferred to neutrons because they are cheaper and less problematic in terms of personnel protection [Speller, 2001]. The main requirements of these systems are:

- **Accuracy**. Low false negative and high true positive rates are desired in detection.
- **Throughput.** Approximately 150 thousand pieces of baggage are checked daily in large international airports, such as Heathrow and Atlanta, allowing an inspection time of few seconds per item [Eidus et al., 2007, Heathrow, 2009].
- **Safety**, for both personnel and passengers.
- **Cost-effectiveness** is a critical aspect of industrial production, and thus it is an imperative factor of this study. It drives the study design and development as it directly related to the constraints and scoped aims.

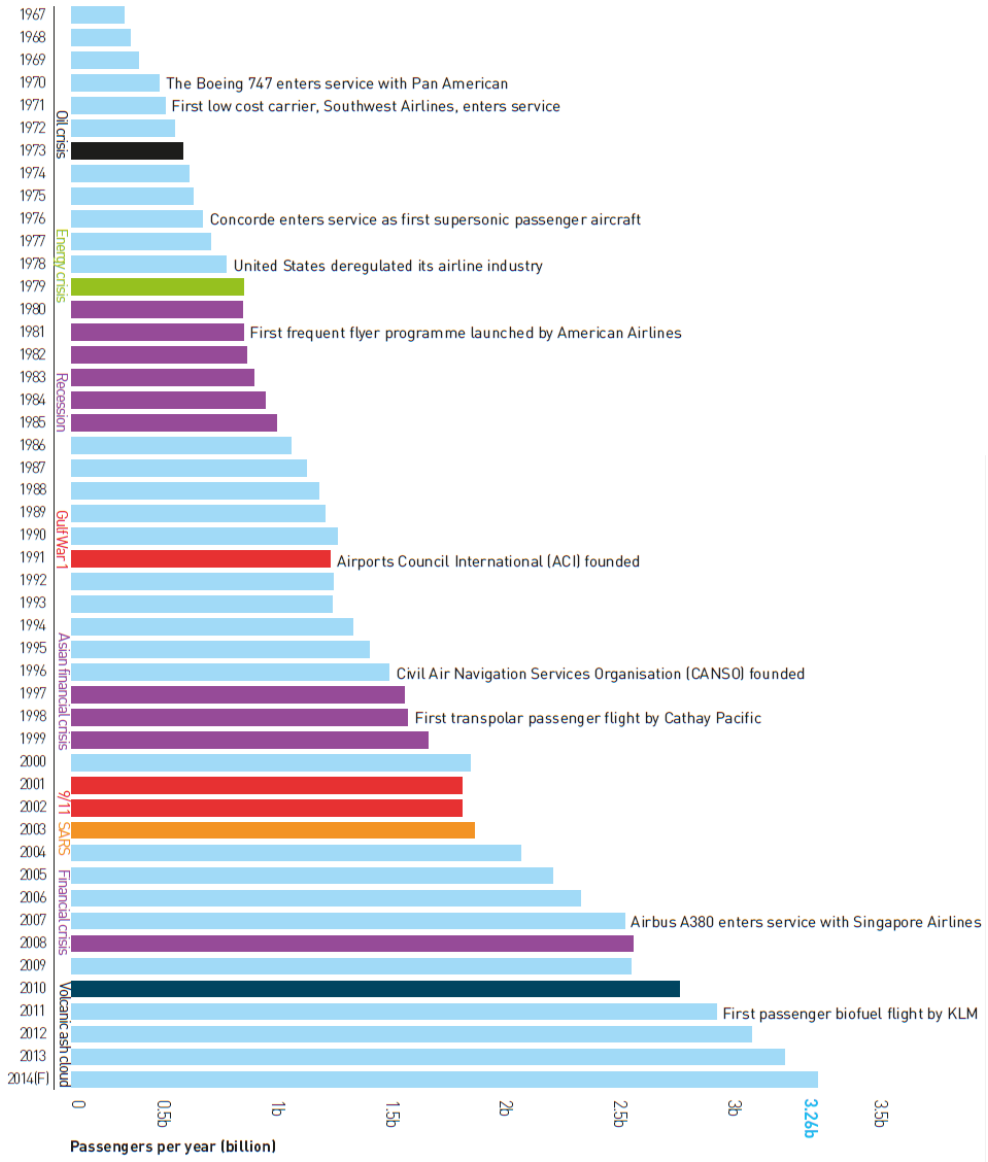


**Figure 1.1:** Air Transport Action Group graph showing total number of commercial flight passengers per year internationaly. Reproduced from ATAG [2014].

## 1.2 Current technology

Currently, the most widely implemented method of imaging baggage for security inspection to detect explosives and illicit materials at airports is *conventional projection radiography* (section 2.3.1) [Speller, 2001, Reid et al., 2011a]. In conventional projection radiography, an x-ray source and detector are positioned on either side of an object to produce 2D x-ray images. Each of these images is formed from single angle transmission measurements. The resulting images depend on the physical properties of the object, which affect the amount of absorption and scatter of the incident x-rays.

However, this method has two principle limitations [Tabar et al., 1995, Rosen-

berg et al., 1996]. First is the superimposition in the projections[2] of the individual items within baggage. This results in flattened images, where the discrimination of objects is more obscure as heavily attenuating object can occlude contents and fine details within the baggage. Second, image information is distorted due to the disparity in x-ray absorption properties among the individual items within the baggage. Both effects lead to a reduction in the amount of important information available, which in turn may result in a larger percentage of baggage being flagged by operators, increasing the baggage handling time. As such, the primary method is called '*phase one*', while an aditional method is '*phase two*' of the baggage inspection process. When baggage is flagged it goes on to being manually searched or screened with more advanced systems, most frequently a Computed Tomography scanner (CT) (section 2.3.4). CT, as a 3D[3] imaging method, is more advanced than conventional x-ray systems. However, it is significantly more complex and costly which is why it is used as an additional check on flagged items in phase two.

## 1.3 Project motivation

In an attempt to create a screening system that overcomes the limitations of conventional projection radiography, while keeping the operational cost low, Reid et al. [2011a] proposed the use of *digital x-ray tomosynthesis* [4] (section 2.5). Tomosynthesis is the creation of pseudo-3D images from a restricted number of 2D projection images, which are acquired at a range of orientations around a static object (Figure 1.2).
In industrial screening, as in airports, objects (such as baggage and cargo) are typically imaged during their transport along conveyor systems. As they move along, their direction of motion often changes, as the conveyor system forms bends. The proposed system would utilise the motion of objects around such bends to create the required conditions for ***'On-belt' Tomosynthesis*** (ObT). This would be feasible with a static x-ray source (offset from centre) and detector arrangement placed at the points of object direction change (illustrated in 1.2(b)). Taking a sufficient number of projection images of the object as it moves through the bend can be reconstructed to create 2D slice images of an arbitrary number of planes, and can then be combined to create a pseudo 3D image of the object. The feasibility of this idea has been demonstrated by a study performed by Reid et al. [2011a]. Through surveys of two London airports (Luton airport and City airport) and through discussions with end-users, it was concluded that suitable bends in airport conveyor systems exist to allow the retrofitting of these systems into airports [Reid et al., 2011a].

[2]Hereafter, the term *projection* is used to mean the *x-ray projection image* produced when a beam of x-rays is projected through an object on to a detector surface.

[3]In the context of this thesis, the term *3D* refers to *three-dimensional volumetric data*, and it should not be confused with the 3D term for *surface data* used in optical measurements, for example.

[4]Hereafter, the term *tomosynthesis* is used to mean *digital x-ray tomosynthesis*.

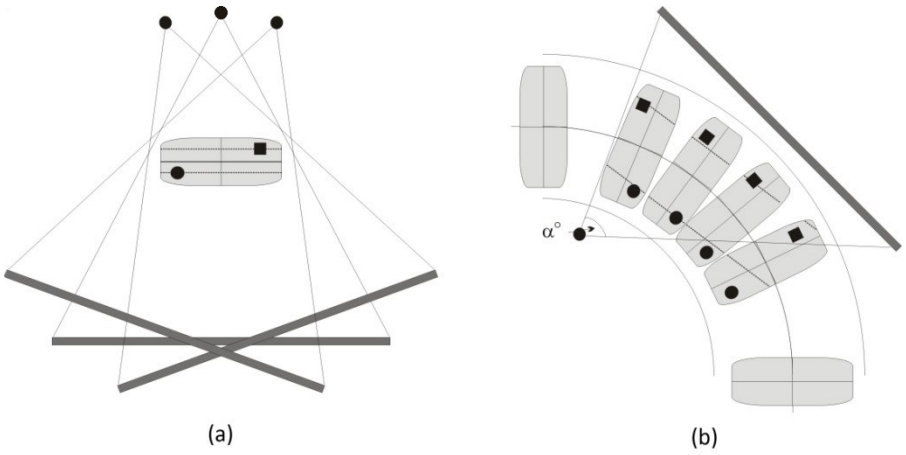


**Figure 1.2:** Schematic of (a) 'normal' tomosynthesis and (b) 'on-belt' tomosynthesis systems. (a) shows an arrangement of moving sources and detectors around a static object and b) shows and arrangement of static sources and detectors around a conveyor bend. The movement of objects around the conveyor bend enables multiple views of the objects to be made. Reproduced from Reid et al. [2011b].

Potential ObT positions were identified at both airports, varying from 40° to 180° (90° being the most common). Additionally, the conveyor systems provided a smooth and steady movement of baggage through the full rotation of the conveyor bends. Therefore, the ObT system could be retrofitted into existing airport conveyor systems, creating a cost-effective 3D primary imaging method for all checked-in passenger baggage. However, the former study was still far from a viable product, because a method for automatic registration of the object location had not been incorporated. As a continuation, a study aiming to advance the potential of the ObT system with the implementation of close-range photogrammetry for accurate non-contact determination of the object location was undertaken. Close-range photogrammetry, a sub-division of geomatic engineering, is a measurement technology which is used to acquire 3D spatial information about an object, that is captured using cameras. More specifically, it is as a flexible tool which can provide the 3D, *six degrees of freedom* (*6DOF*, Figure 1.3) measurements required for the OBT image reconstruction. Kolokytha [2011] concluded by demonstrating the feasibility of this implementation: correlation of the baggage phantom location measurements between the values measured manually and the values measured using close-range photogrammetry showed the differences to be insignificant. Throughout the study, several considerations were made which would advance its potential and viability, which is where this current PhD study found its grounds.

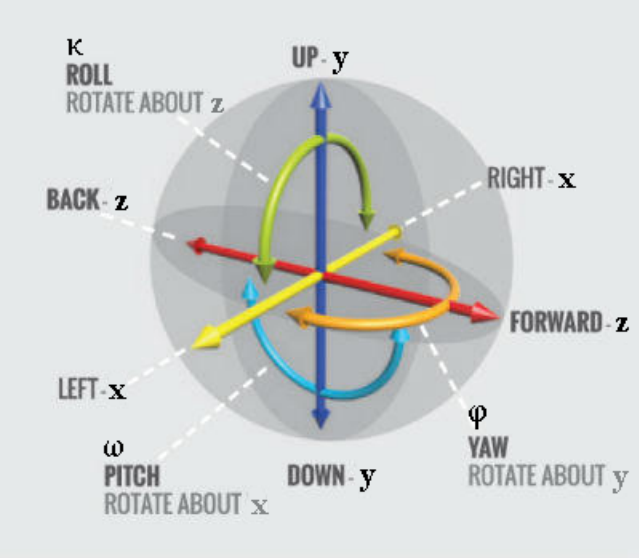


**Figure 1.3:** 6 degrees of freedom (6DOF) refers to the freedom of movement of a rigid body in 3D space. This corresponds to the object's ability for translational movement along three perpendicular axes x, y, z, combined with its ability for rotational movement about these three perpendicular axes, at angles $\omega, \varphi, \kappa$ respectively, which are often referred to as pitch, yaw, and roll. Reproduced from Kerner [2013]

As published by the European Commission's 7th RTD (Research, Technological Development) Framework Programme, a step-change in aviation is needed in order to accommodate the projected growth of three times more aircraft movements by significantly reducing the time spent in travel-related procedures at airports while maintaining safety [Horizon2020, 2007]. This study addressed this issue by exploring a solution of a new security system for checked-in baggage that will be time and cost-effective.

## 1.4 Organisation of this thesis

The thesis is divided into six chapters. The first chapter, *Introduction*, sets the project scene and scope. It starts with a brief overview of security screening's historical evolution to the current state of the art. By highlighting the limitations of the latter, the motivation for the system development comes to rise, and its contribution to the field is given. The second chapter is the *Background theory literature review* upon which this work is based. All the necessary background science required and used within this study is included in this chapter. Next is the *ObT system set-up*, which describes the evolution of the system design: the simulations, tests and constraints it was based on, and the work leading to the final ObT system configuration. The fourth chapter, *Exploring ObT*, includes the experimental work regarding testing, developing and evaluating the ObT system. This includes phantom creation, systems calibration, software development, x-ray acquisition, image correction and reconstruction, results and analysis. This leads to chapter five, the *Low-cost tracking solution development*. Here, the implementation of a close-range photogrammetric system for registering the spatial 3D information of an ob-

ject is explored, tested and analysed. The combined results of the fourth and fifth chapters signify the potential of ObT. The final chapter summarises the thesis offering conclusions and suggestions for future work.

## 1.5 Contribution to knowledge

This study aimed to explore a solution of a new security imaging system for checked-in baggage that will be time and cost-effective.

For this, a prototype system was designed, developed , tested and evaluated based on limited angle digital x-ray tomosynthesis and close-range photogrammetry. The later was used in the implementation of a low cost baggage tracking solution, designed to address the necessary prerequisites for the ObT image reconstruction.

In the thesis chapters 1 and 2, a large number of references is made to other studies in aid of introducing the thesis subject, highlighting its significance, and providing the necessary scientific background. Further than that, in the remaining chapters, the works described were my own my work and contribution to this thesis. This is the case for chapters 3, 4, 5 and 6, unless otherwise referenced. More specifically, my contributions to knowledge arise from exploring and developing the ObT system set-up, On-belt Tomosynthesis, and a low-cost tracking solution.

This study's significant potential is demonstrated by the results presented throughout the thesis, and is the first known study to execute and demonstrate such results. These are summarised in chapted 6, after which, future work suggestions, for developing the ObT into a successful baggage screening solution, are given.

## 1.6 Related Publications

Kolokytha, S., Speller, R., & Robson, S. (2014). Three-dimensional imaging of hold baggage for airport security. ISPRS-International Archives of the Photogrammetry, Remote Sensing and Spatial Information Sciences, 1, 331-336.

Kolokytha, S., Speller, R., & Robson, S. (2013). The development of an 'on-belt tomosynthesis' system for cost-effective (3D) baggage screening. In SPIE Defense, Security, and Sensing (pp. 87090Z-87090Z). International Society for Optics and Photonics.

Kolokytha, S., Costaridou, L., Michopoulou, S., Panayiotakis, G., & Speller, R. (2010). Exploring "intelligence" to maintain image quality and reduce dose in CT. ECR-European Congress of Radiology (C-2936). European Society of

Radiology.

Kolokytha, S., Costaridou, L., Michopoulou, S., Panayiotakis, G., & Speller, R. (2009). Intelligent CT: a method for optimising the image and reducing dose. ITBS-Imaging Technologies in Biomedical Sciences, at the Conference Center G. Eliopoulos, Milos, Greece. 16 September 2009

# Chapter 2

# Background theory literature review

## 2.1 Aviation security screening

In airports, security screening technologies are used to inspect people (passengers and personnel) as well as their baggage (carry-on and check-in). Aviation authorities set guidelines as to what the requirements of a screening system are and its performance characteristics. The screening equipment should report the following [Navvaro et al., 1996]:

- Type of illicit material.
- Minimum quantity (mass).
- Object shape (bulk, sheet, thickness, etc.).
- Location of object in bag.

The properties that are of greatest importance in identifying both drugs and explosives are presented in Table 2.1. For a more detailed analysis of the characteristics of contraband and explosives see Singh and Singh [2003].

| | **Drugs** | **Explosives** |
|---|---|---|
| **H** | | |
| **C** | High | Moderate |
| **N** | - | High/moderate |
| **O** | Low | Very high/high |
| **Cl** | Moderate | - |
| **Density** | Moderate | Very high |

**Table 2.1:** List of properties of greatest importance in identifying drugs and explosives and their characteristic features. Adapted from Gozani [1994].

The requirements set, especially after the Pan-Am 103 disaster, are considerably high, which makes baggage screening a difficult task. Over 50 million pieces of baggage are processed every year at large international airports such as Heathrow [Heathrow, 2009]. This translates to only a few seconds total

inspection time window for each item. Therefore, the most accurate screening systems (with a very low false negative and high true positive rates), besides being highly costly, are too slow and unable to reach this time window. The necessary considerations in aviation security design have thus led to a multi-level screening approach [Speller, 2001] (see '*phase one*' and '*phase two*' mentioned in section 1.2).

Scientific developments have produced a number of methods for baggage screening in aviation security. Among these are x-ray techniques including transmission, dual energy and scatter imaging, X-ray-based computed tomography [Roder, 1991], vapour detection [Chutjian and Darrach, 1996], quadrupole resonance analysis [Rayner et al., 1996] and nuclear techniques [Gozani, 1991]. For a more extensive analysis one may consult Singh and Singh [2003].

## 2.2 X-ray interactions

X-rays can be attenuated by five different methods when passing through a medium. These occur through different ranges of beam energies, the predominant of which are indicated in the respective brackets, and are: Coherent scattering ( <20 keV), the photoelectric effect (>0.5 keV), Compton scattering (30 keV - 30 MeV), pair production (>1.02 MeV), and photodisintergration (>10 MeV). Given that the energy range used for sources in baggage inspection is typically 30-200keV, there are two main types of x-ray interactions which occur: the photoelectric effect and incoherent (or Compton) scatter (Figure 2.1) [Wells and Bradley, 2012]. These are briefly described below, while further information can be found in Beutel [2000].

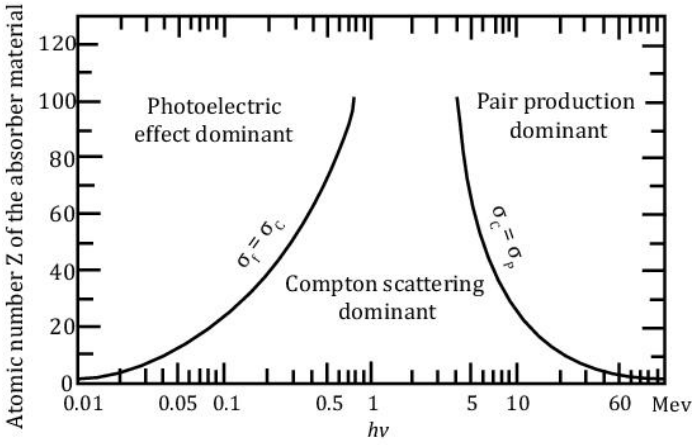


**Figure 2.1:** Graph showing x-ray interactions with matter as a function of material atomic number and photon energy. Reproduced from Evans [1955]

Coherent scattering occurs when the energy of the X-ray or gamma photon is small in relation to the ionisation energy of the atom. The interaction leaves atoms in the same energy state after the scattered photon departs in a direction (possibly) different from that of the incident photon [Macovski, 1983].

The photoelectric effect is observed when a photon passing through matter interacts with an orbiting electron, removing it from its atom, thereby named photoelectron. In this process the incident photon is completely absorbed by that atom, which is one of the reasons why the x-ray beam is attenuated passing through matter. For low energies, such as this study's pre-mensioned inspection energy range, the photoelectric absorption probability ($\tau$) is related to the effective atomic number of the attenuating matterial ($Z_{eff}$), the effective physical density of the attenuating matterial ($p_{eff}$), and the energy of the incident photon (E), by:

$$\tau \propto Z_{eff}^{3} p_{eff} E^{-3} \tag{2.1}$$

Incoherent (or Compton) scatter occurs when a photon of energy much greater than that of an atomic electron's binding energy, interacts with it. From this, the resultant incident photon gets scattered (changes direction of motion) while it also ejects an atomic electron (recoil electron), which causes ionisation. Both the scatter angle of the scatter photon and recoil electron decrease towards the original direction of the incident photon as the energy of the incident beam increases. This can be seen in Figure 2.2. For the corresponding detection energies, the Compton scatter probability ($\sigma$) is proportional to the effective physical density of the attenuating matterial ($p_{eff}$):

$$\sigma \propto p_{eff} \tag{2.2}$$

$\sigma$ is almost independent of $Z_{eff}$, and at a given energy $\sigma$ is effectively constant. Pair production is the simultaneous creation of an electron and a positron from an interaction between a high-energy photon and an atomic nucleus. Photodisintegration occurs when a high-energy (gamma-ray) photon is absorbed by an atomic nucleus, causing it to split forming lighter elements, while releasing a neutron, proton or alpha particle [Macovski, 1983].

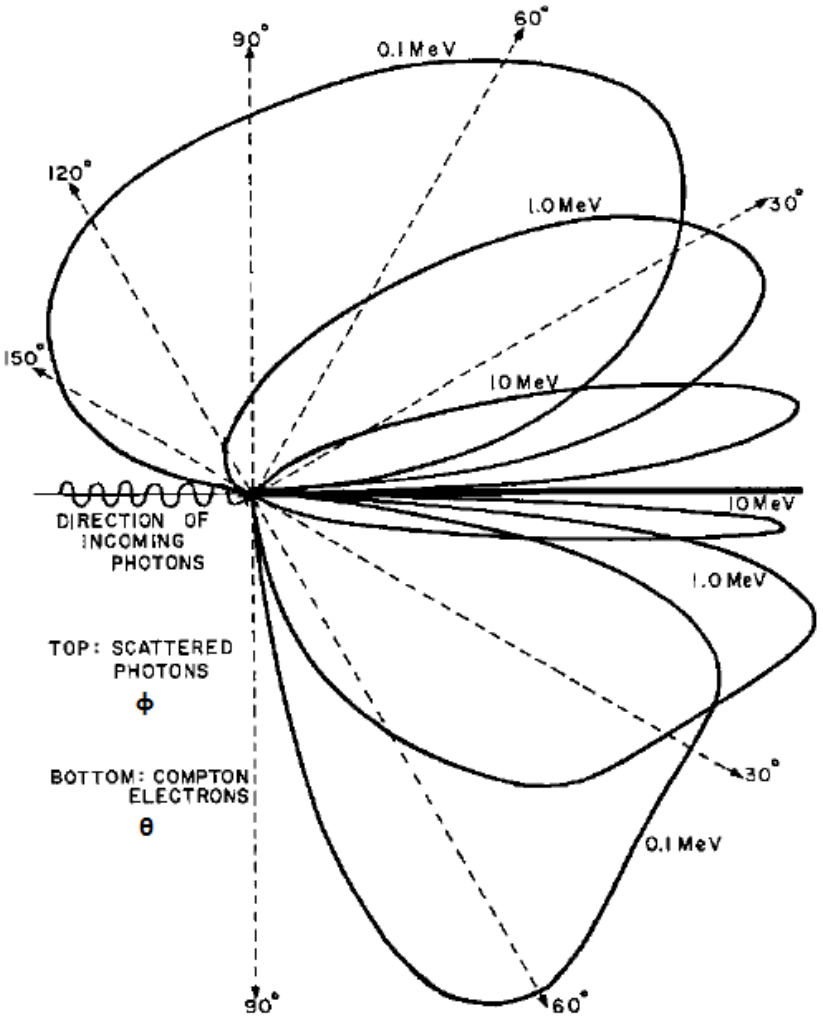


**Figure 2.2:** Schematic of Compton scattering: Electron scattering angle $\theta$ (bottom) and photon scattering angle $\varphi$ (top) as a function of the energy of incident photons. Both $\theta$ and $\varphi$ decrease as the energy of incident photons increases. Reproduced from Hendee and Ritenour [2003].

## 2.3 X-ray based screening systems

X-ray based screening systems are the most popular in aviation security for a number of reasons. X-ray technology has been developed for over a century and is well understood. Additionally, x-ray based systems are considered safer to humans and baggage contents than, for example, nuclear magnetic resonance, as their strong magnetic forces can have destructive effects when metals are present [Singh and Singh, 2003]. They are also less costly and easier to operate than neutron-based systems.

In general, x-ray technology uses the physical principals of x-ray interaction to interpret the results and deduce the type of materials present [Schafer et al., 1991]. Specifically, it provides information on object density $\rho$, and the effective atomic number $Z_{eff}$. The $Z_{eff}$ value is the estimate of the hypothetical single element that will give the same x-ray attenuation as the substance being evaluated. In theory, an object's material type can be uniquely determined

using its density and $Z_{eff}$ [Eilbert and Krug, 1992].

Further detailed reviews of x-ray imaging technique developments can be found in Harding [2004], Thompson and Chimenti [2012], Martz et al. [2013].

### 2.3.1 Conventional projection radiography

A conventional x-ray based system takes linear projections through an object in a so-called line scan mode [Speller, 2001]. The system then measures how many x-ray photons were removed from an illuminating beam at each location of the object [Singh and Singh, 2003]. The result is unrelated to the mode by which the x-ray is removed from the pencil beam. Therefore, conventional projection radiography measures the attenuated x-ray intensity after it has passed through a scanned object, which is the total x-ray interactive cross-section [Kramers, 1923]. Through the relevant x-ray system software, 2D images are formed of the corresponding projections.

Conventional projection radiography is currently the most widely implemented method of imaging baggage in airports. The typical airport baggage screening device has a fan shaped or scanning x-ray beam and a line of detectors measuring the x-ray absorption. It then produces (high quality) x-ray images derived from the degree of absorption produced. The main disadvantage of these systems is that they cannot distinguish between a thin sheet of strong absorber (high-Z) and a thick slab of weak absorber (low-Z), the effect of superimposition. Typical images are shown in Figure 2.3.

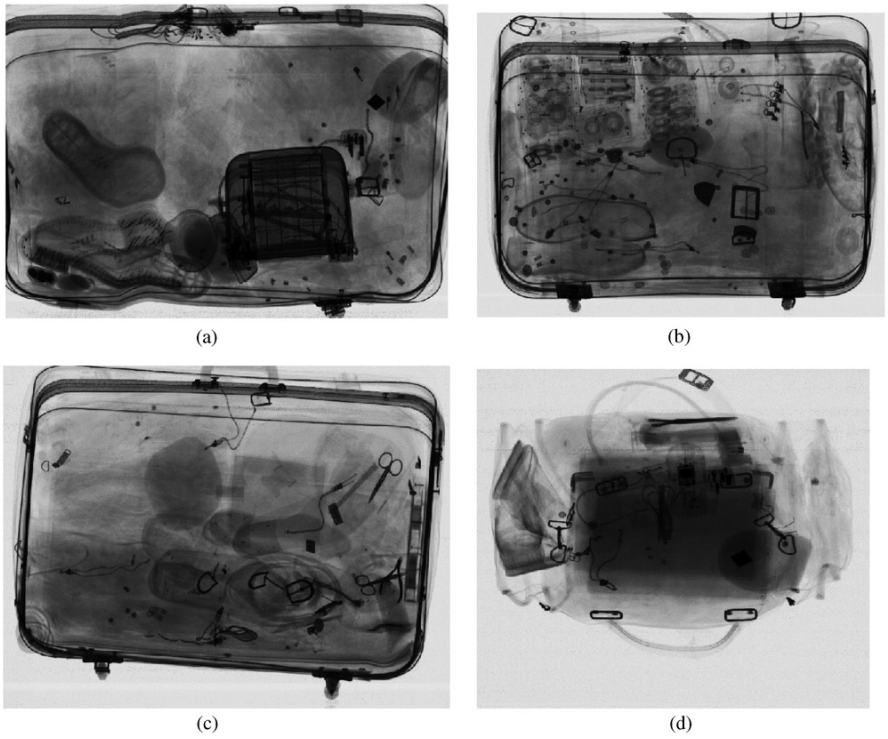


**Figure 2.3:** Examples of typical projection radiography images of airport baggage. Reproduced from Singh and Singh [2003].

More specifically, early security systems were based on detecting weapons, materials of high-Z values, therefore high-energy x-rays were used (Speller, 2001). At these higher energy levels, over 100 keV, the absorbed energy primarily depends on the density of the material. Respectively, the higher the density, the more energy absorbed by the object and therefore the darker the resulting projection image. Due to the material characteristics, objects such as metal or weapons would appear very dark. This fact meant that an explosive object, such as a plastic explosive, could be hidden behind a denser material, which remained a problem.

### 2.3.2 Dual energy

An advancement on conventional projection radiography, created to enhance its effectiveness with chemical analysis, is dual energy radiography. In a single energy system, a thick, low-Z material will have the same attenuation as a thin, high-Z material. Therefore, the resulting projection would be the same and one would not be able to distinguish between the two. In order to resolve this problem, baggage is scanned at two energy levels.

At lower energies, the absorption depends mainly on $Z_{eff}$ and the material thickness. At higher energies the effect of absorption is less significant. Although high-Z materials appear dark in both views, lighter elements are darker in lower energy views. Therefore, dual energy systems can detect light elements such as carbon, nitrogen and oxygen, by comparing both views. Additionally, when screening simple objects, they can calculate an area density that in turn gives a measure of density ($\rho$) and thickness by using a priori information between Z and $\rho$ . However, real baggage items are not simple, hence the real density of objects is poorly known and the system only generates an estimate of Z, i.e. $Z_{eff}$. Hence, dual-energy analysis, which is better than single energy, can be easily confused without the knowledge of material $\rho$ (Figure 2.4) [Singh and Singh, 2003]. Therefore, dual energy systems need to be used in combination with volume imaging (such as CT or stereoscopic imaging) in order to give better estimates of material $\rho$ as well as $Z_{eff}$. Strecker [1998] reports the false alarm rate of dual-energy systems to be around 20%. Figure 2.5 shows more detailed graph representing the relationship between $Z_{eff}$ and density $\rho$ for common items found in airport baggage in addition to certain illicit and explosive materials.

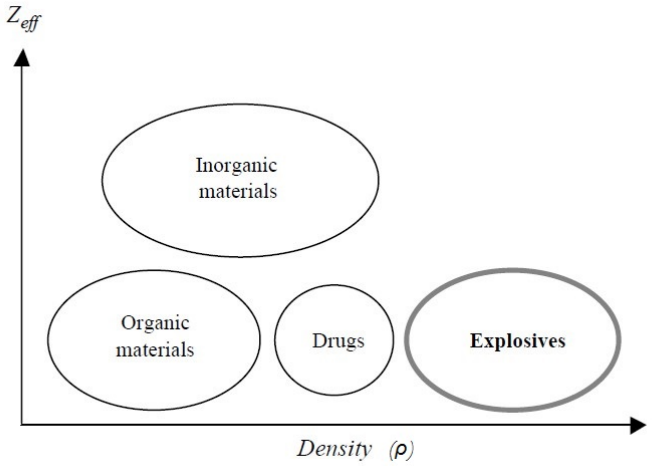


**Figure 2.4:** Graph representing the role of $Z_{eff}$ in separating explosives from other materials based on material density $p$. It should be noted that these are vague generalisations and not absolute comparison. Reproduced from Singh and Singh [2003].

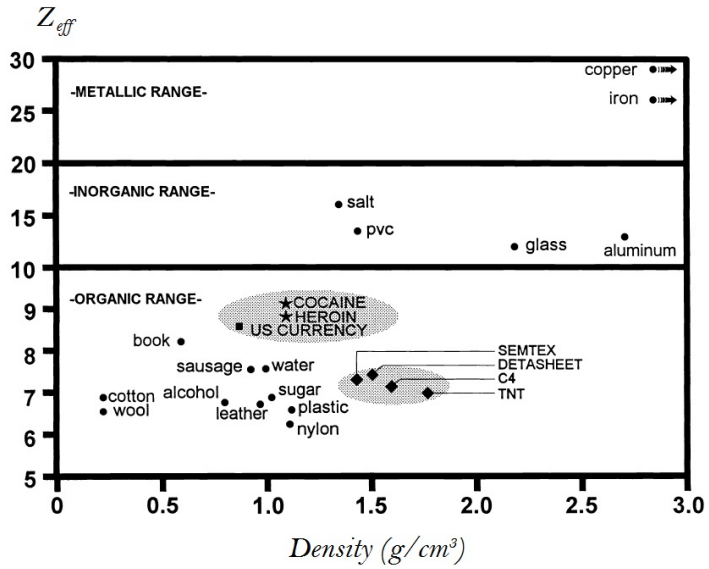


**Figure 2.5:** This graph represents the relationship bewteen $Z_{eff}$ and density $p$ for common items found in airport baggage in addition to certain illicit and explosive materials. Adapted from Eilbert and Krug [1992]

### 2.3.3 Scatter imaging

It is common for explosives to be mixed with harmless materials, making their detection more difficult. However, they have two unique characteristics in terms of their interaction with X-rays. First, they consist of low-Z elements; second, they have a 30-50% higher physical density $\rho$ than common plastics, and about five to eight times higher than typical packed clothing [Annis et al., 1992] (see Figures 2.4 and 2.5).While dual-energy methods attempt to exploit the first of these characteristics, a scatter image exploits both the low-Z and high-$\rho$ characteristics of plastic explosives [Singh and Singh, 2003]. As a re-

sult, the scatter imaging techniques are more specific. There is a number of studies proposing it as an effective baggage inspection method [Annis et al., 1992, Grodzins, 1991, Hussein and Walker, 1999, Schafer et al., 1991].

In scatter imaging, image data is collected from x-ray energy which is scattered from the object and reflected back towards the x-ray source, or scattered x-ray energy that passes forward through the imaged object. These correspond to the back-scattering and forward-scattering images respectively. For scatter images, each location along the pencil beam in the objects adds to the amount of scatter seen in the produced scatter image. The amount of scatter seen in a scatter transmission image is the effect of photons scattering out of the pencil beam. Specifically, this amount depends on the number of x-ray photons reaching the point, the electron density at that point, the scattering cross-section, and attenuation that the scattered photons undergo while exiting the bag [Singh and Singh, 2003]. Because of this, two different materials with the same transmission characteristics would still produce two very dissimilar sets of scatter images (such as aluminum and plastic). Heavy metals can easily be imaged via the transmitted beam which produces a typical x-ray image. Additionally, backscatter signal intensity depends on how much of the transmitted beam has been absorbed, how much is backscattered, and how many backscattered x-rays reach the backscatter detectors. So, its signal depends on the competition between photoelectric absorption and Compton scattering. The photoelectric cross-section increases with the Z of the object, while the Compton cross-section is relatively independent of Z. Therefore, the backscatter signal result provides a direct measure of the $\rho$ of elements with low-Z, such as plastic.

### 2.3.4 Computed Tomography

Computed tomography, initially developed for 3D medical imaging applications, has been applied for baggage screening [Roder, 1991, Roder and Stebler, 1992, Smith and Krall, 1996]. As the name indicates it is an x-ray imaging method employing *tomography* (imaging by sections) created by *computed* processing. CT technology is primarily based on the synchronous movement between the x-ray components (source and detector) and imaged object.The result of digital geometry processing is a 3D image of the inside of an object created by a stack of 2D x-ray images taken around a single axis of rotation [Herman, 2009].

The x-ray transmission through an object is a function of its $Z_{eff}$, $\rho$ and thickness. The linear attenuation coefficient ($\mu$) is the sum of attenuation coefficients of each element in a given x-ray path. Many reconstruction methods have been developed for CT, based on different principles and techniques, including *filtered back projection* (see Katsevich [2005], Singh et al. [2010] and references therein), *rebinning* (see Flohr et al. [2005], Betcke and Lionheart

[2013] and references therein), and *FDK* [Feldkamp et al., 1984, Kak and Slaney, 2001, Natterer and others, 2001] reconstruction algorithms. A CT system produces 2D cross-sectional or transactial projection slice images of an object by reconstructing the linear x-ray attenuation coefficients matrix. 3D images of the objects are generated by these projection slices. The last objective is to measure the object's $\rho$ and $Z_{eff}$. For this, initially, the attenuation coefficient for each volume element in the volume rendered image is determined by the reconstruction algorithm. Attenuation coefficient is then mapped as a direct function of the atomic number and density. This results in two unknown quantities, so taking measurements at two different energies leaves two equations with two unknowns that could be solved for Z and $\rho$ . Therefore, the volume elements can be mapped according to $Z_{eff}$ and $\rho$ , and the correlation of these variables can provide both feature and material discrimination [Dolan et al., 1991].

CT systems have been used for security screening [Heinskanen et al., 1995, Roder, 1991], however they are used only at *phase two* as their operational cost is high (section 1.2). These systems initially produce x-ray scans similar to the conventional airport x-ray scanner, for a 360° view. On a second level, they employ automated inspection algorithms by which the locations within the baggage where the absorption indicates a suspicious area is determined. The characteristics of an object (such as density, texture, mass and shape) are then determined using cross-section CT slices. In these slices, hidden objects surrounded by other materials can easily be identified [Singh and Singh, 2003].

### 2.3.5 Imaging phantoms

*Imaging phantoms*, or simply *phantoms*, are manufactured objects specifically designed to be imaged in order to test, refine and enhance the performance of the respective imaging systems. Their primary developmental function is to enable accuracy and repeatability of experimental measurement. Useful reviews of phantoms used in imaging methods for engineering and medical physics can be found in Pogue and Patterson [2006], Culjat et al. [2010] and Hess (2015: 83-88). In medical imaging, for which they were originally employed, there is extensive use and development of human-like phantoms. This enables scientists to do research using the readily available phantoms, which are made specifically to represent human bodies, or parts. Besides the ease of availability, the existence of phantoms is hugely significant as most imaging technologies are considered harmful to humans. This imitation extends not only to shape of objects but mostly to material composition and characteristics, especially in relation to the respective imaging methods used. Scientists have made impressive developments in this domain, having created phantoms representing whole bodies, internal systems and organs as well as human brains. As this study is focused on security screening the phantoms created are much more simplistic, made based on the scope of representing

passenger baggage items as well as based on the system requirements and capabilities..

## 2.4 X-ray performance evaluation of digital detectors

Prior to going into detail regarding what affects x-ray detector signal quality and how the resulting image quality can be determined, it is important to understand the concept of image quality in security inspection. An image with good quality is an image that fulfills its purpose [ICRU, 1996], in this case detecting prohibited items (section 1.1).

### 2.4.1 Parameters affecting image quality

Image quality deterioration can result from various origins. In addition to visual inspection, which is used in assessing the quality of x-ray images produced, there are a number of quantitative tests designed for the same purpose, which are widely used and approved. In order to better understand the particular use and scope of each method it is advantageous to firstly present the parameters affecting image quality, which are used to describe digital x-ray detectors. These are:

- Noise
- Contrast
- Spatial resolution
- Geometric distortions

The first three are the fundamental parameters affecting image quality of all detector systems (analog or digital). Geometric distortions are not always present or evident.

#### 2.4.1.1 Noise

Digital detectors produce an output signal in the form of a digital number which represents the integrated amount of x-ray energy absorbed by the detector over a specific exposure time. The appropriate readout of the pixels constitutes the formation of digital images which correspond to the x-ray projections. From the detection of the x-ray photons to the formation of the digital images several parameters can affect the resulting images, by overestimation or underestimation of the signal level. Image noise is an important measure of image quality [Dobbins III, 2000, Cunningham, 2000, Illers et al., 2004]. **Noise** is the "image characteristic introduced in all images and (is) measurable as the fluctuations of the image intensities around an average value" [Konstantinidis, 2014: 49].

The specific parameters affecting the signal quality are: *detector noise* sources and system *electromagnetic interference* (*E.I.*) [Konstantinidis, 2011]. E.I. is disturbance that affects an electrical circuit due to either magnetic induction between two circuits or due to conduction or radiation emitted from an external electrical source [Carr, 2000]. These noise origins may be internal (the digital sensor itself or the Data Acquisition, $DAQ$ ) or external (secondary electric circuit beyond the acquisition system, e.g. x-ray tubes, power supplies, computers, etc.) [Konstantinidis, 2011]. This noise results in one or more sinusoidal patterns (of specific period and phase) superimposed on the projection [Hudhud and Turner, 2005, Russ, 2006, Ji et al., 2007, Aizenberg and Butakoff, 2008]. Thisa periodic noise pattern occurs if the (readout) electronic components of a detector are not properly isolated. In the cases of some CMOS APS x-ray detectors, an additional parameter is detector inherent nonlinearity [Bohndiek et al., 2008].

Detector noise can arise from three sources:
**(i)** quantum noise
**(ii)** electronic noise
**(iii)** structure (or fixed pattern) noise

**(i)** and **(ii)** consist of the stochastic variations of the signal in the spatial domain and are thus uncorrelated noise sources [Illers et al., 2004]. This means that they vary in time for each pixel and thus for each detector and therefore need to be corrected for in each individual projection collected. These two noise sources are temporal.

**(iii) Structure noise**, commonly known as *Fixed Pattern Noise* (section 2.4.2.1), is spatial noise: it has a fixed pattern from projection to projection.

Mathematically, noise in the spatial domain is usually described by the ***standard deviation*** ($\sigma$) or ***variance*** ($\sigma^2$) (section 2.12.1) in measurements of the image signal over a specified region of interest (ROI) which is calculated for a homogeneous, signal-free (*flat*) area.

#### 2.4.1.2 Contrast

Contrast ( $\delta$S) is a measure of the relative signal difference between two locations in an image, more specifically between the area of an object and the "background" [Cunningham, 2000]. $\delta$S is given by the absolute differece in signal of an object ($S_{obj}$) to the signal of the background ($S_{back}$):

$$\delta S = |S_{obj} - S_{back}| \tag{2.3}$$

#### 2.4.1.3 Spatial resolution

The *spatial resolution* of an imaging system is defined as the minimum distance required between two point-like objects in order for them to be distinguished in the projection image [Tingberg, 2000, Konstantinidis, 2014]. As such it represents the ability to reproduce small objects, or to separate the images of two adjacent objects, or to represent sharp edges between distinct features [Samei, 2003]. The spatial resolution of an imaging system can be assessed by measuring the modulation of the system as a function of spatial frequency [Morgan et al., 1964, Rossmann, 1969, Doi and Rossmann, 1973, Williams, 1998], as described in section 2.4.2.5.

#### 2.4.1.4 Geometric distortions

Imaging systems with unconventional or irregular system variables such as geometry, motion, and mechanisms can produce geometric distortions of the imaged object in the acquired projections. In the context of this thesis, the global effect of these distortions is termed *warping*. Due to the unconventional set-up geometry of the ObT, warping has a significant effect. The impact of warping on the ObT images and the corrections that can be applied are explored in sections 4.3.1.2 and 4.3.2.3 respectively .

Warping is usually manifested as the deformation of images to arbitrary shapes, a process often named image morphing, deformation, or metamorphosis [Beier and Neely, 1992, Ruprecht and Müller, 1994, 1995, Ishida et al., 1999, Kano et al., 1994].

### 2.4.2 Image quality metrics

As described in section 2.4.1, the parameters affecting digital x-ray detector image quality are noise, contrast, spatial resolution, and warping. Popular quality metrics have been designed to asses these parameters either individually or in combinations and are presented in the following sub-sections.

#### 2.4.2.1 Fixed Pattern Noise

In conventional systems, Fixed Pattern Noise (FPN), as an inherent feature of each pixel, is spatial, correlated noise. It is non-stochastic and is assumed to remain temporally constant. In simple terms it reflects the sensitivity (responsiveness) of the pixels. More specifically, FPN is attributed to the detector sensor, and is related to pixel-to-pixel non-uniformities rising from their variations in sensitivity and in the gain of the imaging system, i.e. differences in the amount of output signal for a given input quantity [Konstantinidis et al., 2011]. In 2D (*flat panel*) digital x-ray detectors there is also column-to-column variation due to the columnar electronic readout non-uniformities from the differences in the gain of column amplifiers [Bohndiek et al., 2008, Zin et al., 2010]. This does not apply to 1D detectors which have a serial

readout, such as in the case of the strip detectors used in this study (section 3.3). Correcting the images for the FPN improves the *contrast to noise ratio* (CNR) of the digital x-ray detector [Konstantinidis et al., 2011]. FPN noise is removed either by normalising with a flat field image or by subtraction of a flat field image, which is divided by $\sqrt{2}$ to remove propagated noise. The *flat field* or *flat* image, also called *flood* or *white* in literature, is a uniformly irradiated homogeneous (signal-free) x-ray projection. The use of this correction assumes a linear detector response and relies on FPN being proportional to the signal level, which, particularly at higher exposures, may not be the case [Evans et al., 2002].

**'Gain and offset' correction**

The most common flat field correction method for a linear flat panel detector is the *'gain and offset'* correction algorithm based on normalisation (equation 2.4). This can be applied to systems, set-up in conventional geometries, which incorporate flat panel detectors. The scaled ($K$ term) gain and offset correction is performed by subtracting an averaged *offset* (or *dark)* image $\overline{I_{dark}(x,y)}$ from the *original flat* image to be corrected $I(x,y)$, and then dividing it *pixel to pixel (x,y)* by the difference between an averaged *flat* image $\overline{I_{flat}(x,y)}$ and an averaged offset image $\overline{I_{dark}(x,y)}$ [Moy and Bosset, 1999]:

$$I_{corr}(x,y) = K \cdot \frac{I(x,y) - \overline{I_{dark}(x,y)}}{\overline{I_{flat}(x,y)} - \overline{I_{dark}(x,y)}} \tag{2.4}$$

$K$ is a scaling factor usually equal to the average over all pixels of the offset-corrected average (over $n$ frames) reference flat image $\overline{\overline{I_{flat}(x,y)} - \overline{I_{dark}(x,y)}}$ [Vedantham et al., 2000, Samei, 2003, Hunt et al., 2004, Medic and Soltani, 2005, Greer and others, 2005, Tortajada et al., 2008]. It is optimised by acquiring each set of images in the numerator and denominator with the same irradiation conditions (tube voltage, external filtration, tube current time product (mAs), detector temperature, aging, etc.) and integration time.

Konstantinidis et al. [2011] demonstrated a method for applying a gain and offset correction in the case of correcting flat images (i.e. no object in field of view), which compensates for any *number of reference flat frames* $n$, which requires a minimum number of one reference frame. This correction method can be employed in the x-ray performance evaluation of digital detectors independently of $n$, such as in measuring the Noise Power Spectrum (NPS, section 2.4.2.4).

#### 2.4.2.2 Image uniformity factor

The pixel sensitivity variation can be investigated by acquiring a flat field image under linear output count rate response conditions. A flat field correction

technique using separately acquired flat field images, such as the *gain and offset* formula, needs to be applied to compensate for the sensitivity variation across pixels. The efficiency of a flat field correction can be evaluated using the *image uniformity factor* $(U)$ . Besides pixel sensitivity, $U$ can be used to evaluate the efficiency of any flat field correction for any noise source by comparing the pre and post-calibration value of $U$ in the respective images. $U$ is calculated using the maximum ($C_{max}$) and minimum ($C_{min}$) counts of an entire image and is given in equation 2.5 [Cho et al., 2014]. This factor can take a value between 0-1: the larger the value the more uniform an image is. It is often expressed as a percentage, once multiplied by 100.

$$U = 1 - \frac{C_{max} - C_{min}}{C_{max} + C_{min}} \tag{2.5}$$

#### 2.4.2.3 Contrast-to-noise ratio

According to Dobbins III [2000], while the difference in signal amplitude of an object relative to the background (contrast) and the noise properties of the image are important characteristics of image quality, it is the ratio between them that is the most significant indicator of image quality. The contrast to noise ratio (CNR) is defined by:

$$CNR = \frac{\delta S}{\sigma} \tag{2.6}$$

where $\delta S$ is given in equation 2.3 and $\sigma$ is the standard deviation of the signal distribution within a background area.

In radiography, CNR describes the ability of a system to reproduce low-contrast objects. CNR is particularly useful in digital radiography systems, where the image noise can be lowered by increasing the number of photons in the image, and the contrast can be varied arbitrary by changing the slope of the characteristic curve of the system [Yaffe, 2000].

Early studies showed that the value of an object's CNR needs to be at least 5 to allow its reliable detection by human observers [Rose, 1948]. This limit, known as the observer's threshold, depends on the detection threshold by an observer during an experiment. The former is in agreement with findings by Marshall [2006] who reported that for good visualisation of an object (e.g., a clear, continuous edge and well-defined position) a strict observer's threshold would correspond to value of 4 or 5.

#### 2.4.2.4 Noise Power Spectrum

The variance, $\sigma^2$, cannot adequately describe the noise of an x-ray imaging system because it does not show the spatial correlation of noise. For example, both 1D profiles in Figure 2.6 have mean value equal to zero and unity spatial variance. However, they look dissimilar due to differences in their noise

correlation. In particular, the noise in (a) is correlated over a greater distance (low frequency) while the noise in (b) is correlated over a much sorter distance (around ten times less than (a)). In this case, a frequency domain response characterisation is more useful than the spatial one.

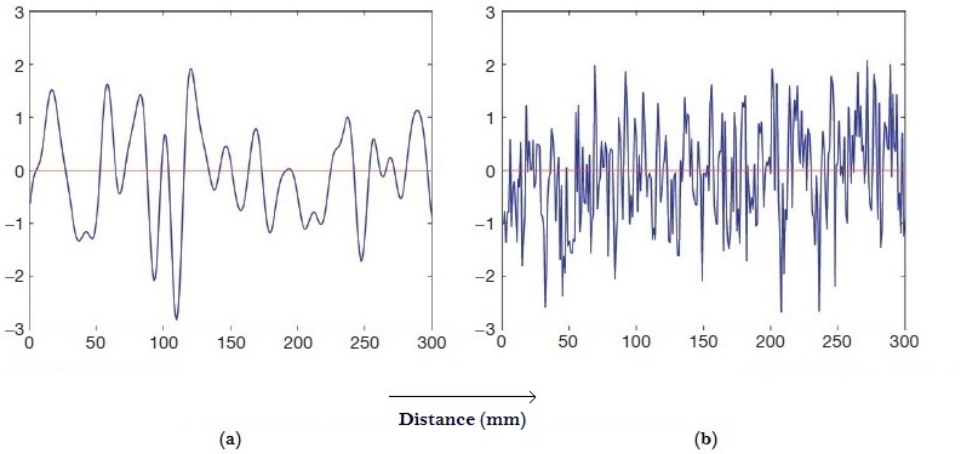


**Figure 2.6:** One-dimensional profiles of noisy images having the same mean and standard deviation. The two profiles look different because the noise in (a) is correlated over a ten times greater distance compared to (b). Adapted from Konstantinidis [2014].

The Fourier transform of a flat image, that is used to calculate the Noise Power Spectrum (NPS), can be used to better describe the noise correlation of the output image because it gives information on the distribution of the noise power in the frequency domain. In other words, the NPS is a spectral decomposition of the variance and it provides an estimate of the spatial frequency dependence of the point-to-point fluctuation in the image [Dainty, 1974, Williams et al., 1999] . Simply, the variance is the total integral of the 2D NPS, where the horizontal and vertical dimensions are $u$ and $v$ respectively:

$$\sigma^2 = \int_{-\infty}^{\infty} \int_{\text{-}\infty}^{\infty} \text{NPS(u,v)dudv} \tag{2.7}$$

In an ergodic system, the NPS can be expressed in two equivalent ways, as: (a) the variance of image noise divided among the various frequency components of the image or (b) the variance (per frequency bin) of a given spatial frequency component in an ensemble of measurements of that spatial frequency [Dobbins III, 2000]. For a digital x-ray system, NPS is the average of spectra obtained from a series of uniformly irradiated images taken under identical conditions. In practice, better results to avoid non-uniformities are obtained by estimating the NPS from a limited area of a series of images rather than from a large portion of a single image [Williams et al., 1999]. When measuring NPS, an infinite summation over the spatial domain as well as over the number of samples to determine the average NPS is assumed. As such, there

is an intrinsic compromise between the size and number of ROIs used for NPS analysis [Konstantinidis, 2014].

As the NPS of each projection direction (vertical and horizontal) cannot be obtained directly, 1D vertical and horizontal NPS (expressed in positive frequencies only) can be extracted from the 2D NPS applying axial averaging (Figure 2.7). Data from a limited number of rows and columns, on both sides of the corresponding axis -omitting the axis itself-, are averaged in measuring the vertical and horizontal 1D NPS [Konstantinidis, 2014].

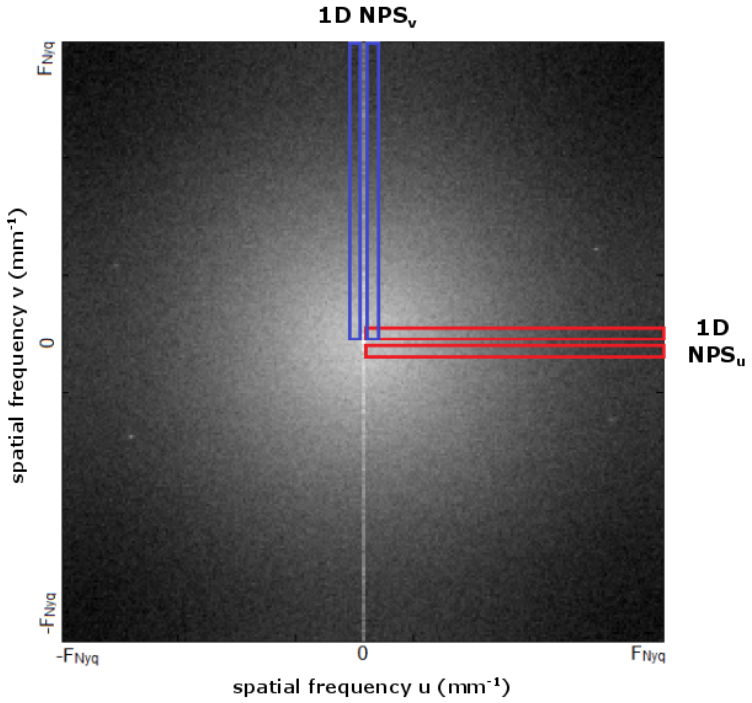


**Figure 2.7:** Example of 2D NPS with 1D 'cuts' for the horizontal (u) and vertical (v) 1D NPS, marked in red and blue respectively. Adapted from Konstantinidis [2011]

#### 2.4.2.5 Modulation Transfer Function

The **spatial resolution** ability of an imaging system (section 2.4.1.3) is most comprehensively described by its *modulation transfer function* (MTF), which describes the signal-transfer capability of an imaging system as a function of spatial frequency [Morgan et al., 1964, Rossmann, 1969, Doi and Rossmann, 1973, Williams, 1998]. MTF is used in performance characterisation of an imaging system, as the most widely accepted measure of spatial frequency response, and is a valuable tool for determining and comparing detector performance [Kuhls-Gilcrist et al., 2010]. MTF directly shows how the contrast between an object of interest and its background changes as a function of spatial frequency. The information transfer of this contrast, which in x-ray imaging corresponds to the signal response of the relationship between the original object (input) and its image (output), is based on the linear-systems theory [Konstantinidis, 2014]. The geometrical elements that make up the

imaging system (focal spot [FS], detector, imaging geometry) all play a role in how the system records fine detail of an imaged object and the quantitative estimate of that property is the MTF. The ideal imaging system would correctly reproduce all spatial frequency information, having an MTF of unity for all spatial frequencies, thus the image would be a perfect representation of the object [Evans et al., 2002]. However, blurring (or unsharpness) caused by FS size, phosphor thickness on the detector, or the geometrical arrangement of source and detector (i.e. the magnification) results in higher spatial frequency being transferred less accurately than lower spatial frequency information, i.e. with reduced modulation. For digital imaging systems with a discrete image sampling a characteristic difficulty arises because the response of the detector to a signal pattern may not only depend on the imaging properties of the detector itself but also on the signal pattern and its location relative to the sampling grid of the detector [Buhr et al., 2003]. The signal transfer is thus influenced by two parts and can be considered as a two-step process [Pratt, 2007]: the analog transfer of the signal, described by the presampled MTF [Dobbins III, 2000], and the stage of sampling. Whereas the effects caused by the sampling depend on both the sampling grid and the signal pattern, the presampled MTF is a physical quantity of the imaging detector alone and independent from the signal pattern [Buhr et al., 2003]. The presample MTF, which is the MTF of the system prior to the digitisation process, is usually measured to overcome the effects of undersampling, therefore, representing the spatial frequency response of the analogue component of the system [Evans et al., 2002].

There have been various methods proposed to determine the presampled MTF of digital x-ray systems based on slit, edge, or bar pattern images. The edge-response method [Giger and Doi, 1984, Hillen et al., 1987, Fujita et al., 1992, Cunningham and Reid, 1992, Samei et al., 1998, Greer and Van Doorn, 2000, Rogge et al., 2002] is widely preferred, while it is also adopted by the IEC [2003]. It has proven to be an accurate and effective method with advantages including simplicity and practicality (simpler construction, less sensitivity to misalignment) [Samei et al., 1998].

Using edge-response, an established method for determining the MTF is to measure its edge spread function (ESF) using an attenuating object with a sharp, straight edge [Jones, 1967, Dainty, 1974, Cunningham and Fenster, 1987]. The edge should be angled between 1.5 and 5 degrees to the detector pixel array [IEC, 2003, IPEM, 2010], in order to calculate the presampled MTF (pMTF) from oversampled ESF and line spread function (LSF). Hence, aliasing effect is not included in the calculated pMTF. The algorithm for the determination of the pMTF generally consists of the following steps [Samei et al., 1998, Greer and Van Doorn, 2000, Reichenbach et al., 1991]:

1. Acquiring a projection image of a slightly tilted edge

2. Constructing/generating a composite, oversampled ESF
3. Differentiating the ESF to obtain the line spread function (LSF)
4. Calculating MTF from the modulus of the Fourier transform of the LSF [Bauer et al., 2012, Cerveri et al., 2003], normalised to 1 at the zero spatial frequency [Evans et al., 2002]

In order to reduce the FS blur, the following set-ups are optimum: a small FS, a long source-to-image distance, and the closest possible distance between the edge object and the detector [Samei, 2003].

The MTF described up till here characterises the spatial resolution capabilities specifically of a detector, and is the detector MTF ($MTF_{det}$). However, in cases where an edge object cannot be positioned directly on the detector, the measured MTF actually corresponds to the system MTF ($MTF_{sys}$), as there is additional unsharpeness owing to the geometric set-up. With appropriate computations, the $MTF_{sys}$ can be corrected to compute $MTF_{det}$, taking into account the system geometry. Geometric unsharpness ($MTF_{geo}$) is computed given a certain size and shape of the FS, and a certain distance between the object point of interest and the detector plane for a given FS-to-detector distance [Sandborg et al., 2003]. The size can be characterised by the standard deviation of the distribution, $\sigma$, using a Gaussian-shaped FS emission profile, and the $MTF_{geo}$ is then given by [Prasad et al., 1976]:

$$MTF_{geo} = exp(-2\pi^2\sigma^2 f^2(m-1)^2) \tag{2.8}$$

$f$ is the spatial frequency, measured in lines per mm. $\sigma$ is related to the *full width at half maximum* as FWHM=2.35 $\sigma$ [Sandborg et al., 2003]. From this, the detector MTF ($MTF_{det}$) can be measured by:

$$MTF_{det} = \frac{MTF_{sys}}{MTF_{geo}} \tag{2.9}$$

#### 2.4.2.6 Warping effect correction

In either case of assessing or applying warping (section 2.4.1.4), local shift vectors or a regular grid are usually implemented [Ishida et al., 1999, Yaffe, 2000, Cerveri et al., 2003, Ruprecht and Müller, 1994, 1995, Bauer et al., 2012]. In the former case, the pixel by pixel shift values can be determined from selected shift vectors by using a surface fitting technique with a polynomial function [Ishida et al., 1999]. In the latter case, appropriate transformation of a regular grid, requires shifting or registration of the image to account for the warping effect distortion, or to purposefully morph an image.

Bauer et al. [2012] present such an example of obtaining accurate knowledge of the relationship between any point in the real object and its counterpart in the produced image. A pair of points consisting of an object point and

its corresponding distorted point in the image is called a correspondence, an example set of which is illustrated in Figure 2.8. The definition of a distortion model of a given system aims to model a set of correspondences over the desired field of view (FOV). By relating these correspondences to points on a grid, its appropriate transformation can effectively account for the warping effect distortion (see Figure 2.9).

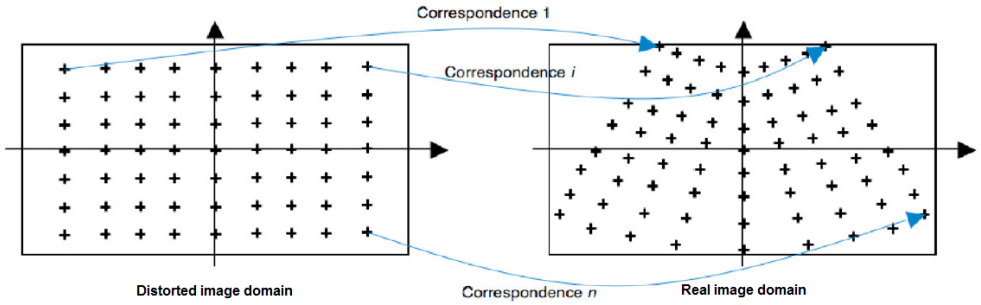


**Figure 2.8:** An example of correspondences between points in the distorted image and the real image domains. Reproduced from Bauer et al. [2012].

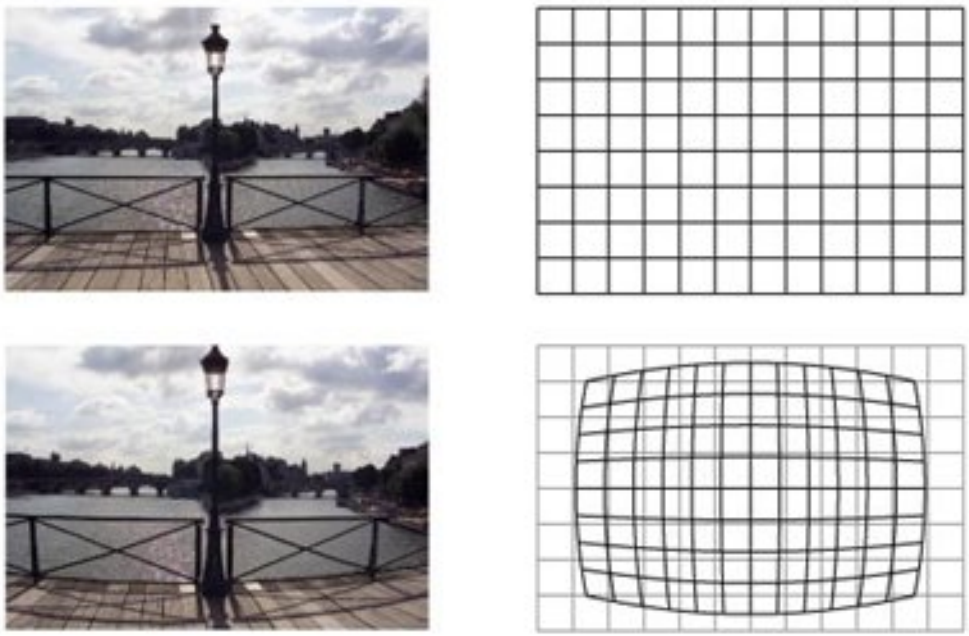

**Figure 2.9:** Above: example of an image scene and grid with no distortion. Below: same image scene as above and grid with distortion. Reproduced from DxOMark [2015].

## 2.5 Digital x-ray tomosynthesis

In broad terms *tomosynthesis* is interpreted to mean any method of generating slice images from a finite set of projection images less than the full 360° rotation required for CT. Digital x-ray tomosynthesis has the ability to suppress the masking effect of superimposition [Niklason et al., 1997, Stevens et al., 2001, Wu et al., 2003, Stevens et al., 2003, Wu et al., 2004b,a]. Using a cone beam of x-rays, 3D images can be created, acquiring views over a typical angle

of 30° to 90°. Figure 2.16 (a) shows the three projected locations of the circle and triangle on the x-ray detector taken from the corresponding three x-ray tube locations. These projection images, through a process of shifting and adding (section 2.6.3), are combined to bring either the circles or triangles into focus, keeping the objects in the other planes smeared out (Figure 2.16: b).

These techniques are already being investigated in the medical field, with particular focus in breast imaging [Park et al., 2007, Chan et al., 2008, Good et al., 2008]. Although the systems currently being developed differ in the manner of movement of the x-ray source and detectors, in all cases, the movement is about a static or fixed object..

Three examples of alternate tomosynthesis configurations are depicted in Figure 2.10. These involve geometries where the x-ray tube and detector or solely the tube move in an arc about some centre of motion. The first type of geometry is demonstrated in Figure 2.10 (a), where the tube and receptor are locked together and rotate about a fixed central point, with the tube and receptor travelling on opposite sides of a circle. In the second type of geometry, demonstrated in Figure 2.10 (b), the detector moves in a plane while the x-ray tube moves in an arc about some centre of rotation. Figure 2.10 (c) is similar to 2.10:b except the x-ray detector is stationary. All of these alternative geometries of tomosynthesis systems have arisen from considerations of the mechanical construction of mammographic devices.

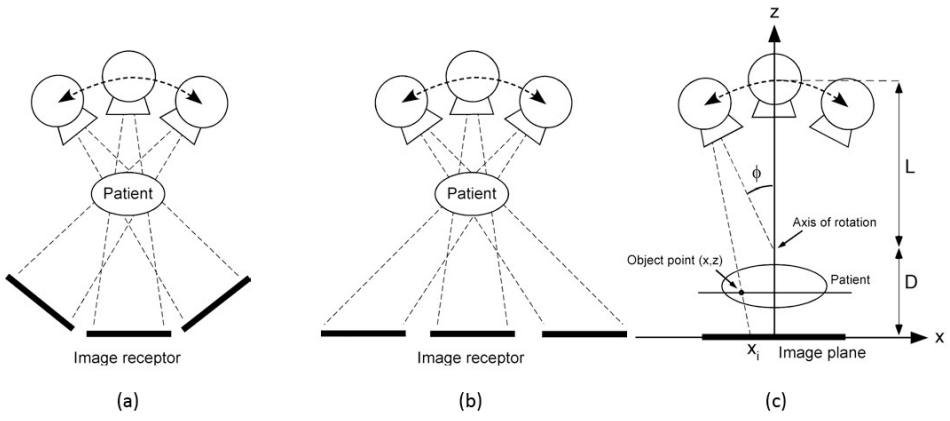


**Figure 2.10:** Tomosynthesis geometries using isocentric motion. (a) Complete isocentric motion, in which both the x-ray tube and image receptor rotate about a common axis. (b) Partial isocentric motion, in which the detector stays in one plane (or is stationary) and the x-ray tube rotates about some point of rotation. (c) Partial isocentric motion in which the detector is stationary. Reproduced from Niklason et al. [1997] and Dobbins III and Godfrey [2003].

Stevens et al. [2003] carried out an extended study of combinations of tomographic angles and number of views, results of which are shown in Figure 2.11. At a tomographic angle of 50° the artefacts in the reconstructed images be-

come more prevalent as the number of views is reduced; substantial artefacts seen when the number of views is reduced to 20 (Figure 2.11: a, b, c). At a tomographic angle of 20°, the reduction in the amount of artefacts in the images obtained with fewer views - as compared with the images in Figure 2.11 (a, b, c) - comes at the cost of a larger section thickness (Figure 2.11: d, e, f). At a tomographic angle of 10° the section thickness is too large to result in adequate blurring of overlying structures, even at the maximum of 100 number of views tested (Figure 2.11: g).

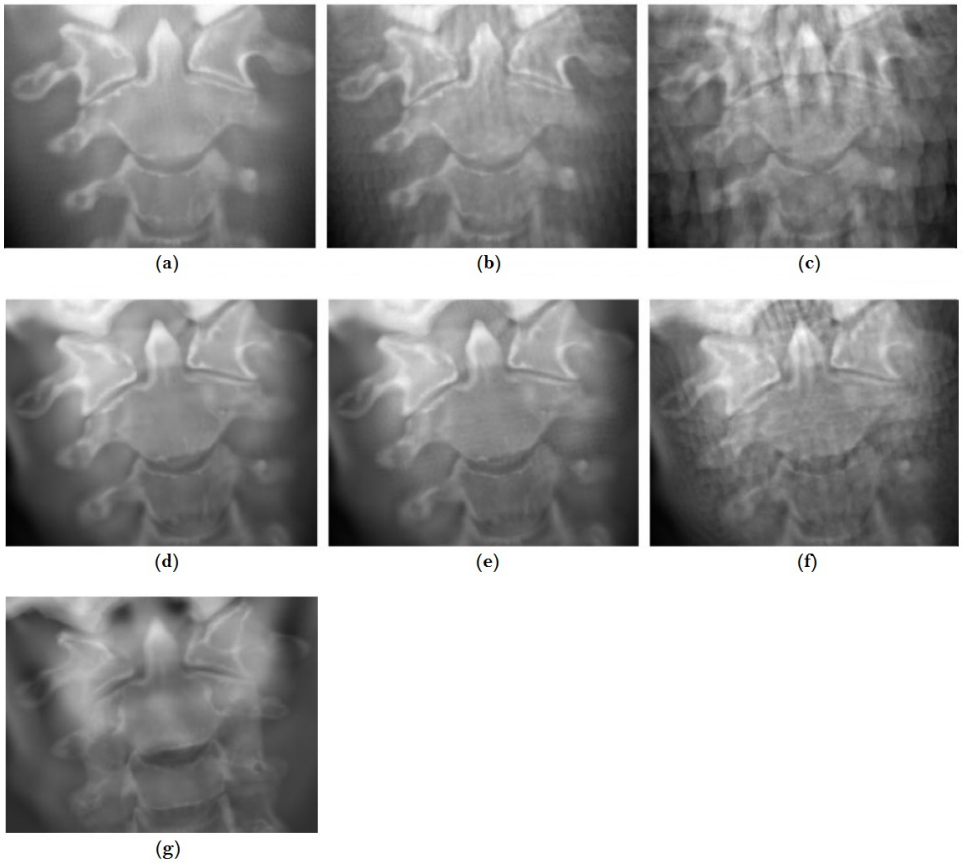


**Figure 2.11:** Tomosynthesis images acquired at a 50° tomographic angle of a phantom with (a) 100, (b) 50, and (c) 20 views. As the number of views is reduced, the artefacts in the reconstructed image become more prevalent; substantial artefacts are seen in c. Tomosynthesis images acquired at a 20° tomographic angle, of a phantom with (d) 100, (e) 50, and (f) 20 views. The reduction in the amount of artefacts in the images obtained with fewer views - as compared with the images in a,b,c - comes at the cost of a larger section thickness. (g): Tomosynthesis image acquired at 10° tomographic angle, 100 views) of the head phantom. (g): At a tomographic angle of 10° the section thickness is too large to result in adequate blurring of overlying structures, even at the maximum of 100 number of views tested. Adapted from Stevens et al. [2003].

### 2.5.1 The 'On-belt' Tomosynthesis system

In tomosynthesis systems used in medical imaging, typical projection angle ranges span from 15° to 120° [Stevens et al., 2003, Badea et al., 2001, Chan et al., 2005]. The 3D image accuracy is directly related to the range of view angles and the number of views used which determine the reconstructed slice thickness [Stevens et al., 2003] (section 2.5).

In an ObT system the relative movement of the baggage to the source and detector is complex. Unlike typical tomosynthesis systems where the x-ray source and detector move around the object, the ObT's principle is based on the motion of the object (baggage) in relation to a static source and detector system. However, to efficiently implement the reconstruction methods, the scanning process is translated and perceived as a static object imaged by a moving system, as typical tomography. This means expressing the scanning process as seen from the perspective of the reference position. So, what is calculated is the source and detector positions with respect to the screened object for each successive projection. In turn, equivalent parallel planes are achieved ensuring the centre of orientation of the baggage is the centre of the baggage itself, i.e. the 'normalised' baggage position.

Figure 2.12 shows two projections from the ObT system of a rectangular object with a single source at its optimal position. Figures 2.12 (a) and (b) show the baggage movement (rectangular object) around the conveyor bend and its corresponding projection onto the detector at two different rotation angles. Figures 2.12 (c) and (d) show the respective effective geometry. These sets of images show the effect of co-registration of baggage locations on the source and detector positions, which are accounted for in the image reconstruction methods [Reid et al., 2011a]. In simple terms, in an ObT system, where the x-ray source and detector remain static, a rotation of the baggage by $+\phi$ around the centre of rotations is equivalent to the rotation of the source and detector by $-\phi$ around the centre of rotation, while the baggage is static. Similarly, by defining a 'reference position' for the baggage, i.e. the normalised baggage position, all rotations of the baggage are able to translate to source and detector rotations with respect to this reference position [Reid et al., 2011a].

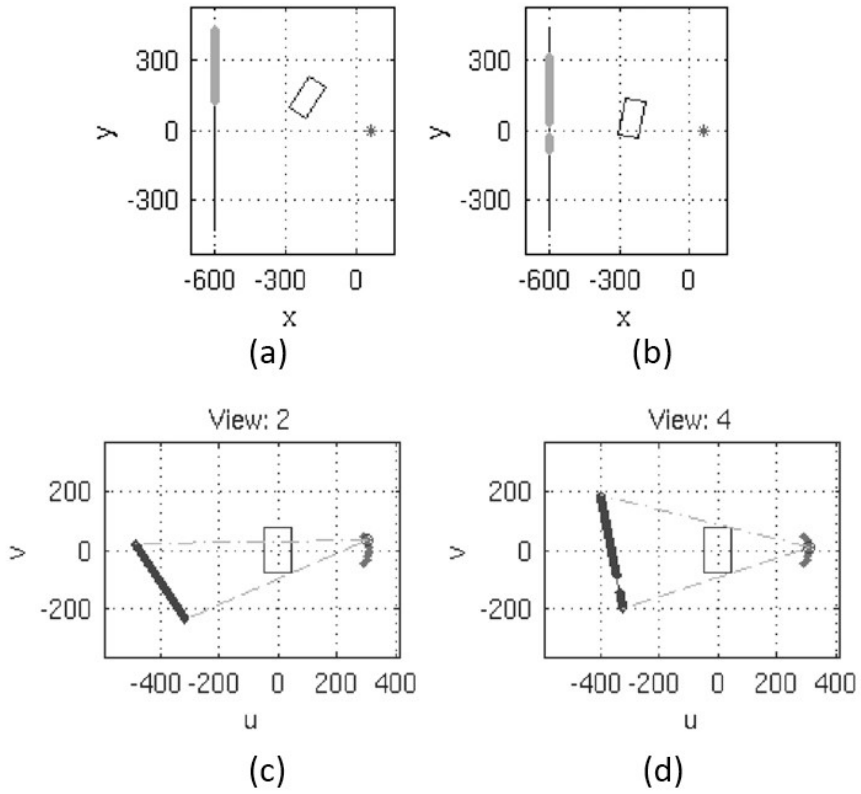


**Figure 2.12:** ObT views for the optimal single source position for the 90° turn (a, b), and their equivalents in the effective geometry (c, d). Due to the source position the system is symmetric w.r.t. x-axis. Reproduced from Reid et al. [2011a].

## 2.6 3D image reconstruction

This section describes the basic concepts of image reconstruction techniques. Reconstruction methods are advanced mathematical techniques implemented to restore the 3D distribution of a given quantity inside an object, formed by a set of its 2D x-ray projections. In advanced computed tomography, which converges to ideal sampling conditions and achieves high CNR, well known analytical reconstruction methods are used [Feldkamp et al., 1984, Isaksen, 1996, Katsevich, 2002, Szafraniec, 2013].

However, in emerging, unconventional, tomographic applications, iterative reconstruction methods are most widely implemented as they have proved significant advantages. More specifically, they are applied in the cases where a limited or non-equiangular number of projection views are available, and, as such, are highly applicable to tomosynthesis, which is defined by the limited number of views [Szafraniec, 2013]. These algebraic iterative reconstruction methods are based on the iterative solution of a system of linear equations generated from discretising the x-ray projection process. Corrections are applied to an arbitrary initial medium distribution with the scope of matching the measured projections [Isaksen, 1996]. The discretisation can be achieved

by modeling each x-ray beam as a straight line and considering the length of intersection of these lines with voxels in the reconstruction volume. In real applications however, it is unrealistic and time-consuming to compute and store all intersection lengths. Computer scientists have made multiple efforts in attacking this issue, offering effective solutions (section2.6.1).

### 2.6.1 Siddon algorithm developments

Siddon [1985] was the first to provide an exact, efficient and reliable algorithm for calculating the radiological path through a 3D CT array. The developed algorithm is able to calculate the intersection lengths by following the path of each ray through a volume, using a paremetric representation and considering the intersection points with the grid edges rather than the individual pixels (Figure 2.13). This is named *ray-tracing*. Siddon's algorithm is summarised in six action steps described in Figure 2.14. A more detailed description can be found in Siddon [1985].

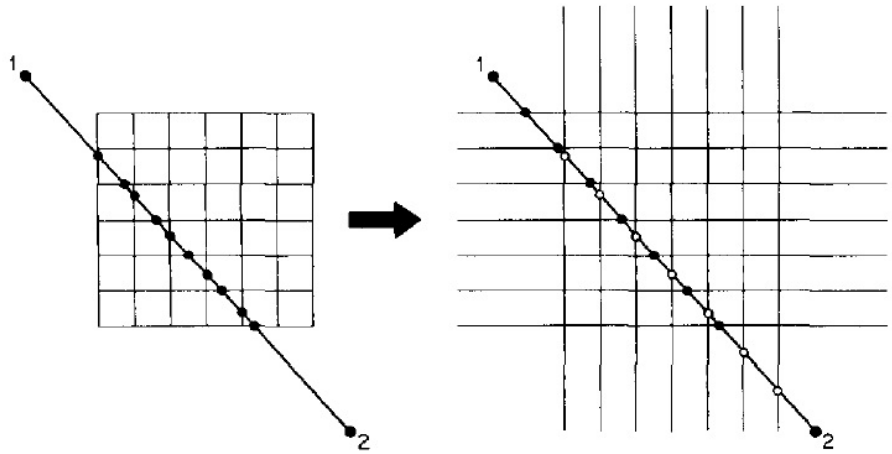


**Figure 2.13:** The pixels of the CT array (left) are consdered as the intersection areas of an orthogonal grid. The intersections of the ray with the grid edges are calculated, rather than the individual pixels. Reproduced from Siddon [1985].

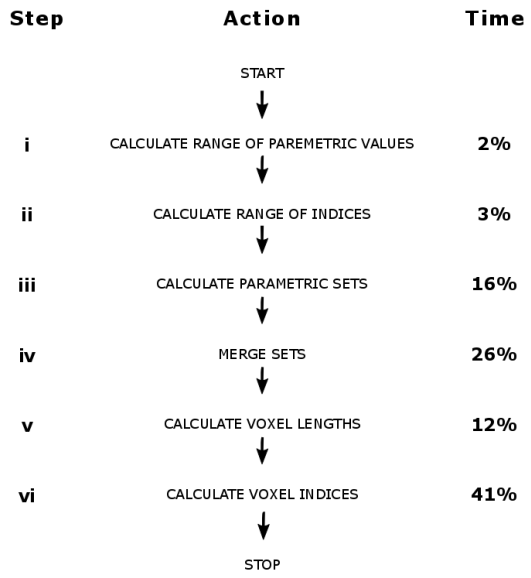


**Figure 2.14:** The flow of Siddon's radiological path algorithm. For the typical problems he studies in 1985, the relative amount of computation time required in each part of the algorithm is given by the respective percentages to the right of each part description. Adapted from Siddon [1985].

The main disadvantage of this approach is that the calculation of the indices of the intersected pixels is very complex and time-consuming. In addressing these, notable improvements were published by Jacobs et al. and Christiaens et al. in 1998 which significantly decreases the required computational time, reaching a speedup of a factor of 5.0 and 13.0 respectively for the total reconstruction time. The main advancement in both methods is that the new algorithms restrict the calculation of the intersected pixel coordinates to once per ray instead of once per pixel. It also surpasses the need to allocate memory for the different arrays.

### 2.6.2 Rigid registration

Image registration is a challenging image processing problem in many applications which is required when comparison or integration of multimodal imaging such as images resulting from different times, devices, and/or perspectives is needed [Haber and Modersitzki, 2006]. Imperative for reliable results in image registration is the incorporation of prior knowledge [Modersitzki, 2007]. One refers to rigid registration when the imaged object is rigid itself. Extensive overviews of image registration techniques can be found in Maintz and Viergever [1998], Brown [1992], Maurer and Fitzpatrick [1993], Van den Elsen et al. [1993].

In simple terms image registration is the process of estimating a mapping between a pair of images. One image is assumed to remain stationary (the *reference* image), whereas the other (the *source* or *template* image) is spatially transformed to match it [Ashburner and Friston, 2004]. The registration task

is illustrated by an example described in Fischer and Modersitzki [2004], shown in Figure 2.15. Starting with the reference $R$ (Figure 2.15:a) and template $T$ (Figure 2.15:b) images, the aim is to find a reasonable spatial transformation such that the resulting transformed template $T'$ matches $R$, or is similar to $R$ subject to a suitable distance measure. In this example, Figure 2.15:c is the result of a *linear matching* strategy which reduces its difference to $R$ by $\sim 35\%$. In Figure 2.15:d, *non-linear* matching is applied which further reduces the difference by another 30%.

There are various methods which spatial transformation is based on for a particular image, such as the use of markers, landmarks, distinct greyvalues, anatomical features, etc. These are used as constraints in the spatial transformation.

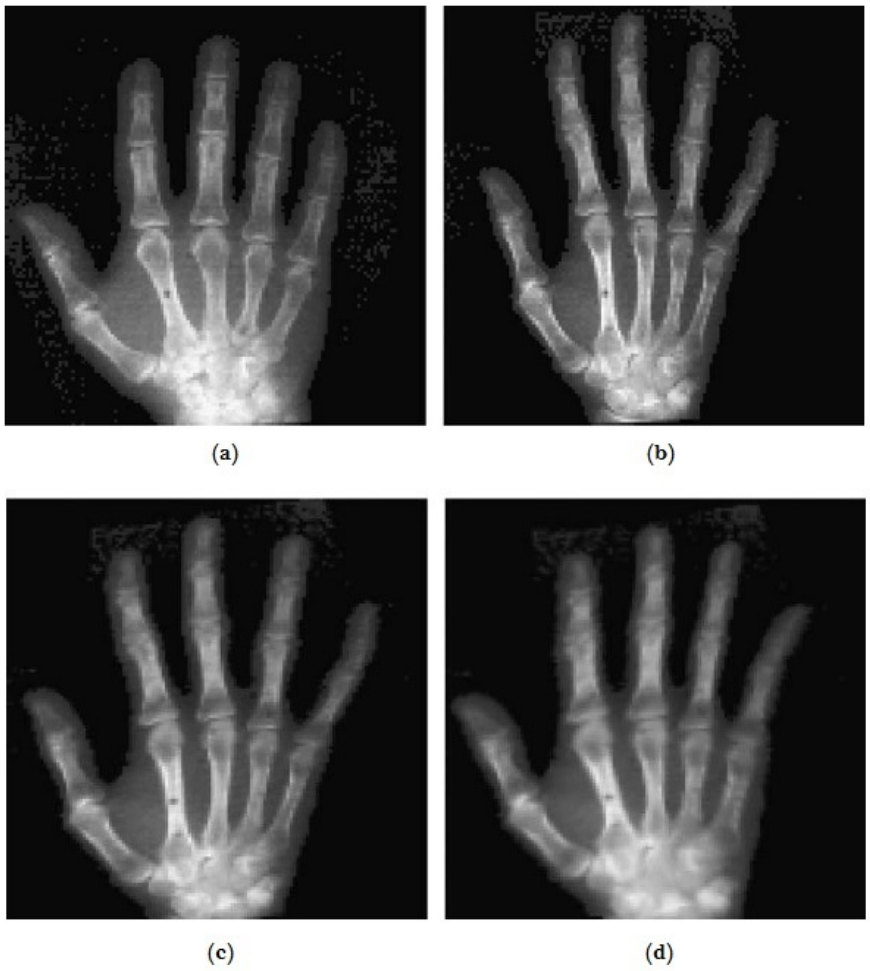


**Figure 2.15:** Registration results for X-rays of a human hand depicting (a): reference R, (b): template T, (c): transformed template T' after (affine) linear registration which reduces its difference to $R$ by ∼35%, and (d): transformed template T' after non-linear (curvature) registration which further reduces the difference by another 30%. Adapted from Amit [1994].

### 2.6.3 'Shift-and-add' reconstruction

Tomosynthesis (section 2.5) is a method of generating slice images from a finite set of projection images. There are various different reconstruction methods used in tomosynthesis, the simplest and most common being the 'shift-and-add' (SAA) technique. SAA involves calculation of the differential shifts of the images which are shifted back to a common centre and added together. It can be used for a number of difference tomosynthesis system set-ups.

The SAA method implements the fact that objects at different height distances $z$ above the detector will experience different degrees of parallax (apparent displacement) as the x-ray tube moves. Hence, the objects will be projected onto the detector at respective positions, relative to $z$.

A basic representation of the principles of SAA are given in Figure 2.16. This figure shows the three locations of an x-ray tube around an object containing a circular and a triangular object in two adjacent planes. If the x-ray tube and detector are moving synchronously in parallel planes, as is the case in the depicted example, the objects' magnification is purely dependent on z and not on the locations of the x-ray system components. Then, by shifting and adding the acquired image, the structures in certain planes (regions or objects of interest) are made to line up and thus come in focus. Structures in other planes are smeared out as they are distributed over the image and appear blurred.This method requires prior knowledge of the dimensions of the imaged volume and the respective rotation angle at which each projection was acquired. By implementing the SAA image reconstruction method in tomosynthesis, full 3D images of the screened volume can be created.

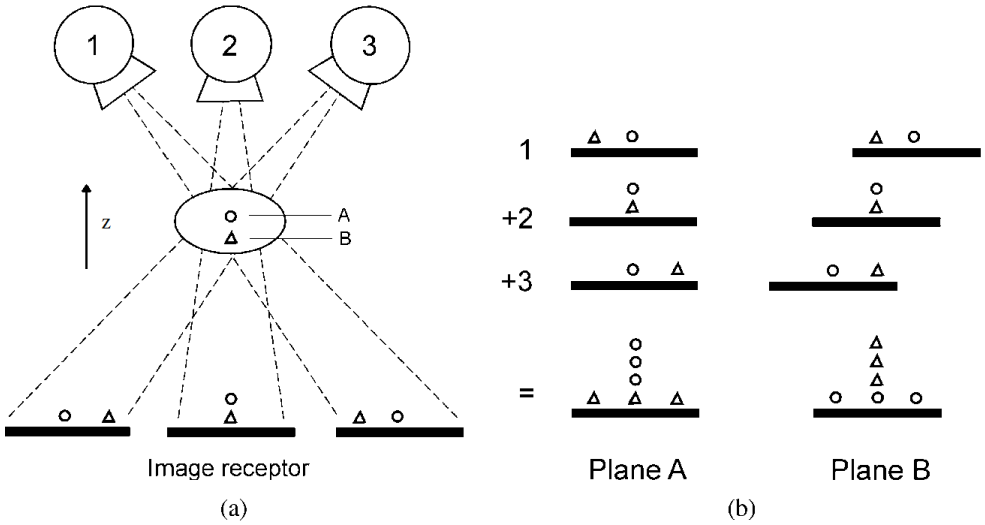


**Figure 2.16:** Principles of tomosynthesis image acquisition and SAA reconstruction. (a) Tomosynthesis imaging. The circle in Plane A and triangle in Plane B are projected in different locations when imaged from different angles. (b) The acquired projection images are appropriately shifted and added to bring either the circle or triangle into focus; structures outside the plane of focus are subsequently spread across the image (i.e. blurred). Reproduced from Dobbins III and Godfrey [2003].

## 2.7 Photogrammetric measurements

***photogrammetry*** photo + gram + metry

<Greek: *phôs* (genitive *phōtós*) "light", *grámma* "something written or drawn", and *métron* "measure".

Photogrammetry is an optical method developed for determining the shape and location of objects through analysing images recorded on cameras. Essentially it produces precise and accurate 3D object space information derived from one or more photographs, or even simpler it reconstructs the object space from images. Accurate photogrammetry incorporating x-rays technology (section 2.3) has also been developed from the reconstruction of the projection rays [Lippert and Hirsch, 1974, Veress et al., 1979], the basic principles of which are described by Brown et al. [1976]. One may consider photogrammetric reconstruction as the inverse process of image formation [Schenk, 2005]. 3D reconstruction of an object can be done either in graphical form (images, drawings, maps) or in digital form (coordinates and geometric elements) [Luhmann et al., 2006], while in modern technologies the latter is principally the method of choice, as in this study. Photogrammetry's prime advantage is the non-contact measurement of object surfaces and the simultaneous coordination of many *target or feature* points (section 2.11).

Photogrammetry, as 3D measurement technology, uses central projection imaging as its fundamental mathematical model. The 3D space information of an object is computed by the reconstruction of rays in which (for each camera)

each image point and its corresponding perspective centre determines the spatial direction of each ray to the corresponding object point [Luhmann et al., 2006]. For this, direct minimal or iterative Least Squares Estimation (LSE) solution (section 2.8.1) is implemented. Thus, given that the location of the imaging system in object space, together with the internal imaging geometry of the camera are known, every image ray can be defined in 3D object space. As follows, an object is defined in 3D object space by intersecting two or more corresponding (homologous), spatially separated image rays.

### 2.7.1 Close-range photogrammetry

Close-range photogrammetry is a term used to be distinguished from aerial photogrammetry, the former normally referring to measurements within a distance of 100 meters [Cooper and Robson, 1996]. The most accurate results are produced when images are obtained from camera positions all around the object with the camera axes highly convergent pointing towards the object centre (convergent network of images, Figure 2.22 on page 49), and is commonly applied to capture target objects [Atkinson, 2001]. The sections below discuss the fundamentals of the convergent network geometry in close range photogrammetry.

Close-range photogrammetry has established significant measurements quality, even with 'off the shelf' digital cameras, achieving precisions higher than 1 part in 100,000 [Peipe, 1997, Peggs et al., 2009]. A low-cost close-range photogrammetry system has been developed at UCL's Geomatic Engineering department for the accurate determination of spatial location for an 'optical topography' system [Wong et al., 2009]. This system has been used to determine 3D coordinates of locations on the skin and sensing pads. For static objects, it has produced results with a mean absolute coordinate discrepancy of $\leq$0.2 mm. For moving objects, the system has displayed an accuracy of $\approx$0.34 mm. Besides its high accuracy, the system is able to operate in real time and is a low cost, contactless measurement process with a simple setup within minimal infrastructure and can maintain calibration for extended periods. Additionally, the system may operate in room light, not interfering with x-ray illumination and detection.

For these reasons, this system was the chosen starting point for this study. However, a review of alternative 3D surface measurement methods for close-range applications can be found in Abreu de Souza [2009, chapter 5.10]. Its significance comes in that it is a flexible tool which can provide the 3D and 6DOF (six degrees of freedom, section 1.3) measurements required for the OBT image reconstruction.

## 2.8 Ideal camera: Central Perspective Projection

First of all, the principles of a single camera (and image) geometry are described, on the basis of an *ideal* camera configuration. This ideal case is grounded on the *central perspective projection* model [Atkinson, 2001]. In the central perspective projection model illustrated in Figure 2.17, $X_A$ is an object point in 3D space, which is projected through the perspective centre of the imaging system $X_O$ onto the *projection plane*, where it produces an image point $x_a$. In other words, light from $X_A$ travels in a straight line creating image point $x_a$ while passing through the camera centre $X_O$.

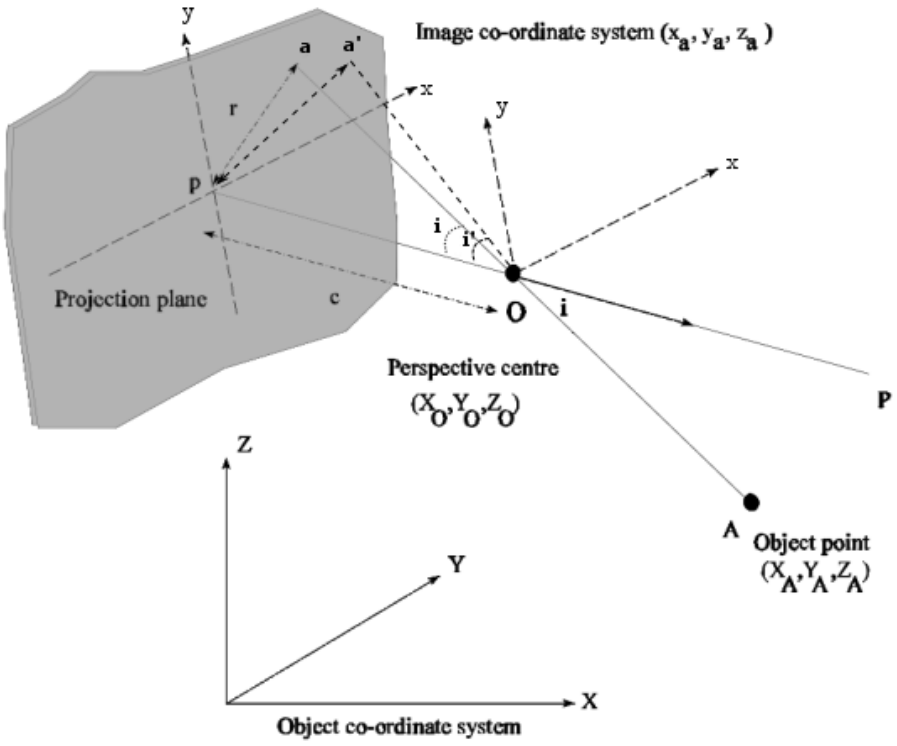


**Figure 2.17:** Central perspective projection graphical representation, including change in theoretical image position due to lens distortion in the camera. For a description of annotation refer to Table 2.2. Adapted from Atkinson [2001].

*Projection plane* is the plane of the image points' formation and its centre in an ideal imaging system coincides with the *principal point p*. $c$ is the *principal distance*: the distance between the principal point $p$ and the perspective centre, perpendicular to the projection plane. As such, $c$ falls on what is called the *principal axis*. {X,Y,Z} is the object space coordinate system located arbitrarily in space, while {x,y,z} is the image coordinate system who's z axis coincides with the principal axis, while the x and y axes are parallel to the projection plane.

Given the points of known coordinates: $A(X_A, Y_A, Z_A)$, $O(X_O, Y_O, Z_O)$ in {X,Y,Z}, and $a(x_a, y_a, z_a)$ in {x,y,z} where $z_a = -c$. The coordinates are

known in their respective coordinate system as noted. Given these, the relative relations can be calculated with appropriate rotation of the image coordinate system {x,y,z} so that it fully aligns with the object coordinate system {X,Y,Z}. This is given by the *collinearity equations* [1]:

$$x_a = \frac{-c\Big(r_{11}(X_O - X_A) + r_{12}(Y_O - Y_A) + r_{13}(Z_O - Z_A)\Big)}{\Big(r_{31}(X_O - X_A) + r_{32}(Y_O - Y_A) + r_{33}(Z_O - Z_A)\Big)} \tag{2.10}$$

$$y_a = \frac{-c\Big(r_{21}(X_O - X_A) + r_{22}(Y_O - Y_A) + r_{23}(Z_O - Z_A)\Big)}{\Big(r_{31}(X_O - X_A) + r_{32}(Y_O - Y_A) + r_{33}(Z_O - Z_A)\Big)} \tag{2.11}$$

where $r_{ij}$ are the elements of a 3x3 *rotation matrix* $R$ which maps the orientation of {X,Y,Z} onto {x,y,z}. The rotation matrix $R$, related to the rotation of angles $\omega, \varphi, \kappa$ around the X, Y, Z axes respectively is mathematically calculated by the second equation below [Cooper and Robson, 1996]:

$$R = R_{\omega\varphi\kappa} = \begin{bmatrix} r_{11} & r_{12} & r_{13} \\ r_{21} & r_{22} & r_{23} \\ r_{31} & r_{32} & r_{33} \end{bmatrix} \tag{2.12}$$

$$R = \begin{bmatrix} cos\varphi cos\kappa & sin\omega sin\varphi cos\kappa + cos\omega sin\kappa & -cos\omega sin\varphi cos\kappa + sin\omega sin\kappa \\ -cos\varphi sin\kappa & -sin\omega sin\varphi sin\kappa + cos\omega cos\kappa & cos\omega sin\varphi cos\kappa + sin\omega cos\kappa \\ sin\varphi & -sin\omega cos\varphi & cos\omega cos\varphi \end{bmatrix} \tag{2.13}$$

| Description | | Coordinates | Details |
|---|---|---|---|
| | **Object space** | | |
| {X,Y,Z} | object space coordinate system | | |
| A | object point | $(X_A, Y_A, Z_A)$ | |
| O | camera perspective centre | $(X_O, Y_O, Z_O)$ | |
| $R$ | rotation matrix | | |
| $r_{ij}$ | the elements of $R$ | | |
| $\omega, \varphi, \kappa$ | rotation angles in $R$ | | related to the rotation around the X, Y, Z axes respectively |
| | **Image space** | | |
| {x,y,z} | image space coordinate system | | |
| $a$ | image point | $(x_a, y_a, -c)$ | |
| | projection plane | | the plane of the image points' formation |
| $p$ | principal point | | centre of image projection |
| | principal axis | | axis perpendicular to the projection plane which goes through the principal point $p$ |
| $c$ | principal distance | | the distance between the principal point $p$ and the perspective centre $O$, perpendicular to the projection plane |

**Table 2.2:** A description of the object and image space parameters, which are used in the central perspective projection illustration in Figure 2.17.

[1] under the assumption of an ideal imaging system (camera)

### 2.8.1 Least Squares Estimate

In statistics, regression analysis is a statistical process for estimating relationships between variables [Sykes, 1993]. Photogrammetric solution uses least squares estimates (LSE) a statistical tool in regression analysis for estimating the relationships among variables, which offers an approximate solution to overdetermined systems. This means that LSE is used in the cases when more measurements are available than the required minimum to evaluate an unknown parameter (more equations than unknowns). LSE takes its name from the fact that the overall solution minimises the errors' sum of squares which are made in the results of each equation. The most important application of the LSE tool is in data fitting. In principle, the LSE method derives a unique set of variable estimates of certain properties minimising the cost function of the model fitting error, i.e. the weighted sum of squared *residuals* [Cooper and Robson, 1996], a residual being the difference between an observed value and the fitted value provided by the LSE model. For further detail on the LSE theory, Cooper [1987], Dermanis [1986], Mikhail and Ackermann [1976], NPL [2001] offer comprehensive coverage.

LSE can be applied to approximating a given function by a weighted sum of other functions. This model can be used to estimate the parameters of a wide variety of functional models from measurements made with sensors. Within this thesis it is applied to the solutions of photogrammetric perspective projection including *resection, intersection* and *bundle adjustment* (sections 2.8.3, 2.8.4, and 2.8.5) and also to 3D circle fitting in order to compute the source location and rotation centres for the OBT system (sections 5.3.2, 5.4.5). The best approximation can be defined as that which minimises the sum of the square of the differences between the compted values of the observations made using the functional model and the actual observations made. This is done by iteratively comparing the estimate of what the computed measurement should be with the actual measurement made; of which the discrepancy between these two values is the residual. All of the cases used in this thesis were non-linear, so solution can be found. The LSE process is iterated to find the minimum value for the sum of squares of the residuals, which determines the quality of the approximation. In the photogrammetric case, best estimates of the parameters in the collinearity equations and potentially systematic errors in the imaging system are modelled.

A stochastic, meaning statistically random, model is considered on the basis that each measurement has a weight which can depend on the sensor used to record it, geometric configurations, angle of incidence, image contrast. Thus the stochastic model allows individual measurements to be weighted according to the sensor expectation. A weight matrix is used to propagate the stochastic model through the LSE.

Using an ideal camera to photogrammetrically compute 3D object space information requires the processes of *resection,* where the targets are fixed, or *intersection,* where the images are fixed, or a *bundle adjustment* which combines both (described in sections 2.8.3, 2.8.4, and 2.8.5respectively).

The underlying assumption of an ideal camera, is that its interior orientation is perfect. This would mean that the angle $i$ determined in the image space is equal to the angle in the object space, such that the formed image point $a$ directly corresponds to the true value. However, with a real camera these angles are not equal (see $i$ and $i'$ in Figure 2.17) and need to be modelled with the camera lens model. The geometry of a real camera and its parameters are described in section 2.9.1.

### 2.8.2 Exterior camera orientation

The position and orientation of a camera consist its pose (Figure 2.18). Camera position relates to the coordinates of its perspective centre $p$ , which are the three translations $(X_O, Y_O, Z_O)$ with respect to the object coordinate system. Camera orientation relates to the three rotations $(\omega, \varphi, \kappa)$ which are expressed with respect to the directions of the X, Y and Z axes respectively. It is considered optimum for the exterior orientation of a camera, or a network of cameras to be re-calibrated before each set of experimental image acquisitions. Given known coordinates in the object space, the pose parameters of the camera can be computed through *resection* (section 2.8.3) or where a simultaneous solution for object and camera pose is required through *Bundle Adjustment* (section 2.8.5).

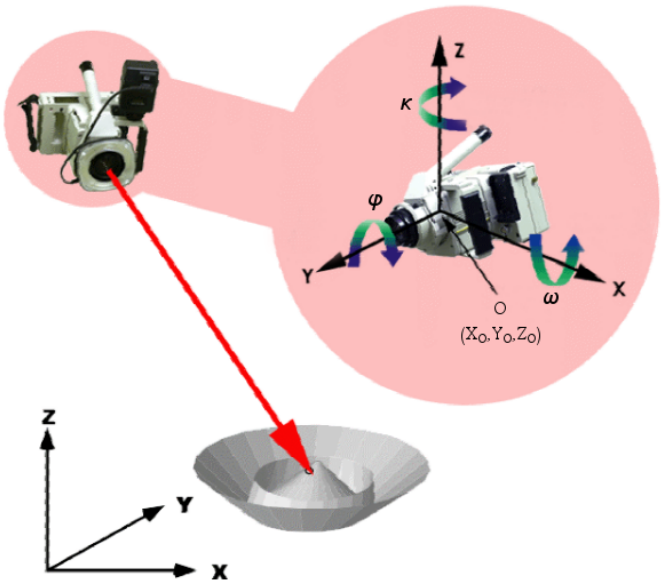


**Figure 2.18:** Representation of a camera pose (exterior orientation parameters) which are its rotation (X,Y,Z) and translation $(\omega, \varphi, \kappa)$ about its perspective centre $O$. Adapted from [Geodetic, 2015].

### 2.8.3 Resection

Resection is a computational process which determines the pose parameters (position and orientation) of a camera, i.e. exterior orientation parameters (section 2.8.2), with respect to an object space coordinate system [Mikhail et al., 2001]. Resection requires a minimum of two images in order to solve the collinearity equations. This results in a pair of collinearity equations with three unknowns $(X, Y, Z)$, which confirms how *LSE* (section 2.8.1) is appropriate. Given the series of collinearity equations, measurements in an image can produce the required parameters to be estimated, the camera's 6DOF, which correspond to its tranlation $(X_O, Y_O, Z_O)$ and rotation $(\omega, \varphi, \kappa)$ parameters (Figures 2.19 and 2.18). The perspective centre $p$ determines a camera's pose $(X_O, Y_O, Z_O, \omega, \varphi, \kappa)$ at the instant the image was taken. Therefore, resection determines the appropriate exterior orientation parameters on a single image. A minimum of three non-collinear targets, also named control points (section 2.11), are necessary for succesful resection [Gomarasca, 2009].

As an example, if the relative locations and orientations of two images are known, a LSE of the coordinates of a 3D point visible in both images can be estimated. Increasing the number of images, increases the degrees of freedom and therefore improves the solution, after which *intersection* (section 2.8.4) can compute the coordinates of new selective points of interest in image space.

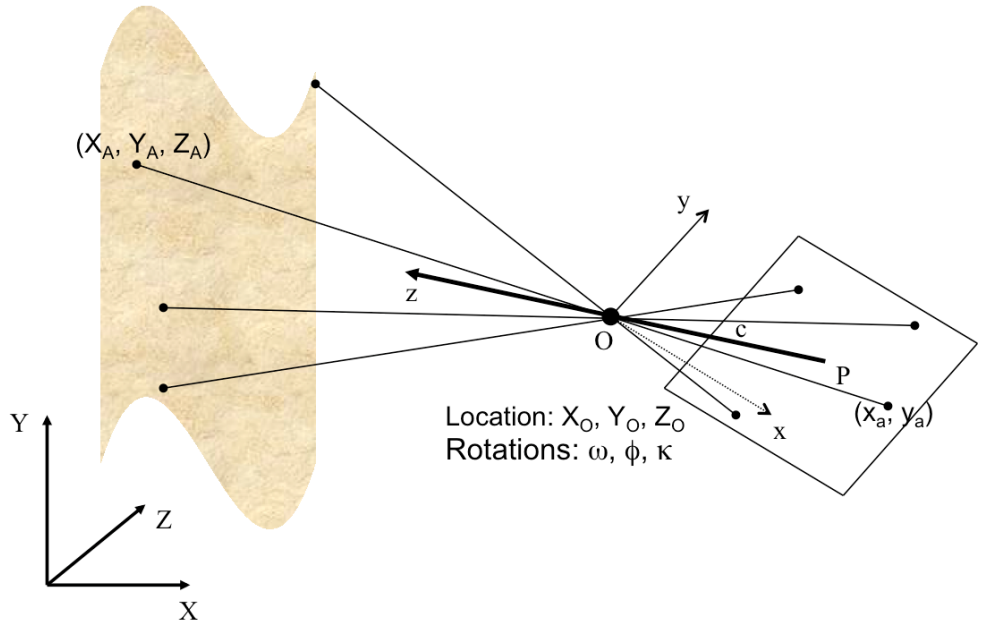


**Figure 2.19:** Photogrammetric resection. Reproduced from Robson [2005].

### 2.8.4 Intersection

In order to measure the coordinates of new (unknown) 3D data points, the process of *intersection* is carried out (Figure 2.8.4). This is done following the resection (section 2.8.3) of a camera determining its pose (section 2.8.2). Intersection is performed using (two or more) overlapping views of an object,

while implementing a camera's interior and pose parameters. Intersection can be performed using single camera systems (with several images, obtained from a range of positions forming a convergent network [Figure 2.22] for sufficient intersection angles) or with stereo camera systems (with pairs of images). In providing an automated technique to identify the necessary homologous points across images, epipolar geometry is used. This is an important photogrammetric assembly tool, since for a selected point in one reference image, in order to find the same point in another (overlapping) image, the search is constrained along a line, instead of searching the whole image [Mikhail et al., 2001]. However, this tool is not required when coded targets (section 2.11) are implemented.

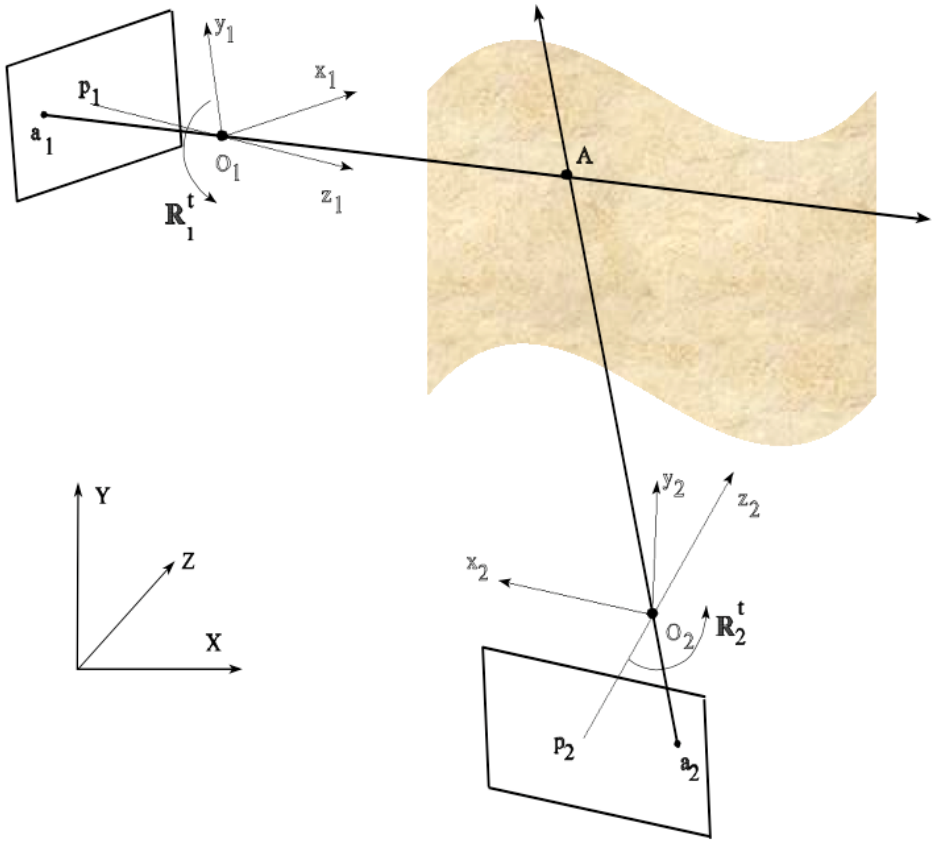


**Figure 2.20:** Photogrammetric interesection. Reproduced from Robson [2005]

### 2.8.5 Bundle Adjustment

In overview, *bundle adjustment* (BA) can be used to simultaneously determine the pose of each image in a network, the coordinates of all targets or features (within), and the internal imaging geometry of a camera (*calibration parameters*, section 2.3) [Granshaw, 1980]. In a real camera, given a strong network geometry, the departures from collinearity can additionally be determined through a calibration process (section 2.9.2), which include the camera parameters discussed in section 2.9.1.

BA is the simultaneous numerical fit of an unlimited number of spatially dis-

tributed images. This implements photogrammetric observations (measured target points - section 2.11), survey observations and an object coordinate system. Single images can be merged into a global model with the use of 'tie' points, producing a 3D reconstruction of the object surface. Through a minimum number of reference (target) points, the global object coordinate system is determined allowing larger areas without reference points to be bridged by multi-image sub-sets [Luhmann et al., 2006]. Simply, it uses LSE (section 2.8.1) in global minimisation of the re-projection errors based on the collinearity equations (section 2.8). Since all parameters are estimated simultaneously in the BA, any errors in object space coordinates, camera pose, and camera calibration are distributed across the LSE model rather than being locked in place, as would be the case for resection with one or more incorrect 3D object coordinates.

BA employs a predominant system of equations in estimating 3D object coordinates, image orientation parameters together with related statistical information about accuracy and reliability (section 2.12). "Bundle adjustment is the problem of refining a visual reconstruction to produce jointly optimal 3D structure and viewing parameter (camera pose and/or calibration) estimates." [Triggs et al., 2000: 1]. Optimal means that the parameter estimates are found by minimizing the cost function that quantifies the model fitting error (weighted sum of squared residuals), while at the same time providing a LSE (section 2.8.1) solution which is simultaneously optimal with respect to structure and camera variations. The name refers to the 'bundles' of light rays travelling from each 3D feature and converging on the camera centre, which are optimally 'adjusted' with respect to both feature and camera positions [Triggs et al., 2000]. The main reasons for selecting the method of bundle adjustment as an appropriate approach for multi-view modelling are its flexibility, efficiency and quality control [Luhmann et al., 2006, Cooper and Robson, 1996, Triggs et al., 2000]. The latter is expanded in section 2.12. BA is a method which has the ability to process large volume data and enable system automation [Rova, 2010]. "Since all measured values, and unknown parameter of a photogrammetric project are taken into account within one simultaneous calculation, the bundle triangulation is the most powerful and accurate method of image orientation and point determination in photogrammetry" [Luhmann et al., 2006:229].

BA is used to accurately derive the interior and exterior orientation parameters (sections 2.9.1, 2.8.2 respectively) using the same collinearity equations as resection (section 2.8.3). It is then able to compute the 3D coordinates of targets through intersection (section 2.8.4). There are several commercial packages which perform automatic BA, recovering the orientation and calibration parameters of a network of images either using retro-reflective or colour coded targets (VMS [Geomsoft, 2015], iWitness$^{TM}$ [Photometrix, 2015]), or

using exterior orientation devices (V-Star$^{TM}$ [Geodetic, 2015], DPA-Pro$^{TM}$ [EOTECH, 2015], Australis$^{TM}$ [Photometrix, 2015]) [Wong, 2012]. For this study, photogrammetric calibration was processed in VMS (Vision Measurement System), which is described in section 5.2.1.1.

## 2.9 Real camera

An ideal camera (described in section 2.8) assumes a perfect interior orientation, such that any formed image point directly corresponds to its true value. In reality, practical cameras have optical imperfections or aberrations that mean that the actual formed imaged point is oset from the value expected from an ideal perspective projection. As the assumptions which the collinearity principle is based on are not achievable in practice, it is necessary to define the real camera deviation (distortions) from the ideal model [Abreu de Souza, 2009]. This is shown as a' in Figure 2.17 which is formed at an angle i', instead of i. In order to adjust for this, camera calibration is performed to determine how the geometry of image formation of a real camera differs from that of an ideal camera [Cooper and Robson, 1996]. This process is the *camera calibration* (section 2.9.1). By precise assumptions, it is meant that the image formed by a real camera will have aberrations that may degrade the image quality and alter the position of the image [Clarke and Fryer, 1998]. These can arise from the nature of the digital imaging system which can cause perturbations such as symmetric radial distortion, decentering distortion, focal plane unflatness and in plane distortions [Fraser, 2001]. In modern systems however, the key issues are image compression and pixel re-sampling for different image formats, which leads to the need to calibrate not just the camera but also the complete imaging system.

### 2.9.1 Interior camera orientation

The interior orientation parameters of a camera correspond to its intrinsic imaging properties defined by perspective projection and systematic image distortions inherent in the camera optics [Karara, 1989]. In order to determine these parameter values, camera calibration is performed. The purpose of the calibration is to determine how much the geometry of image formation in a real camera differs from that of an ideal camera [Cooper and Robson, 1996]. The calibration parameters describing a camera's internal geometric configuration are shown in Table 2.3. Some of these are seen in Figure 2.21, where the departure of a real camera lens from the central projection assumed by collinearity is shown. Using LSE (section 2.8.1), departures from the central projection can be modelled as systematic errors in the collinearity condition (section 2.8). Ideally, the interior orientation of a photogrammetric camera should be physically stable such that it only needs re-calibration over a long time period, which in the case of this project might amount to several months.

| Parameter | | # | Notes |
|---|---|---|---|
| Principal point | $p_x$<br>$p_y$ | 1<br>2 | The point on the image plane where the optical axis of the lens intersects with the image format. In an ideal camera the principal point location would coincide with the origin of the photo coordinate system. |
| Principal distance | $c$ | 3 | The distance between the principal point p and the perspective centre, perpendicular to the projection plane. |
| Radial lens distortion | $K_1$<br>$K_2$<br>$K_3$ | 4<br>5<br>6 | A real lens is subject to aberrations some of which alter the geometry of the image formed. One to three parameters are sufficient to describe most lens distortion profiles. |
| Tangential lens distortion | $P_1$<br>$P_2$ | 7<br>8 | This distortion results from misalignment of individual lens elements during lens construction. The magnitude is typically much smaller than that of radial lens distortion. Two parameters are required to describe the magnitude and alignment. |
| Image deformations | $C_{orth}$<br>$C_{aff}$ | 9<br>10 | Orthogonality and affinity are applied to the image plane but are most often associated with optical effects. |

**Table 2.3:** Calibration parameters describing a camera's internal geometric configuration. [Robson, 2005].

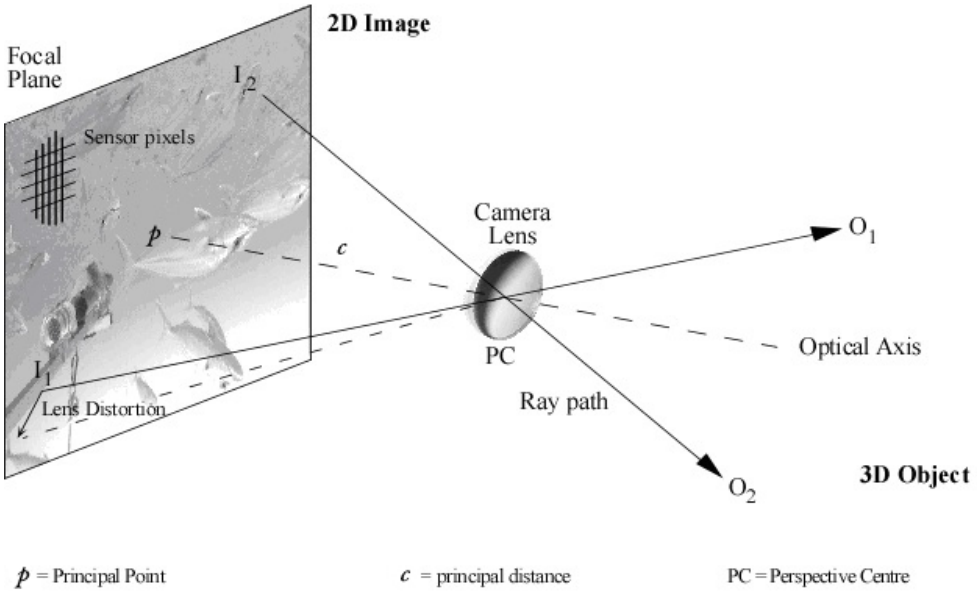


**Figure 2.21:** Collinearity assumes the camera produces a perfect central projection. In real camera lenses many factors contribute towards geometric departures from this situation. These include: principal point variation, principal distance change (due to focus and zoom), lens distortions (due to variations in diffraction), and sensor unflatness. Using *least squares estimates*, departures from the central projection can be modelled as systematic error in the collinearity condition. Adapted from Robson [2005].

### 2.9.2 Estimation of interior camera orientation

Given a strong network of images, BA can simultaneously not only estimate the 3D coordinates in object space and pose parameters, but it can also estimate the parameters of interior orientation of one or more cameras.

The parameters describing the geometry of a camera (Table 2.3) can be determined through a variety of different calibration methods [Fryer, 1996], such as:

**Laboratory calibration**: the properties of a camera system are investigated under carefully controlled conditions. For this, there are several possibilities, all of which have the common feature that the calibration is completely sep-

arately from imaging the object. The laboratory methods rely on a precise knowledge of the position and/or direction of light beam or targets, used to signalise locations on an object (section 2.11).

**Self calibration:** an array of special targets (section 2.11) set within the ROI is imaged from multiple viewpoints and parameters of camera interior orientation are computed using BA techniques (section 2.8.5). This is further described in section 2.9.2.1.

#### 2.9.2.1 Self-calibration

A popular calibration method, which is used in all cases during this study, is self calibrating bundle adjustment, often simply termed *self-calibration*. In this method an array of *targets* (section 2.11) is imaged from multiple viewpoints and the camera interior orientation parameters are calculated using *bundle adjustment* (*BA*, section 2.8.5).

As described in LSE theory, departures from the central projection can be modelled as systematic errors in the collinearity condition. The particular calibration parameters are listed in Table 2.3, some of which are shown in Figure 2.21. The relationships of a subset of the target points require precise known dimensional constraints in providing a complete solution to these equations. Here, this is provided by calibration images, in which the geometry and distances between grid points are known a priori, although in each calibration image the grid pose is unknown. In theory, the equations can then be solved, even though, in practice, the existence of measurement error suggests that this must be an approximate solution. This solution has to be determined by numerical optimization, since the equations are nonlinear. The optimisation process used here is a BA, which is one of the most widely used techniques in photogrammetry [Atkinson, 2001, Hartley and Zisserman, 2003].

A self-calibrating BA is used to simultaneously estimate the positions and orientations of each image as well as a common set of camera calibration parameters (Table 2.3). Robson et al. [1993] reported that the principal point offsets together with their uncertainties can be easily determined and used as the initial approximate values for the subsequent BA process. An efficient technique in recovering the principal point offset and principal distance is creating a strong imaging network from a multiple camera convergent geometry around a calibration reference object such as that shown in Figure 2.24. Clarke [1994] reported that in a single convergent network around the reference object, unreliable or inaccurate estimates of several or all of the interior orientation parameters may occur because each camera contributes only a single image in the network. The solution to this problem is the production of multiple views of the reference object by each camera. Similar work was

carried out leading to a self-calibrating BA, and is presented in section 5.3.

## 2.10 Deployment of photogrammetric solutions

The following sub-sections are possible solutions to photogrammetric measurement deployment, where the task is to track an object in space. The first, is using a group of two or more cameras combined in a network imaging a common ROI. A second method, is using a single camera when the shape being tracked is a rigid body. In both cases photogrammetric methods used in this thesis require that the object has distinct features that can be mapped from image to image across the sequence.

### 2.10.1 The use of multi cameras in an imaging network

Multi-camera tracking methods have rapidly developed in the last twenty years. The knowledge that the researchers have acquired and published has provided valuable insights of creating a system with multiple cameras. Typically, it is concluded that the more cameras included, the better the tracking results in the aspect of shape recovery and tracking accuracy [Wong, 2012]. Nevertheless, the cost of building such a system could decidedly increase with the number of cameras employed. One particular issue reported, is the considerable effort and cost required to synchronise cameras [Kanade et al., 1997].

In a multi camera network, there is a setup process, the calibration and orientation of sensors, which is followed by a live process whereby 3D coordinates are estimated in a sequence over time. In the later, the camera's pose parameters are found by the process of resection (section 2.8.3), using a minimum of three known points in object space to be imaged by all cameras [Wolf and Dewitt, 2000]. A range of practical network design examples can be found in El-Hakim et al. [2003]

A tracking system addressing asynchronous input is a head tracker developed at the University of North Carolina [Gottschalk and Hughes, 1993, Welch, 1996, Welch et al., 1999, 2001, Azuma and Bishop, 1994, 1995]. In this system the sensors (photodiodes) are fixed on a target (section 2.11) and can observe outward infrared light-emitting diodes affixed on the ceiling. During the tracking, only one beacon is seen at any time, and consequently only partial data about the target position is collected. Some example commercial systems developed for motion capture include Motion Analysis Cooperation and Vicon Motion Systems, where Vicon provides a substantial level of automation in its use in UCL Department of Computer Science and NASA. Active or passive markers are required by these systems, affixed on the target, to provide fast and robust 2D feature extraction, with a small increase of the system's intrusiveness. 10 to 20 cameras are typically employed in obtaining a large working volume and to decreasing occlusion [Wong, 2012]. Nevertheless, cameras still

needed to be synchronised, and not much work has been published in applying asynchronous and usage of a combination of different cameras. Additionally, these systems offer a restricted tracking support of numerous point due to the fact that point features are simple and it is difficult to differentiate one from another. Importantly, the pretensioned competitors would be of undesirably high costs, given the cost-effective parameter which defines this study.

As discussed in section 2.7.1, most accurate results are produced in image network geometries with camera axes convergent towards the object centre [Atkinson, 2001]. An example of a convergent image network geometry that is formed for 6 image views imaging a 3D volume for the perspective camera sensor is illustrated in Figure 2.22.

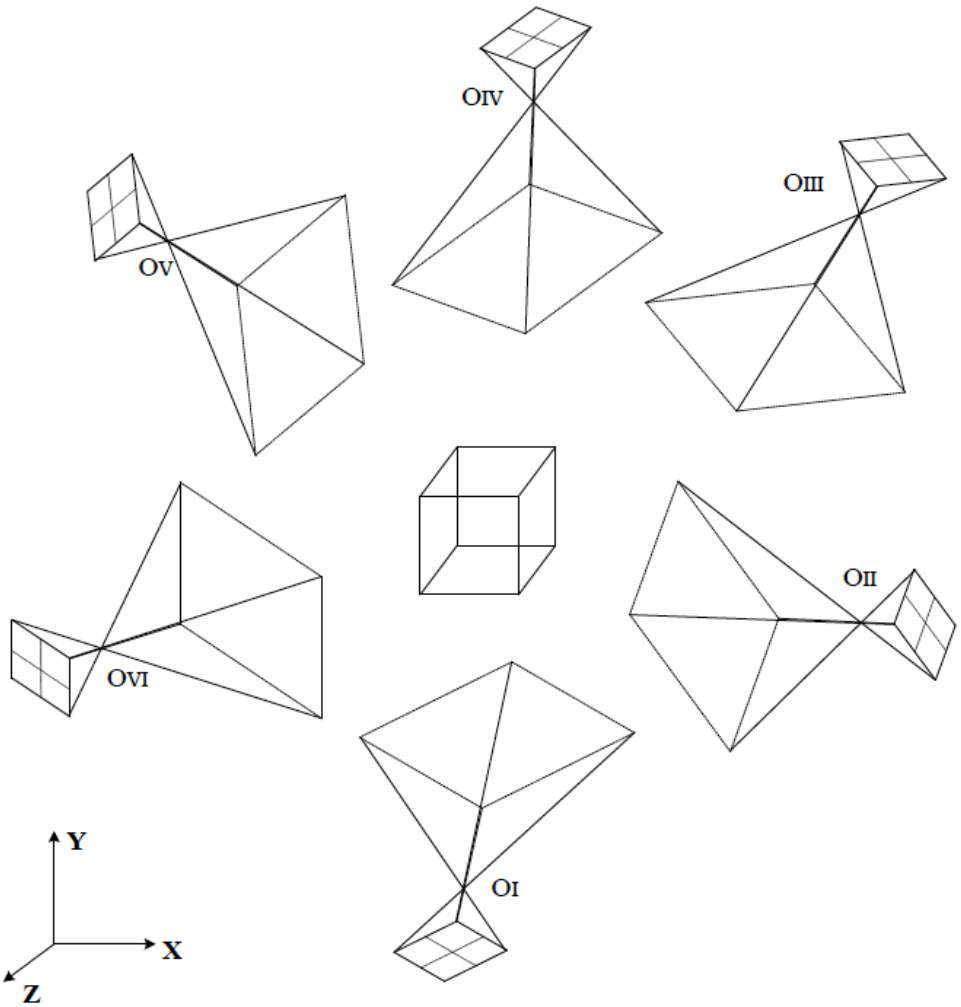


**Figure 2.22:** An illustration example of a convergent image network geometry that is formed for 6 image views imaging a 3D volume for the perspective camera sensor. Reproduced from Rova [2010].

A long cost solution was built by Wong [2012]: a rigid multi-webcam tracking system, incorporating Logitech C500 webcams, with a total cost under £400 which proved to be reliable in terms of delivering consistent target tracking precision and accuracy over time. Outcomes from his study showed a system involving 4 webcams to be adequate in providing coordination on most targets

situated on a surface, while an 8 webcam-system built, proved capable to cover targets in 3D space with occlusion. The latter tracking solution works in general environments, and in more cluttered environments, like those that could be seen in the course of an optical topography test, it was proved to be working particularly well.

### 2.10.2 Single camera photogrammetry

A single image from a single camera can be used to extract 3D information given additional information, for example when the form of the object (such as in the case of this study) or the projection plane of the object is known. [Luhmann, 2005, 2009, Bethmann and Luhmann, 2012, Helle et al., 2015, Aamdal, 1993].

In the scope of this study, the single camera principle can be applied to such tasks where one or more objects (*tracked targets*) can be seen in the 6DOF mode according to a local reference body (*reference*) that is in the same FOV. If the local coordinates of the tracked target and reference system are known, two separate space resections (section 2.8.3) can be computed for the camera. The 6DOF parameters (Table 1.3 on page 6) of the tracked target according to the reference can be extracted from resection without the need of a stable camera position. I.e the 6DOF solution does not assume that the camera is static. In industrial metrology this technique is of growing interest when motion or orientations of an object are detected by only one camera. Single camera solutions are particularly advantageous in applications where cameras involve huge investment expenses, or where several cameras cannot be used because of technical or environmental reasons [Luhmann, 2009]. Additional advantages of such systems are: ease of use (user friendliness, flexibility, portability), stability, fast and reliable point identification, unique mathematical solution, fast convergence, accuracy, and speed [Aamdal, 1993]. The method can be applied to the observation of 6DOF parameters of a moving local object according to a stationary local reference. Additionally, it can be used to track an object in dynamic mode using image sequences, in order to solve for the 6DOF values between adjacent time steps [Aamdal, 1993].

Luhmann [2009] made the observations that pitch and yaw (Figure 41) behave equally, while the roll about the viewing axis is computed much better than the two other angles. While also [Aamdal, 1993] reported higher accuracy results in the x-y plane (lateral and vertical axes which are parallel to the *charge-coupled device* (CCD) sensor inside the camera) than in the z direction (along the depth axis which is perpendicular to the CCD sensor). Accuracy is a function of camera characteristics, camera to object distance and geometry of the targets [Aamdal, 1993].

## 2.11 Object targeting

Artificial targets are used in many applications to signalise locations on an object required to be measured. Shortis et al. report that in the recent decades "...there have been a number of advances in the efficiency and effectiveness of image-based metrology systems... arguably the most important factor has been the automatic detection, recognition, identification and measurement of artificial targets used to signalise points of interest." [Shortis et al., 2003: 202]. In photogrammetry, acquiring a variation of image views of the same target is effective because of its ability to locate homologous features to subpixel accuracy and to assess the dimensional stability of the camera and the object during imaging [MacDonald, 2014]. The process of object targeting involves the two fold task of *recognition* and *location*, in computing the subpixel locations of target images. First, recognition requires the *unambiguous* identification of each target within an image. Second, locating the target requires precise and accurate determination of the target image centre.

Object targeting may implement natural features, based on texture content and geometry (such as natural locators: points, edges, regions), or artificial features [Rova, 2010]. The nature of the latter often make them the option of choice as they can be vastly personalised and adapted to the measurement purpose and set-up. Target artificial features can be manual (natural or retro-reflective, coded, colour, white diffuse spheres, eccentric, LEDs) or projected light (such as lasers) with relation to their form, and passive or active with relation to their illumination (for a more extensive analysis on object targeting consult Clarke [1994], Luhmann et al. [2006]). For unambiguity, targets are optimally designed to produce sufficient contrast against their background (often designed to be the brightest or darkest object in an image), or to form specific patterns which are unlikely to be accidentally replicated by the background features combined with perspective distortion [Shortis et al., 1994].

The coordinates of the targets computed photogrammetricaly produce the 3D network required [Faugeras and Hebert, 1986]. The most widely implemented are circular targets (Figure 2.23:a) due to the radial-symmetric design; as in photogrammetry, where the centre of the target is used to represent the actual 3D point to be measured. *Coded targets*, which are formed high contrast dot with a pattern around it (Figure 2.23:b,c,d) , are also often used as they can be uniquely identified automatically by a software program from the images. Figure 2.23 illustrates a selection of target samples utilised in close range measurement.

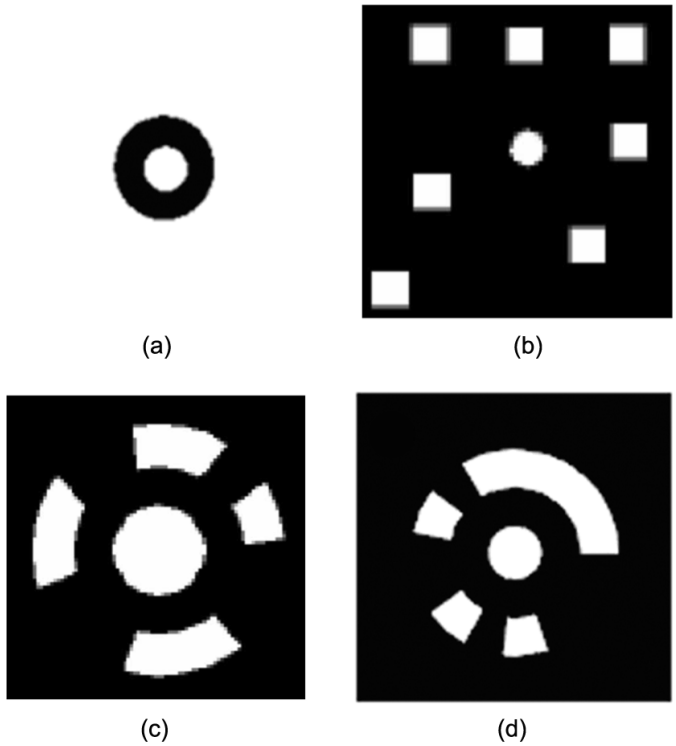


**Figure 2.23:** (a): Typical circular target. (b-d): Example coded targets.

Usefully, the determination of the target centre is rotation-invariant, and, also scale-invariant over a wide range of image magnifications [Luhmann et al., 2006]. In digital imaging the target centre is either calculated by centroid methods, correlation with a reference pattern, or by analytical determination of circle or ellipse centre. In the latter method, target coordinate precision values are computed from the imaging geometry of the photogrammetric network in combination with the uncertainty of the target image measurements through LSE (section 2.8.1). Such information is internal to the network and hence can only provide precision information concerning the computed coordinates [Robson et al., 1993]. External checks, for example against independently measured distances between physical targets are necessary to determine the accuracy of the system (section 2.12).

### 2.11.1 Retro-reflective targets

A large variety of targets have been used for 3D measurement. For many applications the retro-reflective target offers the best overall performance of the manually applied types [Clarke, 1994]. Special object targets have been created consisting a thin retro-reflective material whose characteristic is the high return of light in the direction of illumination. These are either covered by a black surround according to the target pattern, or are stamped in an equivalent form from the raw material. These retro-reflective targets consist either of a dense arrangement of small reflective balls, or an array of microprisms [Clarke, 1994]. For maximum contrast to be obtained between the targets and background, the former must be illuminated from the viewing direction of the

camera. However, normal room lighting conditions have proved sufficient for close-range photogrammetry, which is what was used in this study. This is also an important factor confirming the feasibility of the implementation of this technique in normal airport conditions.

### 2.11.2 Calibration reference object

In order to calibrate the interior and exterior orientation of a camera, a set of images of a reference object must be acquired. Its three imperative characteristics are that it is rigid, 3D of a size as big as the image space as possible (within practical limits), and has fitted targets. The total size of the object should be larger than the objects to be imaged. Also, the reference object targets may have known coordinates and a defined scale.

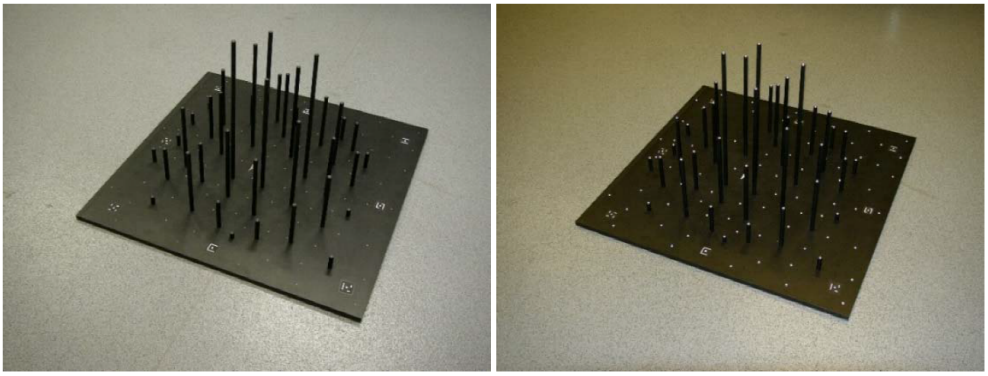

**Figure 2.24:** Two views of the 'Manhattan' test object, with retro-reflective targets placed on vertical rods and on its aluminium baseplate: (left) under overhead room lights; (right) illuminated by an inbuilt camera flash, close to the lens.

The largest existing such test object fitting the ROI, the 'Manhattan' [Robson et al., 2014], was employed in this study is shown in Figure 2.24. It consists a rigid array of 131 3D retro-reflective targets (section 2.11.1) of ∼2.5 mm diameter with predefined coordinates, designed especially for such calibration purposes. These are affixed on the 39 anodised aluminum rods of 8 mm diameter and of varying lengths from 20 to 305 mm, all perpendicular to the base, or affixed on the base itself. The aluminum base is a rectangle of 550 × 550 mm and 10 mm thickness. Under flash illumination the targets are visible in the image from any viewpoint within an incidence angle limit of 50-60 degrees (Figure 2.24 right) [Robson et al., 2015]. Eight machine-readable codes are also fixed onto the baseplate to facilitate automatic orientation of the target array in image processing. As such, this object can be used to coordinate the targets on the OBT system, providing starting values.

In the cases where a test object was needed solely to calibrate the interior orientation of a camera, a secondary test object (Figure 2.25) was used, similar to the Manhattan but of a smaller scale. The metal base of this object is a rectangle of 229×253 mm consisting an array of 64 3D retro-reflective targets. These targets of ∼5mm diameter are placed at different heights, from 0 to 145

mm.

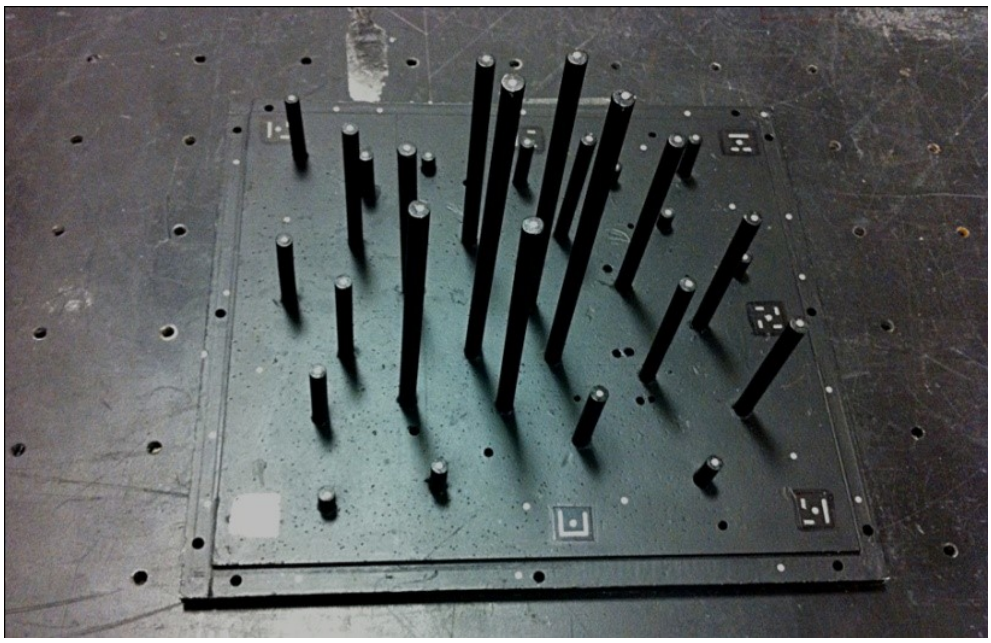

**Figure 2.25:** Photograph of a calibration reference object: a metal platform object with vertical rods, on top of which retro reflective targets are placed in 3D.

## 2.12 Data quality control

The parameter data computed is a result of LSE (section 2.8.1). Statistical error modeling is critical to the analysis of the estimates parameters. As such, Cooper and Cross [1988] define and categorise the quality control into: *accuracy, precision,* and *reliability* to describe the quality of a data set with respect to systematic, random, and gross errors respectively.

- **Accuracy** measures the closeness of an estimate to its parameter. In photogrammetry this signifies the closeness of the calculated object coordinates to the true values [Karara, 1989, Mikhail and Ackermann, 1976]. As a result, accuracy is related to systematic errors in the data. Systematic errors arise from flaws in the equipment or in the design of a measurement.

- **Precision** measures the degree of conformity among a set of observations of the same random variable [Rova, 2010]. As such, it relates to the random errors in measurements and derived values. Cooper and Robson [1996] state that any random variable measured, or estimated by LS, its variance or standard deviation (section 2.12.1) is an indication of its precision.

- **Reliability** refers to the presence of gross errors (blunders) in the data [Cooper and Robson, 1996]. These errors are hard to detect due to the nature of minimisation of the quadratic cost function which is inherent

in LSE (section 2.8.1). As such, Karara [1989] suggests that reliability can be considered to be intuitive.

Figure 2.26 illustrates a graphical representation of the first two, accuracy and precision. It demonstrates how accuracy relates to the mean of measurements made with respect to the true value, while precision represents the spread of these measurements [Flack and Hannaford, 2005].

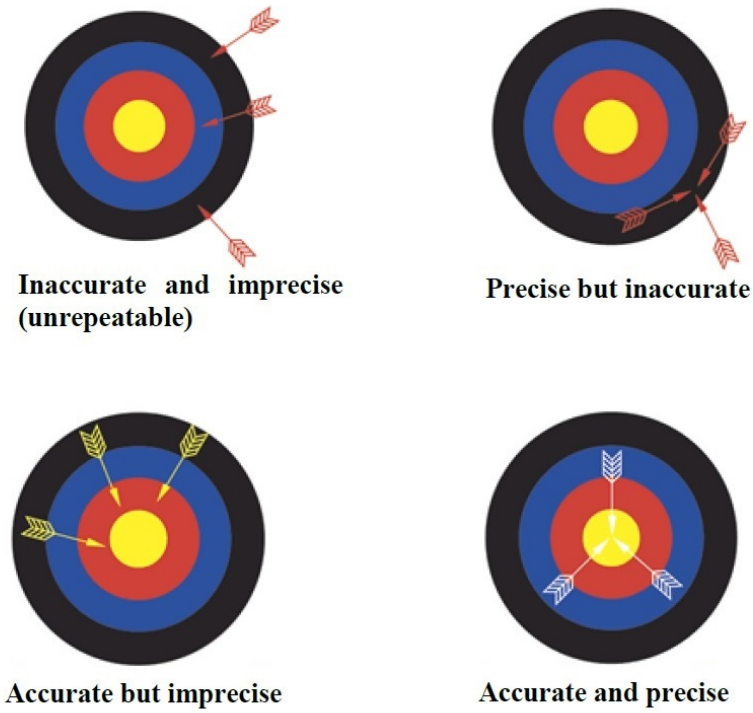


**Figure 2.26:** Graphical representation of accuracy and precision related to data quality control. The bull's eye in the target represents the true value of a measurement. The arrows indicate the measurements made. It demonstrates how accuracy relates to the mean of measurements made with respect to the true value, while precision represents the spread of these measurements. Adapted from Flack and Hannaford [2005]

### 2.12.1 Goodness of fit

The goodness of fit (GOF) of a statistical model is a description of how well that model fits into a set of observations [Maydeu-Olivares and Garcia-Forero, 2010]. The discrepancy between the observed values and the values anticipated under a statistical model is described with the use of GOF indices. GOF statistics are GOF indices with known sampling distributions, commonly acquired with the use of asymptotic methods which are employed in statistical hypothesis testing.

#### Sum of Squares Due to Error (SSE)

SSE measures the total deviation of the response values from a fit to the response values. It is also named the summed square of residuals and is typically

termed as SSE.

**R-square**

The success that a fit has, in describing the variation of assigned data, is measured by the R-square statistic [Lewis-Beck and Skalaban, 1990]. In other words, R-square represents the square of the correlation between the measured response values and the anticipated response values. It is also named as the square of the multiple correlation coefficient and the coefficient of multiple determination.

**Adjusted R-square**

The adjusted R-square uses the above R-square statistic by adjusting it according to the residual degrees of freedom. The latter are described as the number of response values minus the number of fitted coefficients expected from the response values.

**Root Mean Squared Error (RMSE or RMS)**

The square root of the average of the squares of all of the residuals (SSE) gives the RMS. The use of this statistic is very common and it makes a very good general purpose error metric for numerical predictions. RMS shows the absolute fit of a model to the data - in other words, the proximity of the observed data points to a model's anticipated values. While R-squared is a relevant measure of fit, RMS is an absolute measure of fit. Lower values of RMS indicate a better fit [Chai and Draxler, 2014]. RMS is a good measure of how accurately the model predicts the response, and is the most important criterion for fit if the main purpose of the model is prediction.

**Variance**: The variance of estimated parameters, as the square of the standard deviation ($\sigma$), is given by $\sigma^2$, and has the useful property of being in the same units as the response variable. Since the standard deviation is a measure of how spread out numbers are, variance is defined as the average of the squared differences from the mean.

Goodness of fit results are used to analyse results in chapters 4 and 5. RMS, in particular, is used extensively in chapter 5.

# Chapter 3

# ObT system set-up

## 3.1 ObT system design process

A significant proportion of this study went into designing the optimum ObT system. The design was based on the combination of the contributing factors which included background research, tests, simulations and confining practical restrictions (such as budget, cost-effectiveness and laboratory limitations). A logic flow diagram of the ObT system design process is shown in Figure 3.1.

The principals of ObT are based on the movement of baggage on conveyor belts and in particular at points of baggage direction change. At these points, a series of x-ray images (projections) of the object needed to be acquired by placing the x-ray sources and detectors on opposite sides of the conveyor belts. These projections needed to be appropriately processed using image reconstruction algorithms developed to create 2D slice images of an object. Since these are the basic principles of ObT, they are the backbone of the system design.

## 3.2 ObT system components selection

In order to build the ObT system, first of all, the necessary system components need to be selected. The two prime components contributing to the ObT system design are:

- The x-ray components (sources and detectors)
- The conveyor belts system

In the foremost design of the ObT, the combination of the first two components is considered. The third, which corresponds to the web-camera network configuration, is not included in the initial designing process as it is easily adjustable and adaptable to the final ObT configuration.

The baseline idea for the ObT system is the one resulting from the in depth study of current technologies, their limitations and possible novel ways to

overcome these (section 1.3). The decisions for the design are defined by the required system effectiveness and confined by practicality (such as laboratory capabilities) and the project budget. The potential system capabilities, and therefore effectiveness, are estimated based on background research, system simulations and test x-ray acquisitions performed using a micro-CT.

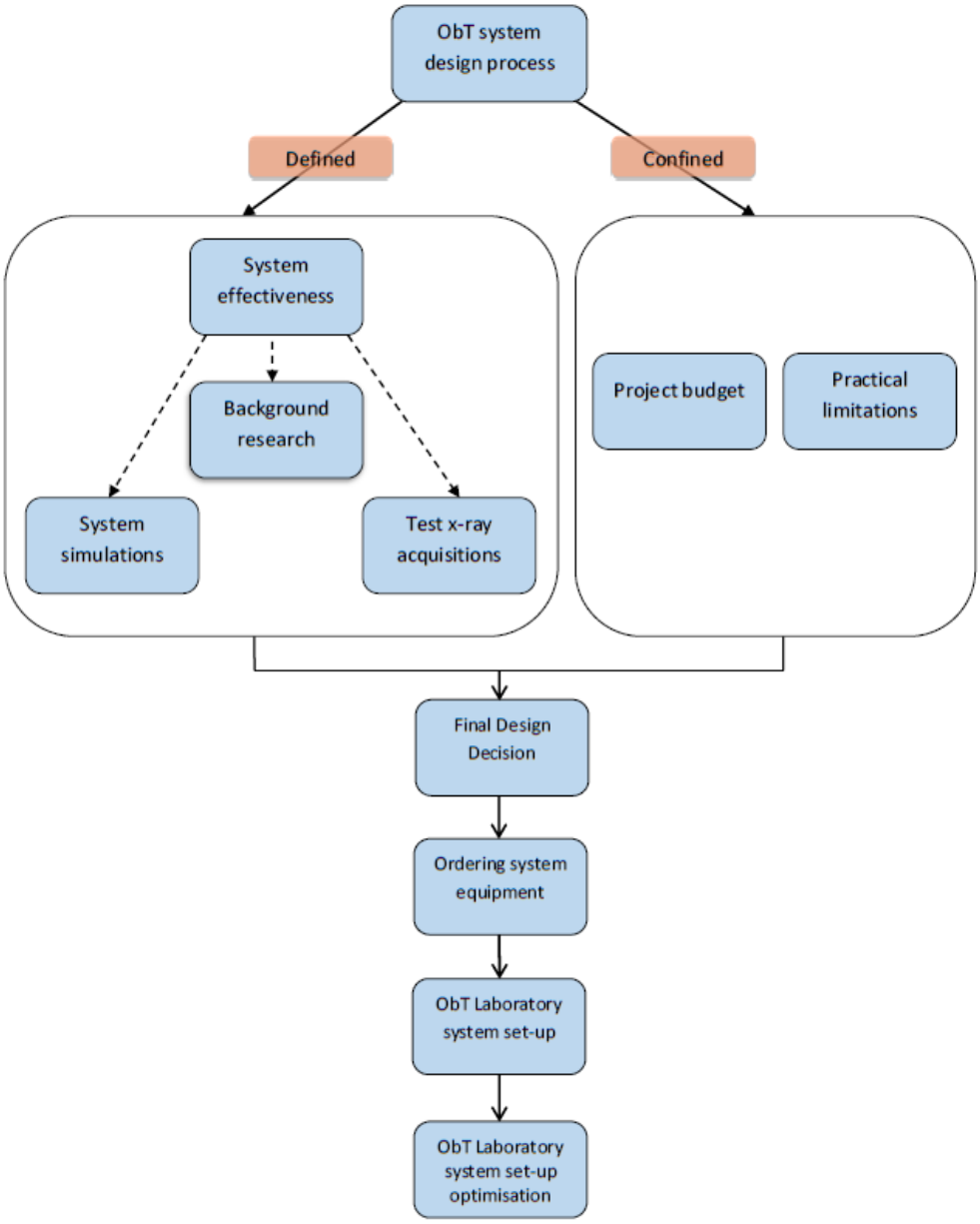


**Figure 3.1:** Logic flow diagram of the ObT system design process.

### 3.2.1 The x-ray components

#### 3.2.1.1 Optimal geometry background review

Background research was performed on published results regarding studies of x-ray acquisition geometry optimisation. Significant appropriate literature found was based on digital breast tomosynthesis screening, as limited angle tomosynthesis is broadly researched and implemented in this scientific sector. In the past six years research has greatly focused on optimisation of acquisi-

tion arc and number of projection images per scanning arc for high quality construction of breast images [Malliori et al., 2012]. The way these were conducted was through simulation studies. Initial, simpler studies showed that in tomosynthesis, increasing the acquisition arc results in improved in-depth resolution, except in the case where a simple back-projection method was used [Zhou et al., 2007]. One of the most extensive optimisation studies showed that an increase in reconstruction quality of masses can be achieved by extending the acquisition angular range [Sechopoulos and Ghetti, 2009]. The same study reported that the vertical resolution can also be maximised by extending the angular range. More recent studies that investigated the detectability of breast lesions in tomosynthesis derived similar conclusions [Reiser and Nishikawa, 2010, Van de Sompel et al., 2011]. However, these findings are from simulation studies and need to be verified by clinical systems. For this, Ren et al. [2006] showed that the maximal achievable contrast-to-noise ratio (CNR) decreases, as the number of projections increase. Zhao et al. [2009] reported that when the angular range was increased, improved mass visibility was attained. These studies' results are presented as they are the most appropriate in relation to the current study. However, there are a number of differences which must be taken into account when using their findings. For one thing, the majority are not clinical studies, but simulations. Those that were clinical experimental studies were limited to the use of homogeneous mammographic phantoms and restricted mass sizes. More generally, these studies focus on breast tomosynthesis, which is different to the focus of the current baggage screening study in many ways. These include the scale of objects screened as well as the scale of objects screened for within. The quality of results in breast imaging is assessed on low contrast objects, which is limiting in relation to illicit baggage contents. There are other differences as well in the parameters of the x-ray screening in each case, including that breast screening is performed at much lower doses than baggage screening. Overall, given the multiplex factors of tomosynthesis for baggage screening purposed (more complex, unknown object contents, more diverse environments etc.) it is evidently more challenging than for breast screening.

#### 3.2.1.2 System simulation software

In order to determine the optimal positions for the x-ray sources and detectors, a numerical computer simulation software package was developed by Dr Marta M. Betcke (UCL). This software was used to study the optimal criteria of the x-ray components of the ObT system. The idea was to use the bend of the conveyor belts positioning the sources and detectors in such a way to obtain projections of a phantom at a maximal range of angles as it moved around the turn. The criteria for this study included the range of effective projection angles (i.e. angles from which the object is viewed), the completeness of views, the uniformity of magnification of the object, the effect of image resolution, and the uniformity of sampling of the effective projection angle range [Reid et al.,

2011a]. All these were incorporated in the simulation software and varied in order for the optimal ObT design to be determined (section 3.3). Additionally to the optimal criteria, limiting factors were taken into consideration when determining an optimal system set-up (such as the feasibility and compactness of the scanner design).

**System geometry** The system geometry set for this work is described as follows. A diagram of the simulation system set-up coordinate system is shown in Figure 4.2.2 (page 85).

Let (x, y, z) be the global coordinate system. The ObT setup comprises number of stationary sources and stationary detectors. The belt lies in the xy-plane (its z-coordinate is z=0). The conveyor belt is rotating in the xy-plane around a point which we choose to be the origin of the global coordinate system (x, y, z) (without loss of generality). This results in the 3D axis of rotation being the z-axis. While the bag is transported on the conveyor belt a number of x-ray views are acquired. The presence of multiple sources allows a number of different source positions from which to take projections.

The volume of interest (VOI) to be imaged is chosen to be large enough such that any object of interest to be scanned can be inscribed into it. The VOI was chosen to be a cuboid with one of its sides lying on the xy-plane and occupying space corresponding to $z \geq 0$. This reflects the fact that the bags rest on the conveyor belt. A bag moving on the conveyor belt around a 180° turn corresponds to a 180° rotation of the VOI around the z-axis. Therefore, the motion of the bag can be sufficiently described through the VOI rotation around the origin.

In the ObT system, the scanner is stationary (up to the different source positions) while the VOI is moving. Therefore it is necessary to co-register the $VOI_p$, with p = 1; ...;P corresponding to the different rotation angles $\varphi_p$ of the VOI at which x-ray views of the bag are taken. The admissible range of angles corresponds to those angles for which the intersection of the VOI with the field of view (FOV) of the source and detectors is nonempty [Reid et al., 2011a]. The latter depends solely on the relative position between the source and detectors; therefore it changes as the source position moves.

The relative orientation of the VOI to the scanner (source and detectors), $VOI_p$, after VOI's rotation by $-\varphi$ around the z-axis is equivalent to the rotation on the scanner by $\varphi$ around the z-axis while keeping the VOI stationary. It is hence possible to use a 'reference position' for the VOI, $VOI_{ref}$ and perform a relative scanner rotation with respect to this reference position.

**Influence of the Scanning Geometry** In the study using the simulation software developed, several factors arise to be taken into account. Choosing the centre of the VOI to be as close as possible to the centre of rotation (COR) will maximise the relative rotation of the VOI in the FOV hence increasing the range of effective view angles $\varphi$ . The detectors should be positioned as close as possible to the VOI to allow the largest sensitivity to the sources' translation. Moving a source towards the VOI is restricted by the VOI itself, while moving it away increases the size of the OBT system.

The variable element of our OBT system is the source position. Therefore, in order to achieve the optimal design, the impact of different source positions on the effective geometry was investigated by Reid et al. [2011b]. From this, some rudimentary conclusions were drawn:

- The closer the source gets to the COR the more alike the projections become, hence less useful information gathered for the tomosynthesis.
- The closer the source gets to the VOI, the more magnified the projections get and the higher the resolution: resolution and magnification are proportional.
- As source nears the VOI (and hence the detectors) the FOV shrinks, thus reducing the admissible VOI rotation angles.
- The FOV size is directly proportional to source-detector distance.

#### 3.2.1.3 Test x-ray acquisitions

X-ray scanning was used to perform tests whose results would be analysed to be used in orienting the ObT system design. As these tests took place prior to the ObT system creation, a pre-existing laboratory x-ray system was used, which was a micro-CT system.

A basic phantom (Phantom A) was manufactured to be x-rayed using the micro-CT. Phantom A, a photograph of which is displayed in Figure 3.2, consisted of a plastic box of $90 \times 40 \times 30\ mm$ dimensions split in four imaginary compartments containing separate objects: wrapped metal wire, four metal pins, two screws, and a Perspex ball. These objects were chosen to represent a variety of material properties, shapes and sizes, whil their placement separation was chosen to facilitate object discrimination and depth of field in the x-ray reconstructions that were afterwards produced. This also corresponds to object contents of a wide range of $Z_{eff}$, as a realistic baggage item would normally have. Moreover, the pins and metal wires, were an approximate simulation of sharp object and explosive components, both types of which could be suspicious in real baggage. Additionally, Phantom A came at no cost as all objects were found in the laboratory.

**Figure 3.2:** Photograph of Phantom A taken from above.

X-ray acquisitions were made of the phantom, at every 1° angle steps to a total angle rotation of 180° (acquisition arc), producing 181 projections of the phantom. From these, 2D slice images of the phantom were reconstructed several times using a different total number of projection images each time. The reconstruction code used was developed by Dr M. M. Betcke in Matlab. A total of fourteen different combinations were used, and fourteen corresponding 2D images of each were compared to each other through visual inspection. In each case, the angle separation of the projections used, determined the total angle scanning range of the phantom. A table of this is shown in Table 3.1. This, in turn, indicates the ideal total angle for which the ObT system should be able to scan the passing baggage. In succession, the ideal number of projections corresponded to the optimum number of strip detectors to be implemented, as these consist of a single array of pixels. The reason strip detectors were chosen is due to their significant lower cost, compared to flat panel detectors.

An example x-ray projection acquired of Phantom A is shown in Figure 3.3.

| Acquisition arc (deg) | Number of projections | Angle separation (deg) |
|---|---|---|
| 60 | 4 | 15 |
| 60 | 5 | 12 |
| 60 | 6 | 10 |
| 60 | 16 | 4 |
| 96 | 4 | 24 |
| 90 | 6 | 15 |
| 90 | 10 | 9 |
| 96 | 16 | 6 |
| 120 | 4 | 30 |
| 120 | 6 | 20 |
| 119 | 7 | 17 |
| 117 | 9 | 13 |
| 121 | 11 | 11 |
| 120 | 16 | 7.5 |

**Table 3.1:** The list of the different x-ray acquisitions made of Phantom A using the micro-CT, corresponding to fourteen different image reconstruction combinations.

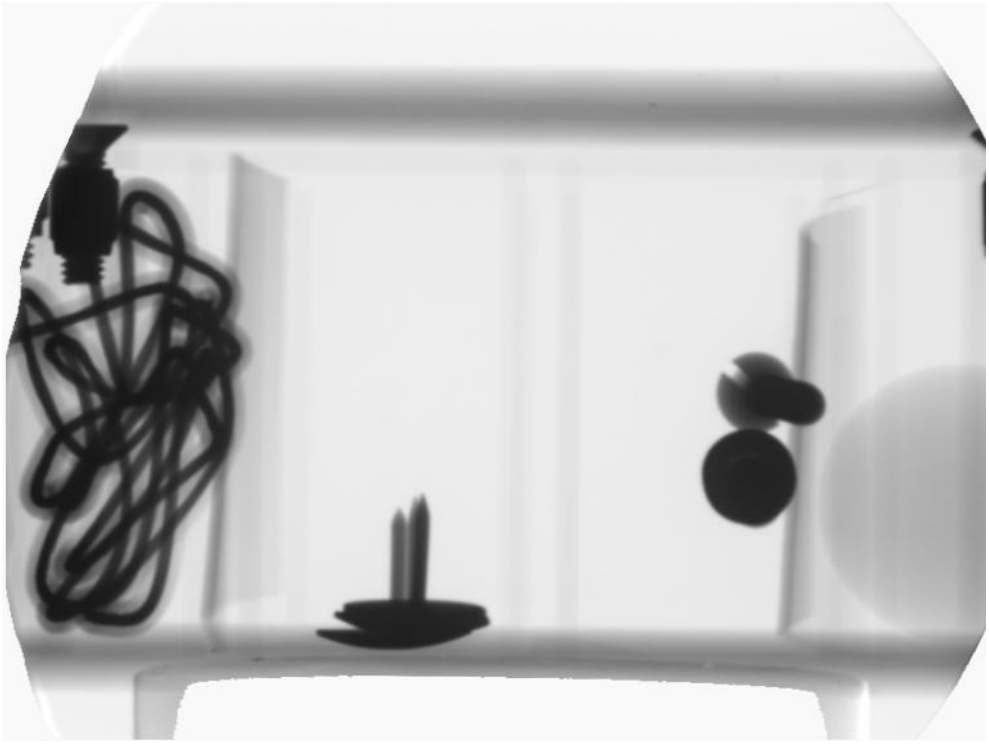

**Figure 3.3:** Example x-ray projection of Phantom A acquired using the micro-CT.

#### 3.2.1.4 Image quality analysis

In order to improve the quality of the initial reconstructions, grey cut was performed on the original projections acquired. Grey cut refers to the image processing technique which changes the greyscale value of pixels (*greyvalue*) which are above or below a certain greyvalue. The logic behind this was to increase contrast among object by making dark objects (pixels) even darker, and light objects (pixels) lighter. After testing various values it was decided to convert all pixels with a value higher than 180, to the value of 255, and all pixels with a value lower than 70 to the value of 0. An example of this is

shown in Figure 3.4.

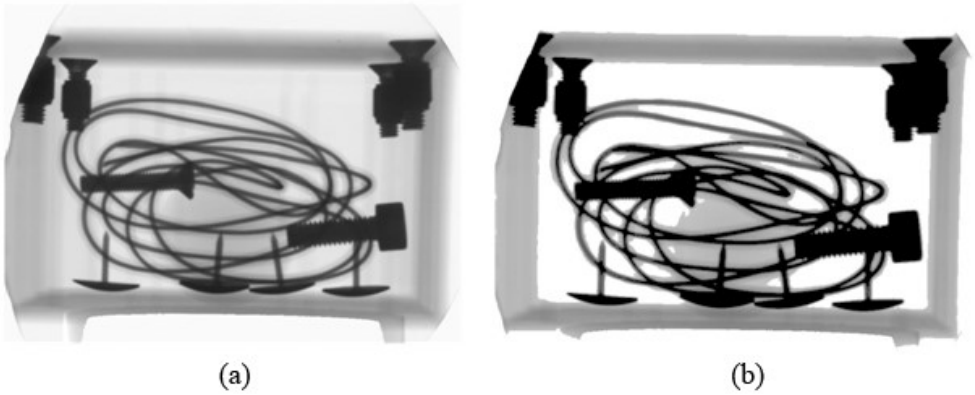


**Figure 3.4:** (a) Example projection image of Phantom A. (b) Example projection image with 'grey cut' applied.

After the grey cut was applied, SAA image reconstruction was performed (section 2.6.3), for each separate combination in Table 3.1, which resulted in 2D slice images of the phantom. The quality of the reconstructed features was assessed both visually and quantitatively. Visually it was noticeable when items came in and out of focus in the sequence of 2D slice images produced for each acquisition set. For example, SAA was performed on the set using 11 projections acquired at an arc of 121°. The image reconstruction algorithm produced 101 sequential 2D slice images of Phantom A. The first and last are shown in Figure 3.5. It is noticeable that the two metal pins are out of focus in the left Figure (3.5: a), but come into focus in the right Figure (3.5: b), while the same occurs for the pins vice versa (Table 3.2). This shows that the different objects were abe to be distinguished in the reconstructed images produced.

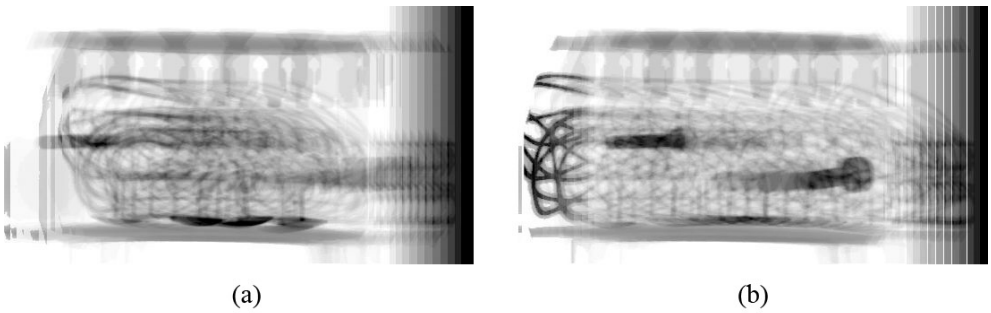


**Figure 3.5:** (a) shows the first, while (b) shows the last 2D image reconstruction out of the 101 sequential 2D slice images of Phantom A.

To quantitatively confirm this, focus was set on selected regions of interest and analysed. For this, three profile lines of regions across three parts of the images corresponding to a specific value on the x-axis, were plotted. These are represented by the red dotted lines in Figure 3.6. These particular three regions were chosen in order to check the depth of field quality by measuring the focal discrimination along those lines.

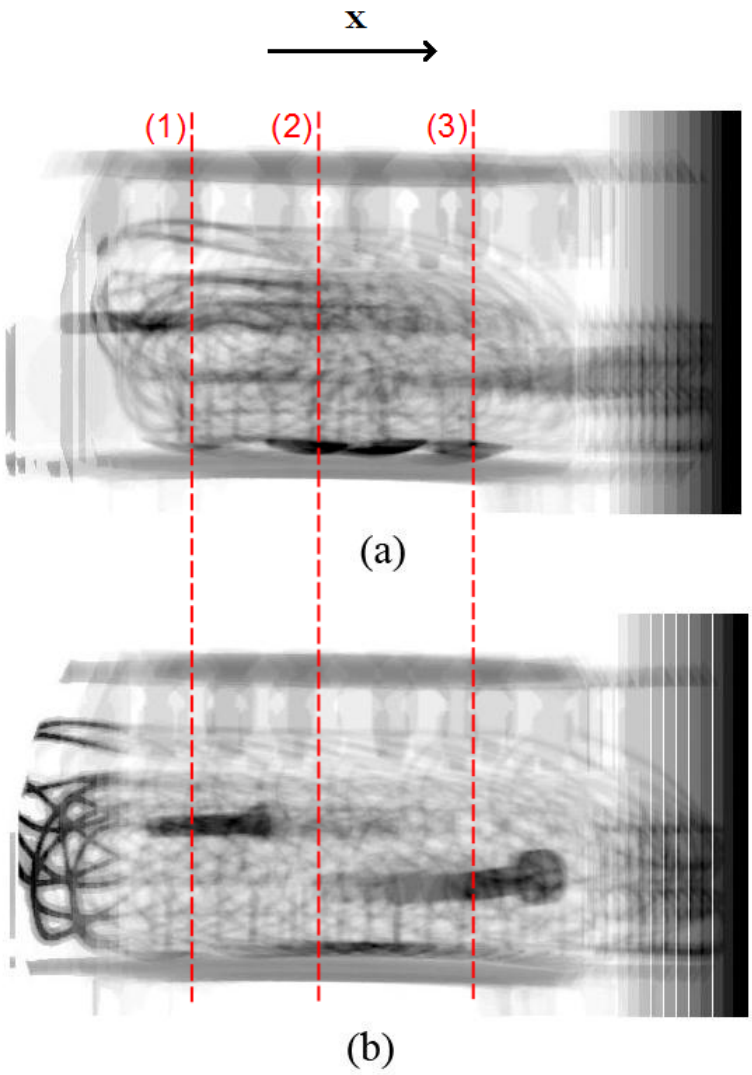


**Figure 3.6:** The three profile line plots 1,2,3 (Figures 3.7, 3.8, 3.9) which correspond to a specific value on the x-axis $(x_1, x_2, x_3)$ correspond to the areas indicated by the respective dotted lines in both images (a) and (b) .

The profile lines were selected at those points specifically:

- Line 1 passes through a screw out of focus in $a$ and in focus in $b$.
- Line 2 passes through a pin in focus in $a$ and out of focus in $b$.
- Line 3 passes through a screw out of focus in $a$ and in focus in $b$, while it also passes through a pin in focus in $a$ and out of focus in $b$.

The focus of these three lines, based on the visual inspection, is organised in Table 3.2 for clarity. These differences should produce a noticeable variance in the profile plots along those lines.

Objects that are in focus should produce a valley (downwards peak) in the profile plot, in this example, as the objects of interest (pin and screws) are of higher density than the background. Here it should be noted that the greyscale in the images is a function of object density: the denser an object the darker

its projection.

By plotting the same profiles lines of $a$ and $b$ on the same graph, it was possible to compare the greyscale intensity at similar regions in the images. It can therefore be noticeable when an object passes in and out of focus on the graph when one of the lines peaks downwards in the area where the screw or pin is in focus, while the other line does not, making the object distinguishable. The results of this work is presented in section 3.2.1.5.

| **Image** | ***a*** | ***b*** | ***a*** | ***b*** |
|---|---|---|---|---|
| **Line** | **screw** | | **pin** | |
| **1** | **out of focus** | **in focus** | n/a | n/a |
| **2** | n/a | n/a | **in focus** | **out of focus** |
| **3** | **out of focus** | **in focus** | n/a | n/a |

**Table 3.2:** Table showing the regions where objects (screw, pin) come in and out of focus, corresponding to images in Figure 3.4 along the lines indicated in Figure 3.5.

#### 3.2.1.5 Results

Matlab was used to plot the profile lines at points (1), (2) and (3) in images 3.5a and 3.5b. The corresponding code developed is shown in Appendix A (page 200). The lines at points (1), (2) and (3) shown in Figure 3.6, correspond to specific vertical lines at three different points on the x-axis of the reconstructed images ($x_1 = 141, x_2 = 215, x_3 = 317$). For each x value, the profile lines corresponding to image a and b are plotted on the same graph to facilitate their comparison. Since three such regions were selected, there are three graphs produced showing the profile lines across those difference points.

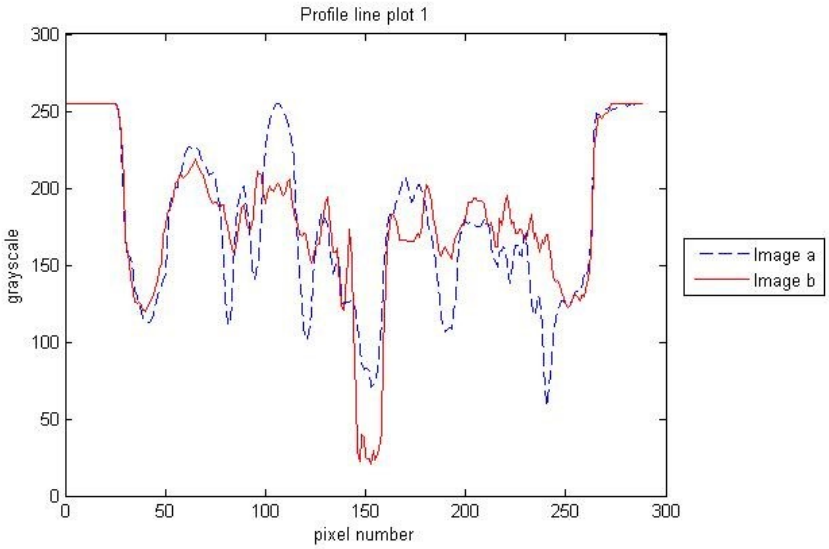


**Figure 3.7:** Graph of the profile line of greyscale vs. pixel $N^o$ corresponding to Images a & b for $x_1$.

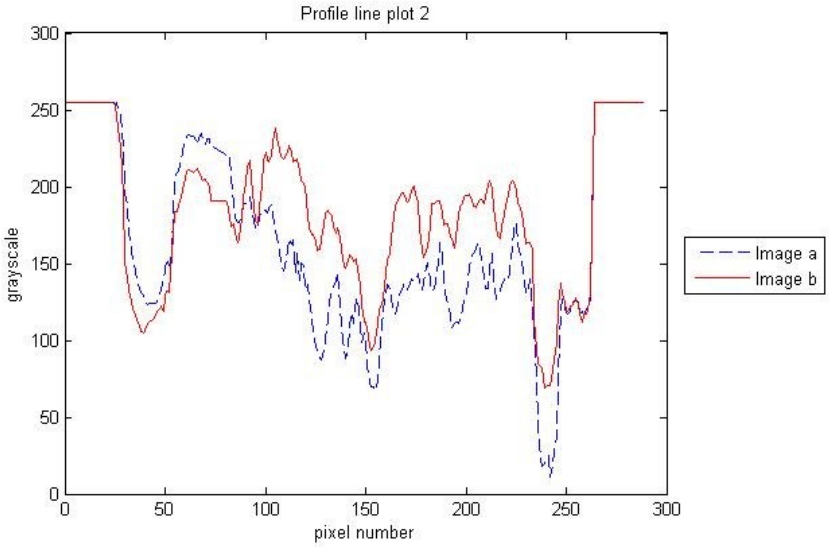


**Figure 3.8:** Graph of the profile line of greyscale vs. pixel $N^o$ corresponding to Images $a$ & $b$ for $x_2$.

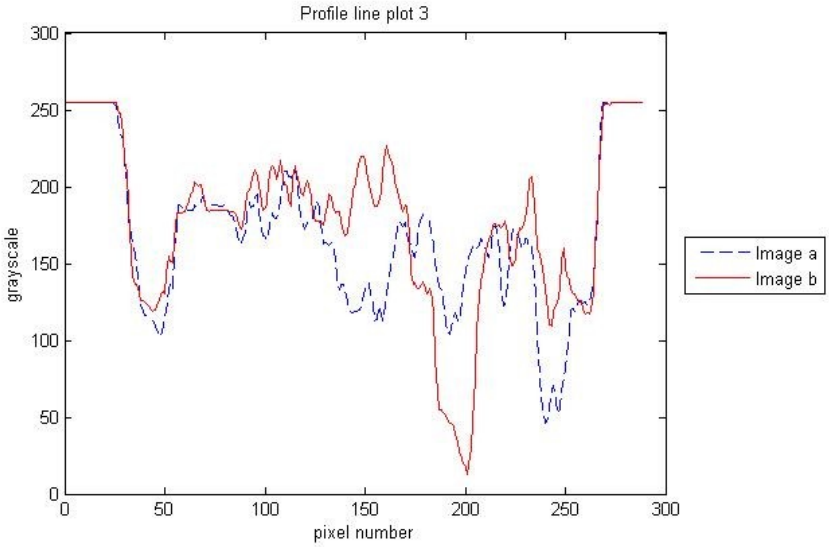


**Figure 3.9:** Graph of the profile line of greyscale vs. pixel $N^o$ corresponding to Images $a$ & $b$ for $x_3$.

In addition, the contrast to noise ratio (*CNR*, section 2.4.2.3 on page 22) for the three objects of interest was calculated. This was done in 'ImageJ' software [ImageJ, 2015], by selecting small ROIs within each object (corresponding to the distinct peak locations in Figures 3.7 and 3.9) as well as an appropriate ROI of each object background. The same ROI's were selected in the two images a and b of Figure 3.5. Using the respective signal and standard deviation values measured in ImageJ, the CNR of each object in each image can be calculated using equation 2.6 on page 22. The results are presented in Table 3.3 on the following page.

| CNR | | | | |
|---|---|---|---|---|
| **Image** | ***a*** | ***b*** | ***a*** | ***b*** |
| **Line** | **screw** | | **pin** | |
| **1** | **2.5** | **8** | n/a | n/a |
| **2** | n/a | n/a | **7** | **1.5** |
| **3** | **2** | **7** | n/a | n/a |

**Table 3.3:** Table showing the calculated contrast to noise ration (CNR) regions where objects (screw, pin) come in and out of focus, along the lines indicated in Figure 3.5.

#### 3.2.1.6 Discussion

The profile line plots created are analysed taking into account the pixel correspondence areas in Figure 3.6.

*Figure 3.7:*
The area near the centre of the graph (around pixel number 150) shows that the screw comes in and out of focus. In Image b , the profile line plotted forms a distinguishable incline on the greyscale axis indicating a high object density at that location. From this, it is inferred that the screw is in focus in Image *b*, compared to Image a where a less deep valley appears.

*Figure 3.8:*
A deep valley around pixel number 245 shows that a pin comes in and out of focus there. In image a, the profile line plotted forms a deep dip on the greyscale axis indicating a high object density at that location. From this, it is inferred that a pin is in focus in Image a, contrast to Image b where the profile line does not reach such low values.

*Figure 3.9:*
A deep valley around pixel number 200 shows that a pin comes in and out of focus there. In image a, the profile line plotted forms a distinguishable dip on the greyscale axis indicating a high object density at that location. From this, it is inferred that the screw is in focus in Image b, contrast to Image a where no such valley appears. A deep valley around pixel number 245 shows that a pin comes in and out of focus there. In image a, the profile line plotted forms a noticeable incline on the greyscale axis indicating a high object density at that location. From this, it is inferred that a pin is in focus in Image a, contrast to Image b where the profile line does not reach such low values.

*CNR:*
The CNR values for the three objects of interest were measured to be between 7-8 in the respective images where each object was in focus, corresponding to Table 3.2. These results are in agreement with the analysis of the three Figures above. This CNR values can be described as sufficient to allow detectability of the respective objects of interest, according to literature findings (section

2.4.2.3). Moreover, the CNR values for the same ROIs in the images where each object was out of focus (i.e. the pin in image b and the screws in a, corresponding to Table 3.2) were measured to be between 1.5 - 2.5. This results further supports the conclusion that objects of interest can be sufficiently detected and distinguished.

**Test x-ray acquisitions' conclusions** The results produced by the quantitative analysis, above, match the results using visual inspection tabulated in Table 3.2.

Performing this on all of the sets of acquired images shown in Table 3.1, the image quality analysis shows that for similar angle ranges (i.e. $60°-64°, 90°-96°$, and $117° - 121°$) image quality improved as the number of projections increases.

#### 3.2.1.7 Conclusions on the X-ray components

The conclusions from the background research, the test simulations and acquisitions were combined in reaching the optimum decision of the ObT design of the x-ray components. All these critical factors were combined in reaching the optimal solution within the budget available. Overall, it was found that better results are obtained, the wider the acquisition angle. Therefore, a 180° acquisition arc was decided upon for the ObT. The results also showed an improvement as the number of detectors used increased. However, the detectors' physical size is a limiting factor in the laboratory set-up. Geometrical calculations showed that the total number of detectors which can be placed adjacently within a 90° radius is six. This meant that a 180° trajectory could be covered using two x-ray sources with sufficient cone beam angle and twelve strip detectors, which was also within budget.

### 3.2.2 The conveyor belts system

In order to design the optimum conveyor configuration the results from the study of the x-ray component set-up were taken into account, along with the available conveyors and any laboratory confinements. Following the study on the x-ray components, twelve detectors needed to be placed on a 180° arc, each illuminated by one of the two x-ray sources. As two 90° arc conveyors were available, each set of six strip detectors was fixed around each conveyor belt bend, with equal separation covering the whole 90° arc of the conveyors' outer edge. Therefore, each x-ray source could be placed near the inner edge of teach conveyor, facing the detectors, with the beam of the x-rays covering all six.

Besides the two 90° arc conveyors there was one 97 cm long straight conveyor available in the lab. The possible conveyor set-up combinations were considered in order to arrive to the optimum one:

(1) The first set-up considered was positioning the two 90° arc conveyor belt bends next to each other so that they formed a "u" shape (Figure 3.10). This would create the desired test 180° bend most simply. However, this set-up would require the two x-ray sources to be placed so close together that there is no physical space for them to fit. Also, the x-ray beam geometry means that X-rays may overlap between the two sets of strip detectors. Therefore, this set-up was rejected.

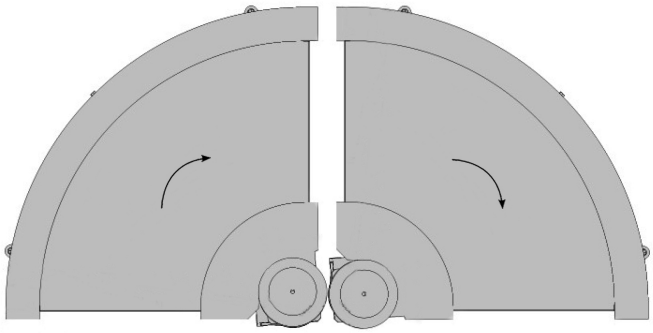

**Figure 3.10:** Conveyor belt set up (1) using two 90° arc belts in 'u' shape.

(2) An alternative set-up considered retaining a compact format of the system was to place the two 90° arc conveyors belt bends next to each other in such a way that the conveyor belts would form an 's' shape (Figure 3.11). When this set-up was considered, two issues arose relating to the fact that, as an object moves along, the two x-ray sources (and corresponding detectors) are placed on opposite sides of its path in either curve bend. The mirrored view of the screened object with respect to each x-ray source in addition to the reverse magnification of items inside it were estimated to result in complications in the tomosynthesis execution and reconstruction. Therefore, this set-up, too, was rejected.

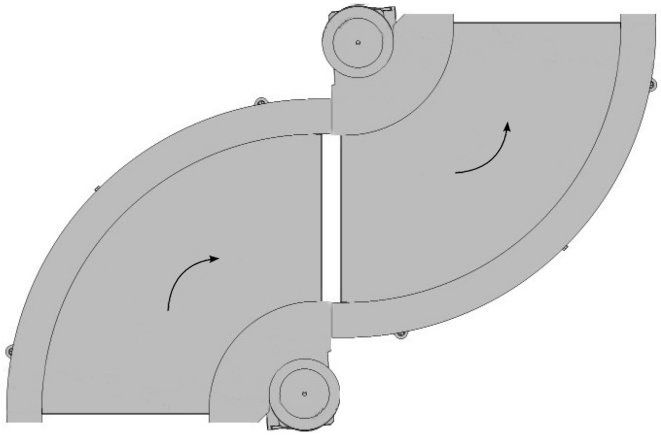

**Figure 3.11:** Conveyor belt set up (2) using two 90° arc belts in 's' shape.

(3) Third was proposed that the two 90° arc conveyor belt bends were positioned forming a 'u' , as in set-up (1), with the straight conveyor placed in between the two (Figure 71). This set-up surpassed the issues which

had arose in set-up (2) since the motion of the object in relation to the sources is in continuous orientation. Also, it eliminated the issues in set-up (1) as this provided enough space between the two curve conveyors for the x-ray sources to be positioned and enough separation between the two sets of detectors so that each was only illuminated by one x-ray source.

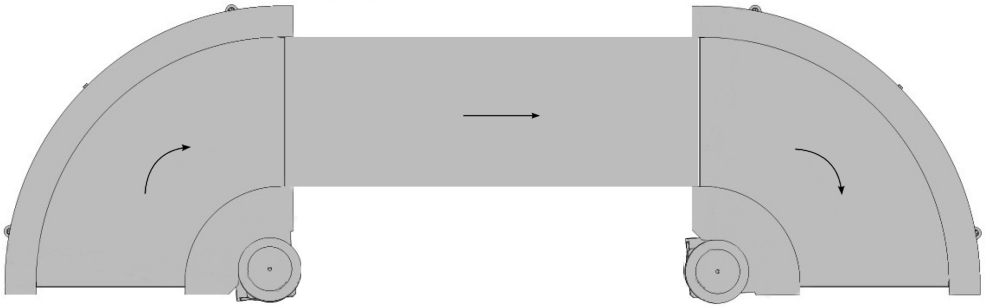

**Figure 3.12:** Conveyor belt set up (3) using two 90° arc belt bends and one straight belt in between. The latter was selected as the optimum set-up for the conveyors, overcoming the issues by the previous set-ups considered.

## 3.3 Final ObT system configuration

Following the study in section 3.2, the final ObT system configuration was designed. The list of the ObT system components chosen, and their specifications, is displayed in Table 3.4.

The prime two systems forming the ObT were the x-ray components and the conveyors. Summing up, two 90° conveyor belt bends (*C1* and *C2*) were placed on the lab bench, with the straight conveyor (*C3*) placed in line between them. Each set of six strip detectors was placed around the outer arc of one of the two conveyor belt bends, with an x-ray source positioned on the inner side of the belts (*S1* and *S2*), facing the detectors. Figure 3.13 shows a 2D top view this set-up. Figure 3.14 shows two photographs of the ObT system. Initial experiments were performed one 'side' of the ObT system, comprising one x-ray source and six detectors; this was named Unit A of the ObT (Figure 3.15).

| **Component** (Manufacturer) | **Type** | **Name** | **Items** | **Specifications** |
|---|---|---|---|---|
| **The x-ray components** (© 3DX-RAY Limited) | x-ray source | 170-DigXbloc | 2 | Tube voltage operational range: 80kV-170kV<br>Tube current: 0.6mA-1.2mA at 170kV, 200W maximum<br>X-ray beam geometry: $80° \pm 2°(40° + 40°) x 60° \pm 2°(20° + 40°)$ |
| | x-ray strip detector | XLINE-OBT | 12 | Array length: 288 mm (active array length)<br>Pixels: 192<br>Pixel pitch: 1.5mm<br>Digital resolution: 12 bit<br>Data rate (pixel): 140kHz<br>Collimation: 1.5mm width Window: 2mm<br>Tufnol power: 110V to 240V ac, 2A single phase |
| | detector control box | XLINE-OBT-Control | 1 | PSU ADCC VconGigE |
| **The conveyor belt system** (© TRANSNORM System GmbH) | curve conveyor belt | TS 1500-50 | 2 | Conveying angle: 90°<br>Max conveyor speed: 0.8 m/s<br>Drive capacity: 0.18kW<br>Conveyor nominal radius: 200mm |
| | straight conveyor belt | TS1200 | 1 | Max conveyor speed: 0.1 m/s<br>Drive capacity: 0.37-1.5kW<br>Nominal width: 200mm |

**Table 3.4:** List of ObT system components and their specifications.

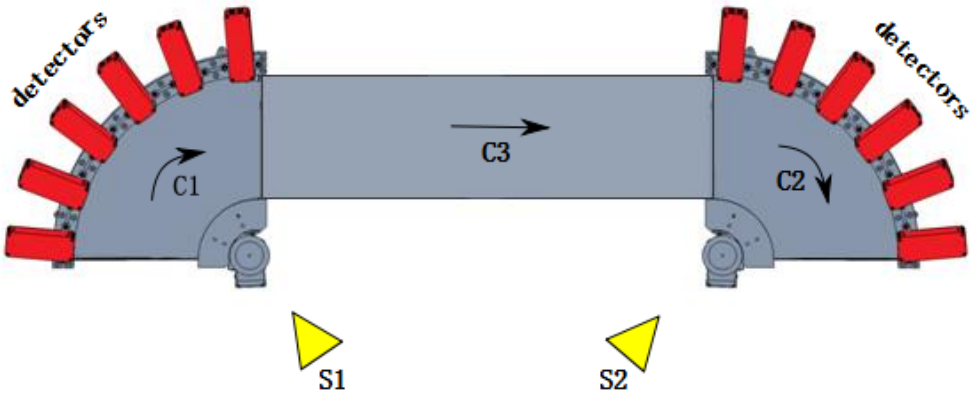


**Figure 3.13:** 2D top view of thw ObT system showing two of the main components: the x-ray sources (yellow triangles) and detectors (red boxes), and conveyor belts (grey platforms).

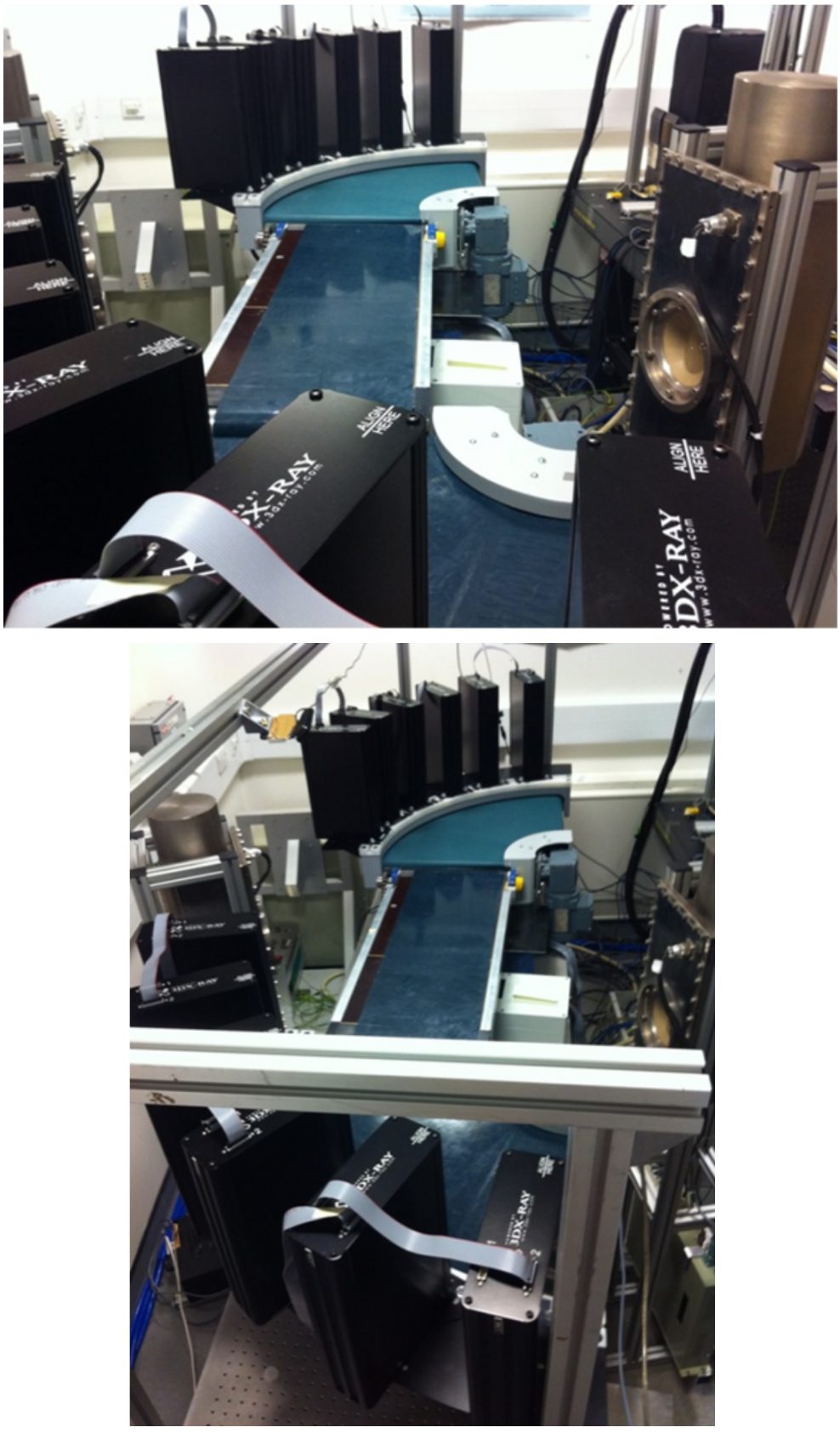


**Figure 3.14:** Photographs of ObT system set up showing conveyor belts, linear detectors and x-ray sources.

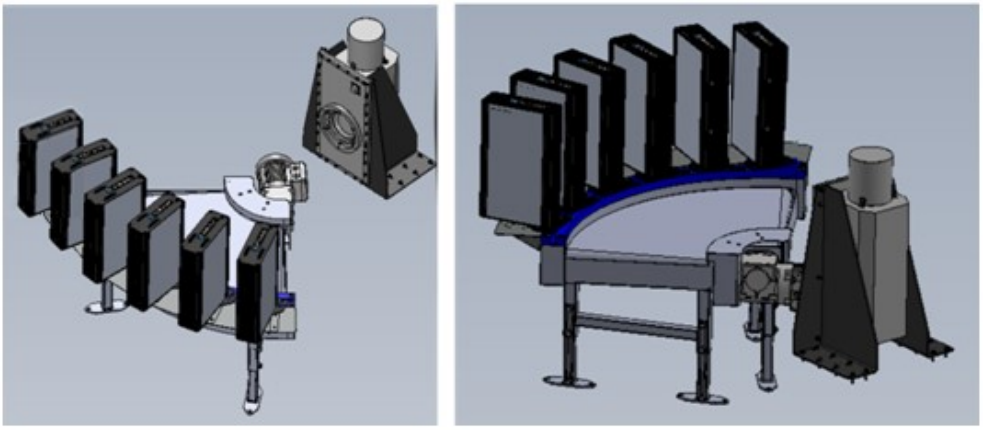

**Figure 3.15:** 3D side views of ObT Unit A set-up (conveyor belt, strip detectors, x-ray source).

## 3.4 Hardware installation

The ObT system components were set-up as described in the final ObT system configuration (section 3.3). The twelve detectors were connected to each other in pairs (i.e there were two sets of six detectors and each set was connected in series) and each pair connected to the detectors' control box (Camera Control Box) (Figure 3.16). This method allowed, the information from the strip detectors to be read out as a continuous string of data through a CAT-6 ethernet cable that connected the control box to the computer used. The computer was situated outside the laboratory room, with a safety door, and all cables fed through a staggered hole in the wall. Two 9-way D-type serial cables connecting each x-ray source to the computer were also installed, as well as four USB extension cables connecting the four web-cameras used for the close-range photogrammetry. The laboratory room had radiation protection walls and a safety door. Safety interlocks were installed on the laboratory door for each x-ray source. This ensured that if the door opened while X-rays are still on, they would immediately be turned off, stopping any x-ray exposure. The power controls for the three conveyor belts were also placed outside the laboratory room, using extension power cables connecting them to their motors.

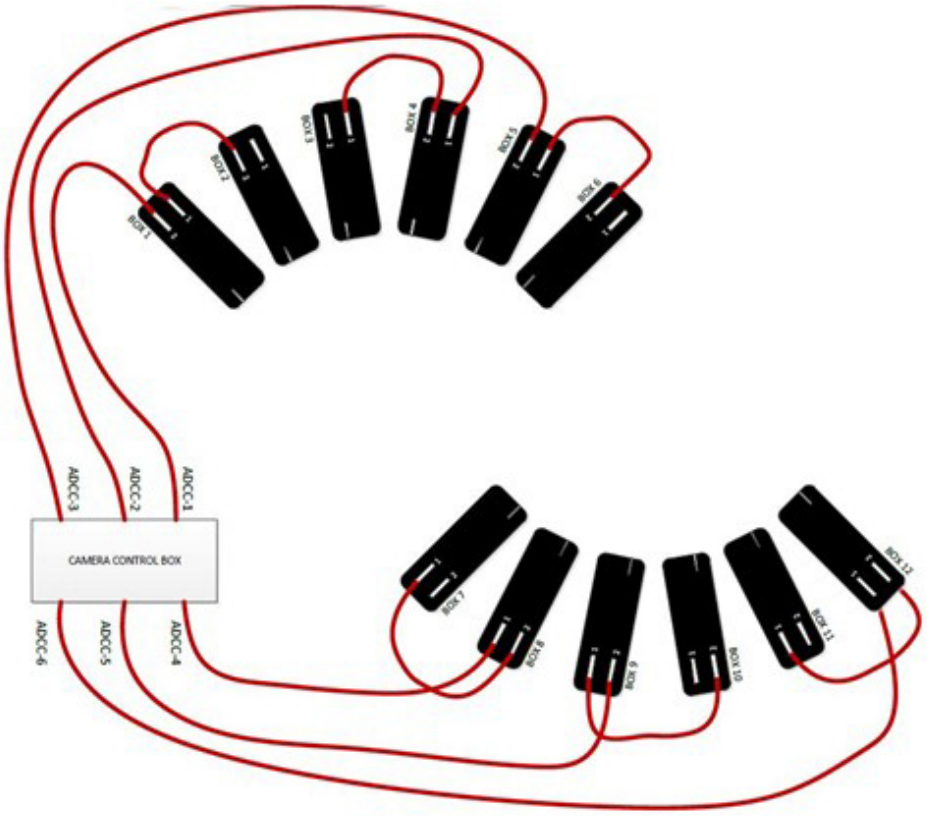


**Figure 3.16:** Schematic of ObT detectors' connections between themselves and the Camera Control Box.

## 3.5 Detector alignment

### 3.5.1 Operating x-ray sources

The software used to control and operate the x-ray sources was provided by the x-ray source manufacturer and is called "XrayControl V4.02". Once installed it is easy to use, with all functions displayed on a single window (Figure 3.17). The kV and mA can be set to the desired value and there is a useful diagnostics log box: a text window displaying the actions and status of the sources.

Using "XrayControl V4.02" it is possible to operate two x-ray sources simultaneously. For this, the first step is to open the software and set the communication port ("Comm. Port") to the value of 2. It is then possible to open the software a second time and have two such windows displayed, corresponding to the two separate sources.

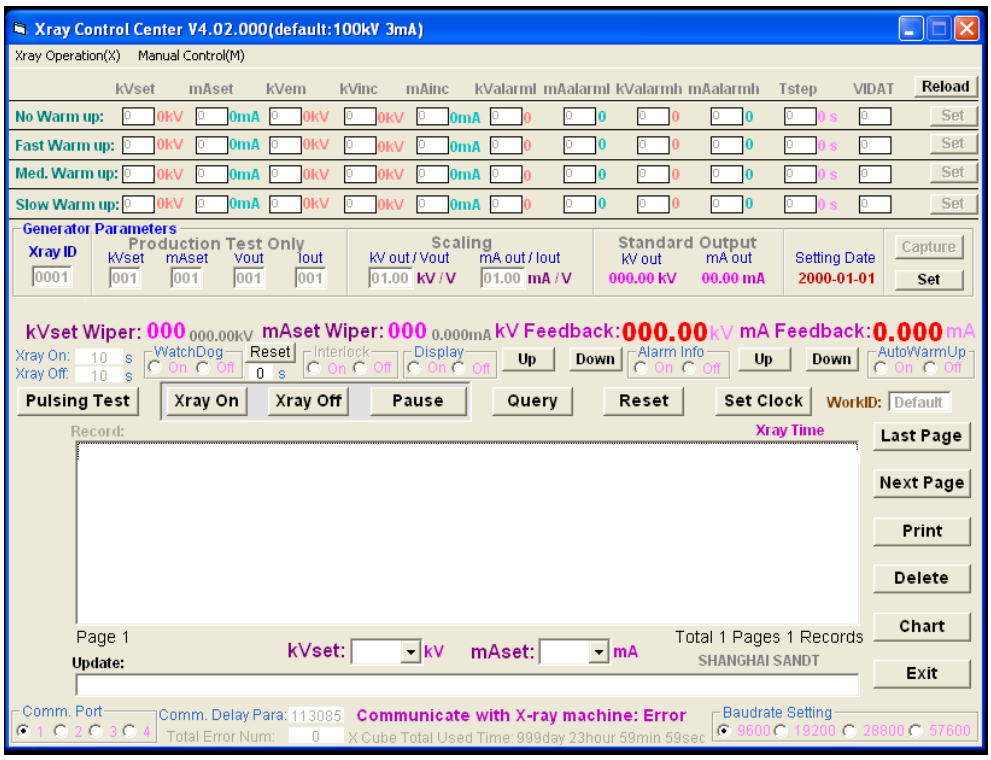


**Figure 3.17:** "XrayControl V4.02" window.

### 3.5.2 Operating x-ray detectors

#### 3.5.2.1 UCL OTB Camera Test App

The custom built software supplied by the detectors' manufacturer 3DX-RAY is named "UCL OTB Camera Test App". Once installed, this consists of a single window with control parameters, a graphical display of the data and a diagnostics log box (Figure 3.18). This software was used initially to calibrate the detectors (see section 3.5) and for preliminary tests. Later, LabVIEW (section 3.6.1) code was developed to operate the detectors (see section 3.6).

For computer software to be able to connect and operate the detectors these steps need to be followed. Steps 1 to 4 establish the connection between the detectors and the computer. Steps 5 to 7 are the operational instruction for using the detectors with the 3DX-RAY software. If alternative software is used, such as LabVIEW (see page 79) then these are unnecessary, but steps 1-4 remain necessary.

1. Install StarTech Ethernet Adaptor software
2. Plug in all connection and power cables.
3. Configuration of Network and Ethernet Adapter (Appendix B, page 202).
4. Install Net Framework 4
5. Install Ish.Ucl.Otb.Camera.TestApp

6. Open the software and click the 'Connect' button to connect. This may take several seconds so wait for the 'Connect' button to grey out and the 'Disconnect' button to become available. When connected the two 'Start...' Buttons should become available, along with the 'Capture Parameters' control.

7. To perform an internally triggered capture:
(a) Select the Capture Period required (b) Select the number of lines required in each data buffer delivered (c) Select whether you want the capture to continue until the 'Stop Capture' is pressed or to stop after the first buffer has been delivered. (d) Click the 'Start Free Running Capture' button. At this point you should see the graph part of the screen showing the data being read from the detector box (such as in Figure 3.20).

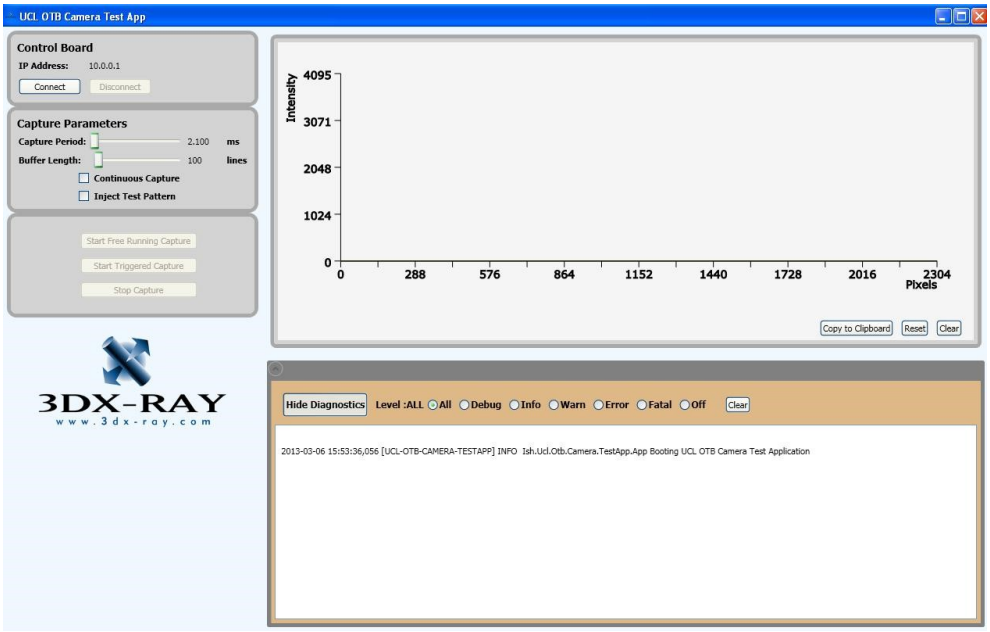


**Figure 3.18:** "UCL OTB Camera Test App" window.

### 3.5.3 Detector alignment

Each detector consisted of a single line of 192 pixels with a pixel pitch of 150 $\mu m$. The detectors' energy calibration had been completed prior to experiments. Detector alignment was performed to get a detector readout signal that was as large and uniform as possible among the twelve detectors.

Having placed the detectors along the conveyor belt bend and the x-ray sources facing them, the individual direction of each detector was checked so that they all were sufficiently illuminated by the x-ray source: what is called detector alignment. The intensity of the X-rays of the detector was read as a continuous string of data, each of the 192 pixels on the x axis representing a separate detector. As such, the first half of the graph corresponds to the first set of

six detectors and the second half to the second set. Figure 3.19 shows the graphical display of data with the x-ray sources switched off.

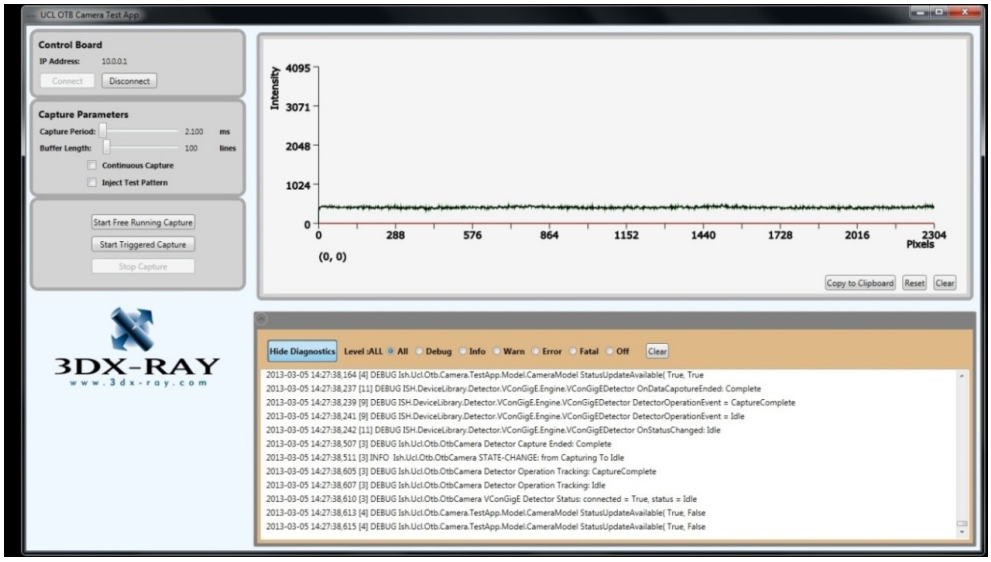


**Figure 3.19:** Graphical display of detectors' data with the x-ray sources switched off.

By switching on the x-ray sources, each facing a set of six detectors, a string of data is acquired. This was repeated until the graphical display of data was of sufficiently high intensity for all detectors. Figure 3.20 shows two such data acquisitions. The lower, black line shows data acquired with the second x-ray source turned off. The green line (line above) shows data acquired with both x-ray sources on, after adjustments had been made for better detector alignment: notice the higher intensity in part of the first half of the graph.

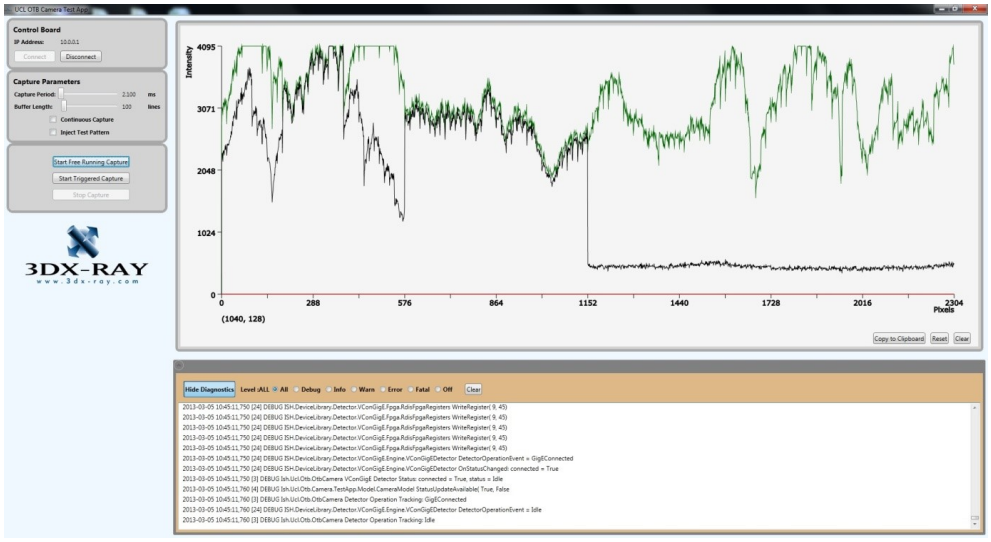


**Figure 3.20:** Graphical display of detectors' data: The lower,black line shows data acquired with the second x-ray source turned off. The green line (line above) shows data acquired with both x-ray sources on, after adjustments have been made for better detector alignment.

## 3.6 LabVIEW software development

### 3.6.1 LabVIEW

LabVIEW, short for Laboratory Virtual Instrumentation Engineering Workbench, is a graphical programming platform which can be used to build data acquisition and instrument control applications. Each graphical programs is called a Virtual Instrument (VI), and is based on the concept of data flow programming. Its two major components are the Block Diagram (BD) and Front Panel (FP). The FP provides the user-interface of a VI while the BD incorporate the corresponding graphical code. An example of a sample VI's FP is shown in the top Figure 3.21, and the corresponding BD in the bottom Figure 3.21.

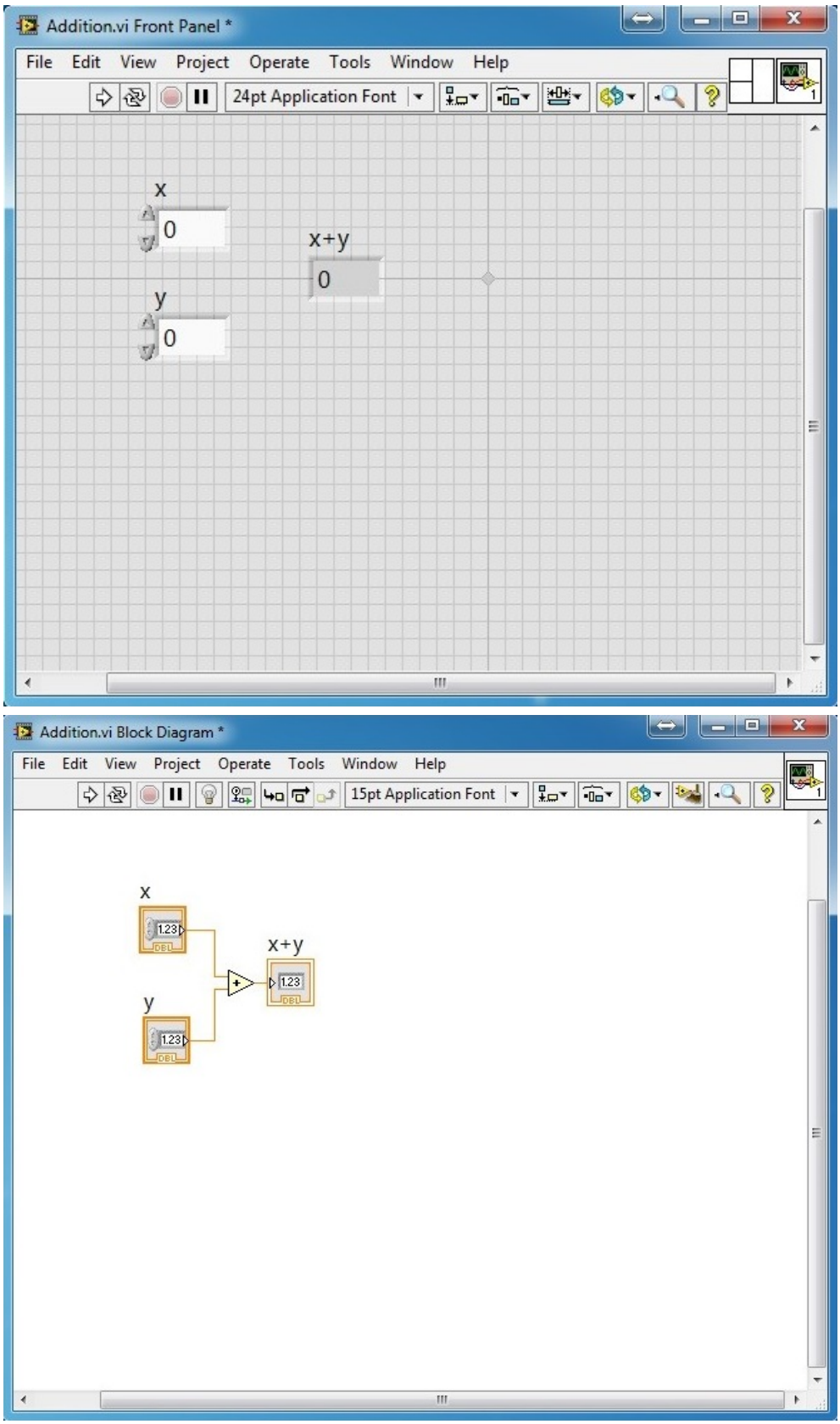


**Figure 3.21:** Example VI of basic addition sample showing the corresponding Front Panel (above) and Block Diagram (below) windows.

### 3.6.2 LabVIEW software development

In order to incorporate the operation of the ObT hardware components within a global software environment, LabVIEW was used. The objective was to control and tune the ObT system in producing the desired outcome by automatically operating its individual components. LabVIEW is a system design platform and development environment for a visual programming language from National Instruments.

The scope of the code developed was to effectively and efficiently operate the x-ray detector system in collecting x-ray projection images. More specifically, the final outcome of the code is to produce images of the acquired projections, either as a single stack of all the 12 detector projections together, or separately as 12 individual images. The x-ray sources were taken to be on and set to the desired value for the duration of the screening, operated by "XrayControl V4.02" as described in section 3.5.1. Additionally, the conveyor belt system was operated separately assuming a continuous movement of the belts at a speed which was defined for each experiment.

The LabVIEW code has been developed to effectively and efficiently operate the x-ray detectors' system in collecting x-ray projection images. The objective was to acquire the individual projection of the phantom on each detector at a specified moment in time. The 'logic flow' diagram of the software developed is presented in Figure 3.22. A print screen of the BD of the LabVIEW code developed is shown in Appendix C (page 204).

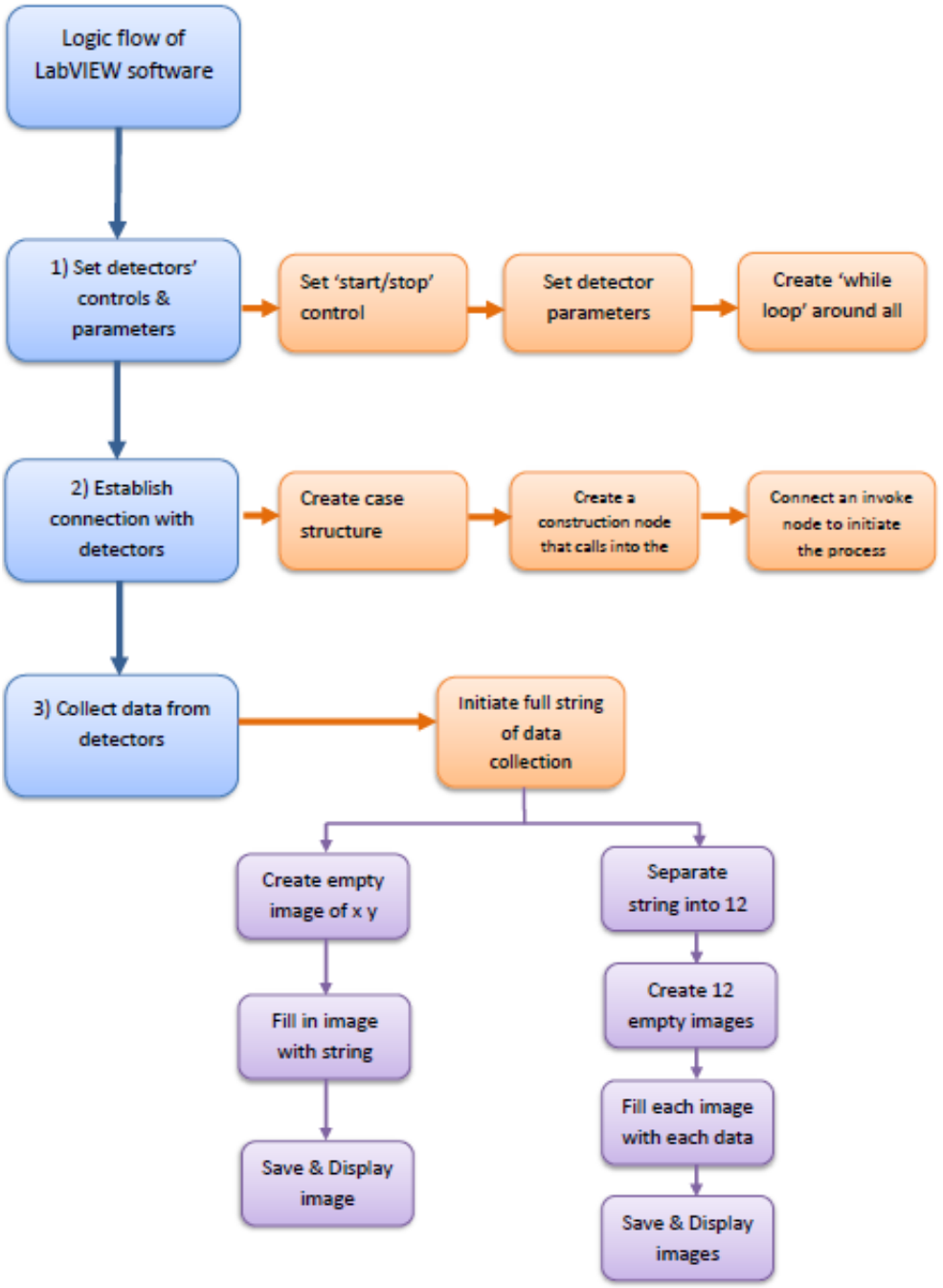


**Figure 3.22:** Logic flow diagram of the software developed for x-ray imaging using LabVIEW.

# Chapter 4

# Exploring On-belt Tomosynthesis

## 4.1 Chapter overview

This chapter includes the experimental work regarding testing, developing and evaluating the ObT system. This includes phantom creation, systems calibration, software development, x-ray acquisition, image correction and reconstruction. The resulting reconstructed images are analysed and further developments are discussed.

## 4.2 Defining coordinate systems & Experimental set-up

The final set up of the ObT system, shown in 3.13 on page 72, consists of two 90° arc conveyor belt bends with a straight belt in between. The reason the central belt was fitted was to ensure that each detector is illuminated by a single source (section 3.2.2). An object moving on the system, travels the exact same path on the two belts bends (Figure 3.13: *C1, C2*) in both set ups (1) and (3), as the middle straight belt *C3* in (3) was assumed to not deviate an object's path. As such, *C3* was disregarded when defining the laboratory coordinate system and set-up, which is presented in section 4.2.1. Therefore, the laboratory coordinate system represents the physical ObT set-up, while the simulation coordinate system was the one used in the image reconstruction (section 4.4.3). The simulation coordinate system had been pre-defined differently by the reconstruction code developer Dr Marta M. Betcke (UCL). As such, the appropriate transformation of the laboratory coordinate system to the simulation one is presented in section 4.2.2.

### 4.2.1 Laboratory coordinate system

The laboratory *coordinate system* ($CS$) is defined as:

$$C_L = (x_L, y_L, z_L) \tag{4.1}$$

$P_i$ is defined as the phantom position at location $i$:

$$P_i = (x_i, y_i, z_i) \tag{4.2}$$

where $i = A, B, C$ correspond to the *initial, medial,* and *final* position of the phantom on the conveyor system during each experiment. These are shown in Figure 4.1. The term phantom position signifies the phantom volume centre position. The phantom is always a cuboid volume with 3D dimensions defined with respect to the conveyor system's COR (point $O$) which is set to (0,0,0). $z$=0 is set at the level of the belt surface. And $x_L$=0 is set as the front side line of the conveyor belts, indicated by the dark blue dash line in Figure 4.1.

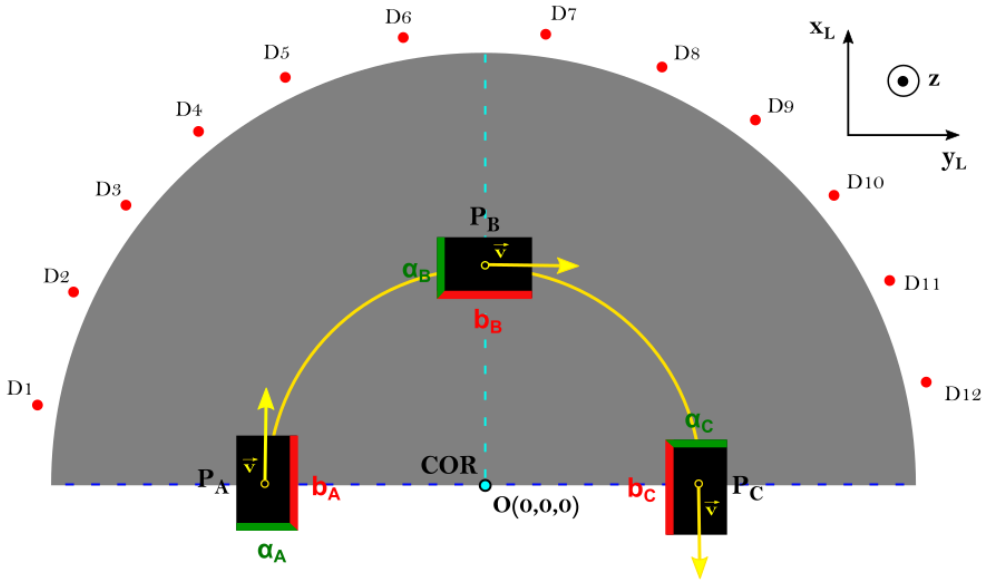


**Figure 4.1:** 2D top view of laboratory system set-up coordinate system showing a phantom at three positions $P_A$, $P_B$, $P_C$ traveling along a circular arc, indicated by the yellow curve, of constant radius $r$ from the COR (point $O$). The yellow arrow indicates the velocity direction of the phantom volume centre at each position.

In all experiments, the z axis is set to be vertical, with the positive direction facing upwards, [1] and we assume that $z_i$ remains constant for each *acquisition set*[2], as it travels along the conveyor system. Its exact value varies for each phantom as it depends on the phantom height $h$, and is equal to $z_i = \frac{h}{2}$. We also set that in each case the centre of the phantom coincides with the trajectory centre of the conveyor system, meaning that the distance of the phantom COR ($P_i$) is at a known distance from the belt COR ($O$). This corresponds to a radial distance of an absolute value of $r$ at any instance of the phantom travel.

As shown in Figure 4.1, at position A and C, $P_i$ is set at a specific with its side $a_A, a_C // y_L$, while $b_A, b_C // x_L$. In position B, it is $a_B // x_L$ and side $b_B // y_L$. Therefore:

[1] By vertical and horizontal direction we globally signify the directions perpendicular and parallel to the horizon respectively.

[2] *Acquisition set* is the collection of projections of a phantom, captured by all 12 detectors, as it travels along the conveyor system.

$$P_A = (0, r, \frac{h}{2}) \tag{4.3}$$

$$P_B = (r, 0, \frac{h}{2}) \tag{4.4}$$

$$P_C = (0, -r, \frac{h}{2}) \tag{4.5}$$

### 4.2.2 Simulation coordinate system

#### Converting laboratory CS to simulation CS

The simulation CS is defined as:

$$C_S = (x_S, y_S, z_S) \tag{4.6}$$

The z axis is defined to be the same in both laboratory and simulation CSs, thus $z_S = z_L = z$. . Therefore, in converting the laboratory CS ($C_L$ ) to the simulation CS ($C_S$) we can consider 2D systems only. In both coordinate systems, z=0 is set at the level of the belt surface. Looking at the way the two CSs have been set up and defined in Figures 4.1 and 4.2, it can be observed that the relationship between the two CSs corresponds to:

$$\begin{pmatrix} x_S \\ y_S \end{pmatrix} = \begin{pmatrix} y_L \\ x_L \end{pmatrix} \tag{4.7}$$

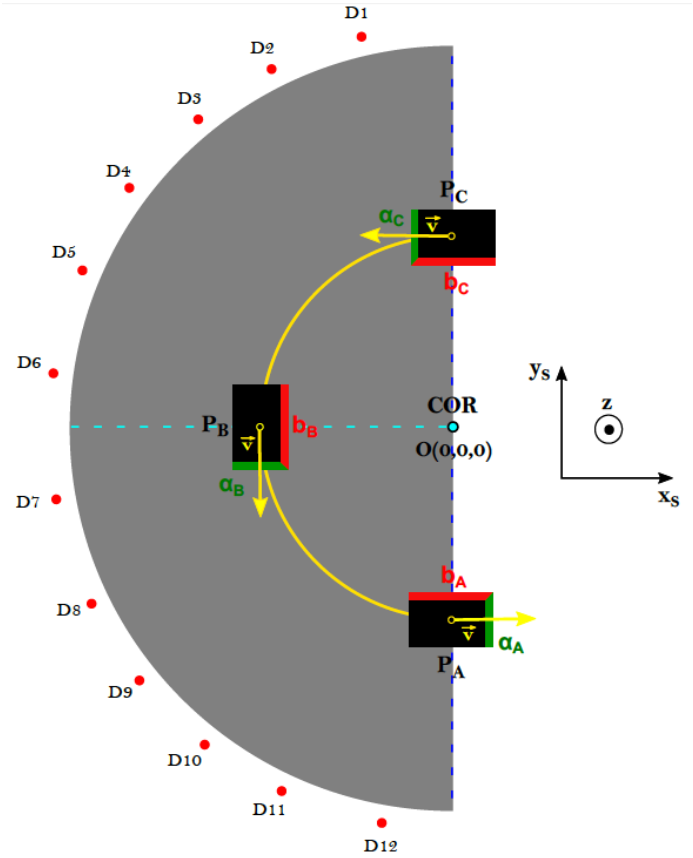


**Figure 4.2:** 2D top view of simulation system set-up coordinate system.

Using a linear transformation, $C_L$ can be related to $C_S$. From equation 4.7 we can deduce the necessary transformation matrix $T$, so that $C_S = TC_L$:

$$T = \begin{bmatrix} 0 & 1 \\ 1 & 0 \end{bmatrix} \tag{4.8}$$

where

$$C_L = \begin{bmatrix} x_L \\ y_L \end{bmatrix} \tag{4.9}$$

and

$$C_S = \begin{bmatrix} x_S \\ y_S \end{bmatrix} \tag{4.10}$$

Therefore, the simulation coordinate system matrix ($C_S$) can be related to the $C_L$ by applying the appropriate transformation matrix $T$:

$$C_S = TC_L = T \begin{bmatrix} x_L \\ y_L \end{bmatrix} = \begin{bmatrix} 0 & 1 \\ 1 & 0 \end{bmatrix} \begin{bmatrix} x_L \\ y_L \end{bmatrix} = \begin{bmatrix} y_L \\ x_L \end{bmatrix} \tag{4.11}$$

## 4.3 ObT detector image quality

### 4.3.1 Raw image quality analysis

#### 4.3.1.1 Measuring image noise in ObT

Identifying, measuring and correcting the parameters affecting image quality is a highly important part of developing an x-ray imaging system, particularly if it is an unconventional prototype, as in the case of this study. As seen in section 2.4 these parameters which describe digital x-ray detector image quality are noise, spatial resolution, contrast and geometric distortions. It is important to understand how each of these affect the projections collected with the ObT by the strip detectors.

Figure 4.3 shows sample projections collected during the same acquisition set with ObT, in order to describe how the projections are formed and, hence, affected by the parameters above. Each detector consists of a single line of 192 pixels, labeled from bottom to top. This corresponds to the vertical axis of a 2D projection, meaning that, within each row, data is collected from a particular pixel, and each consecutive row represents a different pixel. The horizontal axis corresponds to the number of iterations ($I$), which is the number of times a full string of data is collected from the detector control box, and is related to time ($t$). In a perfect system, $I$ would be directly proportional to $t$, however, in reality iteration intervals can vary due to latency in the system's performance, further information on this subject can be found in [Haughn and Blair, 2014]. As such, for each acquisition set, the 2D data correspond to the same iterations and iteration intervals, across the columns. As Figure 4.3 shows, there is a noise pattern across both vertical and horizontal direction, which need to be explored and removed. In addition to these, image geometric distortions due to warping, need to be accounted for.

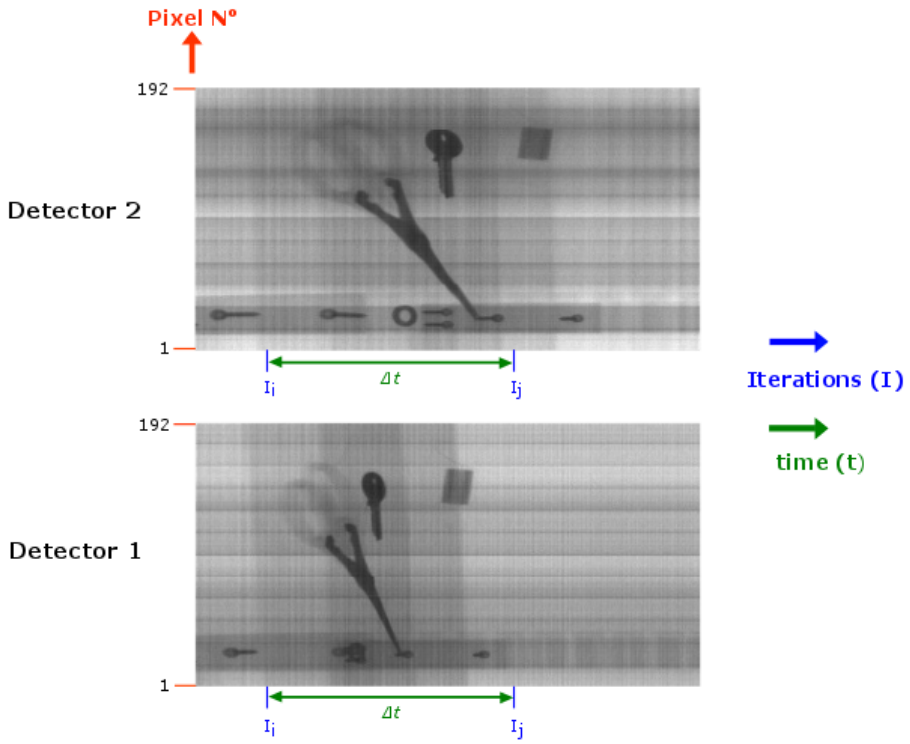


**Figure 4.3:** ObT 2D raw projection samples.

#### 4.3.1.2 Measuring the warping effect in ObT

As seen in section 2.4.2.6, warping can be assessed with the use of a grid (see Figure 2.9 on page 27). These procedures are based on the structure of a grid consisting straight lines and orthogonality, it's deviation from which can be measured. Warping can be investigated using a simple test in which linear and perpendicular test pieces are imaged. The degree to which the imaged objects deviate from 'straight' can be readily measured. For the purpose of investigating the warping effect in the projections formed by ObT, the following experiment was carried out.

Phantom B (Figure 4.4) was created consisting three straight stainless steel rods (R1, R2, R3) placed on a thin upright sheet of perspex (3mm thickness). The rods were of different diameters and lengths, making sure the longest one was greater than the length of the phantoms used in ObT experiments. The mid-points of the rods were aligned with each other on the x-y plane (see $x_L, y_L$ in Figure 4.1 on page 84). In this case *length* corresponds to a straight line parallel to the horizon (perpendicular to $\vec{z}$ ) which, at any instant during an experiment, is parallel to the *direction of motion* at the volume centre of the rod. This is illustrated in the example set-up shown in Figure 4.1, where the length direction corresponds to side $b$ which is parallel to the phantom centre velocity $v$.

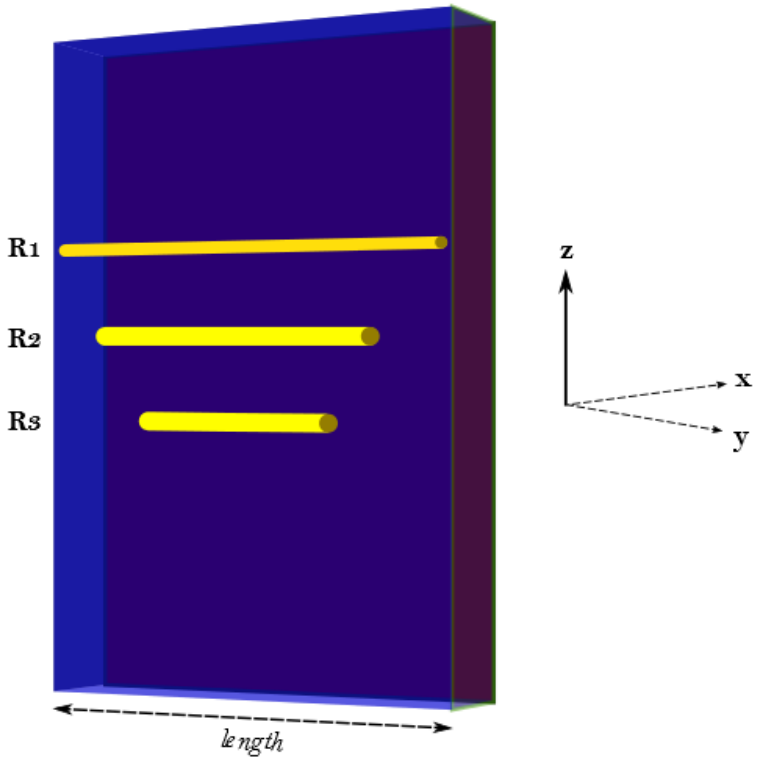


**Figure 4.4:** Out of scale schematic of Phantom B, showing three horizontal rods (R1, R2, R3) placed centrally (aligned with each other on the x-y plane) on a cuboid perspex sheet.

Due to the nature of the origin of this effect it was assumed that a straight horizontal object would appear curved in the acquired projections. The way this was checked, was by fitting a second order polynomial to the rod data of a 2D projection, and checking the *goodness of fit* (section 2.12.1 on page 55). More specifically, by setting a threshold value, the pixels corresponding to the rod data could easily be segmented, due to the large difference in material attenuation between the rods and the background. Therefore, the pixel values of each rod, could be plotted, and the appropriate polynomial fitting could be applied. The Matlab code developed for this process is shown in Appendix D (page 205). Three acquisitions were made under the same conditions as the ObT imaging, at 100kV and 1.2mA (Table 4.2). The three corresponding plots **A1**, **A2**, **A3** in Figure 4.5 show the projection image of Phantom B, converted to Matlab's *'parula'* colormap, upon which the calculated rod plot was superimposed (black, red, blue lines corresponding to R1, R2, R3).

Points that follow a straight line fit, would show a high R-square value when fitting a 1st degree polynomial. In contrast, points that follow a curve fit would show a higher R-square value when fitting a 2nd degree polynomial instead. As such, both 1st and 2nd degree polynomials were fitted on the three rod plots in each of A1, A2 and A3. All of these showed a higher R-square in the later case (fitting a 2nd degree polynomial), of values between 0.88-0.98. Three examples of these results are shown in Figures 4.6,4.7, and 4.8. It should be noted, however that the overall 'curvature' of the rod plots was not of a

large magnitude as the offset from a straight line is between 2-6 pixels.

The observed warping effect was considered to originate in the fact that there was inconsistent object magnification as the object travels through the ObT system. This effect was accounted for in the reconstruction process, as discussed in section 4.3.2.3.

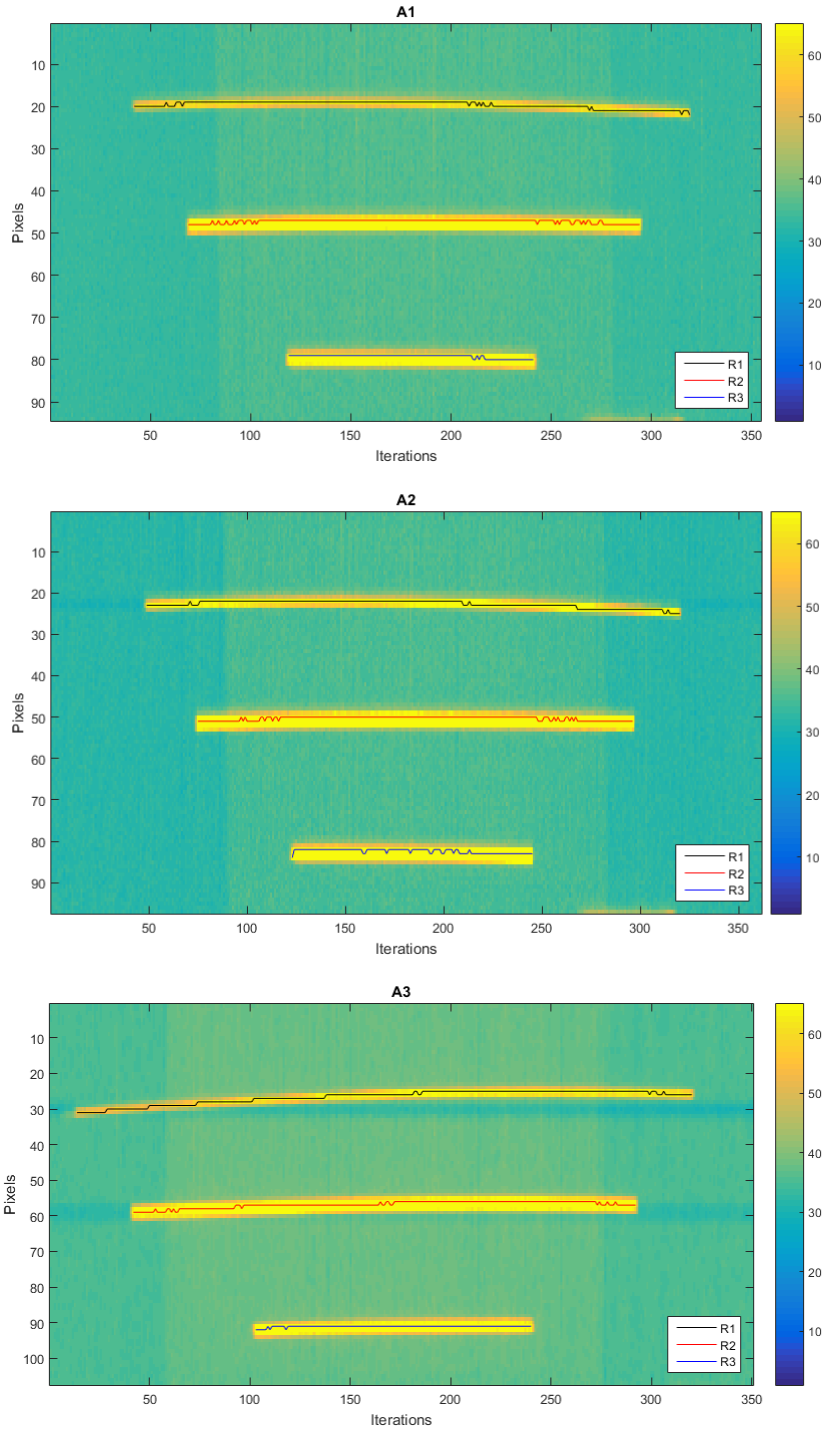


**Figure 4.5:** Plots A1, A2 and A3 of three acquisition sets, showing the projection image of Phantom B, converted to Matlab's *'parula'* colormap, upon which the calculated rod plot is superimposed (black, red, blue lines corresponding to R1, R2, R3).

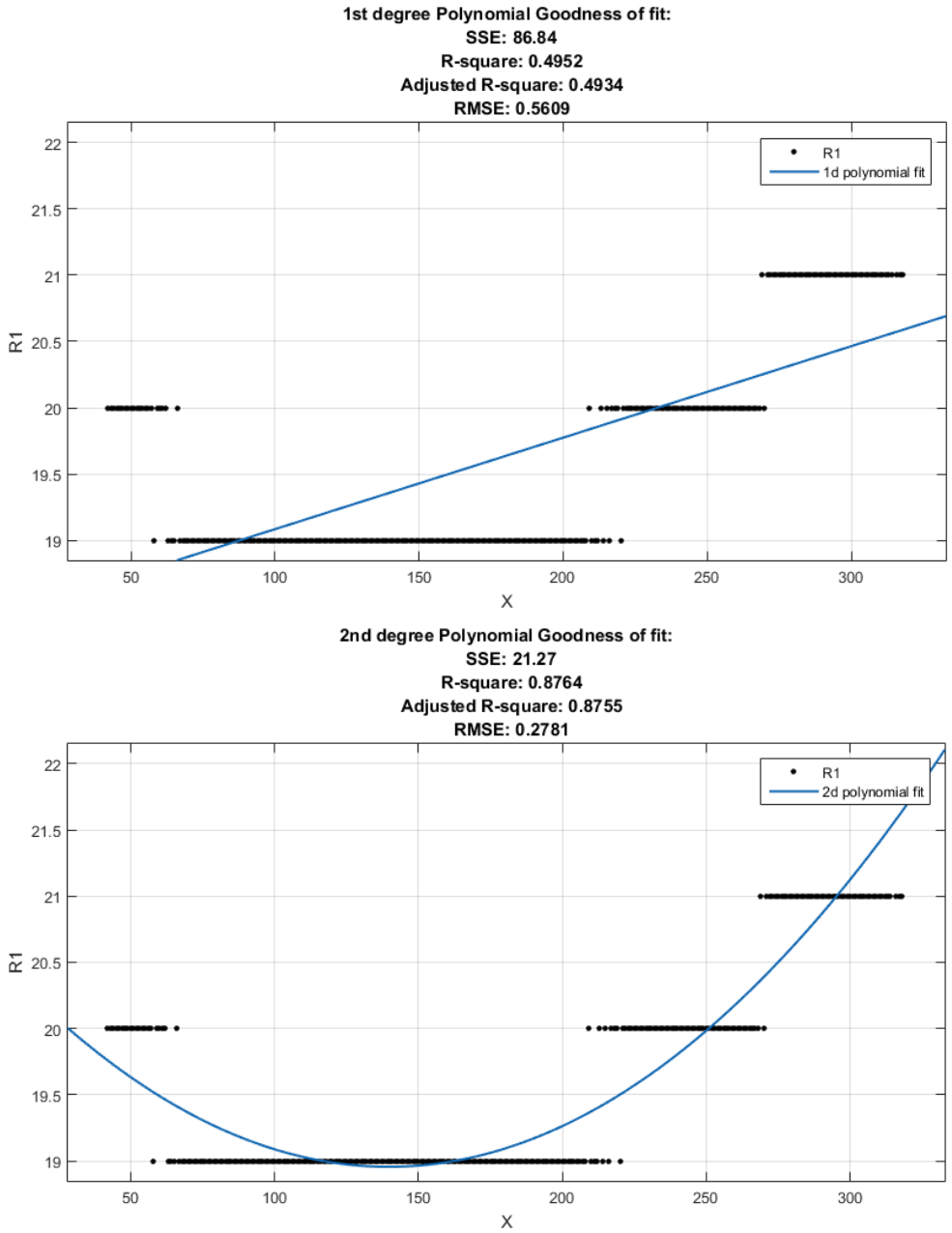


**Figure 4.6:** Goodness of fit results for R1 of A1 showing 1st (above) and 2nd (below) degree polynomial fit.

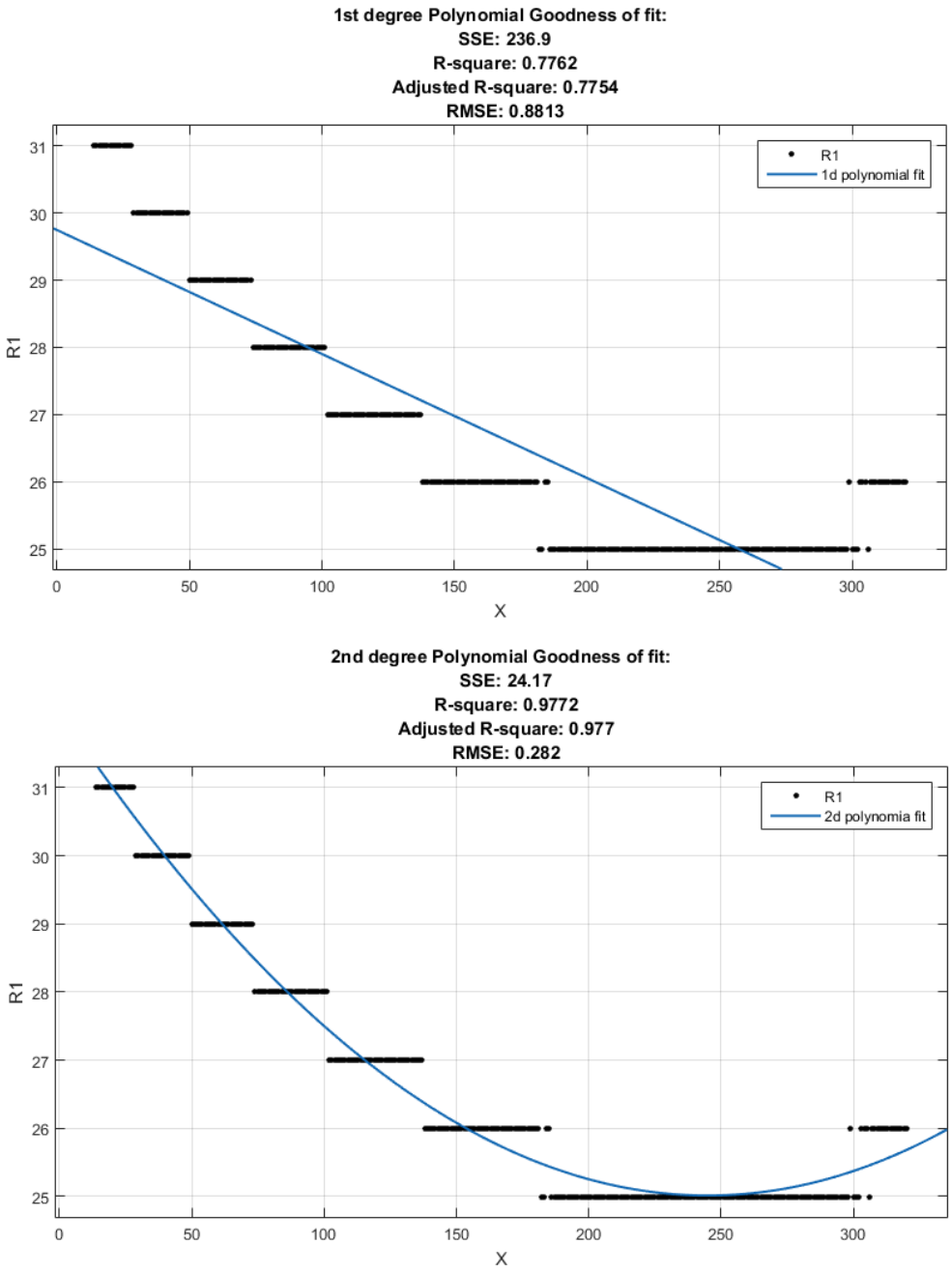


**Figure 4.7:** Goodness of fit results for R1 of A3 showing 1st (above) and 2nd (below) degree polynomial fit.

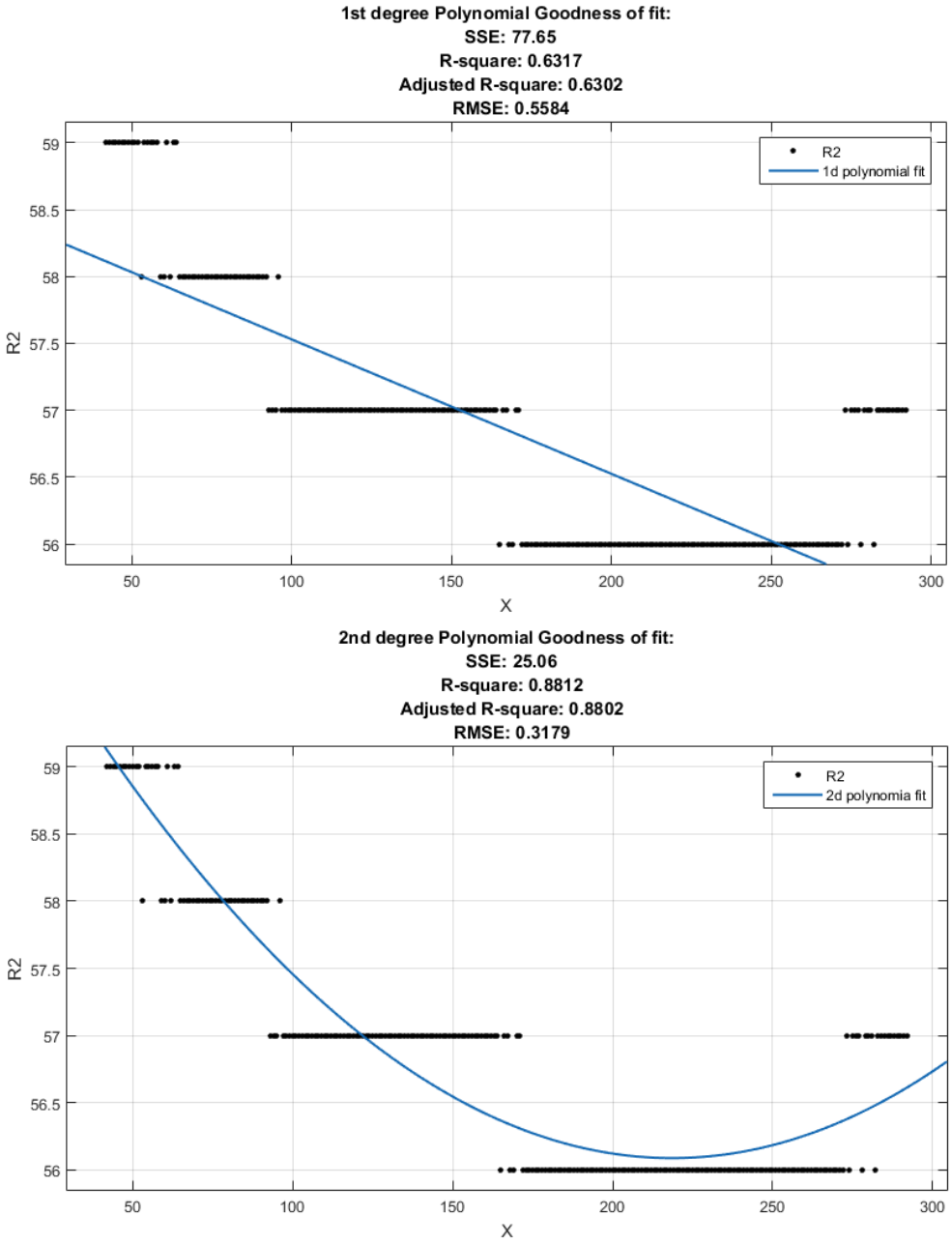


**Figure 4.8:** Goodness of fit results for R2 of A3 showing 1st (above) and 2nd (below) degree polynomial fit.

### 4.3.2 ObT image corrections

The projection calibration, i.e. the technique applied to remove noise and account for the warping effect, was incorporated in the reconstruction software written in Matlab software. The reconstruction code steps can be seen in Figure 4.19.

There are several sources of x-ray detector noise, as discussed in section 2.4.1.1. In ObT, noise patterns were evident in both the vertical and horizontal direction of acquired projections, as is evident in the sample flat field image - the top image in Figure 4.9.

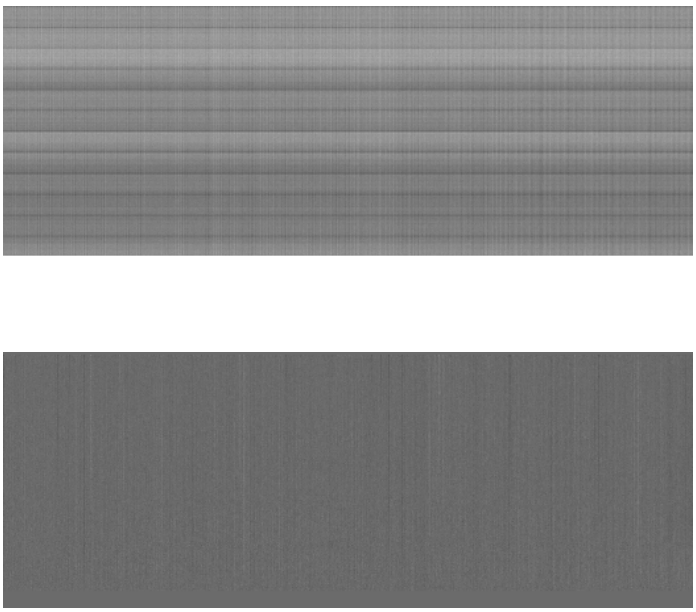

**Figure 4.9:** Sample of pre- and post-calibration of ObT image noise shown in top and bottom image respectively.

In addition, the dark field ObT projections, unlike conventional systems, were inconsistent, as is evident in Figure 4.10 depicting four consecutive dark field projections collected by the same detector. in the same conditions. This inconsistencies are also quantified and displayed in the four respective image histogram plots in Figure 4.11.

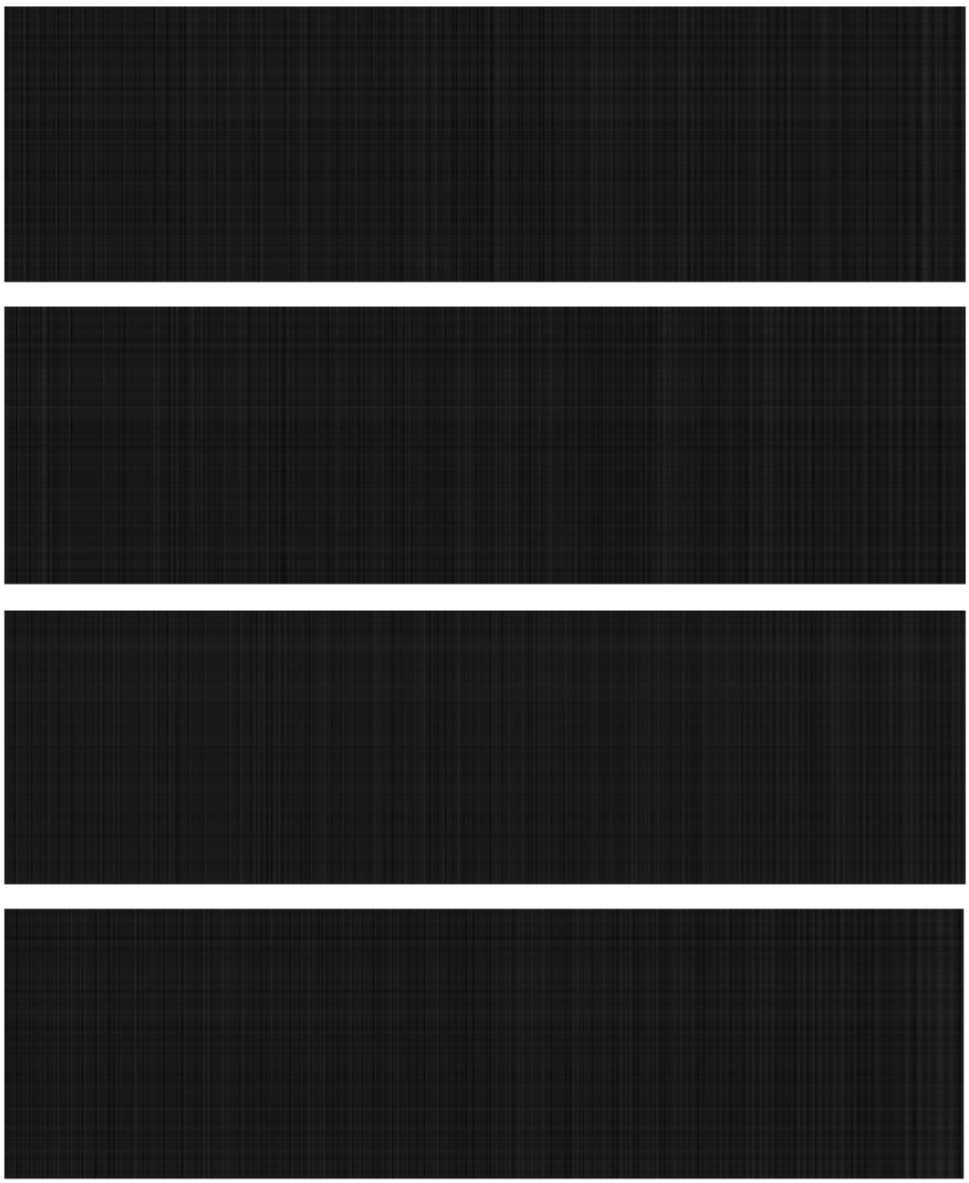

**Figure 4.10:** Dark field projections of the same detector, in the same conditions. Upon visual inspection it is clear that the dark field noise in the vertical plane is inconsistent.

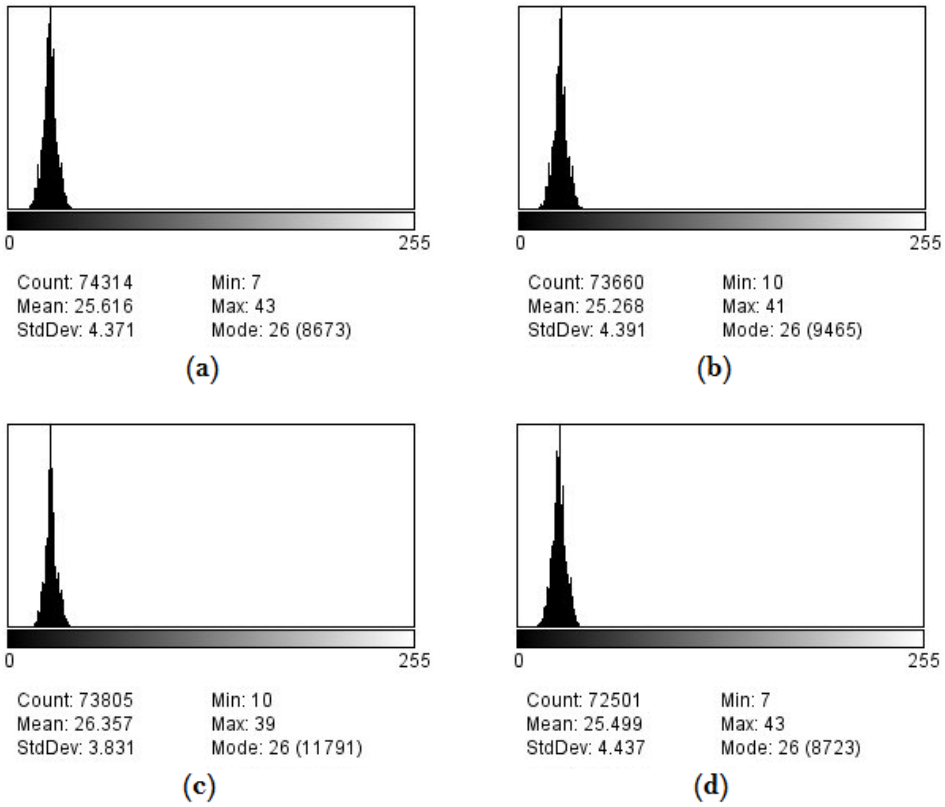


**Figure 4.11:** Histogram plots of the four consecutive dark field projections in Figure 4.10 showing their respective inconsistencies through quantifying the image greyscale values (represented by the horizontal axis).

The logic behind the ObT image corrections applied was based on the existing scientific literature, reviewed in section 2.4.2. However, as the common correction methods were based on set system geometric configurations imaging using flat-panel detectors (such as the 'gain and offset' correction), which are grounded on a fixed dark field noise pattern, they could not be directly applied to the ObT images. Therefore, techniques were developed to address the projection noise in the vertical and horizontal direction individually for better results, in correcting the images. For this, appropriate software code was written in Matlab.

Since the dark field noise was inconsistent, identical lead blocks (20×20×20 mm) were placed at the top end of its detector strip, covering the top 19.5mm of each detector strip, ie. the top 13 pixels of each projection (Figure 4.12). Since lead is a highly attenuating material, the 20mm thickness would block out all x-rays, creating a dark field strip at the top of each projection. This strip was then used to calibrate the projections with respect to the dark field vertical background noise (section 4.3.2.2:a)

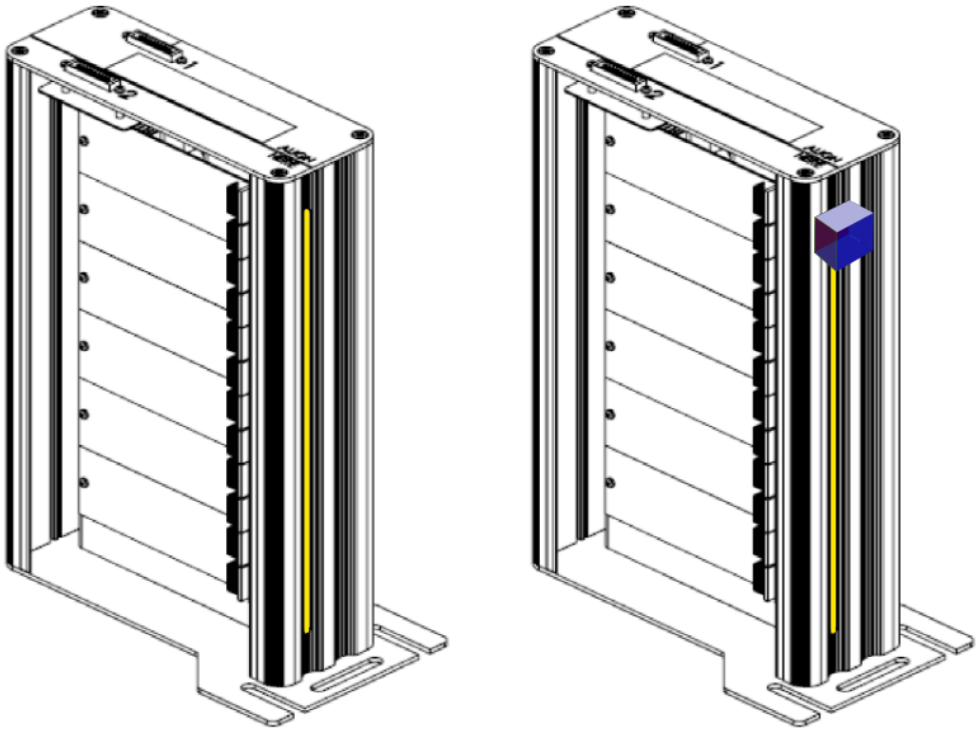

**Figure 4.12:** Detectors with (*right*) and without (*left*) lead block, which is implemented for projection calibration purposes. The yellow line represents the detector 'window', while the blue block is lead.

A sample of a phantom projection is shown in Figure 4.13, showing the areas referenced in the noise calibration processes (sections 4.3.2.1-4.3.2.2), which are applied in either the vertical or horizontal direction, corresponding to rows $R_i$ and columns$C_i$ respectively.

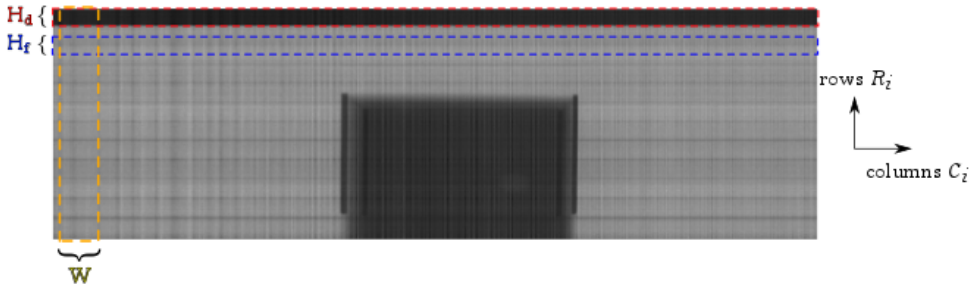


**Figure 4.13:** Sample of a projection showing the area references of the noise calibration processes.

#### 4.3.2.1 Calibrating FPN

As discussed in section 2.4.2.1, FPN, is related to the inconsistent pixel-to-pixel response of the detector. In this case, the FPN manifests itself as horizontal lines across the projections.

The steps taken to calibrate the ObT FPN of each detector were:
1) Determine a *window* which corresponds to a 2D rectangle covering the height of each detector, of a width $W$ detector pixels, shown in Figure 4.13.

This window is empty of phantom and thus corresponds to the flat field.
2) Get average greyvalue for whole window: $GV$
3) In Window get average greyvalue per *row*: $GV_i$, $i$=1...192
4) Multiply each row $R_i$ in each projection by a factor of $\frac{GV}{GV_i}$
5) Multiply whole projection by $\frac{GV_{max}}{GV}$ to equalise the mean value of each detector flat field greyvalue, where $GV_{max}$ is the maximum value over all $GV$ for all detectors. This is done because the horizontal lines are calibrated for each detector independently.

#### 4.3.2.2 Calibrating vertical noise

The vertical noise calibration process was done in two steps, corresponding to the dark field and flat field correction, described respectively in (a) and (b) below.

(a) The steps followed for each detector dark field correction were:
1) Specify the detector rows that are covered by lead we determine a *window* which corresponds to a 2D rectangle covering the width of each projection, of a height $H_d$ which is specified to cover the lead thickness in the projections, shown in Figure 4.13.
2) Get the average greyvalue of the non zero values in the background for each vertical line *column*: $GV_i$, $i$=1...$I$ ($I$=total number of iterations)
3) Subtract the average for each column $GV_i$ from each column $C$ respectively: $C_{i'} = C_i - GV_i$
4) Subtract the minimum greyvalue in each detector projection, $GV_{min}$, from the whole projection. This is to make the data non-negative.

(b) The steps followed for each detector flat field correction were:
1) Specify the detector rows which correspond to the flat field, we determine a 2D rectangle window covering the width of each projection of a specified height $H_f$, shown in Figure 4.13.
2) Get average greyvalue for whole window: $GV$
3) In Window get average greyvalue per column: $GV_i$, $i$=1...$I$
4) Multiply each column $C_i$ in each projection image by a factor of $\frac{GV}{GV_i}$
5) Multiply whole projection by $\frac{GV_{max}}{GV}$ to equalise the mean value of each detector flat field greyvalue, where $GV_{max}$ is the maximum value over all $GV$ for all detectors.

#### 4.3.2.3 Accounting for warping

The way that the warping geometric distortion (measured in section 4.3.1.2) is accounted for, is by defining the imaging geometry with respect to the phantom. To this end, the phantom position with respect to the corresponding source focal spot (FS) and detector needs to be known. In this way, by treating each ray independently, the unorthodox geometry and resulting distortions

are accounted for. More specifically the image reconstruction method, the software code for which was developed by Dr M. M. Betcke, is performed by first recomputing each ray position with respect to the phantom (*iterative reconstruction methods*, section 2.6) and then implementing the Siddon algorithm (section 2.6.1) in order to obtain a projection matrix, whose rows correspond to a ray intersection of the phantom. The steps of this reconstruction code are shown in Figure 4.19 on page 108.

### 4.3.3 Measuring the image quality of ObT

As discussed in section 4.2, the four parameters affecting detector image quality are noise, contrast, spatial resolution and geometric distortions. The former three can be measured using standard images. The later, defined as the warping effect (section 2.4.1.4 on page 20) is accounted for within the reconstruction code at a later stage, described in section 4.3.2.3, and therefore is not discussed further.

#### 4.3.3.1 Noise

The efficiency of any flat field correction for any noise source can be evaluated by comparing the pre and post-calibration value of the image uniformity factor ($U$, section 2.4.2.2) in the respective images. 10 flat field images were collected throughout the duration of the experimental image acquisition (section 4.4.2), under the same conditions. These images were corrected using the methods described in section 4.3.2 and $U$ was mathematically calculated in all 10, pre- and post-correction, the average of the former being 0.53 and the later 0.77. This meant that the pre-correction images were on average 53% uniform, while correction increased their average uniformity to 0.77%, an increase of 45%. These values are listed in Table 4.1.

| **Image** | **Image uniformity factor - U** | |
|---|---|---|
| **#** | **pre-** | **post-correction** |
| 1 | 0.55 | 0.75 |
| 2 | 0.50 | 0.72 |
| 3 | 0.49 | 0.73 |
| 4 | 0.55 | 0.80 |
| 5 | 0.50 | 0.79 |
| 6 | 0.59 | 0.78 |
| 7 | 0.51 | 0.79 |
| 8 | 0.52 | 0.74 |
| 9 | 0.55 | 0.76 |
| 10 | 0.56 | 0.80 |
| **Average** | **0.53** | **0.77** |

**Table 4.1:** Values of uniformity factor $U$ measured in 10 flat field images, pre- and post- correction.

#### 4.3.3.2 NPS

As discussed in section 2.4.2.4, NPS is a measure of noise as a function of spatial resolution of an image. As there is no known technique for measuring the NPS of 1D (strip) detectors, the method of first measuring 2D NPS and then extracting the 1D NPS in both horizontal and vertical directions (named $NPS_u$ and $NPS_v$ respectively) can give us information i) in the vertical direction of the NPS, related to the specific pixels of each detector ii) of the NPS related to the detector average performance, as NPS is measured on a collection of images acquired.

10 flat field images were acquired with the ObT using the same image acquisition parameters shown in Table 4.2 as used in the ObT experimental technique (section 4.4.2 on page 106). Following image calibration procedure of the flat field images, described in section 4.3.2, the NPS was calculated using '*OBJ_JQ_reduced*' software developed by Dr Nick Marshall at Barts and the London NHS Trust [Marshall, 2006, 2009].

In OBJ_IQ_reduced, the NPS was calculated by applying a 2D algorithm to these images. This 2D algorithm was used to determine the NPS Workman and Cowen [1993] using $64 \times 64$ half-overlapping ROIs. The NPS was then calculated from the square of the 2D Fourier transforms of the ROIs. The average NPS was calculated to reduce the uncertainty in the estimation of the spectral values and normalised using the large area signal square (in pixel values square) to calculate the average 2D NNPS (normalised NPS). The output 1D NPS, which was extracted from the 2D NPS applying axial averaging, for both horizontal ($NPS_u$) and vertical ($NPS_v$) direction is plotted in Figure 4.14 for two image samples. A similar trend was noticed for the other 8 image samples.

$NPS_u$

The horizontal NPS was shown to be relatively stable across all frequencies within 0.0010 $mm^2$ and a maximum value of 0.0015 $mm^2$ in all cases. This trend observed was due to the fact that all values corresponded to the same pixel in each case.

$NPS_v$

The vertical NPS was shown to be an equally stable trend as $NPS_u$ except for very small frequencies. At near zero frequencies it was observed to reach a maximum of 0.008 $mm^2$, while dropping to below 0.002 $mm^2$ at a frequency of between 0.02-0.05 $mm^{-1}$ and stabilising thereafter.

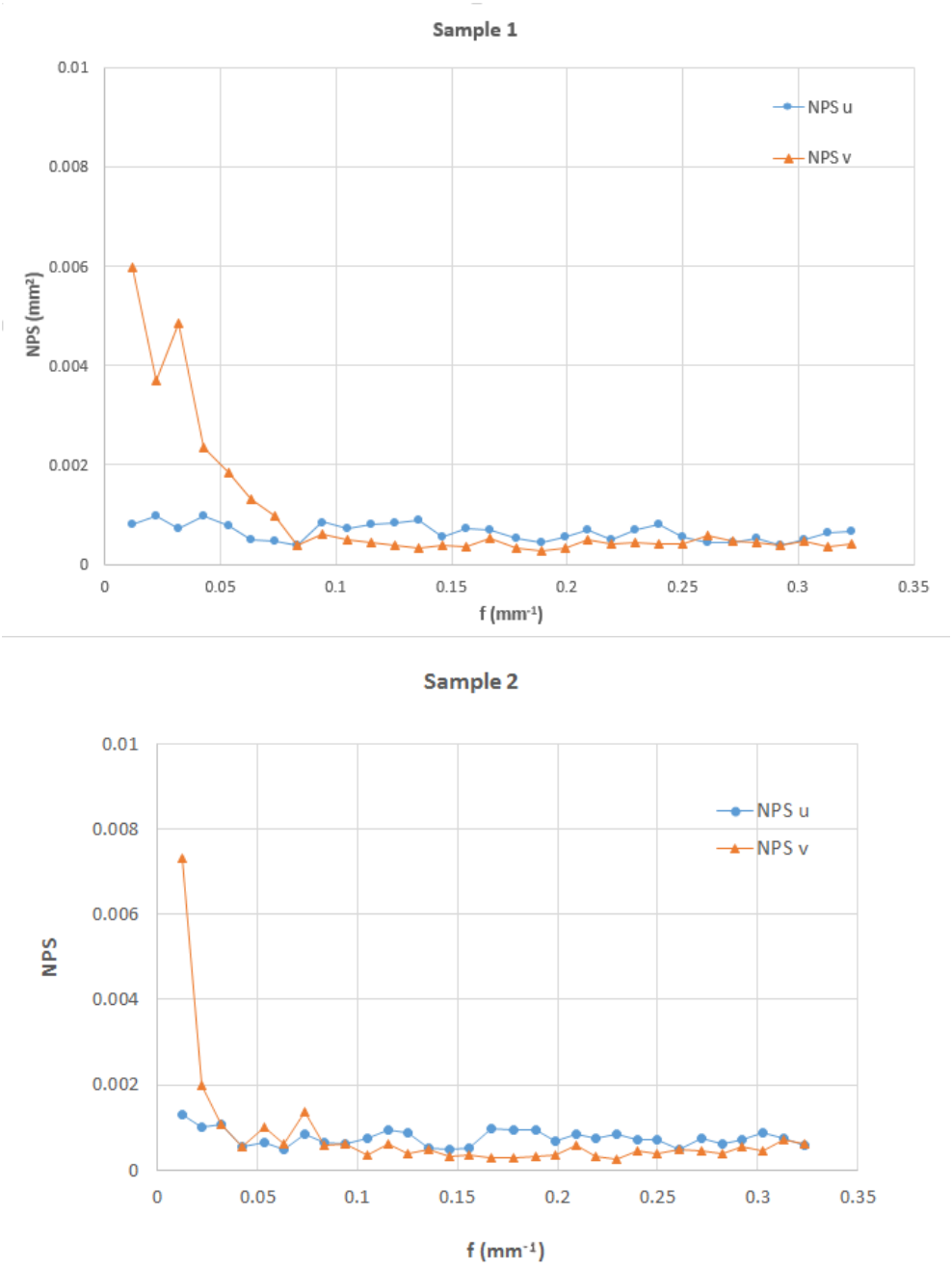


**Figure 4.14:** NPS plotted for two ObT image samples.

#### 4.3.3.3 MTF

The *modulation transfer function* (*MTF*, section 2.4.2.5) expresses the ability of the detector (or system) to reproduce image contrast at various spatial frequencies. As details in the object become finer they are less well represented in the image and will appear at a lower image contrast.

In order to measure the MTF of the ObT system, the edge-response method (section 2.4.2.5) was used, the results of which are presented below. MTF was measured for a single strip detector, as all twelve detectors were assumed to be equivalent, in this case the third detector (*D3,* shown in Figure 4.1, page 84).

Five images were acquired of a sharp edge object, a steel plate of 1mm thickness mounted on a sample holder, with the sharp edge on the top side forming a 4° angle with respect to the belt surface (Figure 4.15). The edge test piece was imaged while traveling in the ObT, from position $P_A$ to $P_B$, shown in Figure 4.1, with the same image acquisition parameters as shown in Table 4.2, used in the ObT experimental technique described in section 4.4.2 on page 106. Following image correction procedure of the acquired images, described in section 4.3.2, the resulting images were loaded in the '*OBJ_JQ_reduced*' software [Marshall, 2009], where the required steps in measuring the MTF (essentially the presampled MTF, described in section 2.4.2.5) were automatically executed, outputting the MTF value as a function of spatial frequency. As the ObT system geometric configuration did not allow for the test piece to be imaged at 0 distance from an ObT detector, the MTF which was initially calculated by '*OBJ_JQ_reduced*' was the system MTF ($MTF_{sys}$). As such, it was necessary to measure the geometric MTF factor of the system ($MTF_{geo}$) based on equation 2.8 on page 26. The detector MTF was then calculated from the system MTF using equation 2.9 on page 26. Both $MTF_{det}$ and $MTF_{sys}$ were plotted for one of the five images, and isshown in Figures 4.16, as results were similar in all five cases.

Appropriate scaling of the spacial frequency axis of the MTF was performed to represent the calculated MTF in terms of the Nyquist frequency of the imaging system, which is equal to one half the sampling rate of the system [Cramér and Grenander, 1959, Stiltz, 1961]. As such, the Nyquist frequency is defined as the highest sinusoidal frequency that can be represented by a sampled signal [Kohm, 2004].

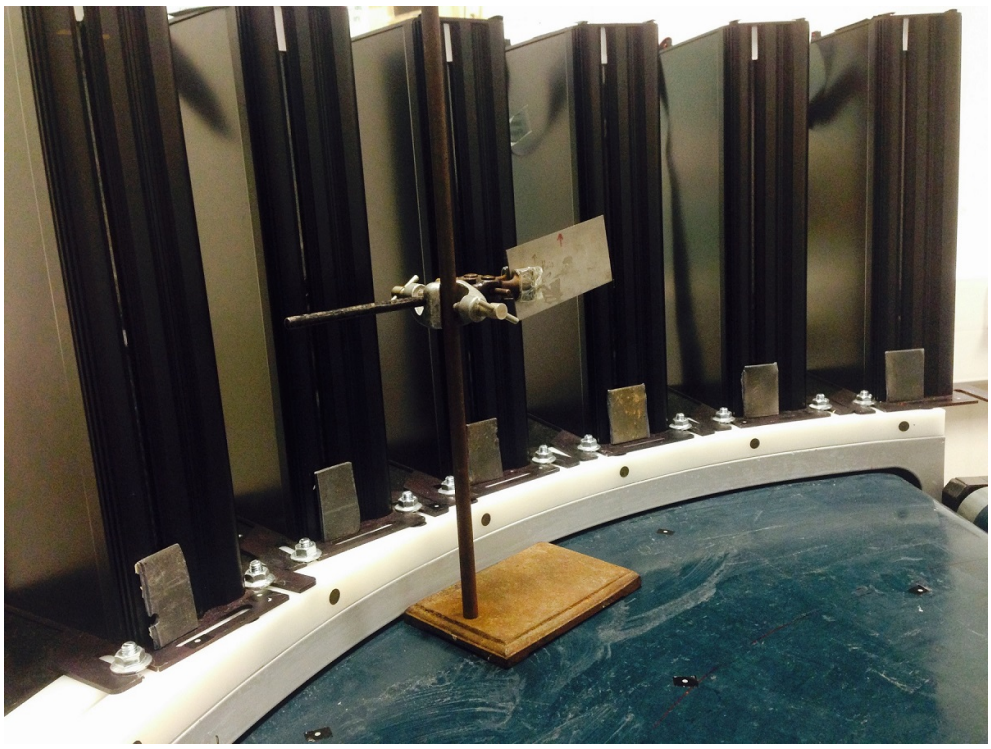

**Figure 4.15:** Photograph of the edge test piece used to measure the MTF of the ObT system with the edge-response method. The photograph shows the test piece placed on a sample mount, located at an intermediate position while travelling in the ObT system, placed as close as physically possible to the respective detector.

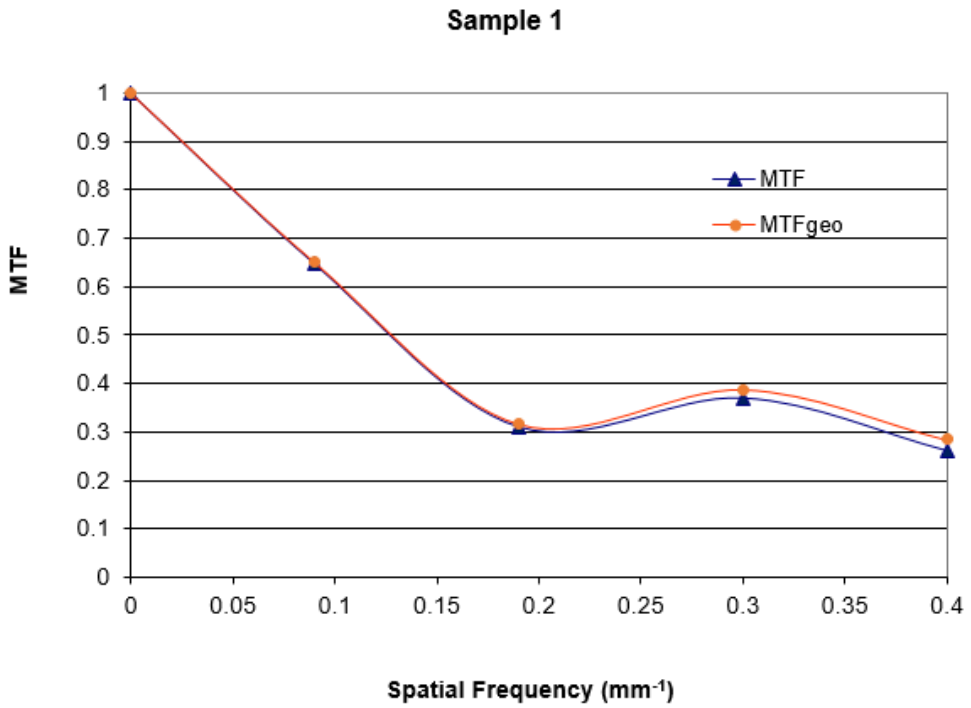


**Figure 4.16:** Graph of the ObT system MTF, and geometrically corrected MTF ($MTF_{geo}$) sample 1.

## 4.4 ObT experimental technique & image simulation

This section, 4.4, describes the experimental technique for ObT data acquisition as well as the work carried out to simulate these results. As outcome of both, the reconstructed image slices of the pseudo-3D volumes are presented and analysed, and further developments are discussed.

### 4.4.1 Phantom creation

Given that the ObT was at its primary stages of imaging experiments and a thoughtfully designed phantom was necessary, Phantom C was created. It primarily consisted of a rectangular perspex block, designed to have a basic clear structure of well-defined contents and dimensions. It's total volume dimensions were $119.7 \times 79.8 \times 229.8\ mm$, the longest side being its height. On the top 10 mm of each side, 3.17 mm diameter stainless steel rods were placed along the four outer sides of the volume, as seen in Figure 4.17. The purpose of the metal rods was to aid the phantom recognition in the reconstruction code (section 4.4.3.2). Two hollow spheres of diameters 9.5 mm and 20.0 mm were made in the positions shown in Figure 4.18. These spheres were purposefully made at different height and width planes (not overlapping) so that they could be more distinguishable in the image reconstructions.

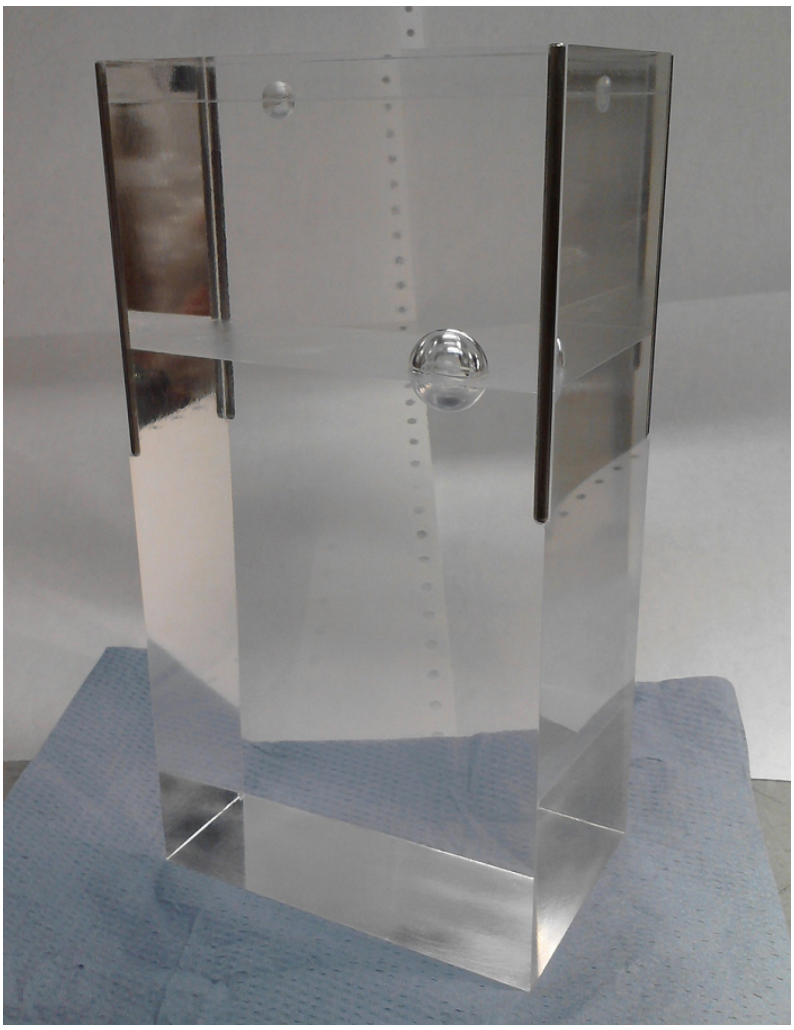

**Figure 4.17:** Photograph of Phantom C. A perspex block with two hollow spheres and four stainless steel rods on the top outer sides of the volume.

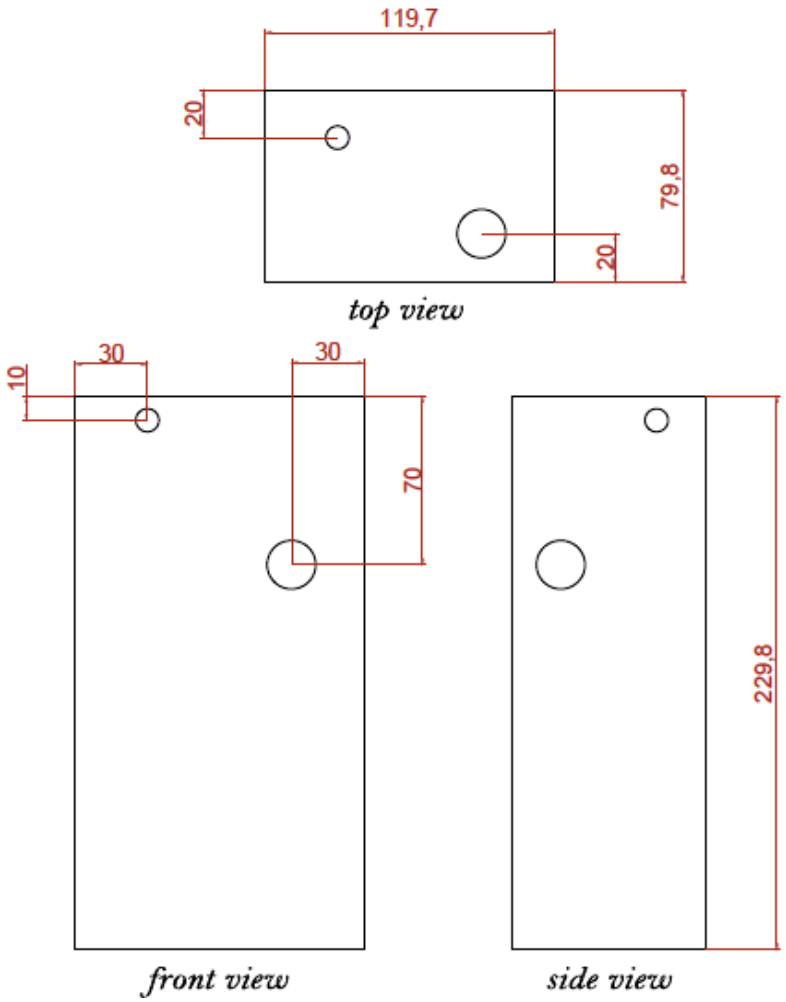


**Figure 4.18:** Schematic of hollow air spheres in perspex Phantom C. Red lines indicate the distance measurements. This schematic does not show the four rods which were placed on the outer sides of the volume.

### 4.4.2 ObT experimental technique

The ObT experimental technique involves image acquisition of the created phantom(s) along with making all the measurements required for the pseudo-3D image reconstruction. All projection calibration techniques pre-described in section 4.3.2, are incorporated in the image reconstruction described in section 4.4.3.

Regarding the ObT image acquisition, it should first be clarified that even though the conveyor and x-ray source systems comprise of two and three system parts respectively, in the steps below we refer to each as a global system. This can be done since the conveyor belts' and x-ray sources' parameters (speed, and kV plus mA respectively) were set to the same value for all corresponding parts.

Prior to initiating an image acquisition set there were additional preparation steps that need to be followed. Firstly, the x-ray source system is warmed up, a process which was automatically done using the x-ray software "Xray-

Control V4.02" (section 3.5.1). Also, the required systems parameters were set accordingly, the details of which are presented in Table 4.2.

| System | Parameter | | | |
|---|---|---|---|---|
| | *Name* | *Unit* | *Description* | *Value set* |
| **LabVIEW software** | capture period | s (seconds) | time between capturing consecutive single lines of data | $1 \times 10^{-2}$ |
| | oversampling rate | - | number of lines of data read from the camera before determining the average value for each pixel | 10 |
| | iterations | - | number of repetitions of the whole process | 3000 |
| **X-ray sources** | x-ray tube voltage | V (Volts) | | $1 \times 10^{5}$ (100kV) |
| | x-ray tube current | A (Ampere) | | $1.2 \times 10^{-2}$ (1.2mA) |
| **Conveyor belts** | frequency | Hz (Hertz) | | 9.5 |
| | angular velocity | m/s (meters/second) | | $1 \times 10^{-2}$ |

**Table 4.2:** ObT image acquisition parameters, set prior to initiation.

Each image acquisition corresponded to a full set of x-ray projections acquired by the ObT (section 3.3 on page 71). Using Figure 4.1 (page 84) as reference, a phantom was placed at $P_A$ and imaged traveling in the ObT until $P_C$. It was ensured that position $P_A$ placed the phantom out of the FOV of the first detector, so that it was fully imaged upon initiating the image acquisition. The image acquisition steps carried out were:

1. Set phantom at position $P_A$.
2. Turn on x-ray power source.
3. Initiate detector data acquisition through LabVIEW.
4. Initiate conveyor belt system motion. (Steps 3 and 4 are almost simultaneous.)
5. Stop conveyor motion when phantom reaches $P_C$.

### 4.4.3 Image reconstruction

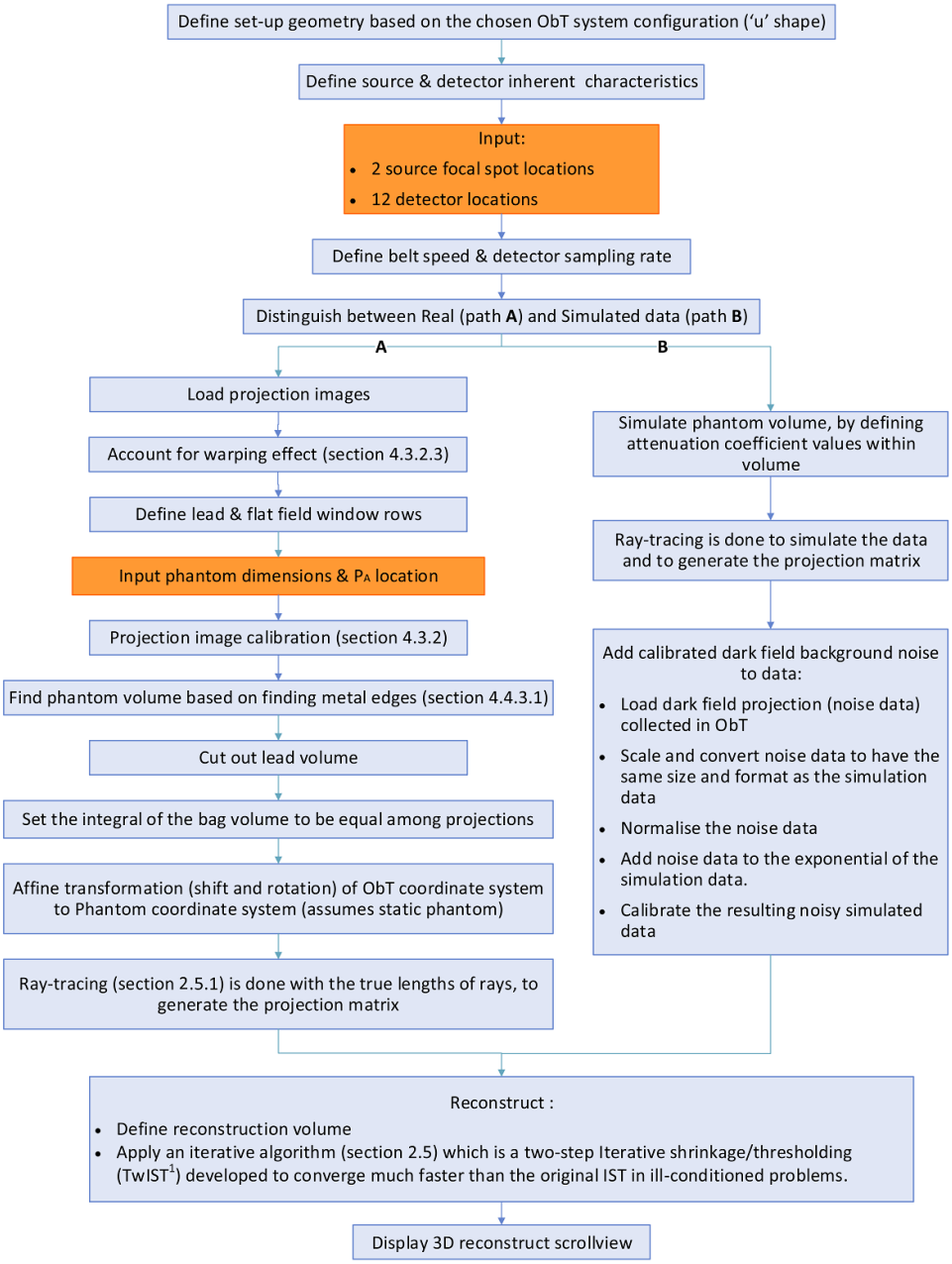


**Figure 4.19:** The ObT image reconstruction code steps, developed by Dr M. M. Betcke in Matlab. [1]Bioucas-Dias and Figueiredo [2007]

#### 4.4.3.1 Prerequisites and assumptions of the required reconstruction input variables.

In the attempt to create an efficient and effective reconstruction method to be applied to ObT image reconstruction, Dr M. M. Betcke developed an iterative reconstruction algorithm implementing the Siddon algorithm (section 2.6.1) developed byJacobs et al. [1998] in order to determine the projection matrix, while also adapting and incorporating rigid registration methods (section 2.6.2). The steps of this reconstruction code, which was written in Matlab, are shown in Figure 4.19.

In order to reconstruct the pseudo-3D images of a phantom there were three sets of data which needed to be implemented in the reconstruction code, referred to as the required input variables. As well as the x-ray projections acquired and the system parameters set for the ObT image acquisition, the geometry of the system needed to be specified. The geometry of the fixed objects could be measured directly while the position of the phantom needed to be calculated and set. The former included locating the sources' FS and the strip detectors with respect to the defined coordinate system, which was done using a measuring tape and caliper. Then, the position of the phantom needed to be known with respect to the ObT system, as it traveled on the conveyor system track shown in Figure 4.1. With the detectors and sources (FSs) pre-determined, being able to locate the phantom position in the same coordinate system would complete the required variables needed for the reconstruction. One way to determine this, which was done in the experiments described below, was to have a known initial position of the phantom ($P_A$) and thereafter assume a smooth circular arc motion travel path. Given this, and the fact that the belt speed was known and constant, it was possible to compute the phantom position at any instant during image acquisition. Thus, all three required variables for the reconstruction code were determined for the required inputs:
a) 2 source FS locations
b) 12 detector locations
c) phantom dimensions & $P_A$ location

These correspond to the orange highlighted text in Figure 4.19. Altogether, the required inputs, as well as the assumptions made, produced the necessary prerequisites for ObT image reconstruction.

All required 3D coordinate values (position and orientation) were initially measured and set with respect to the laboratory coordinate system ($C_L$, defined in 4.2.1) and then converted to the simulated coordinate system ($C_S$) for the image reconstruction, based on the method described in section 4.2.2. A list of the image reconstruction code to work, there are certain necessary variables that need to be known, which are inputted in the code, as well as certain assumptions made. Together, these consist the necessary prerequisites for ObT image reconstruction. A summary of them can be seen in Table 4.3.

Necessary prerequisites for ObT image reconstruction:

- Phantom body:
  - known phantom dimensions
  - rectangular volume, with higher attenuation material down the four side edges of volume (parallel to $z$, in $C_L$)
- Phantom motion:
  - stable circular arc trajectory
  - constant (known) speed
- Phantom initial position ($P_A$) location:
  - perpendicular to $x$=0 in the laboratory coordinate system ($C_L$) which, based on Figure 4.1, corresponds to $a_A//y_L$
  - phantom COR at known distance from $C_L$ COR: i.e. known phantom centre of volume trajectory radius with respect to $C_L$ COR point $O$
- Detector & source FS positions known, with respect to the defined $C_L$.

**Table 4.3:** Summary of required variables to be entered into the image reconstruction code.

.

#### 4.4.3.2 Finding phantom volume based on finding metal edges

In order to find the phantom volume (Phantom C) within the total projection images, the inserted metal rod edges were used (section 4.4.1). The method, which was followed within the reconstruction code, uses the fact and knowledge that the rods have a higher attenuation coefficient than the phantom and background. As such, the code performs calculations estimating the first and last column in each detector projection that has a greyvalue above a set threshold. Based on this, the phantom volume vertical edges were defined.

### 4.4.4 ObT experimental results and analysis

Due to the unconventionality and novelty of the ObT system geometry, extended timely experiments were required. These were focused on developing effective and efficient result for both the ObT image acquisition and the ObT image reconstruction by Dr M. M. Betcke.

Many of the developmental experiments resulted in failed or insufficient outcomes, and were not progressed further; hence, they are not included in this thesis.

The manual measurements made for the required image reconstruction inputs are presented in section 4.4.4.1.

The results of the methods that were able to produce results and were therefore explored, developed, and refined are presented below. Firstly, the original x-ray images acquired of Phantom C (Figure 4.17) are presented in Figure 4.21, followed by a succession of correction processes applied to these images as the image corrections were refined.

It should be noted that the experimental image data below is presented stacking the 12 projections one above the other, as is shown in the example in Figure 4.20. As such, the horizontal direction represents the number of iterations while the vertical direction corresponds to the pixel values as the strip detectors consist of a single stack of pixels.

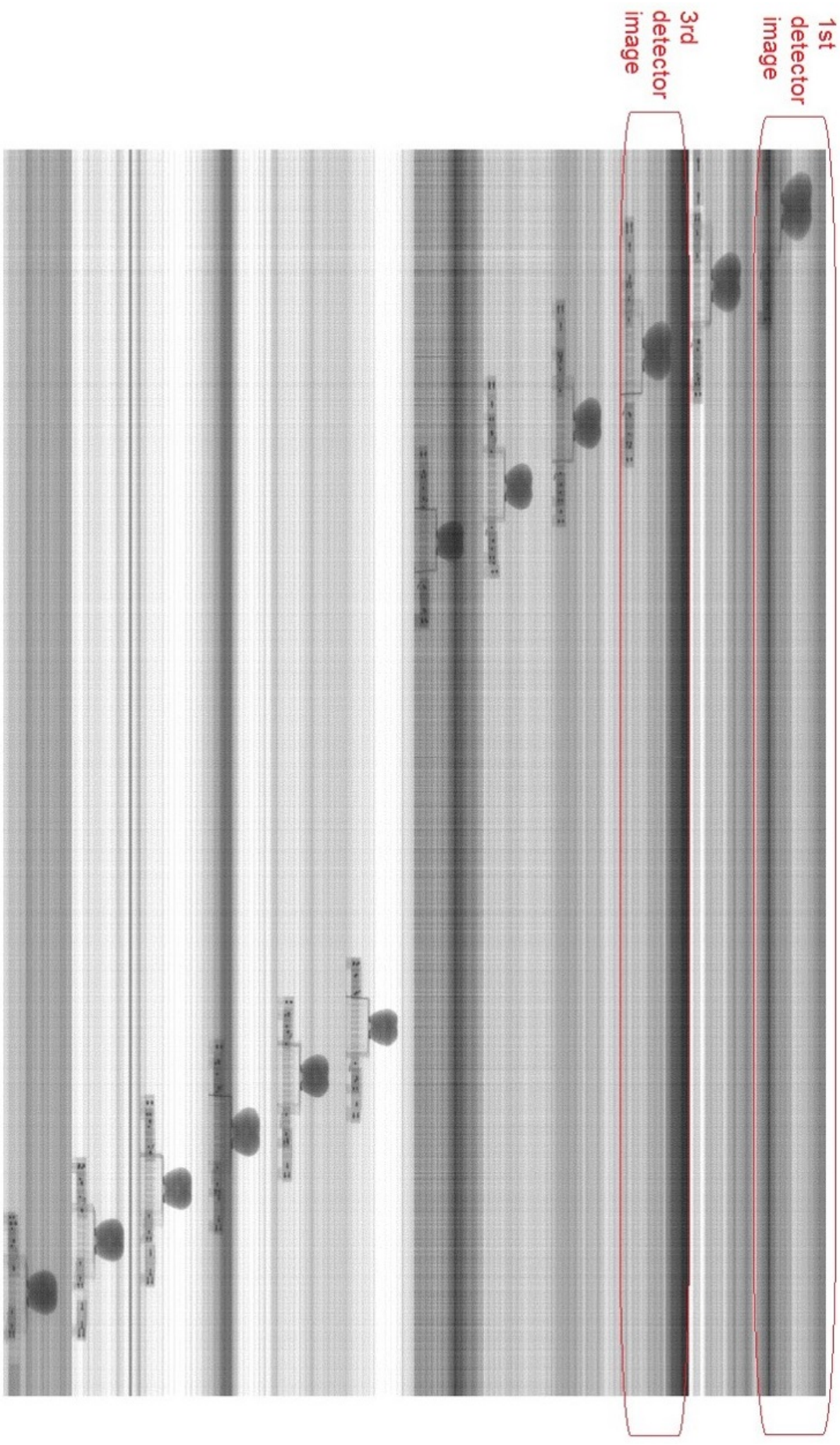


**Figure 4.20:** Example set of x-ray images collected in the ObT, showing how the 12 projection, acquired by the 12 detectors are stacked on on top of the other. Figure is rotated by 90° clockwise for better visualisation.

#### 4.4.4.1 Manual measurements

In order to get first estimates of the necessary measurements, manual methods were applied. These results were taken as ground truth.

Due to the layout geometry of the ObT system and the laboratory environment there are several practical limitations in manually measuring distances of the ObT points of interest. In some cases, these points are not physical points in space and need to be computed using geometrical computations from the known properties. For example, the FS is situated within the x-ray source housing, and was measured through measuring points on the x-ray source frame and then geometrically computed using the calculated offset, based on the x-ray source schematics provided by 3DX-RAY. For these reasons, the required measurements were repeated three times for each (set of) variables and then the average and its precision was estimated. More specifically the measurements were:
a) The coordinates of the source FS
b) The angle of each detector

These values, each computed thrice, are presented in Figures 4.4 and 4.5 respectively. Although they were initially measured with respect to the laboratory coordinate system (CS), their values were converted to the simulation CS and their averaged values were used in the reconstruction code. The conversion method is shown in section 4.2.2. Their measured precision, in terms of standard deviation $\sigma$, is given in the same table. The results show that the measurements for the FS coordinates as well as the detector angles have an average $\sigma$ of 2 mm and 2° respectively.

| | | **Coordinate measurement (mm)** | | | | |
|---|---|---|---|---|---|---|
| **Source:** | **S1** | **i** | **ii** | **iii** | **Average** | $\sigma$ |
| **Coordinates:** | | 227.5 | 231.0 | 227.0 | 228.5 | 2.2 |
| | | -21.5 | -24.5 | -21.0 | -22.3 | 1.9 |
| | | 96.0 | 94.0 | 98.5 | 96.2 | 2.3 |
| Source: | **S2** | **i** | **ii** | **iii** | **Average** | $\sigma$ |
| **Coordinates:** | | 211.0 | 212.0 | 208.5 | 210.5 | 1.8 |
| | | 57.0 | 58.5 | 55.0 | 56.8 | 1.8 |
| | | 94.0 | 97.0 | 97.0 | 96.0 | 1.7 |
| | | | | | **Average $\sigma$** | **2.0** |

**Table 4.4:** Manual measurements of the two sources coordinates, given in the simulated coordinate system (Figure 4.2).

| **Detector** | **Angle measurement (degrees)** | | | | |
|---|---|---|---|---|---|
| **#** | **i** | **ii** | **iii** | **Average** | $\sigma$ |
| **1** | 27.2 | 19.4 | 21.4 | 22.7 | 4.0 |
| **2** | 37.5 | 32.6 | 35.4 | 35.2 | 2.5 |
| **3** | 50.0 | 44.9 | 45.6 | 46.8 | 2.8 |
| **4** | 61.4 | 58.0 | 59.6 | 59.7 | 1.7 |
| **5** | 73.7 | 71.1 | 72.9 | 72.6 | 1.3 |
| **6** | 86.9 | 83.4 | 84.0 | 84.8 | 1.9 |
| **7** | 93.5 | 91.0 | 92.2 | 92.2 | 1.3 |
| **8** | 102.0 | 101.9 | 104.1 | 102.7 | 1.2 |
| **9** | 119.0 | 117.9 | 123.2 | 120.0 | 2.8 |
| **10** | 131.0 | 130.9 | 133.3 | 131.7 | 1.3 |
| **11** | 141.8 | 144.9 | 145.4 | 144.0 | 2.0 |
| **12** | 154.7 | 156.9 | 158.3 | 156.6 | 1.8 |
| | | | | **Average $\sigma$** | **2.0** |

**Table 4.5:** Manual measurements of the 12 detector angle values measured in the simulated coordinate system (Figure 4.2).

#### 4.4.4.2 Experimental data and analysis

Image acquisition was performed using the defined parameters in Table 4.2. Figure 4.21 shows an original, uncorrected, set of x-ray projections acquired of Phantom C (Figure 4.17) traveling in the ObT. Some of the noise corrected images are presented in Figures 4.22 and 4.23. The first is an example of preliminary noise correction methods applied, while the later is an example of the fully developed noise corrections methods applied (described in section 4.3.2). The improvements of the image correction methods are evident in the comparison of these two sets through visual inspection.

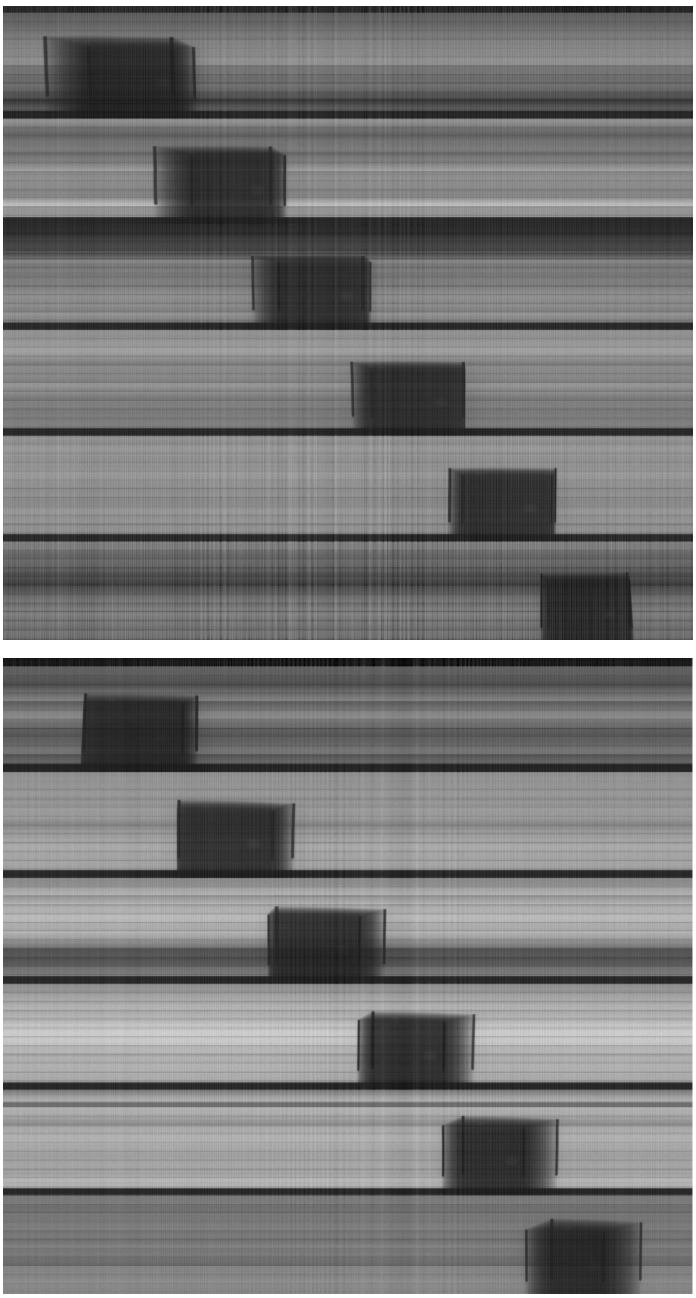

**Figure 4.21:** An original, uncorrected, set of x-ray projections acquired of Phantom C traveling in the ObT, imaged by the 12 detectors.

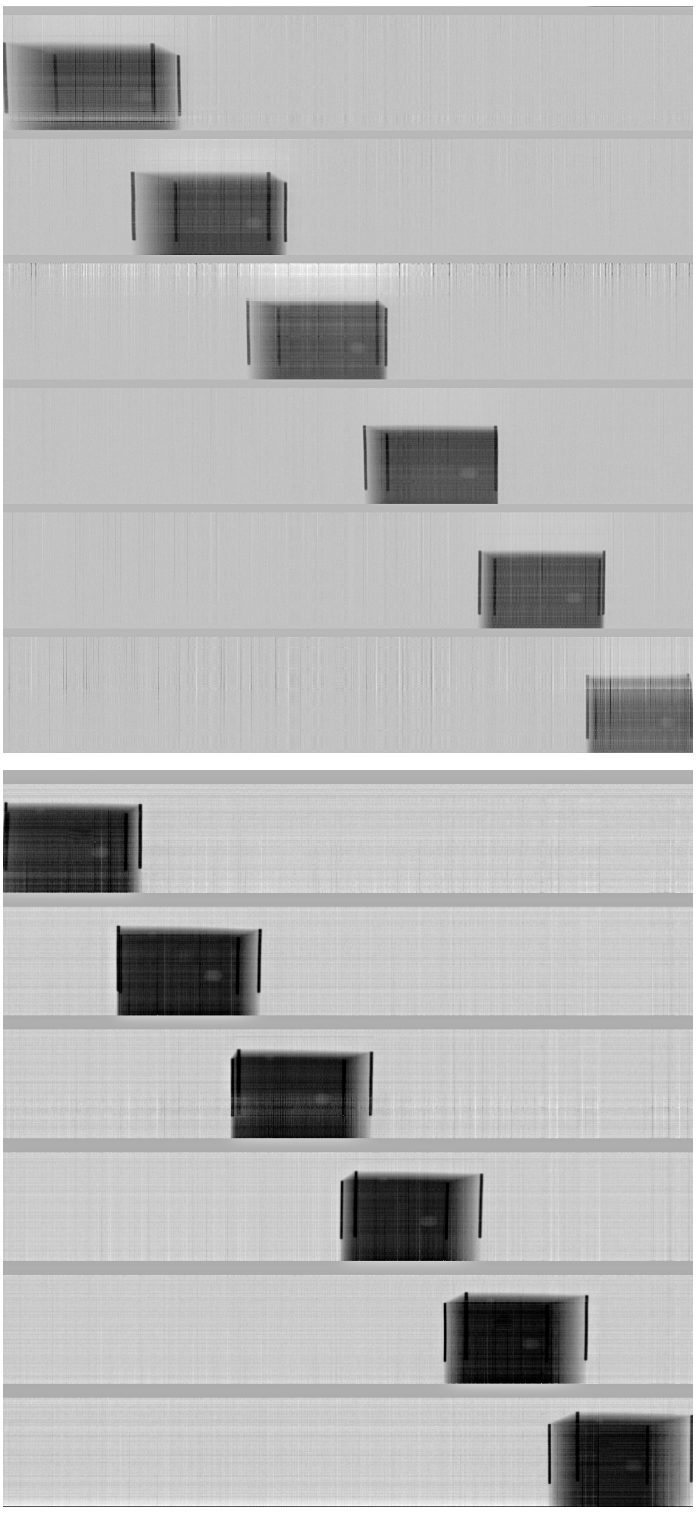

**Figure 4.22:** X-ray images acquired of Phantom C, by each of the 12 detector, after performing initial image correction methods developed.

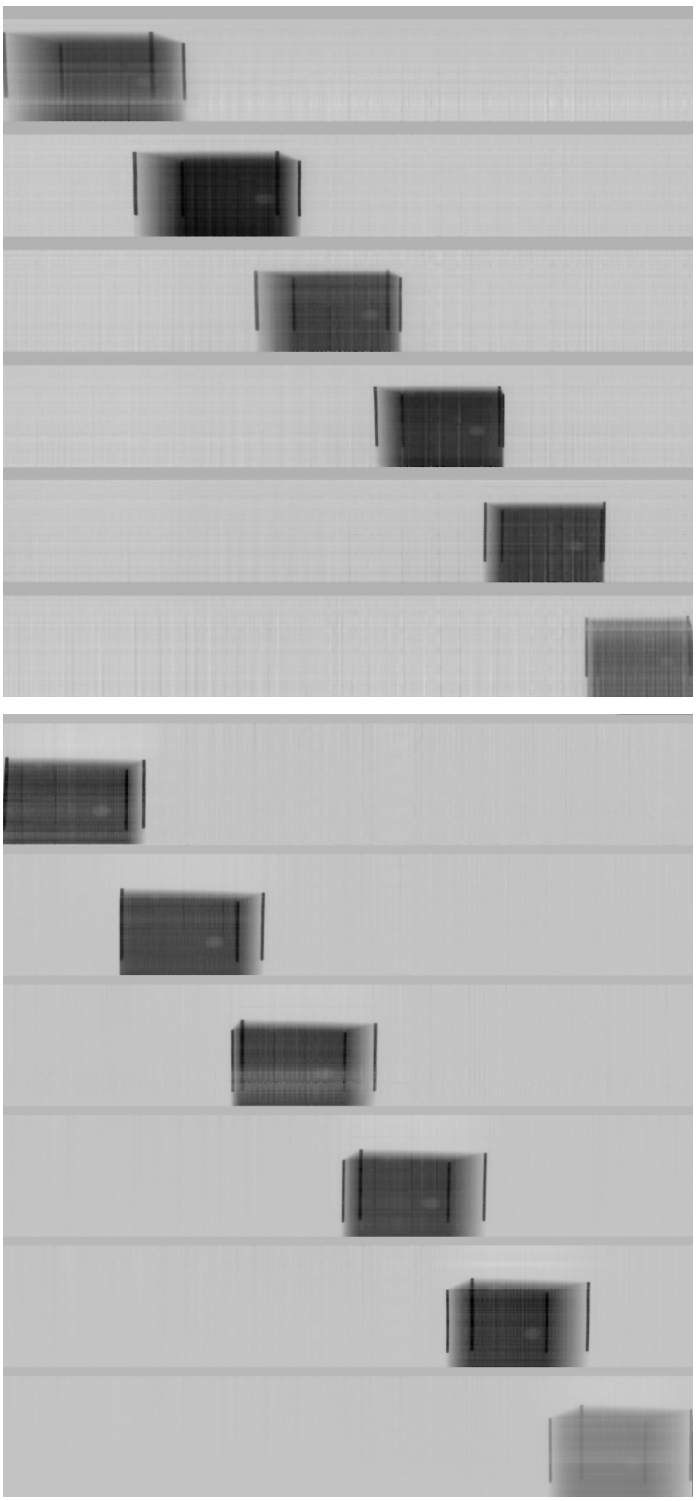

**Figure 4.23:** X-ray images acquired of Phantom C, by each of the 12 detector, after performing further image correction methods, described in section 4.3.2.

The quality of these three sets of data: the original data (Figure 4.21), the first corrections (Figure 4.22) and the more advanced image corrections (Figure 4.23), is also evident in three sample grey value line plots, created in ImageJ [2015], shown in Figure 4.24: a, b, and c, respectively. These line plots correspond to the same y line in the third detector image, which passes through the centre of the largest hollow sphere in Phantom C. It is evident that going from (a) to (c) the image quality improves: the noise pattern of the images'

background becomes smoother, and the contrast of the phantom body (perspex) and its different parts (metal rods and air gap) are more distinguishable since there is are larger grey value differences respectively.

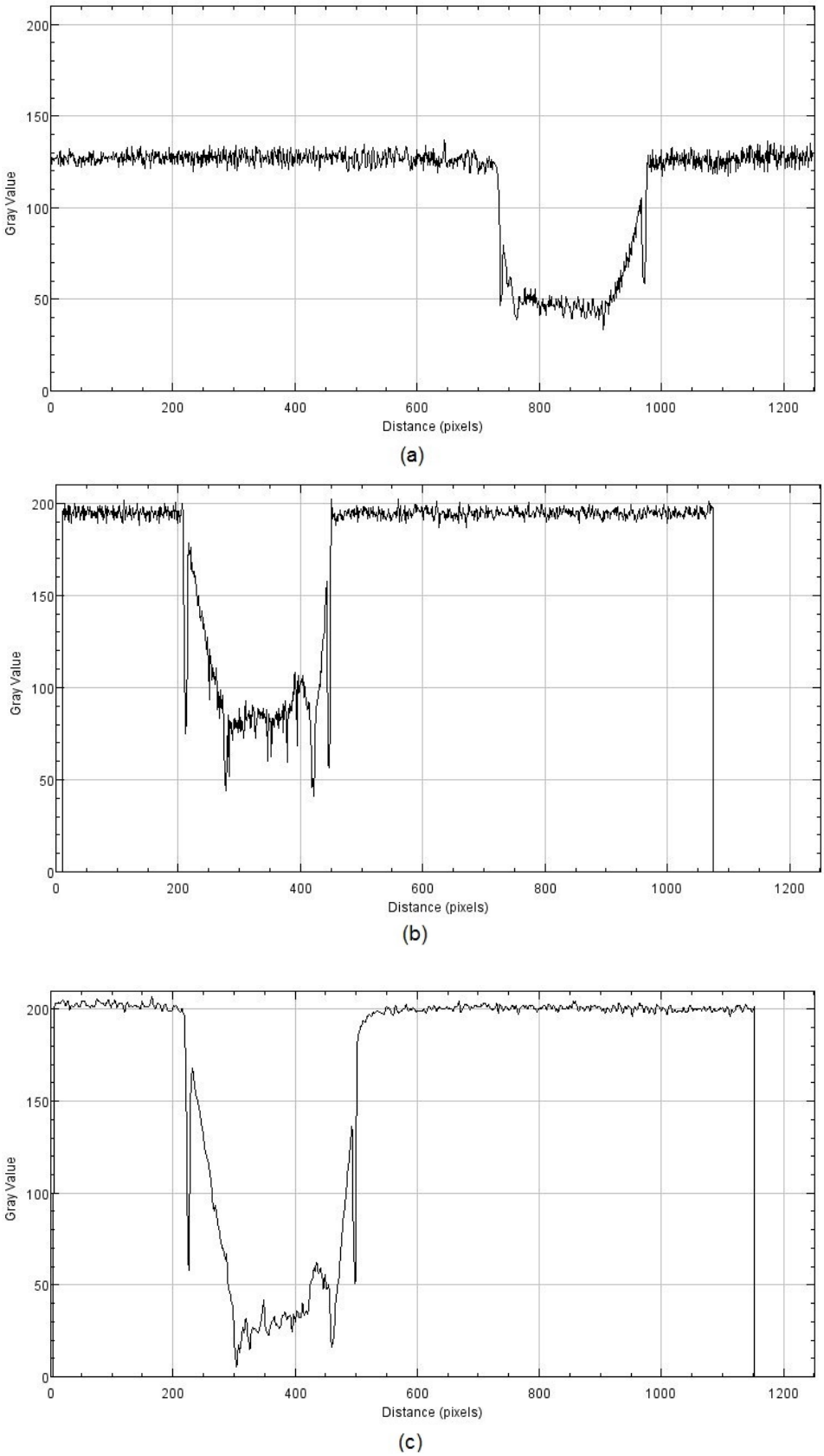


**Figure 4.24:** Line plots corresponding to the same y line of Figures 4.21 to 4.23 respectively.

#### 4.4.4.3 Image reconstruction results

The image reconstruction results were analysed using visual inspection. The reason for which this inspection method was invoked is that the end users of airport screening machines are human operators. If the method had been carried out within the field of computer vision, quantitative analysis would have been required instead.

The first image reconstruction results failed to show any distinguishable features. Even after various methods and developments it was not possible to distinguish the air spheres in the reconstructed images of Phantom C, as can be seen in Figure 4.25 [3]. Therefore, a more attenuating object, a 1 mm thick copper ring of 10 mm outer and 7 mm inner diameter was fixed on one of the vertical sides of Phantom C. Specifically, it was placed flat on the side corresponding to $b$ in Figure 4.1. This was done so that the large surface of the ring would be near perpendicular to the x-ray line of sight with each detector, and thus would have higher likelihood of being observed in the reconstructions. Having imaged the adapted Phantom C, the reconstructed image results are shown in Figure 4.28. In these reconstructions, the copper ring can be distinguished, however there are strong image artifacts which lead to the ring being extendedly evident in the sequence of the reconstruction slices.

[3] The reason for the observed navy blue colour in the lower half of the images, is linked to a preliminary reconstruction method which displayed an 'empty' lower half image reconstruction. In addition, the reconstruction were made at half the resolution of the following reconstructions, which is why half the number of slices were produced.

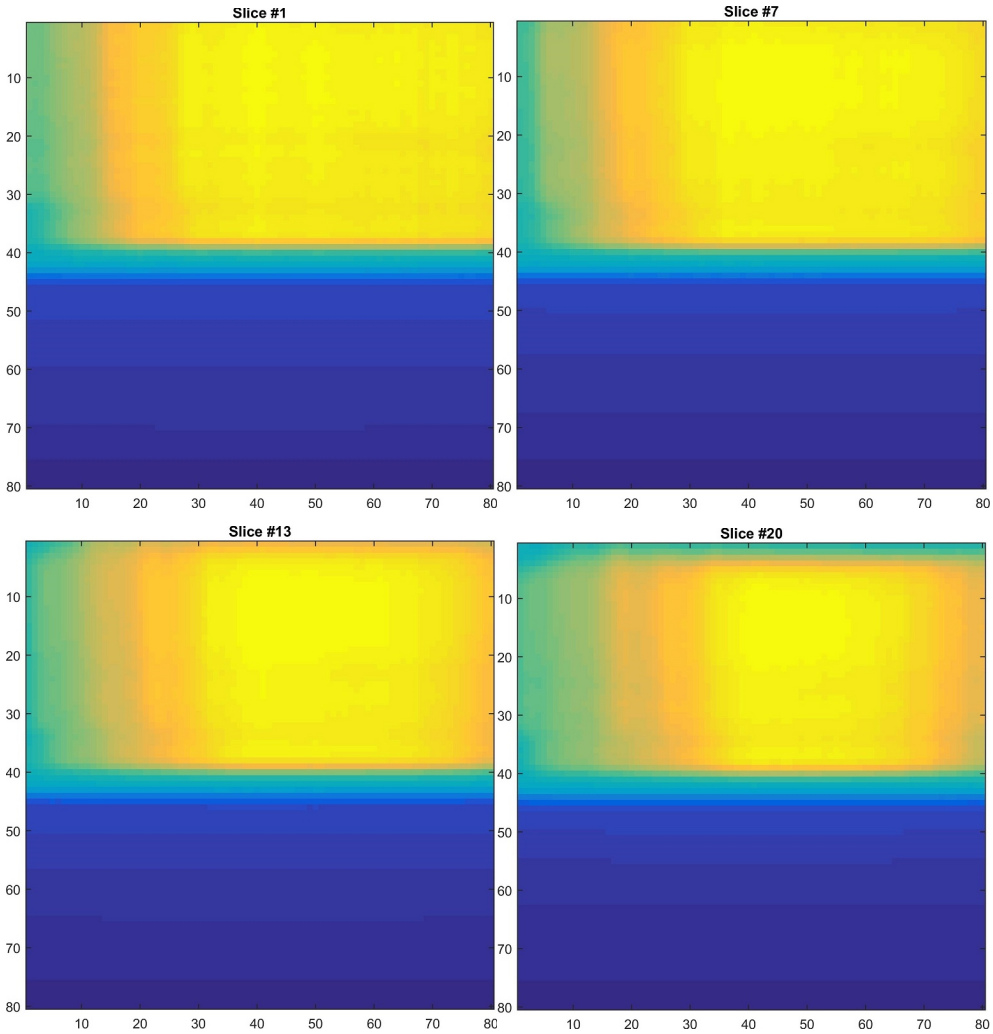


**Figure 4.25:** Image reconstruction results of Phantom C.

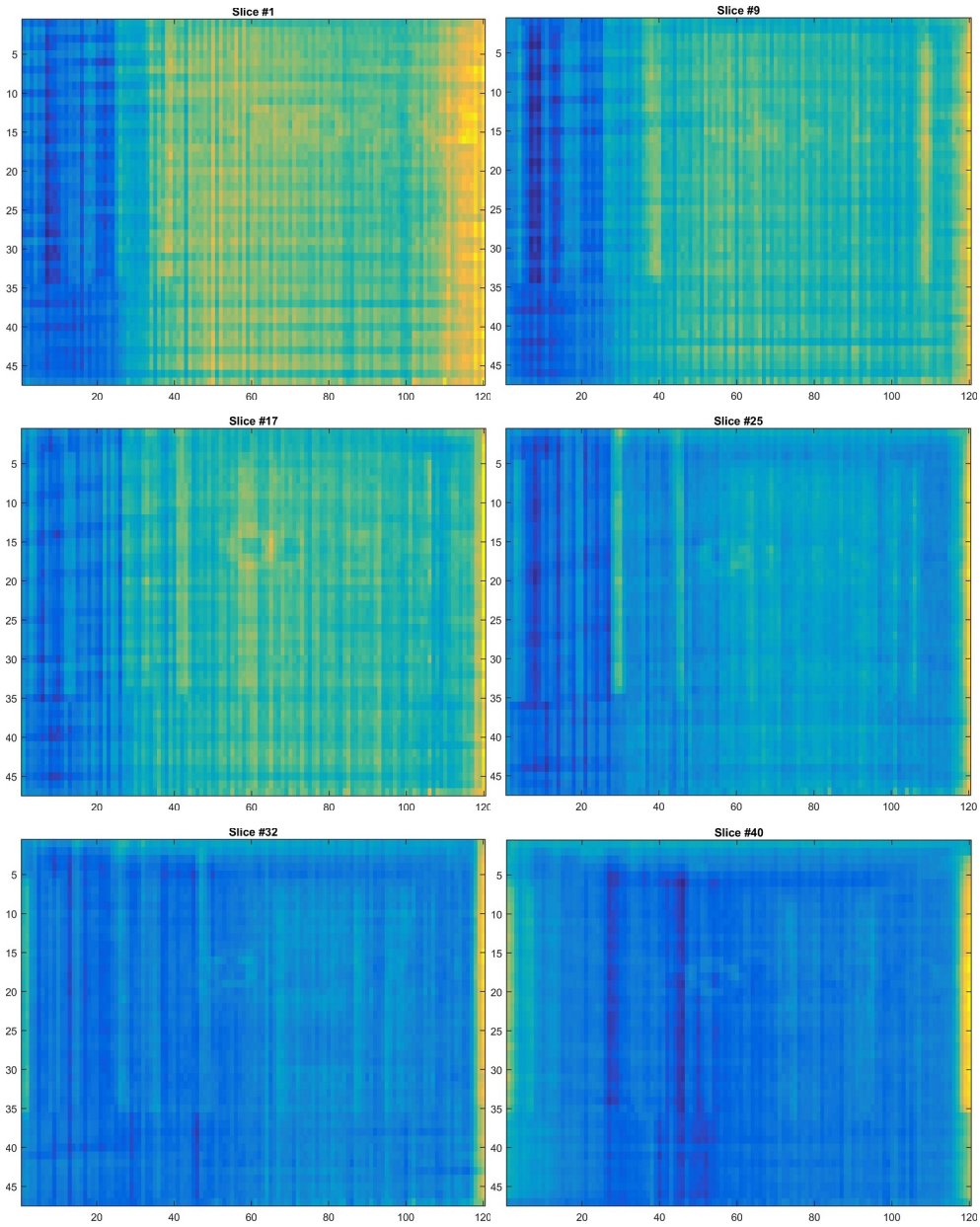


**Figure 4.26:** Image reconstruction results of the adjusted Phantom C, with a copper ring added on a vertical side surface..

### 4.4.5 ObT simulation image reconstruction results

The image reconstruction code developed by Dr M. M. Betcke was also able to reconstruct simulated results, the steps of which are shown in Figure 4.19. Two different phantoms, representing a rectangular perspex block with a hollow sphere within the volume, were simulated. The only difference between these two simulated phantoms is the position of the hollow sphere. The similarity of phantom shape and form (material) to Phantom C, would allow the expected reconstructed results to be observed. Sample slices from the reconstructions of these two simulations are shown in Figures 4.27 and 4.28.

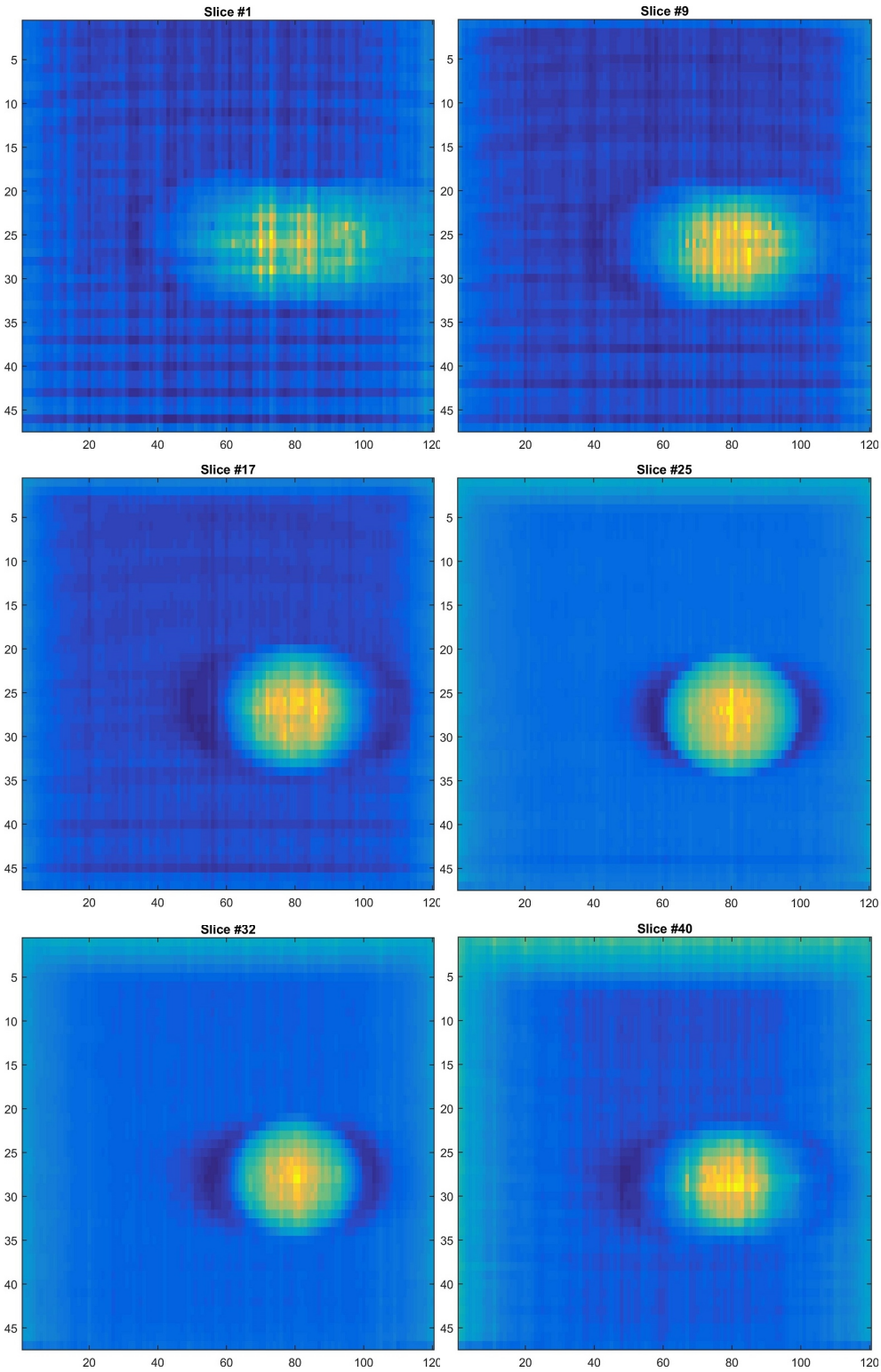


**Figure 4.27:** First sample image reconstruction slices from simulated data.

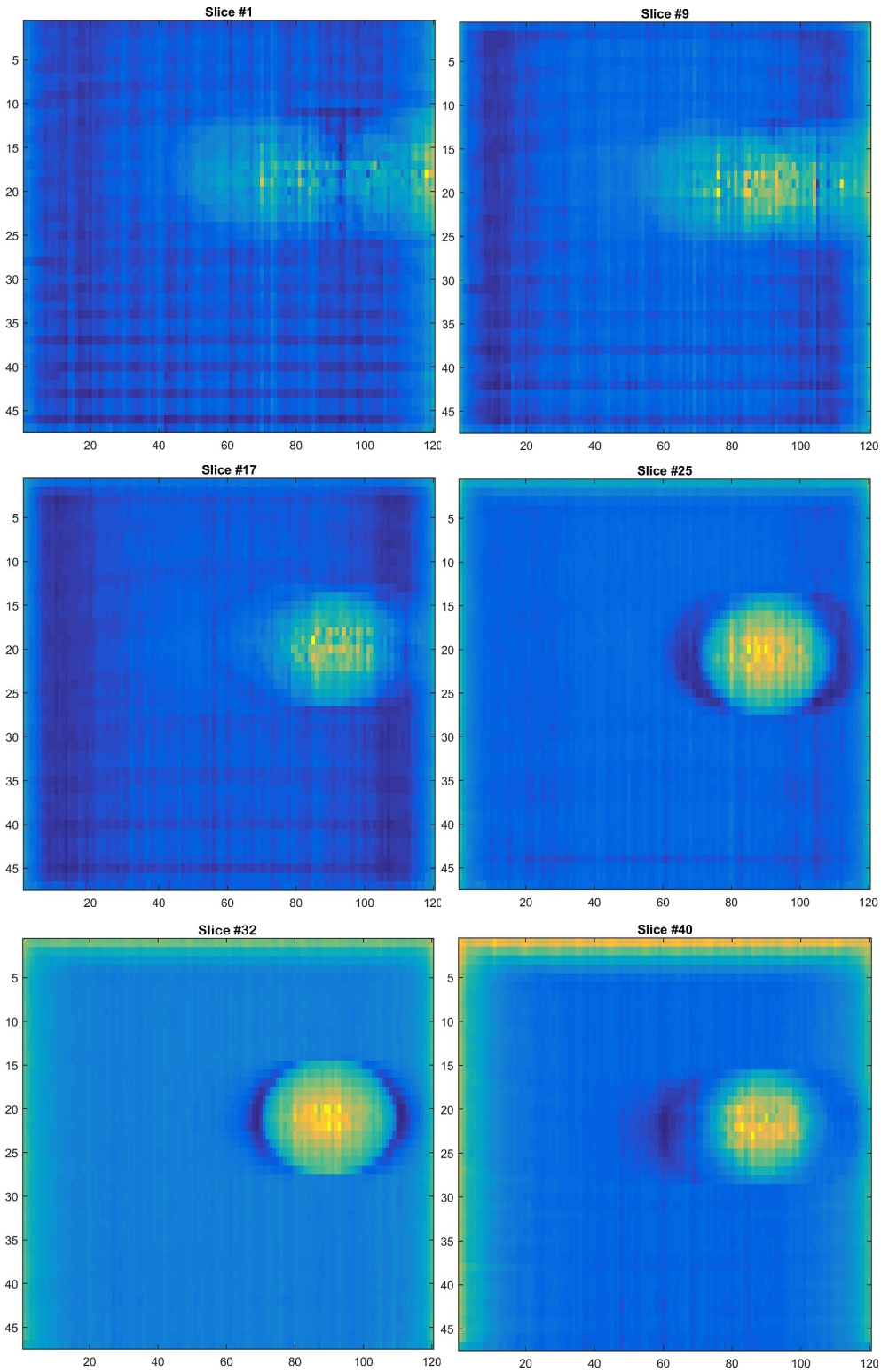


**Figure 4.28:** Second sample image reconstruction slices from simulated data.

### 4.4.6 Accuracy requirements

In order to check the ObT system accuracy requirements, regarding the required variable inputs, maximum errors were introduced. This check was performed on both the real and simulated data reconstructions. This was done by randomly altering the input values by plus or minus the maximum standard deviation of the two variable inputs: (a) FS coordinates, and (b) detector

angles (section 4.4.4.1). This provided a check of the effect of the estimated precision on the image reconstructions. As such, a error value of ±2 mm in the source coordinates and ±2° in detector angles was introduced. This check was performed ten times with real data and ten with simulated data, all of which verified that no difference was observable in the image reconstructions. A sample of a comparison between two such reconstructions is presented in Figure 4.29 for the real data, and in Figure 4.30 for simulated data. This lead to the conclusion that, for the current state of the ObT system, an error of ±2 mm for the source coordinates and ± 2° in detector angles does not affect the image reconstruction results. Therefore, a method that would be able to produce results of a minimum such accuracy was then investigated.

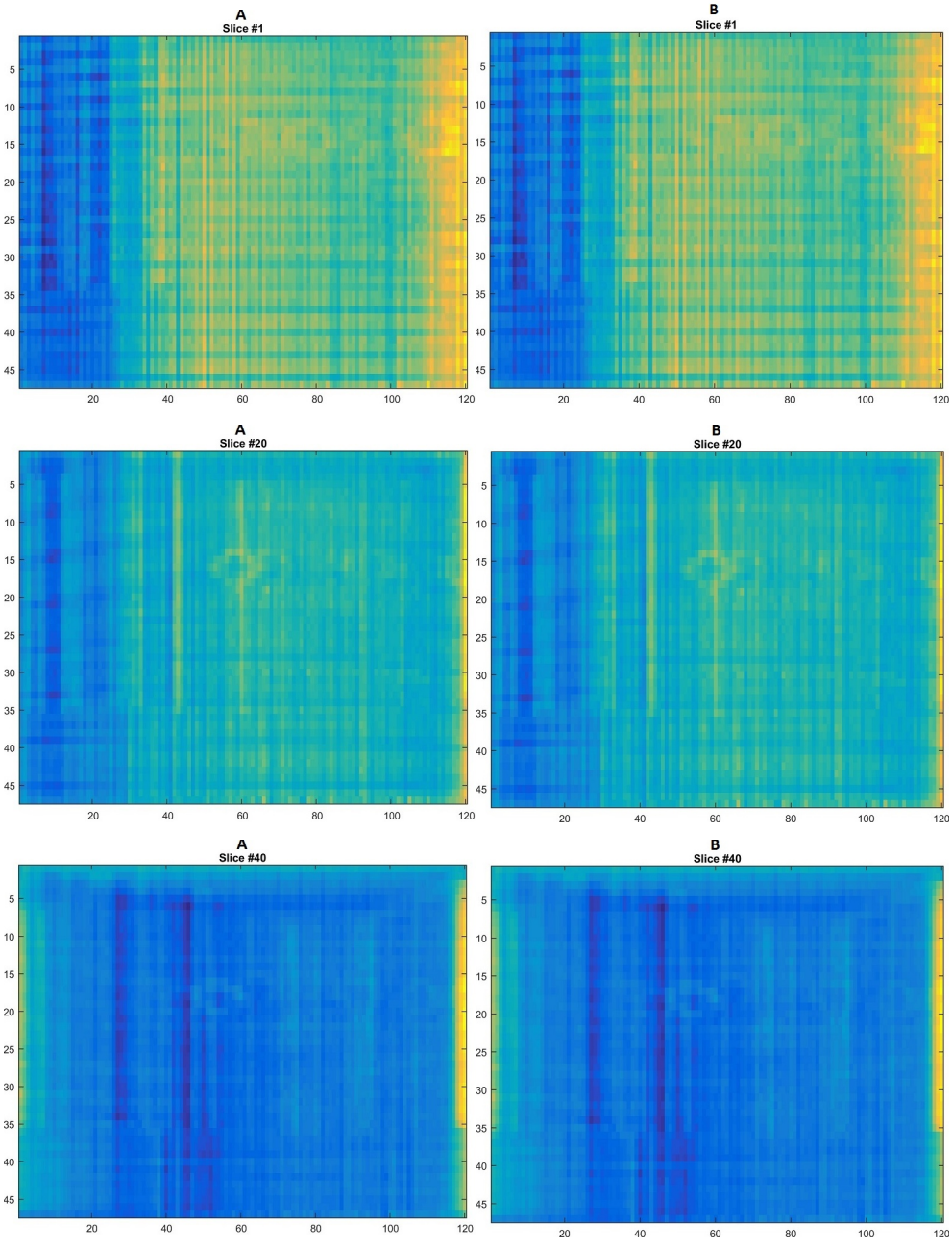


**Figure 4.29:** A sample of a comparison between two reconstruction outputs using real data.

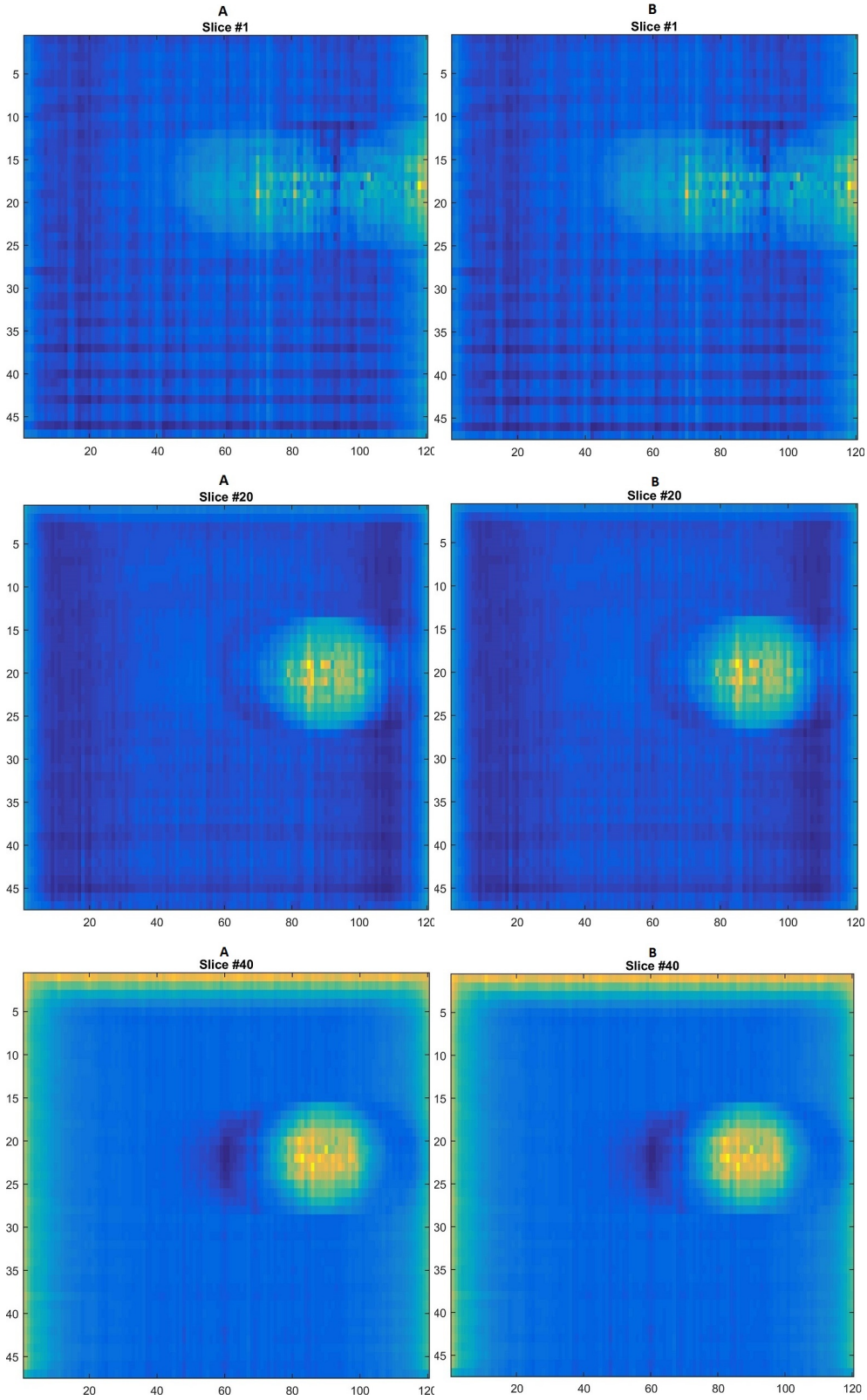


**Figure 4.30:** A sample of a comparison between two reconstruction outputs using simulated data.

## 4.5 Chapter conclusions

This chapter presents the experimental work for the testing, developing and evaluation of the ObT system's design, described in chapter 3. The primary

aim was to investigate the ObT system's capabilities and develop methods to improve the ObT image reconstruction results through exploring the system's limitations, requirements and possibilities.

It should be noted that an driving factor for airport screening, and thus for this project, is cost-effectiveness (section 1.1). Therefore, the implemented developments have been constrained, and the quality of results should be judged taking this into account.

Investigating the acquired x-ray images' noise sources and distortions in ObT, improvements were demonstrated using developed image correction methods, which were applied. Image uniformity, compared between images pre- and post-correction, showed that uncorrected images were on average 53% uniform, while correction increased their average uniformity to 0.77%, an increase of 45%.

Moving on to image reconstruction, the unconventionality and novelty of the ObT system geometry confirmed that it was timely and challenging work. Results from both real data and simulations, of perspex and air block phantoms, showed that the former produced significantly lower quality results than those ones would have been expected, as indicated by the simulations. These, the simulation reconstruction results of low attenuation content phantoms, showed the potential of ObT to clearly distinguish between the two materials: perspex and air.

Since real data reconstructions failed to produce any significant results, a higher attenuating material, copper, was included in the imaged phantom. The reconstruction results, showed that objects of bigger attenuation differences (copper versus perspex, rather than air versus perspex) could be observed. However, the quality of the results still remained low due to the effect of backprojection. This is a very common artifact that small metallic objects may generate, which manifests itself as streaking artifacts on the reconstructed image [Turbell, 2001], as was observed here.

The main conclusion from the reconstruction results was that the current imaging method needed further refinements, regarding the geometry registration and the image reconstruction. The simulation results confirmed that advancing the experimental method could produce better results than those the ObT could achieve at the time. In exploring further development possibilities, the required measurements and their precision were defined.

For the current state of the ObT system, an error of  for the source coordinates and 2°in detector angles does not affect the image reconstruction results. Therefore, a method that would be able to produce results with such a mini-

mum accuracy was required. In addition, an automated way of registering the objects of interest which could additionally eliminate the necessary assumptions (Table 4.3) was needed. This was explored further and is presented in chapter 5.

# Chapter 5

# The development of a low-cost tracking solution

## 5.1 Chapter overview

This chapter describes the development of a low-cost photogrammetric coordination and tracking solution, to replace the previously used manual measurements (section 4.4.4.1) . The system provides the static ObT system geometric layout along with sequential phantom position and orientation six degrees of freedom information (*6DOF*, Figure 1.3 on page 6) required for the image reconstruction, described in section 4.4.3. Three different photogrammetric solutions are explored employing one or more cameras in both static and sequential imaging modes. The accuracy of these solutions is investigated through the comparison of photogrammetrically estimated dimensions and geometry against manual measurements made with tapes and callipers and physical expectations on the circular motion of objects moving through the system. This chapter aims to address the key prerequisites of the ObT image reconstruction method, described in Table 4.3 (page 110). The inclusion of improved ObT geometry and object 6DOF are evaluated with respect to improvements in image reconstruction quality.

The chapter reports how a viable solution was achieved in two parts. The first part, section 5.3, describes how a reference coordinate system for the ObT field was established. The outcome of this section directed the path the work took, described in section 5.4, which explores low-cost tracking solutions of objects traveling in the ObT. The aim of this section was to provide solutions, which deliver the trajectory of an object, while estimating the smoothness of its motion. The measurement capability of each photogrammetric method is quantified, and the most successful method applied in section 5.5, with the aim of improving the image reconstruction capability of the system.

## 5.2 Overview of photogrammetric tools

This thesis uses low cost digital cameras and supporting software to make the measurements for the close-range (section 2.7.1) photogrammetric work . These systems were adapted appropriately as described below in order to provide solutions for the aims of the thesis.

A Nikon D100 DSLR was used initially coordinating the ObT reference system (section 5.3), which is a typical of many modern DSLR cameras used in photogrammetric applications [Smith and Cope, 2010]. A fixed 28 mm lens was used with the Nikon D100 camera body. With no zoom present, the fixed focal length gives a useful angle of view and, with the focus locked, offers stability and high accuracy [Smith and Cope, 2010]. In a zoom lens, not only does the lens change its focal length and focus, but the lens elements correspond to more complex physical groups which makes them less stable.

For the tracking solutions webcams were employed; firstly the Logitech C510, which was later upgraded to the Logitech C920 (see Table 5.1). Although a DSLR, such as the one used in this thesis, has a better image quality compared to the webcams, the latter were chosen as a more practical and lower cost solution. The coordination procedure is only required once at the beginning of a system set-up, in contrast with the tracking solution. Also, the flexibility (lightweight, adjustable body) of the webcams make them easy to be mounted and fitted as necessary in the ObT system. In addition, the webcams are designed to readily integrate with computers, working in both still image and video capture mode, in contrast with the particular DSLR which has no video mode (and is heavier, more rigid and bulky, and dependant on battery power supply). Importantly, similar webcams have been shown to produce good quality tracking results (section 2.10.1). Moreover, an accuracy of 0.5 mm is sufficient for the current requirements of the ObT image reconstruction, of which close-range photogrammetry has shown even better results (section 2.7.1). These reasons made the webcams the most appropriate option to investigate as the required tracking solution.

Table 5.1 gives technical details of the three cameras used in this study: the Nikon D100 and the two Logitech webcams, which are referred to as *DSLR*, *C510* and *C920* respectively hereafter. The DSLR was used for still image acquisition, whilst the webcams deliver both still and video images, albeit at lower image quality due to their low cost lenses and relatively small sensors. Images with the DSLR were read directly from its memory card whilst still images and video from the webcams were captured with Logitech driver software (section 5.4.1) on a Windows® based PC.

The physical layout and specification of the pixels on the sensor and those stored in the digital image are generally well specified for DSLR cameras,

whereas for the webcams there is no equivalent body of evidence. The low cost sensors used in webcams are often unknown as to vendor, physical pixel count and pixel pitch. This fact, combined with factors such as the camera firmware and software driver versions, along with user selection of parameters, results in variation in image size and sampling of both still and video images from webcam devices.

| Name | Description | Picture |
|---|---|---|
| Nikon D100 **DSLR**[1] | Photo capture: up to 6.1 megapixels<br>F-stop: f/14<br>Exposure time: 1/30 sec<br>Lens focal length: 28 mm<br>Built-in pop-up Speedlight flash |  |
| Logitech HD Webcam **C510**[2] | Photo capture: up to 8 megapixels<br>Max digital video resolution: 1280 × 720 pixels |  |
| Logitech HD Pro Webcam **C920**[3] | Photo capture: up to 15 megapixels<br>Max digital video resolution: 1920 × 1070 pixels<br>Carl Zeiss® lens with 20-step autofocus |  |

**Table 5.1:** Characteristics of the three cameras used in this study. [1]Nikon [2015] [2,3]Logitech [2015], LesNumeriques [2015], Prohardver [2015]

### 5.2.1 Photogrammetric software

#### 5.2.1.1 VMS

The software used for photogrammetric coordination of the ObT system and for calibration of the camera systems was Vision Measurement System versions 8.4 and, later, 8.6, released in May 2010 and September 2014 respectively, developed by Geometric Software P/L © [Geomsoft, 2015].

VMS data is designed around the concept of a *project*. The VMS project file specifies the project name and type, the home directory and a number of other data files (camera calibration data, target coordinates and precisions, image measurements, exposure station data, survey measurements) and the image files containing the acquired photograph image exposures [Geomsoft, 2015], referred to as *images* in this thesis. The *target file,* containing the target point coordinates, also includes an index for each target which indicates the target coordinates that are known and those that are unknown. The index can take an integer value between -1 and 7, in correspondence to Table 5.2, and a target with an index of 7, for example, is said to have a 'flag of seven'. Use of these indices allows a coordinate datum to be set for a photogrammetric bundle adjustment (*BA*, section 2.8.5). The coordinate datum is defined by 7-datum elements: an origin (XYZ), a rotation around each axis, and the scale (as in the work done in step 3b, section 5.3.1). Example VMS project, calibration and target files are shown in Appendix E (page 206).

VMS uses the principle of collinearity and least squares estimates (*LSE*, section 2.8.1) for resection (section 2.8.3), intersection (section 2.8.4) and bundle adjustment, so these measures are applicable to all three processes [Johnson et al., 2004]. However, the simultaneous solution in the BA gives the most comprehensive output and is the tool used in following system coordination and calibration processes. Coded targets [Shortis et al., 2003] were used in conjunction with VMS to improve the efficiency of the measurement process. In this work, coded targets were used on the ObT system and on the test piece created (Figures 5.1 and 5.5).

| Index | Known Coordinates |
|---|---|
| 7 | XYZ |
| 6 | XY |
| 5 | XZ |
| 4 | X |
| 3 | YZ |
| 2 | Y |
| 1 | Z |
| 0 | none |
| -1 | indeterminate or not yet computed |

**Table 5.2:** Value correspondence of the target indexing scheme, which indicates which target coordinates are known and unknown. The assigned index value for each target is referred to as the target 'flag'.

### Interpreting VMS results

There are a number of quality measures (section 2.4.2) included in the VMS outputs which indicate the quality of the estimated results. These include the variance (the square root of which, gives the standard deviation) of the estimated parameters from LSE (section 2.8.1), X, Y, Z coordinate estimates, camera locations and pose, and any self-calibration parameters (Table 2.3 on page 46).

Residual in VMS are the discrepancies between measurements and their expected values. An overall measure of the residuals, i.e. of how well the measurements have been estimated in a network, can be shown with RMS (section 2.12.1). Checking systematic patterns in the residuals gives us an idea of any non-random effects which are not accommodated in the mathematical model (collinearity and lens parameters). Checking expected measurement weights against residuals during the iterative LSE process gives us a way of finding errors and eliminating them. For a given camera, image residuals can be considered as a function of the sub-pixel measurement capability of the photogrammetric system. With the expectation of a normal distribution, the maximum residual values are usually 3-5 times the magnitude of the RMS value.

The RMS of the image residuals is an important statistical output to be noted from each VMS process. The magnitude of the RMS image residual is a function of target image quality, the collinearity and lens distortions models agreeing with the geometric distortions in the imagery, the form of the targets being imaged, and the image measurement method used. In the case of high contrast retro-reflective targets which use centroid measurements, the expectation is $\sim$1/10 of a pixel. The use of manual measurements (targets or natural features) is expected to give an order of 1/2 to 2/3 of a pixel [Geomsoft, 2015]. These values can be taken into consideration in order to rapidly evaluate the quality of the measurements throughout the experimental proce-

dure, however to be extended across camera systems with different principal distances and sensor dimensions, the angle subtended by the fraction of a pixel needs to be considered. If the RMS value, for the network as a whole or an image or target, is significantly different to that expected, based on the pixel size and measurement method, it is likely that there are precision, systematic or gross errors in the measurements involved (given that as the photogrammetric camera model used is well established for imaging with this type of sensor) [Geomsoft, 2015].

Outliers are measurement rejections which typically occur for physical reasons, for example when targets are partly or fully obscured or in the outer corners of the field of view (FOV). Outlier detection in VMS is made by comparing the residuals at each iteration of the LSE process to 5 times the measurement standard deviation. Outlying collinearity equations are removed from the solution, an iteration is made and then re-checked to see if the outlier remains at the next iteration. This gives a more robust process capable of working in eliminating erroneous measurements in situations where there are several errors. This is linked to the fact that LSE spreads the error across all of the measurements as it looks for the minimum sum of squares of the residuals. As a result, a single error in a measurement will result in a large residual which will be dispersed across the complete network. Detection of such outliers is discussed in section 5.4.3.2.

#### 5.2.1.2 SCT

The software used for tracking and retrieving object targets using a single camera video sequence was Single Camera Tracker (SCT) version 0.7 released in December 2014, developed by Prof. Mark R. Shortis (Royal Melbourne Institute of Technology) and Prof. Stuart Robson (UCL). SCT was used in sections 5.4.3 and 5.4.4 where tracking solutions using a single webcam (the C510 and C920 respectively) were developed.

## 5.3 Coordinating the ObT reference system

The initial part of the photogrammetric work was done to establish a reference coordinate system for the ObT field using a Nikon D100 DSLR (Table 5.1) with a 28 mm lens. DSLR images captured at a resolution of 3008× 2000 (at a pixel size of 7.8 × 7.8 $\mu m$), were acquired while operating the DSLR flash to achieve a higher contrast between targets and background in the images. Additionally, it was operated using auto-focus made with a fixed 28 mm focal length lens. The lens focus ring was set to give sharp images of the ObT field and then locked in place against the lens body with electrical tape to ensure a constant focus setting for all images in the network.

The scope of this section was to coordinate key geometric parameters of the

ObT system which are required as inputs in the image reconstruction method, as described in section 2.6. To achieve this, two things were needed, first to physically place appropriate targets on ObT points of interest, and second to run a photogrammetric adjustment in order to coordinate these target points. The former is described in this section, while the later is described in section 4.4.3.1.

40 retro-reflective circular and coded targets (section 2.11) were placed around the ObT field*: 'ObT targets'*. This was done for one side of the ObT system, Unit A (Figure 3.15 on page 74), comprising one x-ray source and six strip detectors. These ObT targets were positioned as such to allow each of the key elements of the system to be referenced. Specifically, what needed to be coordinated were the source focal spot (FS), the detectors and the belt COR in a common reference frame, with the camera tied in the same system. Following this, the specific locations of the targets were used in the photogrammetric computation of a test object position with respect to the ObT points of interest. This coordination then provided the basis for object 6DOF tracking, which in return provided the required measurements, as listed in section 4.4.3.

Each detector was coordinated by placing targets on its top surface. A ring of targets around the x-ray source was used to give an offset and direction from the front of the source cage and the physical centre of the source (i.e. the FS). Some of these targets can be seen in Figure 5.1. The first condition for the layout of the positioned targets was that the maximum FOV was covered. This is a condition of the imaging technique, where it is optimum want to cover the image space with targets to ensure complete calibration. In the case of target placement, the aim is to signalise all points of interest and to ensure that there are no solitary targets - i.e it is important to densify the targets where needed. Placing targets on various flat surfaces also establishes the key heights in the system: the conveyor belt plane, the base of the detector position arc, the top of the detector arc, and a plane orthogonal to the source so that its location can be determined. The targets on the top surface of each detectors were placed in order to establish the orientation of each detector with respect to the optional line of sight. The targets on the source cage ring were placed in order to be able to determine the FS, as the FS itself is within the cage and cannot be directly targeted.

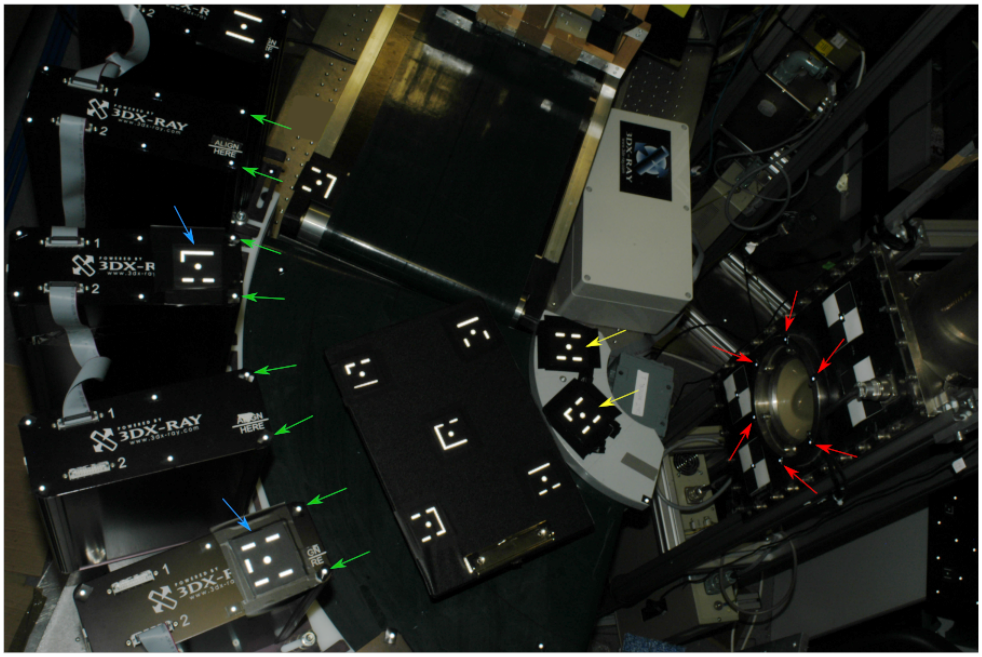


**Figure 5.1:** An image view of the ObT Unit A showing the fitted ObT targets: green arrows points to some of the round targets and blue to some of the coded targets on the top surface of the detectors; yellow arrows point to some of the coded targets on flat surfaces around the conveyor platform, and red arrows point to the circle targets on a ring co-centric to the FS within the x-ray source cage.

The 'Manhattan' reference calibration object (Figure 2.24 on page 53), with known dimensions, was used to provide appropriate 3D geometry starting values for the ObT coordination process. Whilst simple assumptions of planarity and known distances could have been used, the reference object improved the certainty of the photogrammetric process and helped in first understanding how the technique functioned and what it was capable of delivering in 3D space. This process is grounded on the pre-defined coordinates of the 131 target points on the reference object. The Manhattan, placed within Unit A, along with some of the ObT targets can be seen in the top image in Figure 5.2, the lower image showing these targets assigned target name values, displayed in VMS.

With the Manhattan in place, the coordination of the ObT targets, was done with the DSLR as part of a self-calibrating BA (section 2.9.2.1), where the ObT target coordinate locations were estimated simultaneously with the camera calibration parameters in a commonly used photogrammetric procedure. This process is described in the following sub-section 5.3.1.

### 5.3.1 Coordination of the ObT targets: DSLR self-calibration

A BA with the DSLR images employing self-calibration of the camera system was carried out to simultaneously estimate the pose of each image as well as a common set of camera calibration parameters. This measurement process

required three steps:

1) Establishing the starting values for the pose of each image in the network using resection (section 2.8.3). This used coded targets on the Manhattan as a means of automatically finding the initial relative positions between the ObT targets and the known calibration object targets.
2) The process of intersection (section 2.8.4) was then be used to obtain initial position coordinates for the ObT targets.
3) Having achieved steps 1 and 2, a BA (section 2.8.5) was used to simultaneously estimate the ObT target coordinates, the image pose and the camera interior orientation.

The practicalities of the above three steps are described in more detail below.

- Step 1:

In addition to the DSLR interior orientation, the pose of each image with respect to the ObT system targets needed to be determined. Establishing an image pose required the coordinates of identified targets within the FOV to be measured, and then, using the known object coordinates of the targets, the pose to be estimated by a resection process. Figure 5.2 shows the Manhattan placed centrally in Unit A on the corner conveyor belt C1 (Figure 3.13 on page 72). With the Manhattan and ObT field static, 20 images were acquired from a practical height ($\sim$1.5 m) from varying orientations, making sure that the majority of the Manhattan and ObT targets were visible in each image. These images were taken at a range of 90° around the optical axis, primarily to determine the principal point coordinate and the affinity parameters (Table 2.3 on page 46) [Luhmann et al., 2006]. In this study the first 12 known target coordinate points of the Manhattan were previously measured manually to sub-pixel accuracy in each acquired image in order to determine the provisional orientation of each of the images in the network. Dependent on where the Manhattan was placed, an initial coordinate system (arbitrary datum) was thus determined, wallowing the transfer of known coordinates to the unknown ObT targets.

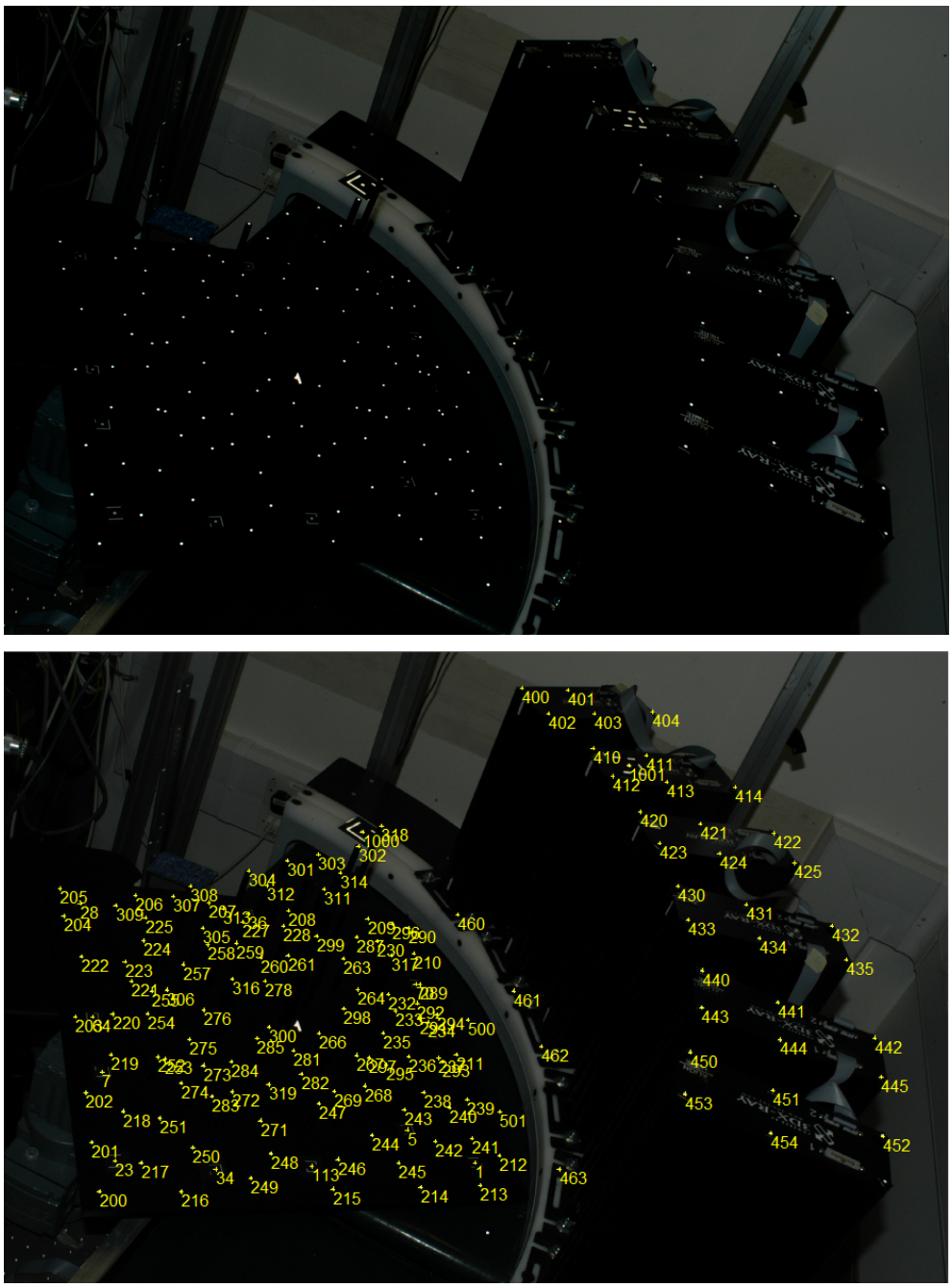


**Figure 5.2:** Above: 1 of the 20 images of the Manhattan in the ObT field, captured with the DSLR, to be processed for its self-calibration. Below: The same image, showing the assigned target name values, displayed in VMS.

The images acquired by the DSLR were inserted into a network image project in VMS to initially determine the parameters of the camera model (internal geometry). Suitable imaging configurations were employed in order to avoid unwanted correlations between the calculated parameters of the numerical calculations. This is why it is important that the network of images acquired are highly convergent, meaning that each target point has multiple lines of sight to it. The object space view, produced in VMS, is shown in Figure 5.3 and demonstrates the resulting network. The relatively narrow angles in the network were dictated by the FOV of the 28 mm lens on the DSLR. This FOV was sufficient to cover the complete ObT system from a ceiling vantage point

that would be effective for tracking objects on the ObT conveyor belt.

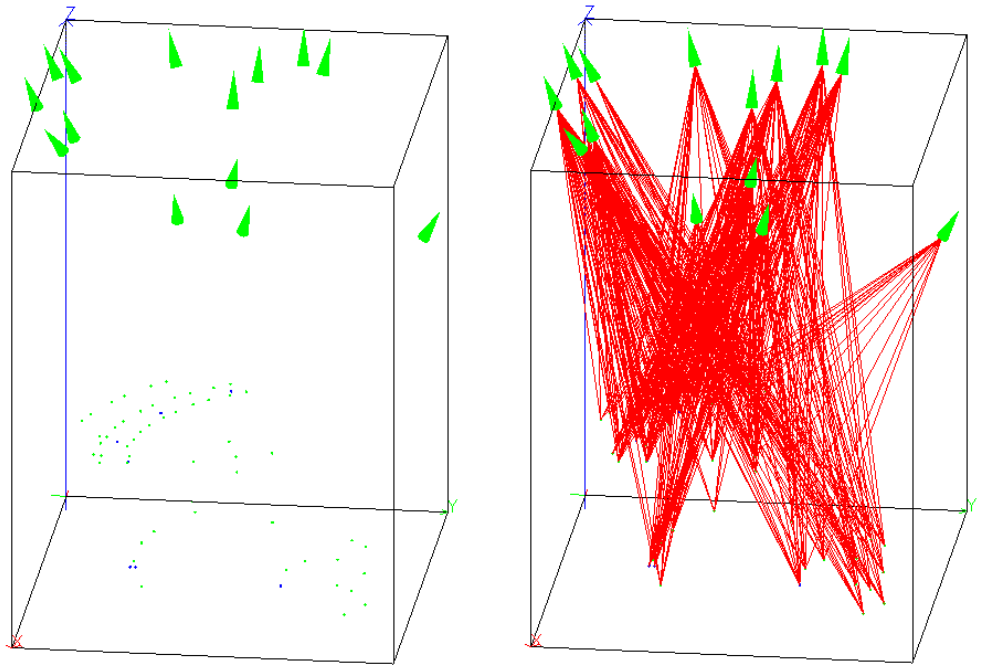

**Figure 5.3:** Sample schematic of VMS image object space. The green cones indicate the location and direction of the camera (perspective centre) at each image captured. The red lines escaping from each point correspond to the principal distance to the centre of each image (or target) principal point.

In addition, to scale the imaged space, it is essential to provide at least one piece of scale information along the viewing direction in order to reliably compute the principal distance. This is achieved with the calibration object, as its coordinates were originally determined using a photogrammetric network and scale bar.

- Step 2:

The next step is determining the coordinates of the ObT targets in the same VMS project. This was done by using the orientations of the images computed above, and computing a space intersection (section 2.8.4 on page 42) to estimate starting 3D coordinates for each of the ObT target locations. For this, each new target was allocated a unique numerical name and was measured in all images in which it can be identified. The lower image in Figure 5.2 includes a caption from VMS showing the visible targets within the image FOV and their assigned numerical name.

- Step 3:

3a) Once all visible Manhattan and ObT targets were named and intersected, a BA was performed, following the steps described in Appendix H (page 212). The results of this process, which is referred to as BA:3a, are presented in section 5.3.1.1, and are later used to compute the ObT target coordinates from which the ObT reference coordinate system is defined using BA:3b, described in the next step.

3b) In order to ensure that the measurements are correctly scaled, and avoid extrapolating beyond the size of the calibration object - since the volume of the Manhattan is smaller than the ObT field by roughly 1/4 - 20 *slope distances* (which specifies a displacement through the X-Y-Z planes) were measured and inserted in a new VMS project. 5 of these were conditioned as *height differences* (which specifies the vertical displacement through the Z plane). Then BA was repeated again. In addition, the output target file from BA:3a was used when creating this VMS project, having changed the target indices to provide a useful datum in the presence of distance measurements to define the scale. As such, 7 of the targets' flags were changed as following described, making the targets respective coordinates constrained according to Table 5.2. One target flag was set to '6', three others to '4', three others to '1', and the rest to '0'. It is not only the flag that is important to define the coordinate system, but also the respective coordinate values of the flagged targets. A flag of '6' on the first target, meant that its X and Y coordinates are constrained and enabled the definition of the X-Y coordinate origin. Following that, a flag of '1' means that the Z target coordinates are constrained, hence all of the targets with a flag of '1' have been assigned the same Z value ($\sim$ 500 mm). Since the targets with '1' flags are distributed across the conveyor belt space, these describe the height of the X-Y plane and set the direction of the Z axis. However the relative $\varphi$ angle around Z is yet undefined (Figure 1.3 on page 6). By setting three targets flag to '4', each of which was parallel to the direction from COR to the first detector window (indicated by the red dashed line in Figure 5.6), meant that their X coordinate is fixed and these lie on a straight line. Thus, the relative direction of the X-axis and the horizontal rotation in the X-Y plane are defined. All 7 flagged constrained target coordinates are plotted in Figure 5.4.

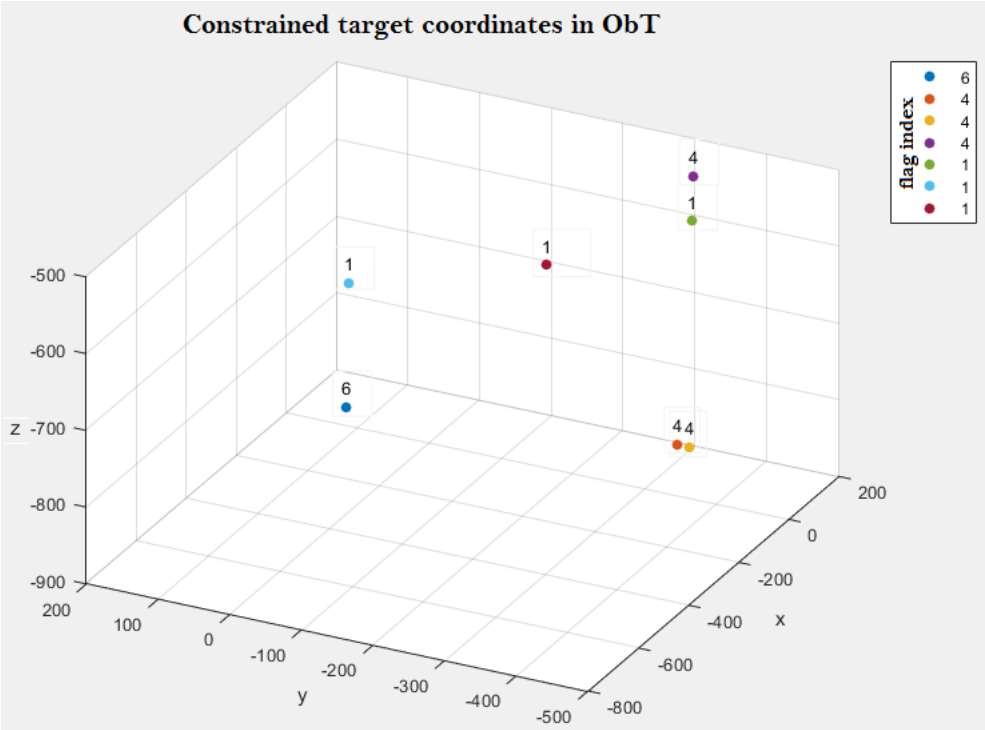


**Figure 5.4:** Flagged targets coordinates plotted in 3D space.

The starting values for these targets came from the BA:3a, incorporating the Manhattan calibration object. Therefore, the initial position of the calibration object defined the coordinate datum. The exception was the '4' flag where the X coordinate of three targets was set along the desired line parallel to the X axis, which introduced a small rotation about Z. Similarly the Z coordinates of the targets flagged as '1' ensured a small rotation to be made, in order to level up the coordinate system to the required reference plane, since the calibration object was tilted in its original placement (with respect to the belt). This set the X-Y plane to be parallel to the belt surface.

Each target with an index greater than 0 was then treated as a measurement in the BA, with the standard deviation ($\sigma$) of its given coordinates defining the quality of that measurement, as discussed in section 5.2.1.1. These standard deviations were obtained from the output of BA:3a. As such all 7-datum elements (scale, origin (XYZ), and axes rotations - section 5.2.1.1) are defined. Therefore by running a new BA, this method would allow an ObT system of any size to be coordinated since a similar set of 3D points could be marked, and the distances measured between them to define the scale .

#### 5.3.1.1 DSLR self-calibration results & analysis

The number of observables, unknowns, and redundancies in the network give an idea of 'how overestimated' the LSE (section 2.8.1) is, as there are many many more measurements than unknowns.

The scale for the datum of BA:3b is defined by tape and calliper measure-

ments with an uncertainty of ± 0.5 mm or ± 0.1 mm respectively, whilst the Manhattan defines the scale to a level an order of magnitude better. However, in the following work, BA:3b was used as the final output, because the effects of extrapolation from the Manhattan, which is smaller than the ObT system, are unknown. Using BA:3b could allow for the process to be used for any ObT system setup - for example on a full size airport ObT system.

| **Calibration Solutions Results** | | |
|---|---|---|
| **Computed Network Adjustment** | **BA:3a** | **BA:3b** |
| unit weight estimate (sigma zero) | 1.00 | 1.00 |
| RMS image residual (mm) | 0.49 | 0.58 |
| number of images in the network | 20 | 20 |
| number of rejected target images | 91 | 3 |
| number of observable in the network | 9085 | 924 |
| number of unknowns in the network | 737 | 274 |
| number of redundancies in the network | 8348 | 650 |
| **Target Precision Summary** | **BA:3a** | **BA:3b** |
| mean precision of target coordinates ($\mu m$) | 10 | 83 |
| relative precision for the network | 1:160000 | 1:19000 |
| **Survey Measurements** | **BA:3a** | **BA:3b** |
| RMS Residual (average) | n/a | 0.5mm |

**Table 5.3:** Results for the calibration solutions of BA:3a and BA:3b (section 5.3.1).

An independent measurement check was additionally performed: comparing slope distances resulting from photogrammetric computations to the equivalent distances measured manually. The former can be calculated from the output target coordinates from BA:3b, using equation 5.1 to measure the distance $D$ between two coordinate points A$(X_A, Y_A, Z_A)$ and B$(X_B, Y_B, Z_B)$:

$$D = \sqrt{(X_A - X_B)^2 + (Y_A - Y_B)^2 + (Z_A - Z_B)^2} \tag{5.1}$$

The manual inter-target distance measurements were made using a calliper with an accuracy of 0.1 mm, measuring from target outside edge to target inside edge − which corresponds to the target inter-distances, assuming identical target diameters.

In order to compare these manual measurements ($D_M$) to the photogrammetrically computed values ($D_P$) for the scale distances, a statistical *pair sample t-test* was used [Student, 1908, Easton and McColl, 1997, Zabell, 2008, Ha and Ha, 2011]. Comparison between these data sets represents an independent check on the accuracy of the photogrammetric results. In such tests, the difference between the two values of the same parameter (paired values) in each pair - in this case, the distance $D$ between two target points - is the variable of interest. The pair sample $t$-test assumes that the differences between pairs are normally distributed. Analysis of data from a pair sample experiment compares the two measurements by subtracting one from the other and

basing a test hypotheses - the null hypothesis $H_0$ - upon the differences. $H_0$ assumes that that the mean of these differences ($\overline{d}$) is equal to zero, while the alternative hypothesis ($H_a$) claims that $\overline{d}$ is not equal to zero and can be either positive or negative (two sided $t$-test) [Yale, 1998]. Using the differences between the paired measurements ($d_i$) as single observations, the standard $t$ procedures with *N-1* degrees of freedom were followed, where $N$ is the total number of $n_i$ distance pairs measured. If the difference between each pair $n_i$ of targets is given by $d_i$, then the average difference of all sets is given by:

$$\bar{d} = \frac{\sum d_i}{N} \tag{5.2}$$

The standard deviation $\sigma$ of all $d_i$ values is given by:

$$\sigma = \sqrt{\frac{\sum \left(d_i - \bar{d}\right)^2}{N-1}} \tag{5.3}$$

From these, the $t$ value can be calculated by:

$$t = \sqrt{N}\frac{\bar{d}}{\sigma} \tag{5.4}$$

The significance level $\alpha$, for a given hypothesis test, is the probability of rejecting $H_0$ when it is true. For example, a significance level of 0.01 indicates a 1% risk of concluding that a difference exists between the two pairs, when there is no actual difference. In other words, for $\alpha$=0.01 there is a 99% degree of confidence for $H_0$. To check the test, a popular table shown in Appendix G (page 211) is used to determine the corresponding *critical value* $t$ ($t_{N-1,\frac{\alpha}{2}}$) with which the measured $t$ needs to be compared with, for a given $\alpha$ with *N-1* degrees of freedom. In order for $H_0$ to be confirmed with a 99% degree of confidence the measured $t$ value must be:

$$-t_{N-1,\frac{\alpha}{2}} \leq t \leq t_{N-1,\frac{\alpha}{2}} \tag{5.5}$$

Performing a $t$-test to compare the the photogrammetrically computed distances $D_P$ to the manually measured distances $D_M$, resulted in $t$=3.15 (Table 5.4). For N-1=9 and $\frac{\alpha}{2}$=0.005, the table in Appendix G indicates that $t_{N-1,\frac{\alpha}{2}} = 3.25$, which verifies equation 5.5. Based on the above, $H_0$ in this case is not rejected, meaning that there is no significant difference between the two aforementioned measurement methods, with a 99% confidence level.

| $n_i$ | **targets** | **distances D (mm)** **photogrammetrically computed ($D_P$)** | **manually measured ($D_M$)** | $\lvert d_i \rvert$ | $d_i - d$ | $(d_i - d)^2$ |
|---|---|---|---|---|---|---|
| 1 | 10-400 | 649.20 | 649.20 | 0.00 | $-2.3 \times 10^{-2}$ | $5.3 \times 10^{-4}$ |
| 2 | 410-604 | 781.52 | 781.50 | 0.02 | $-3.0 \times 10^{-3}$ | $9.0 \times 10^{-6}$ |
| 3 | 450-605 | 870.56 | 870.56 | 0.00 | $2.3 \times 10^{-2}$ | $5.3 \times 10^{-4}$ |
| 4 | 8-606 | 339.99 | 340.00 | 0.01 | $-1.3 \times 10^{-2}$ | $1.7 \times 10^{-4}$ |
| 5 | 7-607 | 670.75 | 670.70 | 0.05 | $2.7 \times 10^{-2}$ | $7.3 \times 10^{-4}$ |
| 6 | 7-440 | 793.16 | 793.10 | 0.06 | $3.7 \times 10^{-2}$ | $1.4 \times 10^{-3}$ |
| 7 | 401-461 | 440.77 | 440.80 | 0.00 | $-2.3 \times 10^{-2}$ | $5.3 \times 10^{-4}$ |
| 8 | 12-601 | 912.93 | 912.90 | 0.03 | $7.0 \times 10^{-3}$ | $4.9 \times 10^{-5}$ |
| 9 | 8-23 | 661.15 | 661.10 | 0.05 | $2.7 \times 10^{-2}$ | $7.3 \times 10^{-4}$ |
| 10 | 24-608 | 881.41 | 881.40 | 0.01 | $-1.3 \times 10^{-2}$ | $1.7 \times 10^{-4}$ |
| | | | $\Sigma d_i$ | **0.23** | $\Sigma(d_i - d)^2$ | $4.8 \times 10^{-3}$ |
| | | | $\overline{d}$ | **0.023** | $\sigma^2$ | $5.3 \times 10^{-4}$ |
| | | | | | ***t*** | **3.15** |

**Table 5.4:** Photogrammetric and manual measured values of slope distances D between 10 sets of ObT targets. A $t$-test performed on these values resulted a $t$ value of 3.15 which shows that there is no significant difference between the two measurement methods, with a 99% confidence level.

### 5.3.2 Finding ObT Centre Of Rotation

The next part of the study was to estimate the coordinates of the centre of rotation while an object travels in ObT Unit A. Since the motion of an object placed in the ObT is purely due to the conveyor belt, this was done by retrieving the 3D centroid information of an object at discrete positions of its travel, assuming a perfect circular arc motion. This limited number of discreet positions were used to extrapolate the circular arc of the object motion. Thus, a 3D LSE best circle fit, including centre, planar orientation and radius, was made from three measured positions, described below. This could have been done by placing and tracing targets on the conveyor belt surface, as each of these would describe a circle with the same centre but different radii. However, it was done by tracking an object on the belt instead, which has the advantage of being at a similar height as the objects of interest to be imaged in the ObT (section 4.4.1). Tests were performed to check the smoothness of the object motion. For this, a test piece (TP) was created, which is a solid black rectangular (3 mm thick) platform of 228 × 332 mm, upon which coded retro-reflective targets were placed on a common plane (Figure 5.5).

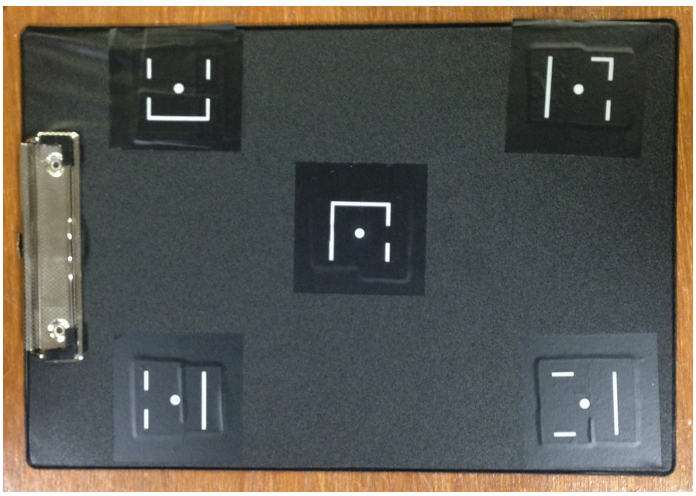

**Figure 5.5:** The test piece (TP) created for photogrammetric work, was a solid black rectangular (3 mm thick) platform of 228 × 332 mm, upon which coded retro-reflective targets are placed

By adding at least three reference control points on a TP in a camera's FOV - or alternatively at least four non co-planar points as a practical minimum - a local coordinate system for the TP can be defined [Schenk, 2005, Helle et al., 2015]. As such, the camera pose can be photogrammetricaly computed through resection, which is needed for the 6DOF computation (sections 5.4.3 and 5.4.4). As such, five different coded retro-reflective targets (section 2.11.1) were added on the TP (Points $A$ to $E$), to play the role of a coded rigid body. Even a single such target would suffice for a circle fit, since it would describe a circular arc as part of the motion. The TP was then mounted on a base, rising it to 30 mm above the belt level in the z direction, which is approximately the height of phantoms imaged in Chapter 4, exploring ObT.

The TP was placed in the middle of C1 (Figure 3.13 on page 72), the Unit A conveyor belt, and another network of images was taken to coordinate the five TP coded target coordinates: essentially another BA such as BA:3b. From this, the TP target positions were established relative to one another, and thus the TP was then assumed to be a rigid body. The later BA output coordinate values of the 5 TP coded targets, and their errors, are shown in Table 5.5. These inter-target distances are measured and compared to the manual measurements. Given that the photogrammetric coordinate precision is better than 0.1 mm, having rounded up all values to 0.1 mm, the relative differences are equal to zero. As such, the mean residual RMS of the difference between measurements is 0, at a precision of 0.1 mm. The precision expectations come from BA:3b (Table 5.3) which shows a network RMS of 0.5 mm.

With a precision better than 0.1mm, and having confirmed the TP point manual distances agree with the photogrammetrically computed values, within the same precision, the results from BA:3b are therefore accepted.

The TP positions were also imaged from single locations with each webcam so that this information could also be used in later work developing a tracking system using single webcams (sections 5.4.3 and 5.4.4). The work on object tracking was aimed at validating initial positions of the object motion, and comparing static and dynamic tracking imaging solutions.

| | **Coordinates and respective errors (mm)** | | | | | |
|---|---|---|---|---|---|---|
| **Point** | **X** | **dX** | **Y** | **dY** | **Z** | **dZ** |
| **A** | -241.474 | 0.012 | -39.444 | 0.053 | -582.263 | 0.028 |
| **B** | -174.807 | 0.024 | -167.710 | 0.013 | -580.624 | 0.029 |
| **C** | -366.414 | 0.055 | -77.082 | 0.039 | -578.192 | 0.028 |
| **D** | -109.873 | 0.048 | -21.052 | 0.061 | -586.626 | 0.031 |
| **E** | -294.160 | 0.028 | 68.431 | 0.094 | -584.843 | 0.030 |

| | **Distance (mm)** | | **difference (mm)** |
|---|---|---|---|
| **Points** | $D_P$ | $D_M$ | $\sigma$ |
| **AB** | 144.5659 | 144.6 | 0.0 |
| **AC** | 130.5492 | 130.5 | 0.0 |
| **AD** | 132.9519 | 133.0 | 0.0 |
| **AE** | 120.0806 | 120.1 | 0.0 |
| **BC** | 211.9726 | 212.0 | 0.0 |
| **BD** | 160.5022 | 160.5 | 0.0 |
| **BE** | 264.6226 | 264.6 | 0.0 |
| **CD** | 262.7236 | 262.7 | 0.0 |
| **CE** | 162.6003 | 162.6 | 0.0 |
| **DE** | 204.8705 | 204.9 | 0.0 |

**Table 5.5:** TP target coordinate values, and their errors, resulting from photogrammetric bundle adjustment. Their relative distances were measured and compared to manual measurements resulting that there was no difference between the two pair sets.

Three positions are chosen, named *Start, Middle* and *End* and symbolised $P_S$, $P_M$ and $P_E$ respectively. The TP was placed at $P_S$, imaged, then the conveyor belt was switched on moving it to $P_M$ at the middle of the Unit A conveyor track, where it was paused while it was imaged, and then moving to the end of that track $P_E$ where it was imaged again. These are shown in Figure 5.6. In each of these three positions the DSLR was used to acquire 15 images of the TP from a range of orientations around Unit A. It was important to ensure that as many ObT targets as possible are visible within images, while each individual target is in the FOV of at least 4 of them. One of the acquired imaged at $P_S$ is shown in Figure 5.7.

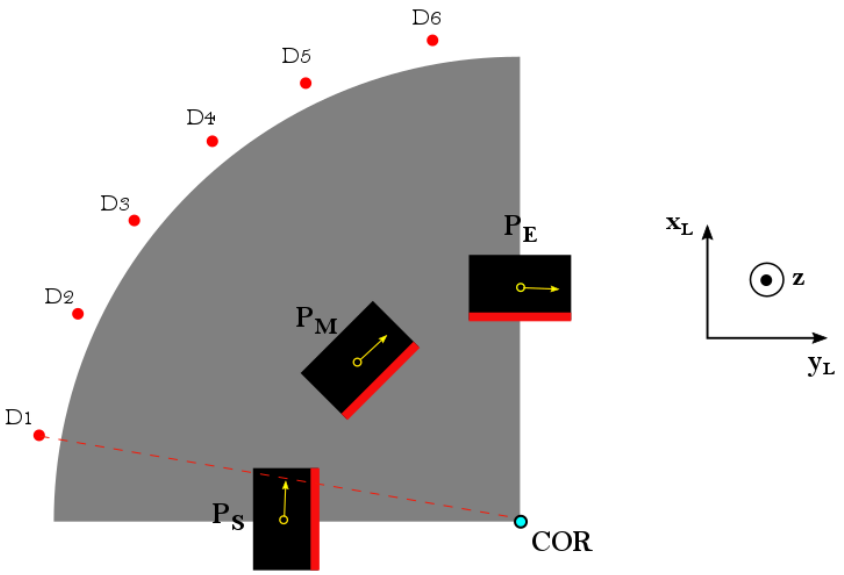


**Figure 5.6:** ObT Unit A showing the TP at the three chosen positions $P_S$, $P_M$ and $P_E$ corresponding to the start, middle and end of its travel along the Unit A conveyor belt track.

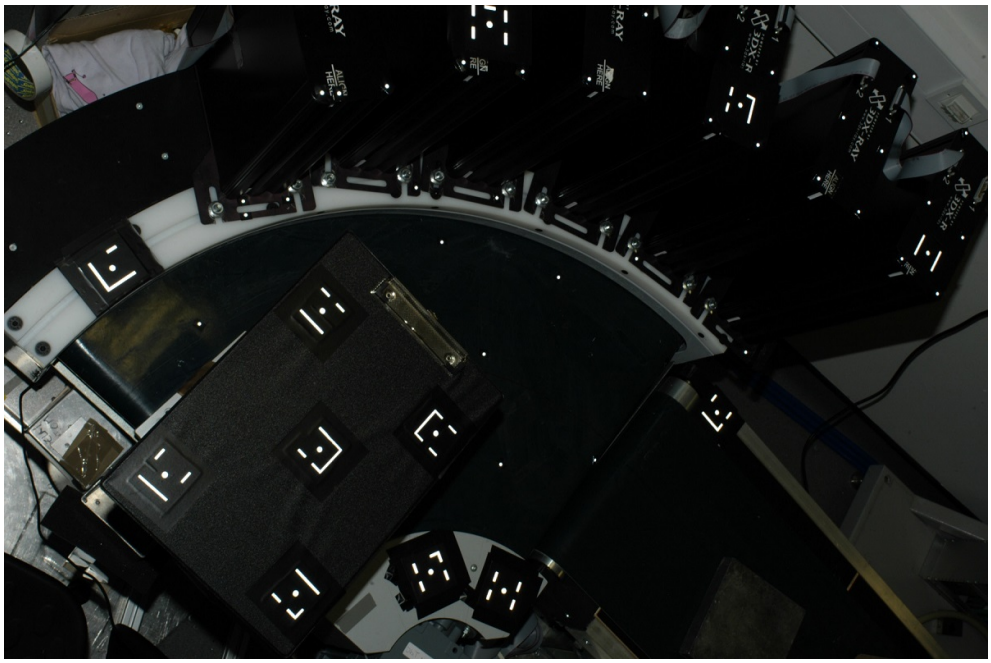

**Figure 5.7:** One of the 15 acquired imaged taken with the DSLR, with the TP placed at $P_S$ (corresponding to Figure 5.6), used for running a VMS project.

The output target file resulting from the DSLR self-calibration using scaled measurement inputs (BA:3b, section 5.3.1) was used as the basis of a new VMS project for each position. This target file, along with the original DSLR calibration file and the respective acquired images for each position, a DSLR self-calibration was performed thrice. In each case, initial coordinates for the TP targets were found by intersection. These allowed a BA, similar to BA:3b, to be computed for each case: *BA:S, BA:M, BA:E*. The results from this give the reference ObT target coordinates as well as the TP target coordinates in

each position. Since the X-Y plane was set to be horizontal, all TP targets have the same Z coordinate and thus a 2D graph can be plotted, as the ObT system would be viewed from above, which is illustrated in Figure 5.8. This comes from the '1' flagged targets from the datum definition, which were all located on a plane parallel to the belt. The five TP targets are plotted in the graph in Figure 5.8, based on the output coordinates from the respective BA in each position, which provide definitive data coordination.

The centroid of the output coordinates of each of the three TP positions were then used in a LSE 3D circle estimation process, using 'Shapes' software: a 3D shape fitting tool developed by Fryer et al. [1992]. The output from the 3D circle fit is shown in Appendix F (page 210), which includes the estimated coordinates of the circle centre, which physically coincides with the COR. This is also plotted in the graph in Figure 5.8, in addition to one target from each detector, each of which is placed at the same location on the top of the detector. The 'Shapes' output RMS of the residuals normal to the plane of the circle is 0, while the average RMS of the radial residuals in the plane is $\sim$0.002mm.

The weakness of the 3D circle fit solution is that there were only three points fitted to the circle, which also correspond to less than a quarter of a full circle arc. The solution could be improved by taking more positions along the circular arc. Additionally, from Table 5.3, if it was possible to have measured the calliper distances which were inputted in BA:3b, even higher accuracy and precision could have been achieved. However, the quality of the results with an RMS of better than 0.1mm are far better than the manual measurements attained in section 4.4.3, Table 4.3.

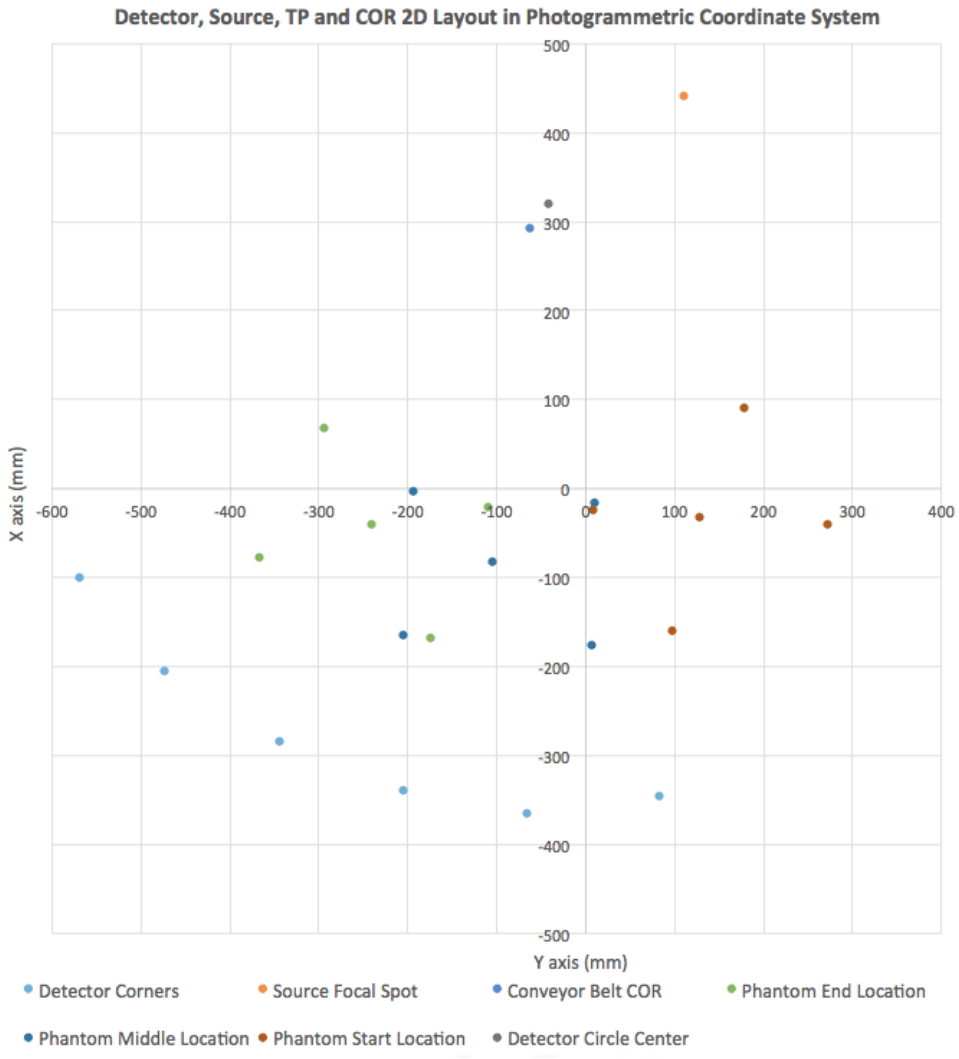


**Figure 5.8:** Graph of detector, source FS, TP and COR 2D layout in the photogrammetric coordinate system.

## 5.4 Object tracking solution

This section describes the webcam solutions used to provide a tracking system for finding a reference object, in this case the test piece ( *TP*, Figure5.5 on page 144), traveling on the conveyor belt. More specifically, the aim is to explore low-cost tracking solutions able to deliver the trajectory of an object in the ObT. For this, the smoothness of its motion and the quality of the measurements are analysed.

In the future, a method to replace the target tracking, incorporating non-contact detection methods, could be a more practical and efficient solution (section 6.3).

### 5.4.1 Webcam image capture

The videos and images from the webcams were acquired using Logitech® Webcam Software v2.0 . Operating this software to capture videos or photos

with the webcams is straight forward. Open Logitech® Webcam Software and click on 'Quick Capture'. A window displaying the live view of the camera appears along with control and parameter buttons (Figure 5.9). This window has an option to use the webcam in 'Photo' or 'Video' mode and a central button which initiates and terminates caption. By clicking on 'Advanced Settings' one is able to adjust the camera settings to provide an optimal view. The settings fixed for the operation of the C510 webcams employed in this work are shown in Figure 5.10.

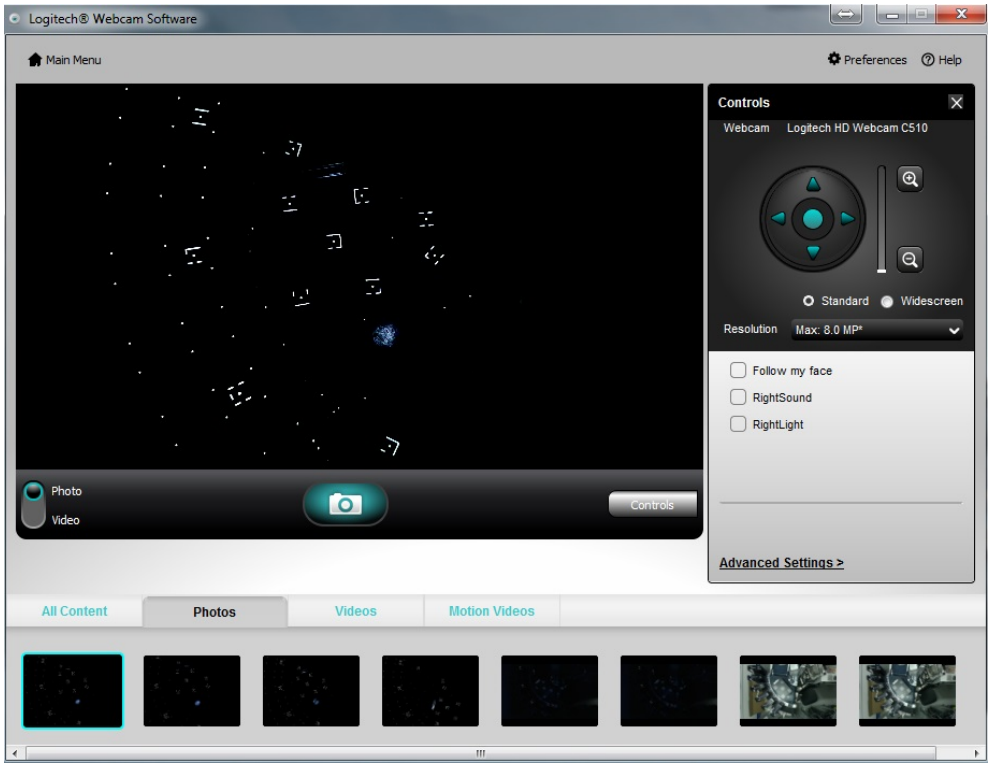


**Figure 5.9:** Logitech® Webcam Software v2.0 Controls display window.

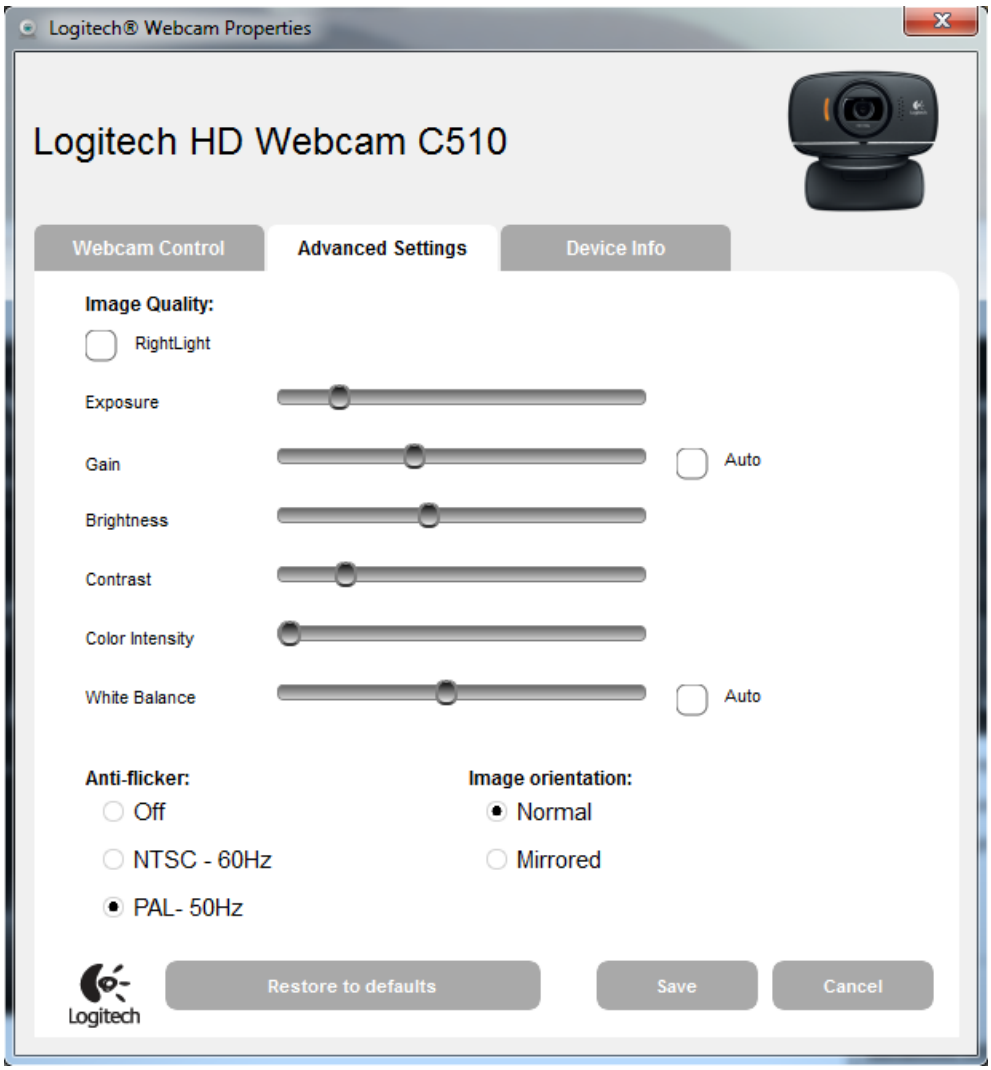


**Figure 5.10:** Logitech® Webcam Software property settings, at which the C510 webcams were operated.

### 5.4.2 Initial multi camera solution

As seen in section 2.10.1, Wong [2012] developed a multi-camera photogrammetric system employing 4 (or 8) Logitech C500 webcams demonstrating consistent target tracking accuracy over time. Taking a modified version of this system, a 4-webcam configuration employing the next generation Logitech C510 webcam was constructed to provide a 6DOF tracking solution.

A rigid aluminum frame was installed around the ObT system, in order for the 4 webcams to be mounted on top of Unit A (partly visible in Figure 3.14 on page 73). This structure provided a convergent imaging geometry (example Figure 2.22 on page 49) with each camera looking down at the centre of the FOV for maximum coverage at distance of 1.5 m from the belt surface. The approximate distance from the centre of the belt surface to each camera was 1.5 m.

In order to test the multi-webcam system, each webcam first needed to be

calibrated, the process of which is described in sub-section: 5.4.2.1.

#### 5.4.2.1 Logitech C510 webcam calibration

The calibration process was performed in order to estimate the camera interior orientation parameters (section 2.9.1) and was the same for each webcam. Having fixed the webcams in place, around Unit A, a calibration object (Figure 2.25 on page 54) was placed on the centre of the belt (position $P_M$, Figure 5.6). The calibration object was then rotated and tilted 15 times while images were captured with all 4 webcams at each position. The reference calibration object's position is adapted to be imaged perpendicularly and obliquely and have a relative rotation of 90° around each camera's optical axis. Then, a BA is executed for each camera, using the full set of network images and targets from the individual camera calibration. Images were measured and processed in a similar way to that used to coordinate the ObT system in section 5.3.1, based on Appendix H (page 212). The resulting estimated calibration parameters of each webcam are shown in Table 5.6. It should be noted that only one of the three radial lens distortion parameters (#4-6) is used and estimated, as it gives a smooth curve with no points of inflection, which is what is seen in many basic lenses [Swaminathan and Nayar, 2000]. Table 5.7 highlights the particular calibration solution results for each of the four webcams. The observed inconsistencies can be related to the differences among the network geometry coverage of each webcam.

| | **Logitech C510 Webcam #** | | | |
|---|---|---|---|---|
| **Parameter #** | 1 | 2 | 3 | 4 |
| 1 | -0.099 | -0.135 | -0.101 | -0.089 |
| 2 | -0.072 | -0.158 | -0.076 | -0.12 |
| 3 | 5.663 | 5.647 | 5.661 | 5.653 |
| 4 | -3.38E-04 | -3.04E-04 | -3.32E-04 | -2.84E-04 |
| 5 | *not estimated* | | | |
| 6 | *not estimated* | | | |
| 7 | 1.19E-05 | 7.73E-05 | -1.12E-05 | -1.34E-04 |
| 8 | -6.01E-05 | 1.88E-04 | -1.04E-04 | -1.11E-04 |
| 9 | -1.38E-04 | -1.02E-04 | -8.80E-05 | -3.71E-04 |
| 10 | 3.82E-04 | 3.02E-04 | 3.85E-04 | 3.58E-04 |

**Table 5.6:** Calibration parameter results, corresponding to Table 2.3 on page 46, of the 4 individual Logitech C510 webcam calibrations. Note that $E$ is a scientific notation which represent "times ten raised to the power of" ( $\times 10\hat{}^n$ ).

| Results for the Calibration Solution (interior orientation parameters) | | | | |
|---|---|---|---|---|
| **Computed Network Adjustment** | **Logitech C510 Webcam #** | | | |
| | **1** | **2** | **3** | **4** |
| unit weight estimate (sigma zero) | 1.00 | 1.00 | 1.00 | 1.00 |
| RMS image residual (mm) | 0.25 | 0.49 | 0.27 | 0.24 |
| number of images in the network | 15 | 15 | 15 | 15 |
| number of rejected target images | 26 | 4 | 7 | 10 |
| number of observable in the network | 2044 | 1848 | 1871 | 1561 |
| number of unknowns in the network | 311 | 275 | 291 | 276 |
| number of redundancies in the network | 1733 | 1573 | 1580 | 1285 |
| **Target Precision Summary** | **1** | **2** | **3** | **4** |
| mean precision of target coordinates ($\mu m$) | 11 | 5 | 17 | 14 |
| relative precision for the network | 1:37000 | 1:76000 | 1:23000 | 1:27000 |

**Table 5.7:** Individual calibration solution results of 4 Logitech C510 webcams.

As an additional check, to confirm the webcam stability over an extended period of time, webcam 4 was re-calibrated two more times, 7 and 16 months after its first calibration. The calibration parameters measured for webcam 4 in all three cases (*Calibrations a,b,c*) are shown in Table 5.8, which also shows the respective value percentage changes among the three sets. Given the consistency of the results, and the fact that the average parameter value change among all sets is 1%, with a maximum of 3%, it is shown that the webcam calibration is sufficiently stable for a period of at least 17 months.

| **Parameter** | **Calibration** | | | **Value** | **%** | **change** |
|---|---|---|---|---|---|---|
| **#** | **a** | **b** | **c** | **a-b** | **b-c** | **a-c** |
| **1** | -0.089 | -0.090 | -0.091 | 1.12 | 1.11 | 2.25 |
| **2** | -0.12 | -0.12 | -0.12 | 0.00 | 0.00 | 0.00 |
| **3** | 5.653 | 5.695 | 5.739 | 0.74 | 0.77 | 1.52 |
| **4** | -2.84E-04 | -2.86E-04 | -2.88E-04 | 0.79 | 0.59 | 1.39 |
| **5** | *not estimated* | | | - | | |
| **6** | *not estimated* | | | - | | |
| **7** | -1.34E-04 | -1.36E-04 | -1.38E-04 | 1.38 | 1.48 | 2.89 |
| **8** | -1.11E-04 | -1.13E-04 | -1.14E-04 | 1.23 | 1.32 | 2.57 |
| **9** | -3.71E-04 | -3.75E-04 | -3.80E-04 | 1.10 | 1.25 | 2.37 |
| **10** | 3.58E-04 | 3.55E-04 | 3.57E-04 | 0.64 | 0.56 | 0.08 |
| | | | **Average** | 0.70 | 0.71 | 1.31 |
| | | | **Maximum** | 1.38 | 1.48 | 2.89 |

**Table 5.8:** Three consecutive calibrations (a,b,c) of the same Logitech C510 webcam (#4) with a total time difference of 17 months (7 months between a-b, 9 months between b-c) shows that the webcam calibration is sufficiently stable for that period, with a maximum parameter value change of 3%.

#### 5.4.2.2 3D coordination with webcams

Having determined the 4 webcam interior orientation parameters, the joint coordination of the cameras was done in new VMS project, following the steps in Appendix H. Since the ObT targets will be visible to the webcams during tracking, whereas the calibration object used to define the system will be removed, the ObT points must be recognised as control points by the VMS software. This further insured that the calibration of the 4 webcams agreed

with the coordinated ObT space, and 'locks' the system, which is why the network mean precision is better when comparing results from Table 5.9 to 5.3 or 5.7. This is achieved by changing their flag from 0 to 7 (Table 5.2) in the target file produced by BA:3a (section 5.3.1), and using the updated target file in this new VMS project. In addition, a single image caption from each camera and the calibration output file produced earlier (section 5.4.2.1) were incorporated. A resection check was carried out using a fixed webcam calibration, along with an intersection check which was then performed to confirm that 3D points could sufficiently be coordinated. A screenshot of this VMS project is shown in Figure 5.11. Analysis of the RMS residual and a check for overall magnitude allowed the use of the camera to continue.


**Figure 5.11:** Screenshot of VMS project with a single image caption from each of the 4 webcams. Figure is rotated by 90° clockwise for better visualisation.

The RMS of the residuals was of the order of 4 $\mu m$ from the previous photogrammetric BA, whilst this is an optimistic estimate, it can be seen in table 5.9 that the network of images was in agreement giving an RMS image residual of 0.28 mm.

| **Results from photogrammetric network adjustment with 4 webcam images** | |
|---|---|
| **Target Precision Summary** | |
| mean precision of target coordinates ($\mu m$) | 4 |
| relative precision for the network | 1:102000 |
| **Computed Network Adjustment** | |
| unit weight estimate (sigma zero) | 1.00 |
| RMS image residual (mm) | 0.28 |
| number of images in the network | 4 |
| number of rejected target images | 0 |
| number of observable in the network | 549 |
| number of unknowns in the network | 165 |
| number of redundancies in the network | 384 |

**Table 5.9:** Control target precision summary from photogrammetric network adjustment with 4 webcam images.

Of the BA results, the radial and tangential lens distortion, which are plotted in Figure 5.12, show that there is a similar distortion trend among all four cameras, while the absolute magnitude is below 4.5 $\mu m$ and 1.2 $\mu m$ respectively in all cases. Webcam 4 goes up to a 2.5 mm radius simply because the coverage of imaged points for that webcam extends to the edges of the image format. The other webcams have data that are more central, and go up to a 2 mm radius. The observed differences, particularly in the tangential distortion, suggest some variations in lens alignment, but the differences in magnitude are very small, of the maximum order of 0.4 $\mu m$, which shows that the misalignment among the 4 webcams is negligible for ObT requirements.

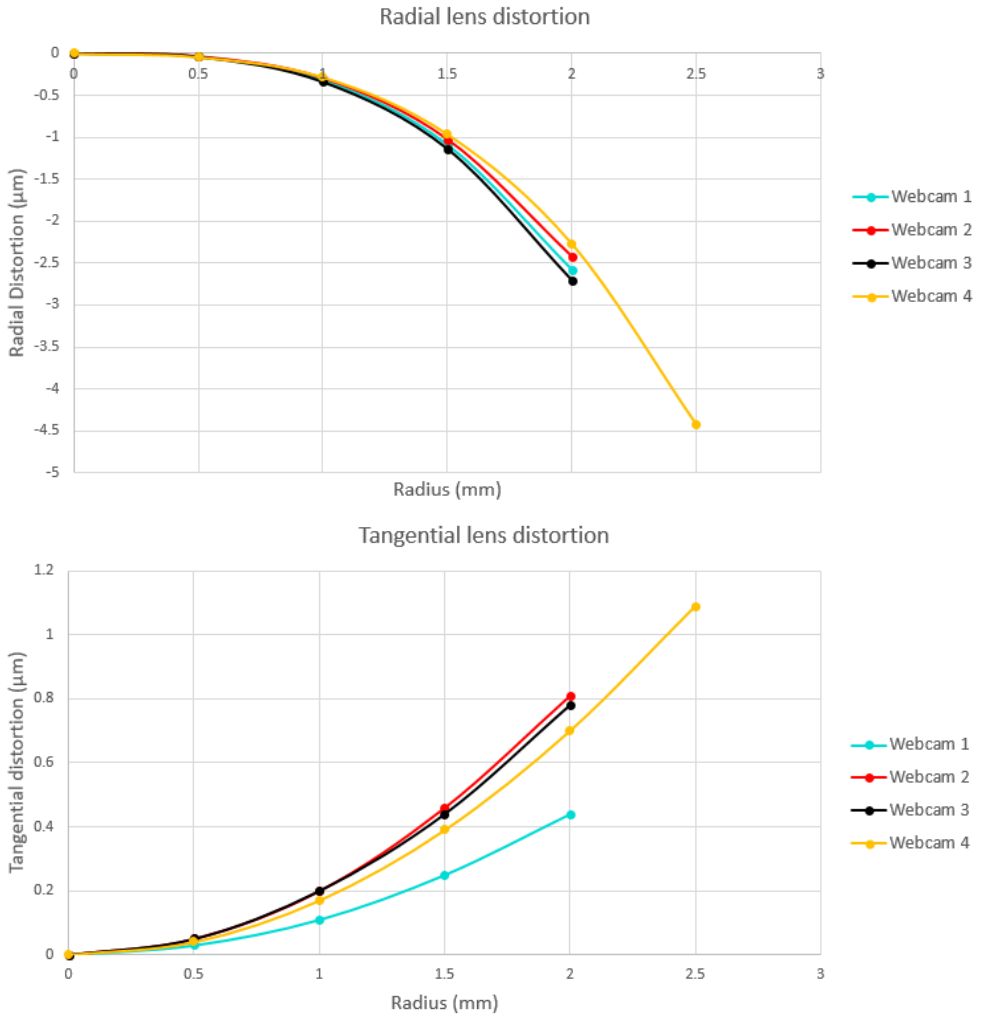


**Figure 5.12:** Radial (above) and tangential (below) lens distortion of the 4 webcams, measured in VMS.

Having established that the calibration of the webcams was appropriate, an effort to implement these together using the 'VI' software developed by Wong et al. [2009] was made. 'VI' had been demonstrated to have good results, and thus was chosen with the scope that its implementation would be able to track an object in the ObT, without assuming it is a rigid body. The primary aim was to check whether the static ObT targets could be located and coordinated by the 4-webcam network. For this, the camera calibration and photo orientation files from the later BA were used to populate 'VI'. However, this method could not be successfully implemented as it failed to give reliable information. More specifically, aside all efforts to make this method work, which are listed in Table 5.9, the data acquisition and data transfer was unstable and there were problems with the image synchronisation. Therefore, this method was rejected and single webcam solutions were explored, which are described in sections 5.4.3 and 5.4.4.

| Actions taken to develop the 4-webcam network tracking solution |
| --- |
| • changed computer USB card to match the one used by Wong [2012] |
| • upgraded software: re-installed Windows (7), in case there was some overhead |
| • upgraded other hardware: new computer's i7 processor versus the older computer's AMD 95 |
| • upgraded computer, to check computer bandwidth |

**Table 5.10:** Actions taken to develop the 4-webcam network tracking solution.

.

### 5.4.3 C510 single camera solution

Since the 4-webcam network solution (section 5.4.2) failed to provide reliable data for object target tracking, a single camera network was investigated, based on the successes of other studies reported (section 2.10.2). For this, work was carried out in two parts. Firstly, it was necessary to confirm that it was possible to get a webcam to reliably detect the TP (Figure 5.5) coded targets (section 5.4.3.1) while operating the webcam in video capture mode. Secondly, the tracking of the TP moving along the ObT conveyor belt in Unit A was tested (section 5.4.3.2). This work was carried out using SCT (section 5.2.1.2) software developed for such works.

With the use of a single camera, the position and orientation (6DOF) between two rigid objects can be determined by resection, if both are observed in the same FOV. Given that the ObT targets were used to define the ObT coordinate system (section 5.3.1), tests were made to determine the TP's 6DOF with respect to the former. The ObT targets were set as control points and, thus, consist the *reference*, while the TP consists the *tracked target*.

Having already calibrated the webcams (section 5.4.2.1), one of the Logitech C510 webcams was employed for this purpose. The webcam was fixed at a central position above Unit A, making sure all necessary ObT targets were in its FOV (Figure 5.13).

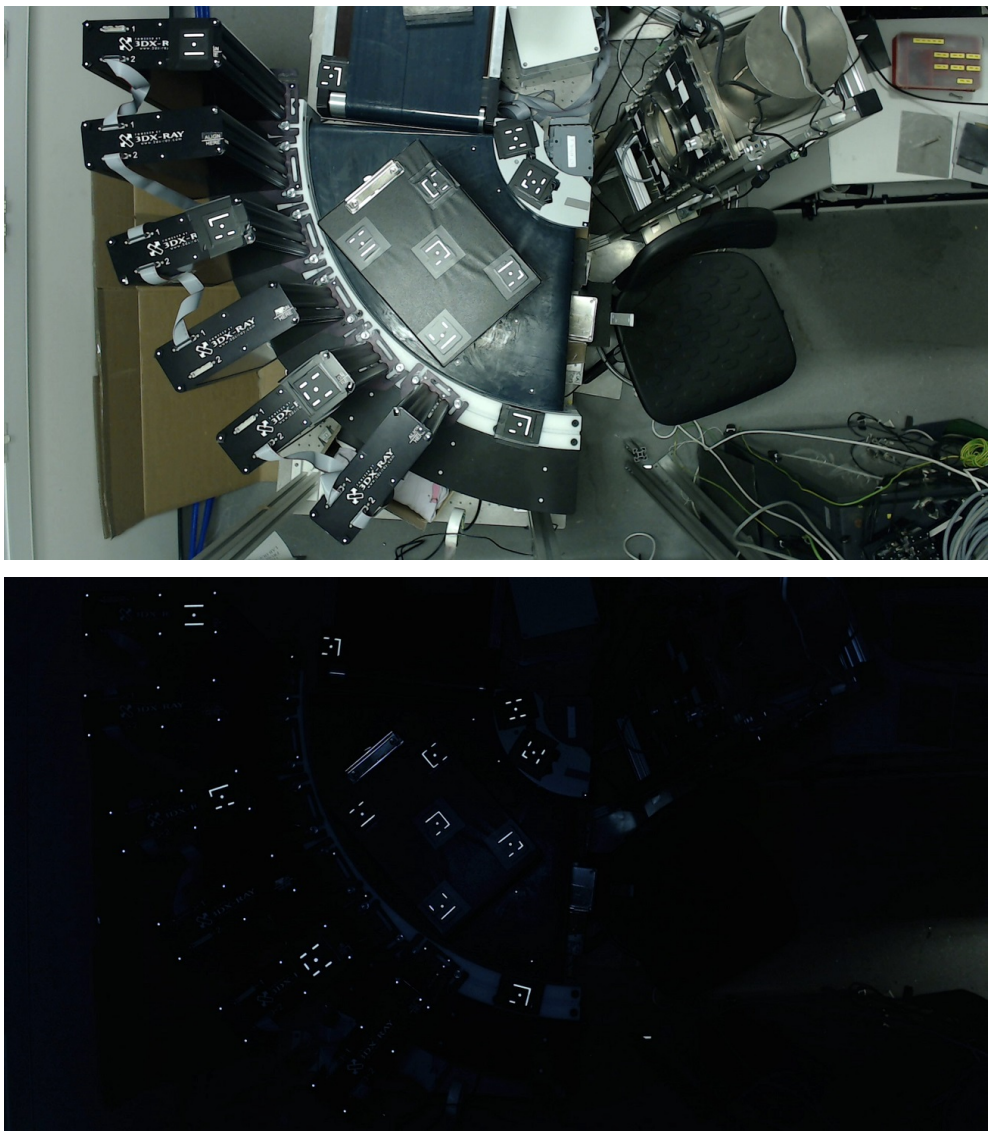

**Figure 5.13:** Image caption using Webcam 4 having placed it above Unit A, in a suitable position for developing a single camera tracking solution: (above) using room lighting, (below) using a ring LED light placed around the webcam.

#### 5.4.3.1 Detecting coded targets

The scope of the first part, was to check that consistent recognition of the TP, set as the tracking target, could be made. This was checked using the webcam in video capture mode, as this would be a necessity for the later live tracking of the TP in motion. Using the C510, a single image caption as well as a short video were acquired of the TP, static at each position: Start, Middle, End (Figure 5.6). For this, the output VMS target file from BA:3b (section 5.3.1) was used, overwriting the 5 TP coordinate points with the respective coordinates measured in section 5.3.2. This was done three time, producing two new reference target files for each of the three positions from the respective BA output files (*BA:S, BA:M, BA:E*). Additionally, the respective VMS resections gave the starting photo values, for SCT.

The VMS resection performed gave an output RMS of 1 $\mu m$ (0.001 mm).

The individual target residuals are shown as yellow line vectors in Figure 5.14. Establishing that the consistent recognition of the still TP targets was possible using SCT, the next step was to test the tracking of the TP trajectory, as it traveled in the ObT (section 5.4.3.2).

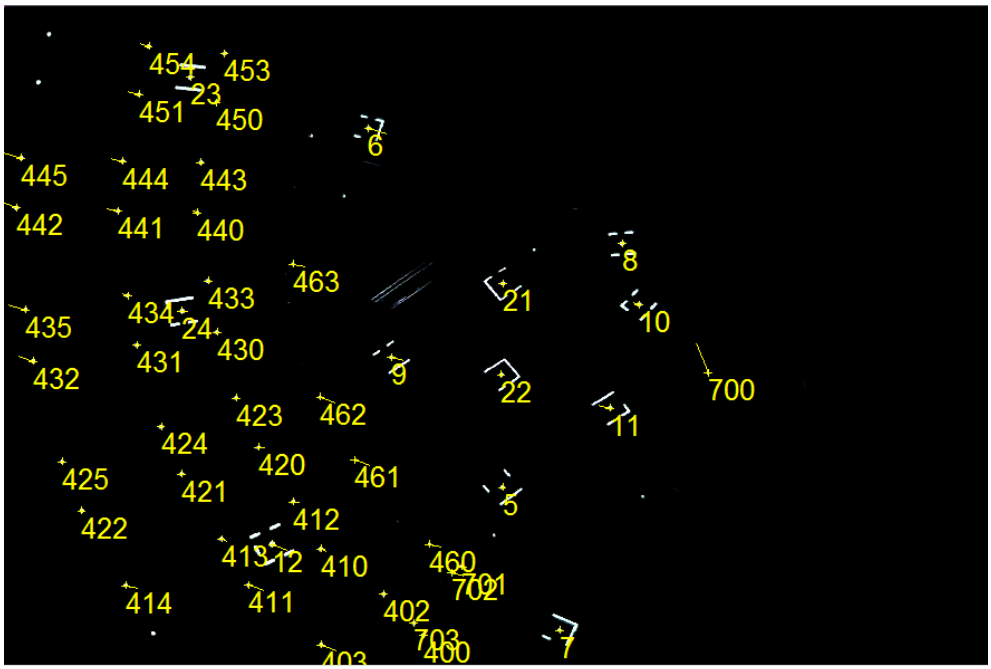


**Figure 5.14:** Screenshot caption of a still image acquired with Logitech C510, prcessed in VMS, showing the target residuals as yellow line vectors.

### 5.4.3.2 Tracking test piece trajectory with C510

The 6DOF tracking was implemented to determine the six transformation parameters forming the 6DOF of the tracked target with respect to the reference. This was a part of a wider test set carried out using SCT by its developers, Profs M. R. Shortis and S. Robson. The calculation of the transformation parameters was based on the pose of the camera derived from measured image coordinates of the targets of the reference and the TP. The interior orientation parameters were known from the prior webcam calibration (section 5.4.2.1). Having a system of two known objects (the TP and the ObT targets), SCT was able to retrieve their relative sequential 6DOF information automatically, through resection (section 2.8.3).

Similarly to section 5.4.3.1, the same target and photo files were used as inputs for the SCT. Since, in this part, the aim was to track the relative 6DOF between the tracked target and reference, using either one of the TP photogrammetric adjustment outputs for the coordinate starting values produced 6DOF results in an arbitrary coordinate datum in each case. In this case, the outputs from BA:S (section 5.3.2) was used.

The initial tracking tests showed problems in the method. Using the same conveyor belt parameters used in ObT imaging (Table 4.2 on page 107), SCT

was run thrice while the TP was traveling backwards and forwards in the ObT. 4 captions of a forward motion video sequence are shown in Figure 5.15.

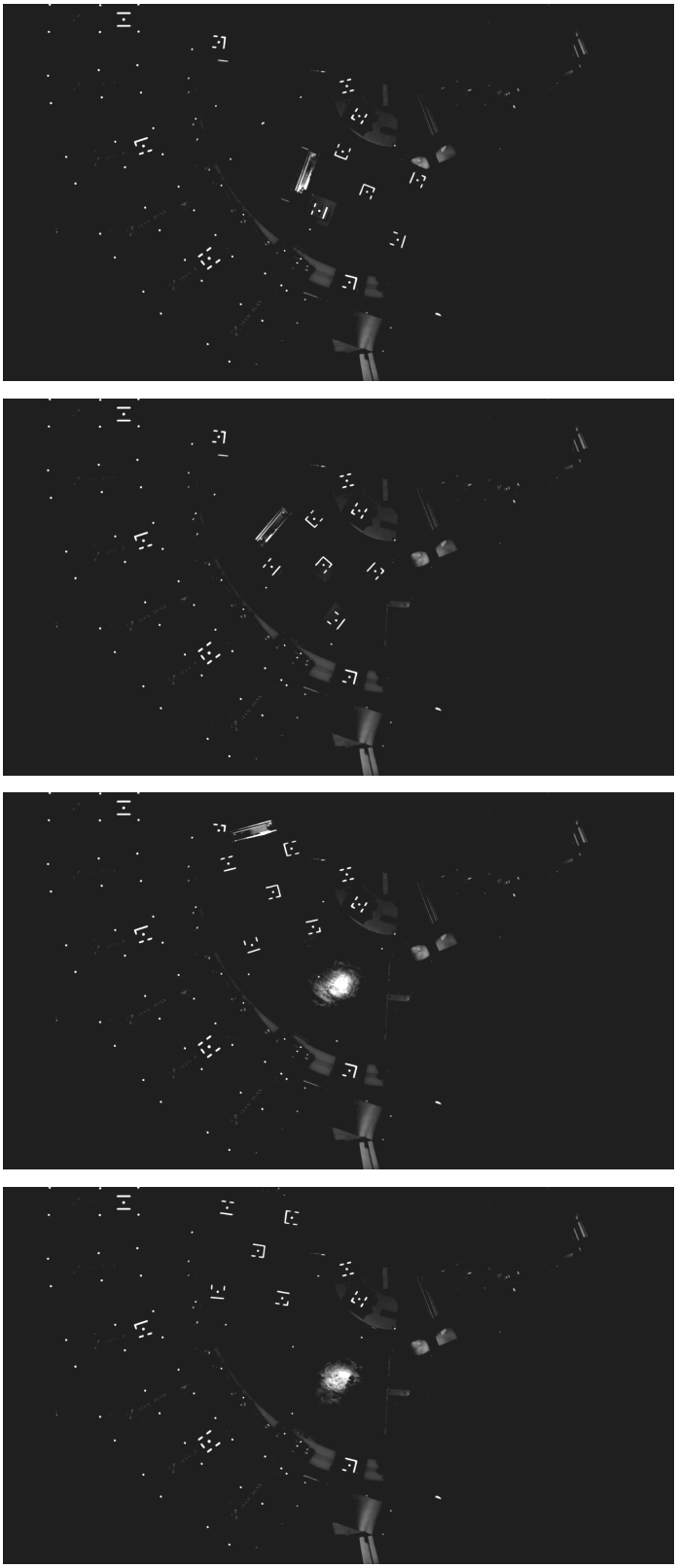

**Figure 5.15:** 4 captions of a video, recorded using the C510, of the TP traveling in the ObT Unit A, in forward motion.

The 3 consecutive data acquisitions of the TP trajectory, named A1, A2, A3, are shown in Figure 5.16. Since, only the conveyor belt controls were used in

controlling the TP motion, each of the three trajectories should in principal overlap. Although as is noted in th Figure, A1-A3 show a similar general trajectory, there are two points to be made regarding the insufficient quality of the data. First, approximately 10-30% of the data set points are outliers, and second, the three trajectories formed by the three sets do not geometrically coincide with each other. The latter was confirmed when checking the output values of the last and first coordinates measured in two consecutive sets. Given, the operational mode followed, the final position of A1, should coincide with the starting position of A2, and similarly between A2 and A3. These coordinates are shown in Table 5.11 where it is confirmed that there is a discrepancy between these values. This check needed to be done, making sure the outliers were not taken into account in the comparison; therefore the coordinate points considered as "first" and "last" are selected logically, disregarding the outlier points. These observed discrepancies were accounted to software faults, and efforts in improving SCT were made jointly with its two developers (Profs. M. R. Shortis and S. Robson), both in addressing this issue and in general improving the quality of the SCT results.

A third point to be made regarding the quality of the data acquisition was that there were several dropped frames (i.e. "Insufficient tracked targets for a 6DOF solution computation", as SCT reported). In these earlier tests, approximately 10-20% of the attempted computations failed to give a 6DOF solution. This could have been caused by unidentified coded targets. Aside the software improvement efforts, in order to address the latter point, as well as the first point made (regarding the observed outliers), a number of measures were taken.

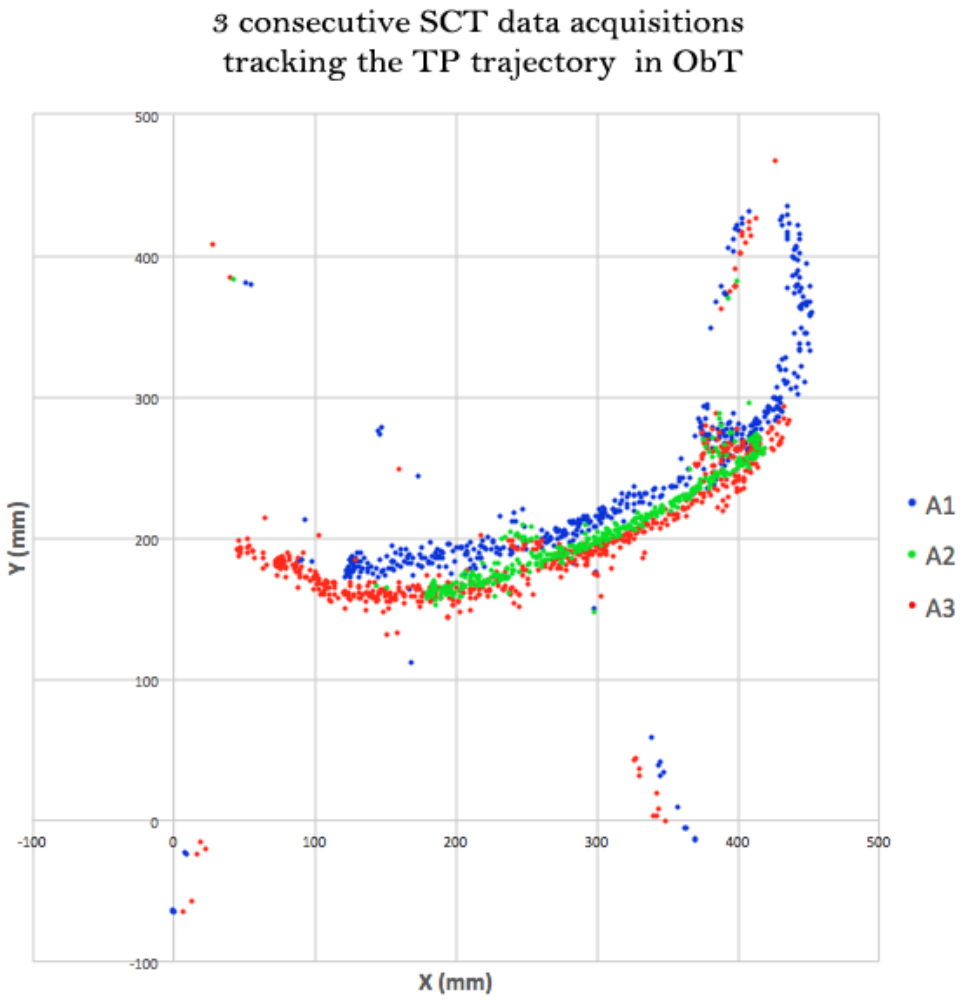


**Figure 5.16:** Initial comparison between three consecutive SCT data acquisitions tracking the TP trajectory in the ObT (A1-A3).

| Coordinate | X(mm) | Y(mm) |
|---|---|---|
| **"last" A1** | 121.8 | 172.7 |
| **"first" A2** | 179.9 | 157.6 |
| **"last" A2** | 419.1 | 263.2 |
| **"first" A3** | 436.4 | 283.8 |

**Table 5.11:** Coordinate outputs of consecutive data sets which should match, show discrepancy between acquisition sets using the C510.

As the majority of the outliers were observed to be grouped in specific areas in the graph (Figure 5.16), it could have been likely that light glare was predominant in those areas. Moreover, near the edges of the FOV the quality of the calibration drops, which may be an additional reason for the observed effects. Refinements to targets included increasing the dark black background surrounding the coded targets both on the TP and ObT system. Additionally, to improve the consistency of target recognition, a ring LED (light emitting diode) light was mounted around the webcam. This LED ring had a 66 mm outer and 52 mm inner diameter. This ensured that lighting is constant, as opposed to typical room lighting which may flicker, eliminated light glare, and

offers better target versus background contrast. The difference between the two lighting methods is shown in Figure 5.13.
Following the laboratory and software developments and refinements, tests were repeated checking the tracking of the TP travelling in the ObT. 3 of these consecutive sets are plotted in Figure 5.17. The data acquisitions showed an improvement of all the aspects previously noted to affect the quality of the results. There were far fewer outliers and dropped frames in each set, a maximum of 1% and 4% respectively of the total attempted computations. In addition, sowftare developments, corrected the geometric displacement discrepancies, as can be seen both in the plots of Figure 5.17 and in Table 5.12. The next step taken in an attempt to refine this method further was to employ a newer generation webcam, described in section 5.4.4.

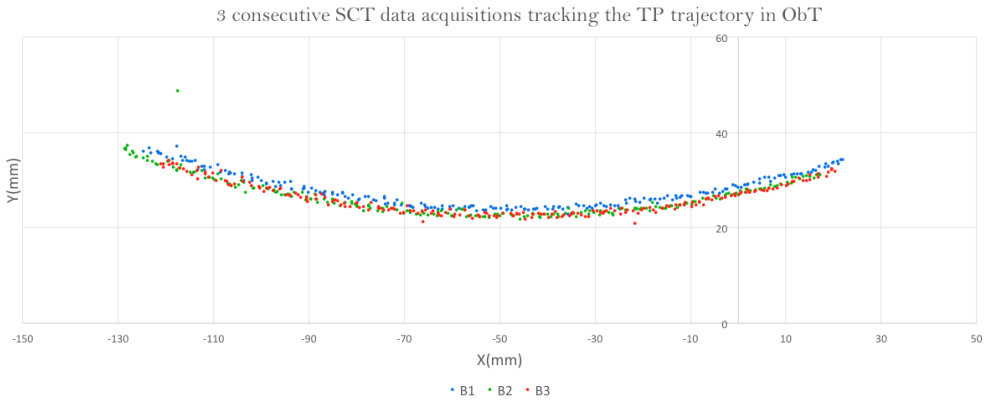


**Figure 5.17:** Comparison between 3 consecutive SCT data acquisitions tracking the TP trajectory in the ObT (B1-B3).

| Coordinate | X(mm) | Y(mm) |
|---|---|---|
| **"last" B1** | -123.6 | 36.8 |
| **"first" B2** | -120.5 | 33.4 |
| **"last" B2** | 20.3 | 31.9 |
| **"first" B3** | 17.2 | 31.1 |

**Table 5.12:** Coordinate outputs of consecutive data sets which should match, show better correlation between acquisition sets using the C920 in relation to the C510.

### 5.4.4 C920 single camera solution

Following the single camera solution developments using the Logitech C510 webcam, the newer generation Logitech C920 webcam (refered to as *the C920*) was employed in an attempt to further refine the quality of the solution. The settings fixed for the operation of the C920 webcam are shown in Figure 5.18.


**Figure 5.18:** Logitech Webcam Software settings, at which the C920 webcam was operated at.

Having performed the possible practical refinements and made improvements in the SCT (section 5.2.1.2) software used (as described in section 5.4.3.2), the webcam upgrade decision was based on the scope of addressing the persistent outliers and dropped frames, which were not totally eliminated. The C920 has a better camera chip than the C510, and also incorporates manual lens focus [Logitech, 2015]. In addition to the new hardware, the Logitech software drivers were also upgraded.

The process of investigating the employment of the C920 as a single camera solution followed the same two basic parts as the earlier work with the C510 (section 5.4.3). Initially, the C920 was calibrated, the process and results of which are presented in section 5.4.4.1. Having retrieved sufficient calibration results, the consistent recognition of the TP in static mode was established. Following that, the tracking of the TP trajectory, as it traveled in the ObT, was tested and results were analysed and compared to the equivalent results using the C510 are presented in section 5.4.3.2. This tracking testing work is presented in section 5.4.4.2.

#### 5.4.4.1 Logitech C920 webcam calibration

The calibration procedure for the C920 was the same as that carried out for the C510 in section 5.4.2.1, except that instead of a calibration object, the TP was placed in the FOV, centrally in Unit A as can be seen in Figure 5.19. Also, instead of rotating the TP, the C920 was moved around Unit A, capturing 14 different images with the same logic of maximum target coverage and image view convergence. The output target file from BA:3b (section 5.3.1) were used as starting values for this VMS project calibrating the C920, with flags of '7' (corresponding to Table 5.2), while the TP targets were given a flag of '0' (since they had not been included in BA:3b). The VMS project BA output showed good calibration results with an RMS image residual of 0.4 mm.


**Figure 5.19:** Screenshot of VMS project executed to calibrate the Logitech 920 webcam. Figure is rotated by 90° clockwise for better visualisation.

The estimated calibration parameters are shown in Table 5.13, for two calibrations (A and B) which were performed with a time distance of 6 months. The comparison of these two re-confirms earlier findings (related to the C510) that the C920 webcam calibration is sufficiently stable for a period of at least 6 months, with a maximum calibration parameter value change of 1%. The first calibration (Calibration A) results are highlighted in Table 5.14.

| **Parameter** | **Calibration** | | **Value % Change** |
|---|---|---|---|
| **#** | **A** | **B** | **A-B** |
| **1** | 0.103 | 0.102 | 0.97 |
| **2** | 0.03 | 0.03 | 0.00 |
| **3** | 3.775 | 3.767 | 0.21 |
| **4** | 7.25E-03 | 7.20E-03 | 0.72 |
| **5** | -8.74E-04 | -8.70E-04 | 0.41 |
| **6** | 5.12E-06 | 5.11E-06 | 0.20 |
| **7** | -1.73E-04 | -1.74E-04 | 0.69 |
| **8** | -1.70E-04 | -1.71E-04 | 0.42 |
| **9** | 5.74E-05 | 5.71E-05 | 0.46 |
| **10** | 1.12E-03 | 1.11E-03 | 0.78 |
| | | **Average** | 0.49 |
| | | **Maximum** | 0.97 |

**Table 5.13:** Two consecutive calibrations (A,B) of the Logitech C920 webcam, with a time difference of 6 months, shows that the webcam calibration is sufficiently stable for that period, with a maximum parameter value change of 1%.

| **Results for Calibration A Solution (interior orientation parameters)** | |
|---|---|
| **Logitech C920 webcam** | |
| **Computed Network Adjustment** | |
| unit weight estimate (sigma zero) | 1.00 |
| RMS image residual (mm) | 0.44 |
| number of images in the network | 15 |
| number of rejected target images | 9 |
| number of observable in the network | 930 |
| number of unknowns in the network | 220 |
| number of redundancies in the network | 710 |
| **Target Precision Summary** | |
| mean precision of target coordinates ($\mu m$) | 25 |
| relative precision for the network | 1:51000 |

**Table 5.14:** Calibration solution results of the Logitech C920 webcam.

The radial and tangential lens distortion results included in the two calibration BA results of Calibration A and B are plotted in Figure 5.20. These show a similar trend between the two calibrations with very similar values, of a maximum difference in magnitude of the order of 0.7 $\mu m$ and 0.3 $\mu m$ in radial and tangential distortion respectively.

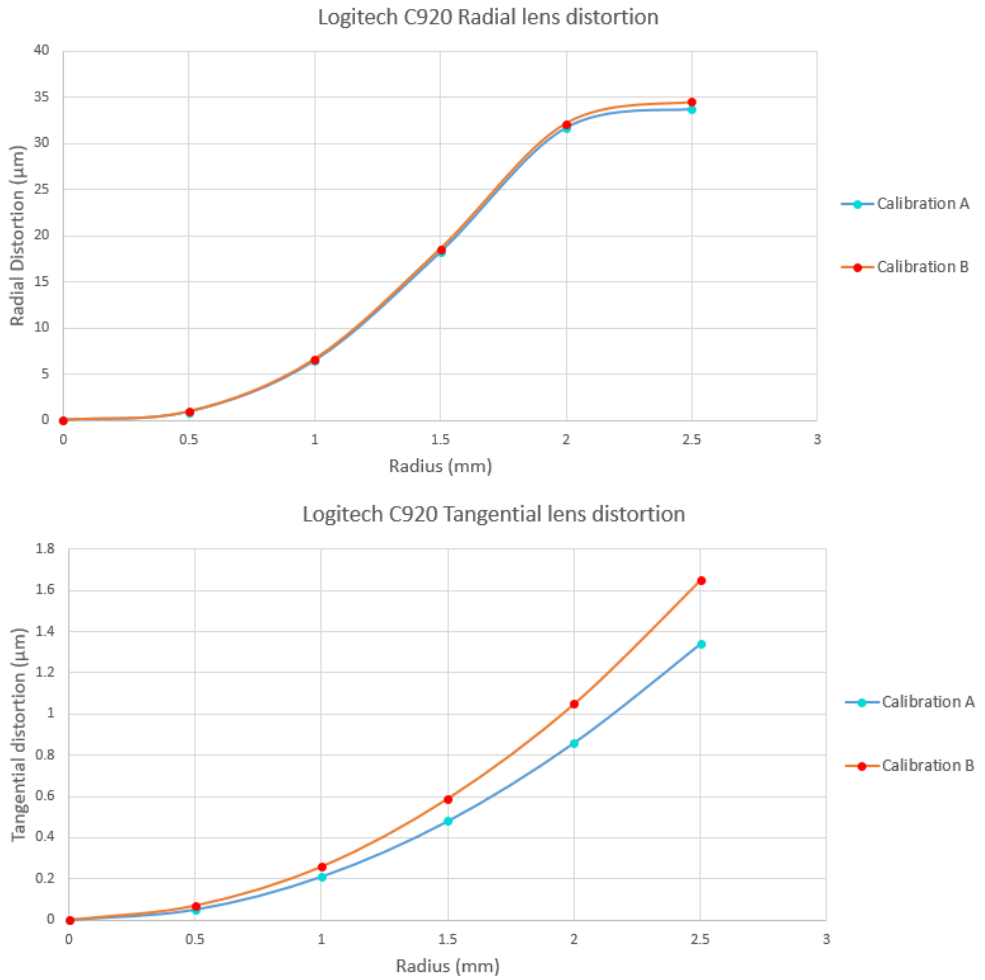


**Figure 5.20:** Radial (above) and tangential (below) lens distortion of the Logitech C920 webcam, measured in VMS.

#### 5.4.4.2 Tracking test piece trajectory with C920

The tracking solution using the C920 was carried out in the same way as was done using the C510 in section 5.4.3.2. Data was collected from running SCT many times while tracking the TP in Unit A of the ObT. Examples of 4 consecutive such acquisition are plotted in Figure 5.21. The results showed no outlier points or dropped frames, an improvement to the work carried out using the C510. Additionally, the quality of the results is confirmed as the computed 6DOF data among consecutive sets are very similar, as visually observed when plotted (Figure 5.21). Checking a few examples of coordinate values, more specifically the last and first value of each consecutive set, this is further confirmed. Table 5.15 shows that each set of coordinate values agrees with a maximum difference of 0.5mm. Therefore, results collected using the C920 were the ones carried forward to be compared with the previous manual measurements of chapter 4, which are required for the x-ray image reconstruction.

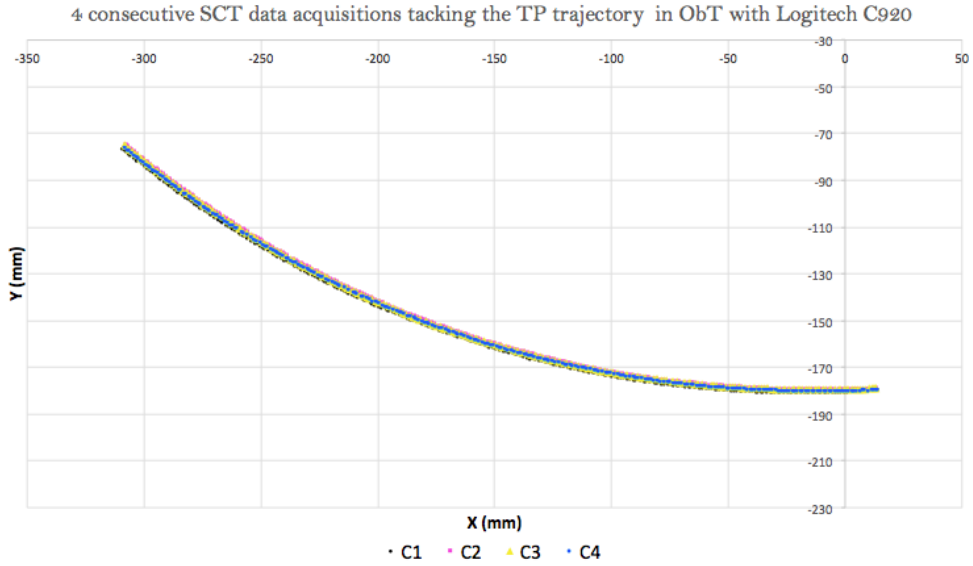


**Figure 5.21:** Comparison between 4 consecutive SCT data acquisitions (C1-C4) tracking the TP trajectory in the ObT using the Logitech C920 .

| Coordinate | X(mm) | Y(mm) | Coordinate | X(mm) | Y(mm) |
|---|---|---|---|---|---|
| **first C1** | -307.9 | -76.9 | **last C1** | 13.4 | -179.3 |
| **last C2** | -308.1 | -76.5 | **first C2** | 13.1 | -178.9 |
| **first C3** | -307.8 | -76.8 | **last C3** | 13.3 | -179.2 |
| **last C4** | -308.1 | -76.4 | **first C4** | 13.1 | -179.0 |
| **Max differences (mm)** | 0.2 | 0.5 | | 0.3 | 0.4 |

**Table 5.15:** Table of the first and last coordinate values of 4 consecutive data acquisition sets, tracking the TP traveling the same trajectory in ObT. Since each consecutive set had the reserve motion direction the first and last value are taken accordingly for each set.

### 5.4.5 Single camera tracking solution analysis

As is evident in Figure 5.21, the single camera tracking solution employing the Logitech C920 produces good quality results. Using the C920 in SCT to track the TP traveling in Unit A, results show that tracking could be performed consistently (no outliers or dropped frames) and with good precision. The later is evident through the comparison of consecutive data sets of the TP traveling identical paths with coordinate discrepancies of maximum 0.5 mm between equivalent points.

Performing a check on the coordination results of the ObT targets, the resulting standard deviation value of 0 (Table 5.5) defined the capability to successfully coordinate points within the ObT space.

The calibration of the webcams showed good quality results, with an RMS less than 0.5 mm for both both C510 and C920 photogrammetric network adjustments. In addition, the measured calibration parameters proved stable of the order of 1-3% for a period o 6-17 months for these Logitech webcams.

The quality of the photogrammetric computations for each webcam can additionally be seen by comparing the same target recognition, in images taken in the same environment and parameters. Taking a single image caption with each webcam and computing a VMS resection, this check can be made by closely observing corresponding targets between the two webcam images. Figure 5.22 shows two sets of targets with their respective residuals, where, through visual inspection, it is obvious that while the target recognition quality for both the C510 and C920 is good, the latter is the best of the two. Clearly C920 has better quality targets because they are larger, indicating a higher resolution sensor, and have better modulated grey levels, which results in a higher computed precision of the centroid.

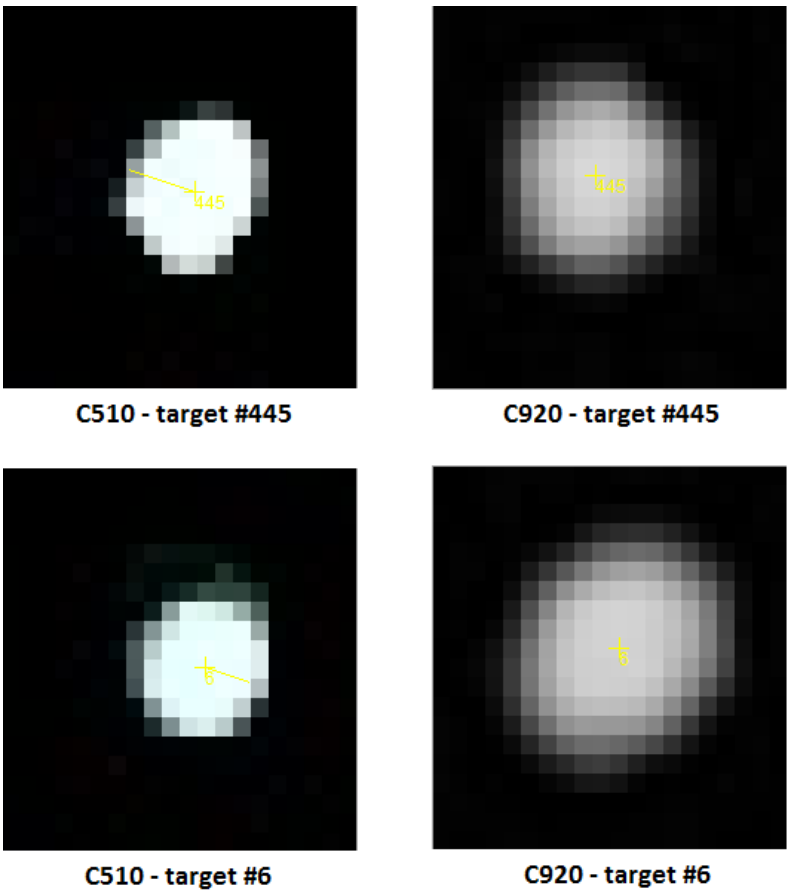


**Figure 5.22:** Target recognition comparison between the C510 and C920 showing two of the targets and their residuals (yellow vector line) measured in VMS.

In addition, 'Shapes' [Fryer et al., 1992] was used to compute 3D circle fits of the tracking data collected with each webcam, using SCT. The radial residual outputs for two sample data sets are plotted in Figure 5.23. Both webcams show good quality results, with residuals smaller than 0.5 mm, while the C920 proves better than the C510 overall. Among the two webcams, a similar trend is seen in the residuals' magnitude, which could suggest the existence of a systematic error in the method.

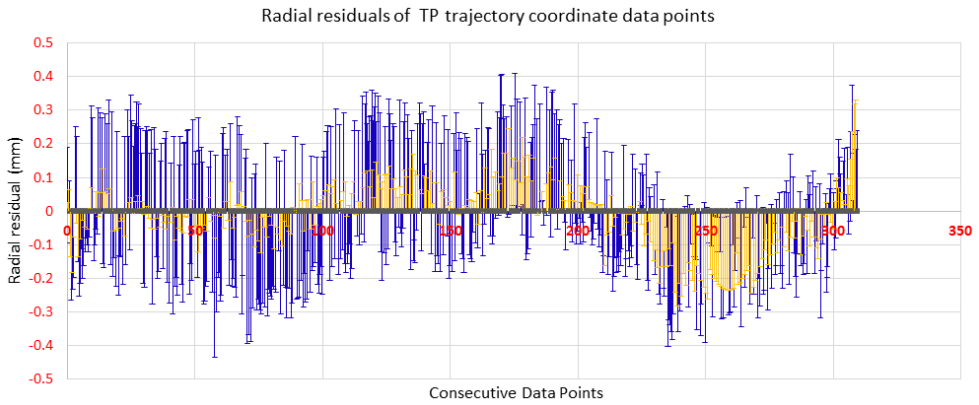


**Figure 5.23:** Radial residuals of consecutive data sets collected using SCT with C510 (blue lines) and C920 (yellow lines). While the former shows higher residual values, both webcams show a similar trend in the residual magnitude oscillation.

Having established that the C920 produces better targeting and tracking results than the C510, and having confirmed its consistent imaging capabilities and geometry, it was chosen as the preferred method to be implemented as the single camera solution in ObT. Importantly, the C920 demonstrated quality results better than the order of magnitude initially required by the ObT, given its developmental stage, as shown in section 4.4.6.

Last, the action taken to develop the 4-webcam network tracking solution (Table 5.10), as well as the system refinements which evidently produced better results (target contrast, room lighting, etc) should be noted for further studies.

## 5.5 Implementing single camera solution results to ObT

The results obtained by the developed single camera solution method demonstrated that the necessary prerequisites for the ObT image reconstruction, described in Table 4.3, could be addressed.

Using the C920 could prove a low cost solution for the necessary automated way of registering the objects of interest in the ObT and eliminate the former assumptions made. In order to check this implementation, the required variable inputs needed to be measured with the C920 and compared to the manual measurements, which are taken as ground truth. This was done for (a) the source FS coordinates, and (b) the detector angles of the systems in Unit A. This corresponded to one of the two sources and 6 of the 12 detectors. Having computed these values from the photogrammetric results, they were compared to the average respective values measured manually. These comparisons are shown in Table 5.16 for the FS coordinates and in Table 5.17 for the detector angles. To distinguish the two methods, A represents the average measurement computed manually in each case, and B represents the

photogrammetrically computed measurement. The resulting standard deviation was an average of 0.4 mm and 1° degree for (a) and (b) respectively.

These findings were used to check the effect of these discrepancies in image reconstructions of ObT. For this, maximum errors were introduced in sample data sets by randomly altering the input values by plus or minus the maximum standard deviation of the two variable inputs: (a) source FS coordinates, and (b) detector angles (section 4.4.4.1). This check was performed on both the real and simulated data reconstructions.

Discrepancies between these two sets of values were insignificant, as they show no differences with respect to the manual measurements in the results of the image reconstructions, both for real and simulated data. This is visualised in Figures 5.24 and 5.25, where image reconstructions, using variable inputs measured manually (set A) and photogrammetrically (set B), show no difference in the results for real and simulated data respectively.

| | | **Coordinate measurement (mm)** | | |
|---|---|---|---|---|
| **Source:** | **S1** | **A** | **B** | $\sigma$ |
| **Coordinates:** | | 228.5 | 229.0 | 0.4 |
| | | -22.3 | -22.1 | 0.2 |
| | | 96.2 | 97.3 | 0.8 |
| | | | **Average $\sigma$** | **0.4** |

**Table 5.16:** Comparison of manually (A) versus photogrammetrically (B) computed values for the first source coordinates show an average standard deviation of 0.4 mm.

| **Detector** | **Angle measurement (degrees)** | | |
|---|---|---|---|
| **#** | **A** | **B** | $\sigma$ |
| **1** | 22.7 | 20.6 | 1.5 |
| **2** | 35.2 | 33.5 | 1.2 |
| **3** | 46.8 | 45.9 | 0.6 |
| **4** | 59.7 | 58.4 | 0.9 |
| **5** | 72.6 | 71.5 | 0.8 |
| **6** | 84.8 | 83.5 | 0.9 |
| | | **Average $\sigma$** | **1.0** |

**Table 5.17:** Comparison of manually (A) versus photogrammetrically (B) computed values for the detector angles shows an average standard deviation of 1°.

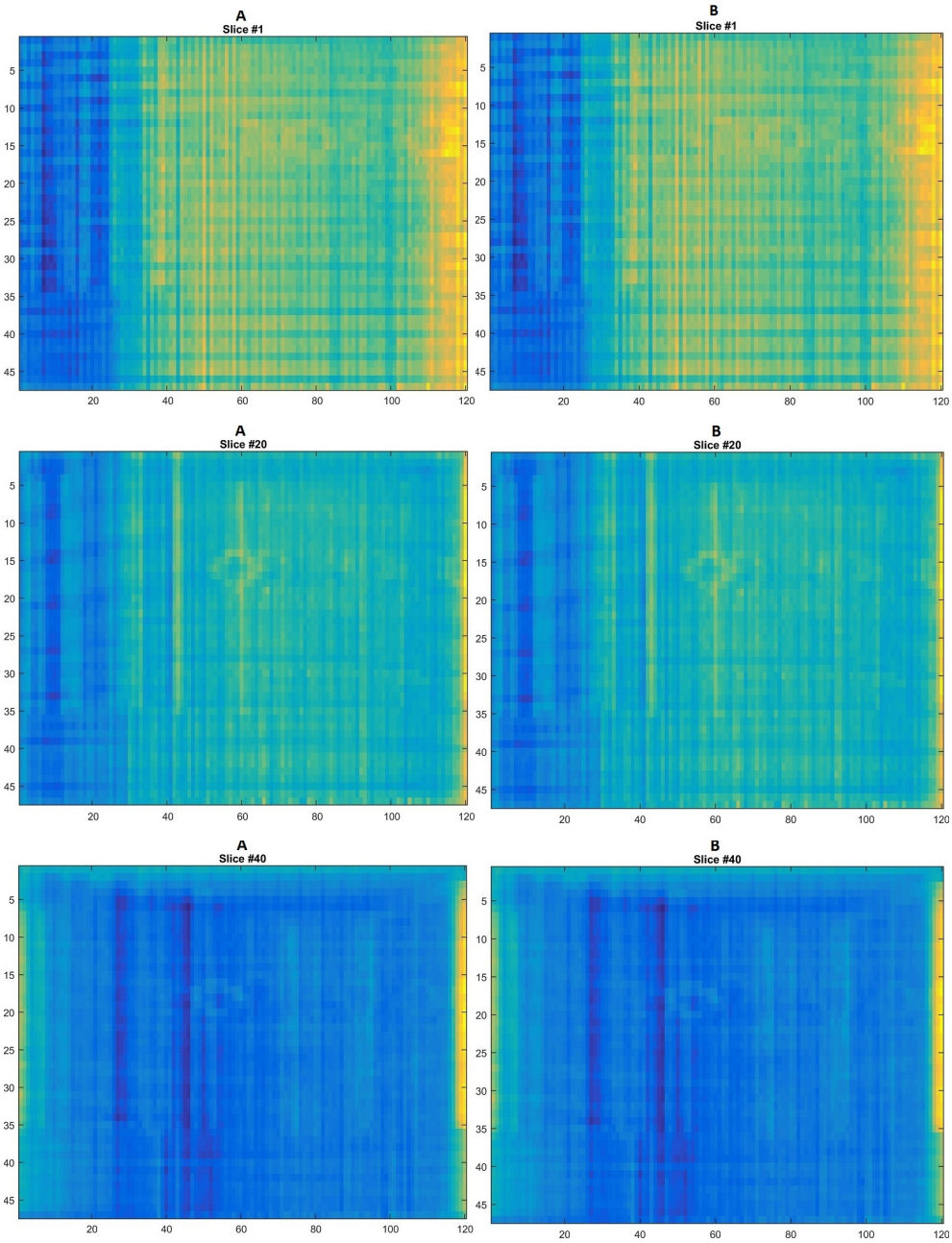


**Figure 5.24:** Image reconstructions of real data using variable inputs measured manually (set A) and photogrammetrically (set B) show no difference in the results among the two upon visual inspection.

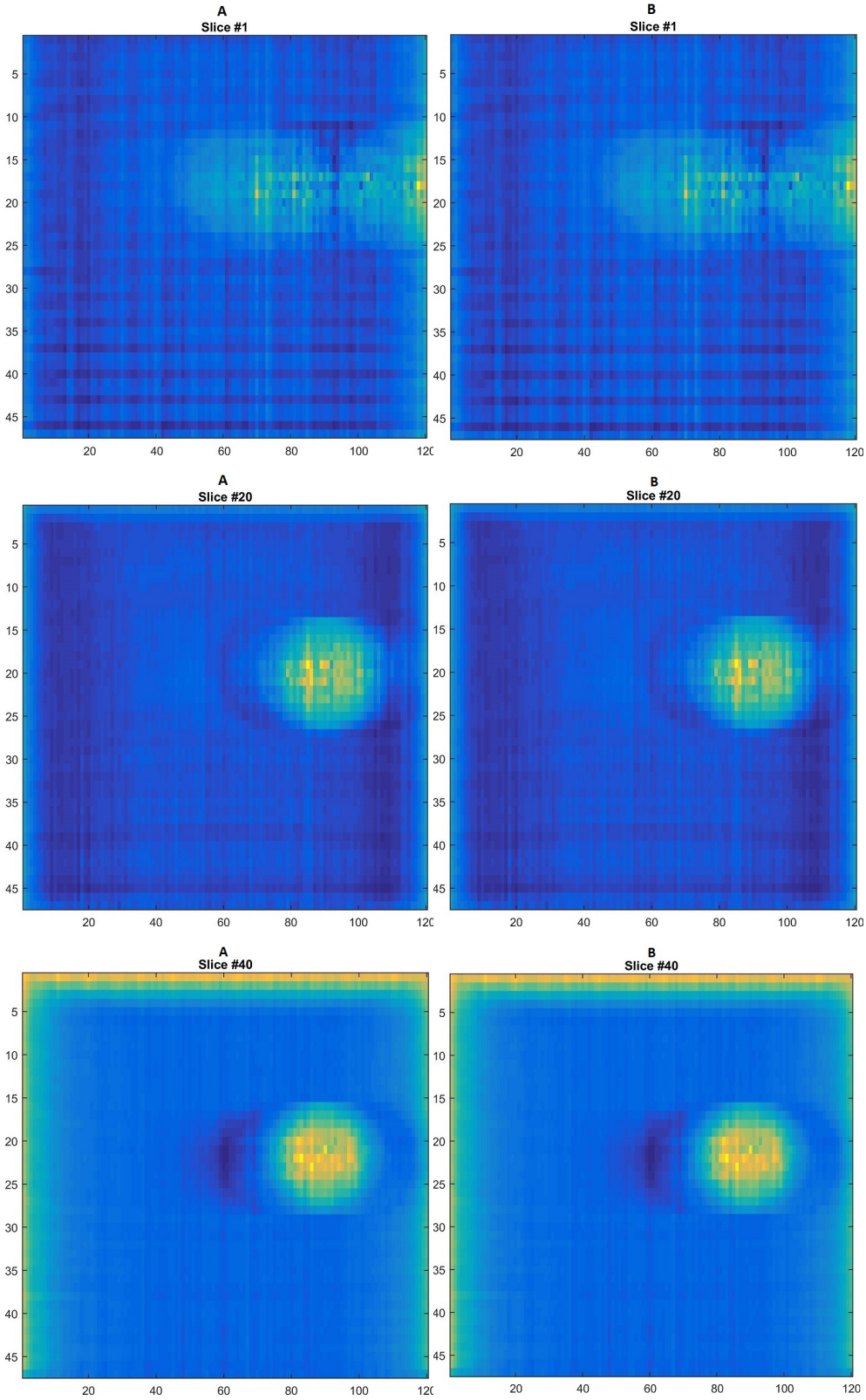


**Figure 5.25:** Image reconstructions of simulated data using variable inputs measured manually (set A) and photogrammetrically (set B) show no difference in the results among the two upon visual inspection.

## 5.6 Chapter conclusions

This chapter describes the experimental work of a photogrammetric coordination and tracking solution developed to replace manual measurements for

the On-belt Tomosynthesis baggage screening system, as described in Chapter 4. This work was carried out in accordance with the key prerequisites of the ObT reconstruction method, described in Table 4.3 (page 110) .

From the work presented in Chapter 4, it was shown that the errors which the ObT system produces during imaging do not affect the image reconstruction results.. Specifically these values were of a standard deviation of $\pm 2$ mm in (a) the source coordinates, and $\pm 2^{\circ}$ in (b) the detector angles. Therefore, the primary aim of this chapter was to develop a low-cost tracking solution of equal or smaller standard deviation values in both (a) and (b).

This photogrammetric method was based on the recognition and tracking of retro-reflective targets using a multi camera solution initially, and later single camera solutions which showed better results. The later was done with two different Logitech webcams the C510 and the C920. The calibration of both webcams showed good quality results, with an RMS less than 0.5 mm for both photogrammetric network adjustments.

Following that, both webcams were tested for object tracking with identical methods and results showed better image quality with the C920. .This model also showed better stability, as its calibration proved to be sufficiently stable for a period of at least 17 months. In addition it was shown that the necessary prerequisites for the ObT image reconstruction could be addressed. Its resulting standard deviation was of an average of 0.4 mm and $1^{\circ}$ degree for (a) the source coordinates and (b) the detector angles respectively. This proved that implementing the C920 as an object tracking solution produced results of sufficient quality within the scope of this study.

# Chapter 6

# Summary & Future potential

## 6.1 Chapter overview

This chapter scopes to bring the findings of this study together, highlighting all the key results and demonstrating this study's significance. It is the first known study to execute and demonstrate such results. The combined results of chapters 4 and 5 signify the potential of ObT. This final chapter summarises the thesis offering conclusions and suggestions for future work in developing the ObT into a successful baggage screening solution.

## 6.2 Thesis conclusions

As published by the European Commission's 7th RTD Framework Programme, a step-change in aviation is needed in order to accommodate the projected growth of three times more aircraft movements by significantly reducing the time spent in travel-related procedures at airports while maintaining safety [Horizon2020, 2007]. This study addressed some of the issues outlined in that framework programme, by exploring a solution of a new security imaging system for checked-in baggage that will be time and cost-effective. It should be noted that the latter factor, cost-effectiveness, is one of the prime requirements for airport screening systems, and thus for this project (section 1.1). Although other factors that are related to the quality of a system naturally increase analogously with the cost of a system, cost-effectiveness is inversely related. It entails that the cost of a system should be kept low as such so that there is a reasonable balance between system effectiveness and product cost. Therefore, this project's implemented developments have been constrained by this factor, and the quality of results should be judged by also taking this into account.

### Design of On-belt Tomosynthesis

As the focus of this thesis, the testing and evaluation of a cost-effective baggage screening system, was based on limited angle digital x-ray tomosynthesis and close-range photogrammetry. 'On-belt Tomosynthesis' (ObT) is a project designed to overcome the limitations of current systems creating a cost-effective,

pseudo-3D imaging system by combining x-ray and optical imaging to form digital tomograms. The system is designed to be retrofitted to existing airport conveyor belt systems.

The ObT design and set-up consists a configuration of two x-ray sources illuminating 12 strip detectors around a conveyor belt curve forming an 180° arc (Figure 3.13 on page 72). Investigating the acquired x-ray images' noise sources and distortions in ObT, improvements were demonstrated using developed image correction methods. An increase of 45% in image uniformity was shown as a result, in the post-correction images. The image quality improvement was additionally evident through visual inspection.

Moving on to image reconstruction, the unconventionality and novelty of the ObT system geometry confirmed that it was timely and challenging work. A reconstruction algorithm, designed specifically for the purposes of ObT, was developed by Dr Marta M. Betcke. Results from real and simulated perspex and air block phantoms showed that the former produced significantly lower quality results than those ones which would have been expected, as indicated by the latter. The simulation reconstruction results of low attenuation content phantoms (such as perspex and air) showed the potential of ObT to clearly distinguish between the two materials.

Since real data reconstructions failed to produce significant results for these, a higher attenuating material, copper, was included in the imaged phantom. The reconstruction results showed that objects of bigger attenuation differences (copper versus perspex, rather than air versus perspex) could be observed. However, the quality of the results still remained low due to the effect of backprojection, which manifested itself as streaking artifacts on the reconstructed images.

The main conclusion from the reconstruction results was that the current imaging method needed further refinements, regarding the geometry registration and the image reconstruction. The simulation results confirmed that advancing the experimental method could produce better results than those currently achieved.

**Implementation of a low cost tracking solution**

In its current form, the errors which the ObT system produces during imaging are of a standard deviation of $\pm 2$ mm in (a) the source coordinates, and $\pm 2°$ in (b) the detector angles, which were shown to not affect the image reconstruction results. Therefore, a low-cost single camera coordination and tracking solution was developed to replace the previously used manual measurements. This photogrammetric method was based on the recognition and tracking of retro-reflective targets. A number of different cameras were tested leading to

single webcam methods being chosen to be further developed. This work was done with two different Logitech webcams the C510 and the C920. First, the quality of results, using the webcams to register target points and to coordinate reference systems, was explored. The calibration of both C510 and C920 webcams showed good quality results, with an RMS less than 0.5 mm in their respective photogrammetric network adjustments. In addition, the measured calibration parameters proved stable of the order of 1-3% for a period of 6-17 months for these Logitech webcams. Performing a check on the coordination results of the ObT targets, the resulting standard deviation value of 0 (Table 5.5 on page 145) defined the capability to successfully coordinate points within the ObT space.

The tracking method was carried out using SCT software which was being developed in conjunction with the progression of this project, jointly with Profs Mark R. Shortis and Stuart Robson. While the tracking method was the same for both, results showed improved image quality with the C920. Results obtained by the developed solution showed that the necessary prerequisites for the ObT image reconstruction could be addressed. The resulting standard deviation was of an average of 0.4 mm and 1° degree for (a) and (b) respectively.

More specifically, using the C920 in SCT to track the TP traveling in ObT, results showed that tracking could be performed consistently (no outliers or dropped frames) and with good precision. The later was evident through the comparison of consecutive data sets of the TP traveling identical paths with coordinate discrepancies of maximum 0.5 mm between equivalent points.

The actions taken to develop the 4-webcam network tracking solution, described in Table 5.10 (page 157), as well as the system refinements which evidently produced better results (target contrast, room lighting, etc) should be noted for following studies.

### Study potential

This study's significant potential has been demonstrated by the results presented throughout the thesis, and summarised above. The ObT system designed and developed constitutes a platform for an automated cost-effective product. Close consideration of the most important and promising future work suggestions are given in section 6.3.

## 6.3 Future work suggestions

With the final goal being to make the ObT system a viable cost-effective baggage screening system solution, there are some important aspects to be addressed. These are related to the current state of the ObT development

and directed by the outcomes of this project and the end-user requirements. These are categorised and highlighted below.

**Image reconstruction code**

Further developments of the image reconstruction code and/or testing the implementation of alternative algorithms could be explored with the scope of producing better quality image reconstructions. For this, more advanced and representative phantom objects could be manufactured and tested in the imaging system.

**Image registration**

The development of the photogrammetric single webcam coordination and tracking solution could be refined and adapted to fit the purposes of ObT imaging. For example, incorporating non-contact detection methods, such as edge detection, to replace the target tracking method, could be a more practical and efficient solution.

The observed systematic errors in SCT output, shown in Figure 5.23 (page 171 ), could be explored further in checking if they were a source of camera/object/belt motion or further investigation. However, the importance of this was not significant to current result requirements.

**Dual energy**

A popular, more advanced approach, for airport screening are dual energy x-ray systems, which are reported to reduce false alarm rates [Eilbert and Krug, 1992, Krug et al., 1994, Singh and Singh, 2003]. Dual energy techniques allow for a more detailed chemical characterisation of object material , using measurements from two distinct x-ray spectra. The x-ray attenuation of each material is energy-dependant and can be reflected by plotting the linear attenuation coefficient versus x-ray energy. As such, by imaging at two (or more) distinguished x-ray beam energies, atomic number and density measurements of scanned objects can be computed, resulting in material discrimination [Engler and Friedman, 1990]. Therefore, the possibility and the benefits of implementing dual energy techniques in ObT could be explored. A further suggestion is to make two energy-discreet images of baggage by screening it at two different conveyor belt bends, for example by placing two ObT systems, and combining the collected data.

**Ease of use & practicality**

The ObT solution scoped for, needs to be as autonomous and automatic as possible. For an ObT system to be incorporated into an airport, aside abiding local authority criteria and conditions, it would need to be user friendly, fast and reliable.

For example, the LabVIEW operational environment could be further developed to incorporate the photogrammetric solution in a common framework. This could further ensure the accurate registration of the objects screened and also offer the facility to combine the system with other sensors. Within this, it would be useful to investigate the effect and control of the baggage orientation, as well as of baggage spacing, based on realistic conditions and application. This would be a relatively easy study to carry out, given existing technological achievements, and its implementation could further advance the quality of the final ObT product.

**Scaling**

The scale and size capabilities of the ObT would need to be enlarged in order to accommodate imaging typical airport baggage items. In addition, it would need to be made to appropriately retrofit on existing airport conveyor belt systems.

**General**

The potential of ObT in applications beyond airport baggage screening could be explored. For example, it could be implemented in product quality control, in production factories, or in mail letter and parcel screening processes.

# List of References


K. Aamdal. Single camera system for close range industrial photogrammetry. *International Archives of Photogrammetry, Remote Sensing and Spatial Information Sciences*, 29:6–6, 1993.

M. Abreu de Souza. *Acquiring accurate head surfaces of newborn infants for optical tomography using digital photogrammetry.* PhD thesis, Ph. D. thesis, Department of Medical Physics and Bioengineering, University College London, England, 2009.

I. Aizenberg and C. Butakoff. A windowed Gaussian notch filter for quasi-periodic noise removal. *Image and Vision Computing*, 26(10):1347–1353, 2008.

Yali Amit. A nonlinear variational problem for image matching. *SIAM Journal on Scientific Computing*, 15(1):207–224, 1994. URL `http://epubs.siam.org/doi/abs/10.1137/0915014`.

M Annis, P Bjorkholm, and D Schafer. Automatic detection of explosives using X-ray imaging. *Access Security Screening Challenges and Solutions*, pages 68–81, 1992.

John Ashburner and K. Friston. Rigid body registration. 2004. URL `http://discovery.ucl.ac.uk/65600/`.

ATAG. Aviation Benefits Beyond Borders, April 2014. URL `http://aviationbenefits.org/media`.

K. B. Atkinson, editor. *Close range photogrammetry and machine vision.* Whittles Publishing, Caithness, Scotland, 2001. ISBN 1-870325-73-7.

Ronald Azuma and Gary Bishop. Improving static and dynamic registration in an optical see-through HMD. In *Proceedings of the 21st annual conference on Computer graphics and interactive techniques*, pages 197–204. ACM, 1994. URL `http://dl.acm.org/citation.cfm?id=192199`.

Ronald Azuma and Gary Bishop. A frequency-domain analysis of head-motion prediction. In *Proceedings of the 22nd annual conference on Computer graphics and interactive techniques*, pages 401–408. ACM, 1995. URL `http://dl.acm.org/citation.cfm?id=218496`.

C Badea, Z Kolitsi, and N Pallikarakis. Image quality in extended arc filtered digital tomosynthesis. *Acta Radiologica*, 42(2):244–248, 2001.

Aaron Bauer, Sophie Vo, Keith Parkins, Francisco Rodriguez, Ozan Cakmakci, and Jannick P. Rolland. Computational optical distortion correction using a radial basis function-based mapping method. *Optics express*, 20(14): 14906–14920, 2012.

Thaddeus Beier and Shawn Neely. Feature-based image metamorphosis. In *ACM SIGGRAPH Computer Graphics*, volume 26, pages 35–42. ACM, 1992. URL `http://dl.acm.org/citation.cfm?id=134003`.

Marta M. Betcke and William R. B. Lionheart. Multi-sheet surface rebinning methods for reconstruction from asymmetrically truncated cone beam projections: II. Axial deconvolution. *Inverse Problems*, 29(11):115004, November 2013. ISSN 0266-5611. doi: 10.1088/0266-5611/29/11/115004. URL `http://iopscience.iop.org/0266-5611/29/11/115004`.

F. Bethmann and T. Luhmann. Monte-Carlo simulation for accuracy assessment of a single camera navigation system. *Int. Archives of Photogrammetry, Remote Sensing and Spatial Information Sciences*, 39:B5, 2012.

Jacob Beutel. *Handbook of Medical Imaging: Medical image processing and analysis*. SPIE Press, January 2000. ISBN 978-0-8194-3622-1.

José M. Bioucas-Dias and Mário AT Figueiredo. A new TwIST: two-step iterative shrinkage/thresholding algorithms for image restoration. *Image Processing, IEEE Transactions on*, 16(12):2992–3004, 2007.

Sarah E. Bohndiek, Andrew Blue, Andy T. Clark, Mark L. Prydderch, Renato Turchetta, Gary J. Royle, and Robert D. Speller. Comparison of methods for estimating the conversion gain of CMOS active pixel sensors. *Sensors Journal, IEEE*, 8(10):1734–1744, 2008.

Lisa Gottesfeld Brown. A survey of image registration techniques. *ACM computing surveys (CSUR)*, 24(4):325–376, 1992. URL `http://dl.acm.org/citation.cfm?id=146374`.

Richard H. Brown, Albert H. Burstein, Clyde L. Nash, and Charles C. Schock. Spinal analysis using a three-dimensional radiographic technique. *Journal of Biomechanics*, 9(6):355–IN1, 1976. ISSN 0021-9290. doi: 10.1016/0021-9290(76)90113-5.

Egbert Buhr, Susanne Guenther-Kohfahl, and Ulrich Neitzel. Simple method for modulation transfer function determination of digital imaging detectors from edge images, 2003.

John F. Burns. Yemen Bomb Could Have Exploded Over U.S. East Coast. *The New York Times*, November 2010. ISSN 0362-4331. URL `http://www.nytimes.com/2010/11/11/world/europe/11parcel.html`.

J. Carr. *The technician's EMI handbook: clues and solutions*. Newnes, 2000.

P. Cerveri, C. Forlani, A. Pedotti, and G. Ferrigno. Hierarchical radial basis function networks and local polynomial un-warping for X-ray image intensifier distortion correction: A comparison with global techniques. *Medical and Biological Engineering and Computing*, 41(2):151–163, 2003. ISSN 0140-0118. doi: 10.1007/BF02344883.

Tianfeng Chai and Roland R. Draxler. Root mean square error (RMSE) or mean absolute error (MAE)?–Arguments against avoiding RMSE in the literature. *Geoscientific Model Development*, 7(3):1247–1250, 2014.

H.P. Chan, Wei J., Sahiner B., Rafferty E. A, M. A. Roubidoux T.Wu, Moore R. H., Kopans D. B., Hadjiiski L.M., and Helvie M.A. Computer-aided detection system for breast masses on digital tomosynthesis mammograms: Preliminary experience. *Radiology*, 237(3):1075–1080, 2005.

H.P. Chan, J. Wei, Y. Zhang, B Sahiner, L.M. Hadsiiski, and M.A. Helvie. Detection of masses in digital breast tomosynthesis mammography: Effects of the number of projection views and dose. *Digital Mammography*, pages 279–285, 2008.

Hyo-Min Cho, William C. Barber, Huanjun Ding, Jan S. Iwanczyk, and Sabee Molloi. Characteristic performance evaluation of a photon counting Si strip detector for low dose spectral breast CT imaging. *Medical Physics*, 41(9): 091903, September 2014. ISSN 0094-2405. doi: 10.1118/1.4892174.

Mark Christiaens, Bjorn De Sutter, Koen De Bosschere, Jan Van Campenhout, and Ignace Lemahieu. A Fast, Cache-Aware Algorithm for the Calculation of Radiological Paths Exploiting Subword Parallelism. In *Journal of Systems Architecture, Special Issue on Parallel Image Processing*, 1998.

A Chutjian and M.R Darrach. Improved portable reversal electron attachment (READ) vapor detection system for explosives detection. pages 176–180, 1996.

T. A. Clarke and J. G. Fryer. The Development of Camera Calibration Methods and Models. *The Photogrammetric Record*, 16(91):51–66, April 1998. ISSN 1477-9730. doi: 10.1111/0031-868X.00113.

Timothy A. Clarke. Analysis of the properties of targets used in digital close-range photogrammetric measurement. In *Photonics for Industrial Applications*, pages 251–262. International Society for Optics and Photonics, 1994.

M. A. R. Cooper. Chapter 5: Principles of least squares estimation. In *Control surveys in civil engineering*, pages 159–193. Collins, 1987.

M. a. R. Cooper and P. A. Cross. Statistical Concepts and Their Application in Photogrammetry and Surveying. *The Photogrammetric Record*, 12(71): 637–663, 1988. ISSN 1477-9730. doi: 10.1111/j.1477-9730.1988.tb00612.x.

M. A. R. Cooper and S. Robson. Chapter 2: Theory of close range photogrammetry. In K. B. Atkinson, editor, *Close Range Photogrammetry and Machine Vision.*, pages 9–51. 1996. ISBN 1 870325 46 X. URL `http://discovery.ucl.ac.uk/39129/`.

Harald Cramér and Ulf Grenander. *Probability and statistics: the Harald Cramér volume.* Almqvist & Wiksell, 1959.

Martin O. Culjat, David Goldenberg, Priyamvada Tewari, and Rahul S. Singh. A Review of Tissue Substitutes for Ultrasound Imaging. *Ultrasound in Medicine & Biology*, 36(6):861–873, June 2010. ISSN 0301-5629. doi: 10.1016/j.ultrasmedbio.2010.02.012.

I. A. Cunningham and A. Fenster. A method for modulation transfer function determination from edge profiles with correction for finite-element differentiation. *Medical physics*, 14(4):533–537, 1987.

I. A. Cunningham and B. K. Reid. Signal and noise in modulation transfer function determinations using the slit, wire, and edge techniques. *Medical physics*, 19(4):1037–1044, 1992.

Ian A. Cunningham. Applied linear-systems theory. *Handbook of medical imaging*, 1:79–159, 2000.

J. C. Dainty. *Image science : principles, analysis and evaluation of photographic-type imaging processes /J.C. Dainty and R. Shaw.* Academic Press, London, 1974. ISBN 0-12-200850-2.

A. Dermanis. Adjustment of observations and Estimation Theory. *Editions Ziti, Greece*, 1986.

Viet D. Dinh. Foreword–Freedom and Security after September 11. *Harv. JL & Pub. Pol'y*, 25:399, 2001.

J. T. Dobbins III and D. J. Godfrey. Physics in Medicine and Biology. 48 (R65), 2003.

James T. Dobbins III. Image quality metrics for digital systems. *Handbook of medical imaging*, 1:161–222, 2000.

Kunio Doi and Kurt Rossmann. Computer simulation of small blood vessel imaging in magnification radiography. *Small Vessel Angiography*, pages 6–12, 1973.

K.W. Dolan, R.W. Ryon, D.J. Schneberk, H.E. Martz, and R.D. Rikard. Explosives detection limitations using dual-energy radiography and computed tomography. pages 252–260, 1991.

C. Dougherty. *Introduction to econometrics.* Oxford University Press, Oxford, 2nd edition, 1992. ISBN 0198776438.

DxOMark. DxOMark: The reference for image quality, 2015. URL `www.dxomark.com/About/In-depth-measurements/`.

Valerie J. Easton and John H. McColl. Statistics Glossary v1. 1. *The Steps Project*, 1997.

ECORYS. Study on the Competitiveness of the EU security industry Within the Framework Contract for Sectoral Competitiveness Studies – ENTR/06/054. Technical report, ECORYS Research and Consulting, Brussels, November 2009. URL `ec.europa.eu`.

R. Eidus, A. Bell, S. Remondi, M. Zee, T. Flodin, J. Vetter, and J. Connor. OmniCare Airport Baggage Tagging System, 2007. URL `http://www.indabook.org/d/Delta-Baggage-Tracking.pdf`.

R.F. Eilbert and K.D. Krug. Aspects of image recognition in vivid technology's dual-energy X-ray system for explosive detection. *SPIE*, 1824:127–143, 1992.

Sabry El-Hakim, Jean-Angelo Beraldin, and François Blais. Critical factors and configurations for practical 3d image-based modeling. 2003.

Philip Engler and William D. Friedman. Review of dual-energy computed tomography techniques. *Materials Evaluation*, 48:623–629, 1990.

EOTECH. EOTECH - 3d Digitisation - Systems - DPA Pro$^{TM}$, 2015. URL `www.eotech-sa.com/3D-Digitisation/Systems`.

D. S. Evans, A. Workman, and M. Payne. A comparison of the imaging properties of CCD-based devices used for small field digital mammography. *Physics in Medicine and Biology*, 47(1):117, January 2002. ISSN 0031-9155. doi: 10.1088/0031-9155/47/1/309. URL `http://iopscience.iop.org/0031-9155/47/1/309`.

R. D. Evans. *The Atomic Nucleus*. McGraw-Hill, New York, 1955. URL `https://archive.org/details/atomicnucleus032805mbp`.

Olivier D. Faugeras and Martial Hebert. The representation, recognition, and locating of 3-D objects. *The international journal of robotics research*, 5(3): 27–52, 1986. URL `http://ijr.sagepub.com/content/5/3/27.short`.

L. A. Feldkamp, L. C. Davis, and J. W. Kress. Practical cone-beam algorithm. *Journal of the Optical Society of America A*, 1(6):612, June 1984. ISSN 1084-7529, 1520-8532. doi: 10.1364/JOSAA.1.000612. URL `http://www.opticsinfobase.org/abstract.cfm?URI=josaa-1-6-612`.

Bernd Fischer and Jan Modersitzki. A unified approach to fast image registration and a new curvature based registration technique. *Linear Algebra and its Applications*, 380:107–124, March 2004. ISSN 0024-3795. doi: 10.1016/j.laa.2003.10.021.

David Flack and John Hannaford. *Fundamental good practice in dimensional metrology.* National Physical Laboratory, 2005.

Thomas G. Flohr, Stefan Schaller, Karl Stierstorfer, Herbert Bruder, Bernd M. Ohnesorge, and U. Joseph Schoepf. Multi–Detector Row CT Systems and Image-Reconstruction Techniques. *Radiology*, 235(3):756–773, June 2005. ISSN 0033-8419. doi: 10.1148/radiol.2353040037. URL `http://pubs.rsna.org/doi/full/10.1148/radiol.2353040037`.

Clive S. Fraser. Photogrammetric Camera Component Calibration: A Review of Analytical Techniques. In Professor Armin Gruen and Professor Thomas S. Huang, editors, *Calibration and Orientation of Cameras in Computer Vision*, pages 95–121. Springer Berlin Heidelberg, 2001. ISBN 978-3-642-08463-8 978-3-662-04567-1.

Fryer. *Close Range Photogrammetry and machine vision. Chapter 6: Camera Calibration.* Whittles, Scotland, 1996.

J. G. Fryer, R. D. Parberry, and S. Robson. Analysis of as-built cylindrical shapes. *Australian Journal of Geodesy, Photogrammetry and Surveying*, 56: 91–109, 1992.

Hiroshi Fujita, Du-Yih Tsai, Takumi Itoh, Junji Morishita, Katsuhiko Ueda, Akiyoshi Ohtsuka, and others. A simple method for determining the modulation transfer function in digital radiography. *Medical Imaging, IEEE Transactions on*, 11(1):34–39, 1992.

Geodetic. The Basics of Photogrammetry © 2015 Geodetic Systems, Inc., 2015. URL `http://www.geodetic.com/v-stars/what-is-photogrammetry.aspx`.

Geodetic. V-STARS™ © 2015 Geodetic Systems, Inc., 2015. URL `http://www.geodetic.com/v-stars.aspx`.

Geomsoft. VMS: Vision Measurement System © Geometric Software P/L 2002-2015. All rights reserved., 2015. URL `http://www.geomsoft.com/VMS`.

Maryellen Lissak Giger and Kunio Doi. Investigation of basic imaging properties in digital radiography. I. Modulation transfer function. *Medical Physics*, 11(3):287–295, 1984.

Mario A. Gomarasca. *Basics of geomatics.* Springer Science & Business Media, 2009.

W.F. Good, G.S. Abrams, V.J. Catullo, D.M. Chough, M.A. Ganott, C.M. Hakim, and D. Gur. Digital breast tomosynthesis: A pilot observer study. *Am. J. Roentgenol.*, 190(4):865–869, 2008.

Stefan Gottschalk and John F. Hughes. Autocalibration for virtual environments tracking hardware. In *Proceedings of the 20th annual conference on*

*Computer graphics and interactive techniques*, pages 65–72. ACM, 1993. URL http://dl.acm.org/citation.cfm?id=166124.

T. Gozani. Principles of nuclear-based explosive detection systems. pages 27–55, 1991.

T. Gozani. Novel applications of fast neutron interrogation methods. *Nuclear Instrumentation Methods A*, (353):635–640, 1994.

S.E. Granshaw. Bundle adjustement methods in Engineering Photogrammetry. *Photogrammetric Record*, 10(56):181–207, 1980.

Peter B. Greer and others. Correction of pixel sensitivity variation and off-axis response for amorphous silicon EPID dosimetry| NOVA. The University of Newcastle's Digital Repository. 2005.

Peter Brian Greer and Timothy Van Doorn. Evaluation of an algorithm for the assessment of the MTF using an edge method. *Medical Physics*, 27(9): 2048–2059, 2000.

L Grodzins. Photons in-photons out: non-destructive inspection of containers using X-ray and gamma ray techniques. pages 201–211, 1991.

Renee R. Ha and James C. Ha. *Integrative statistics for the social and behavioral sciences*. Sage, 2011.

Eldad Haber and Jan Modersitzki. A multilevel method for image registration. *SIAM Journal on Scientific Computing*, 27(5):1594–1607, 2006. URL http://epubs.siam.org/doi/abs/10.1137/040608106.

G. Harding. X-ray scatter tomography for explosives detection. *Radiation Physics and Chemistry*, 71(3):869–881, 2004.

Richard Hartley and Andrew Zisserman. *Multiple view geometry in computer vision*. Cambridge university press, 2003.

M. Haughn and E. Blair. Latency: Definition, 2014. URL http://whatis.techtarget.com/definition/latency.

Heathrow. Baggage handling at Heathrow, 2009.

K. Heinskanen, T. Meyer, D. Pillor, E. Scheinman, S. Wolff, and F. Roder. Illicit drug detection using CTX5000. pages 6–33, 1995.

A. M. Helle, J. Pilinski, and T. Luhmann. Precise head tracking in hearing applications. *International Archives of the Photogrammetry, Remote Sensing & Spatial Information Sciences*, 2015.

William R. Hendee and E. Russell Ritenour. *Medical imaging physics*. John Wiley & Sons, 2003.

G.T. Herman. *Fundamentals of computerized tomography:Image reconstruction from projection*. Springer, 2009.

M. Hess. *A metric test object informed by user requirements for better 3D recording of cultural heritage artefacts*. PhD thesis, UCL University College London, 2015.

Walter Hillen, U. Schiebel, and T. Zaengel. Imaging performance of a digital storage phosphor system. *Medical physics*, 14(5):744–751, 1987.

Horizon2020. Increasing time efficiency (AAT.2), 2007. URL `http://www.2020-horizon.com/Increasing-time-efficiency-t57.html`.

G. A. A. Hudhud and Martin J. Turner. Digital removal of power frequency artifacts using a Fourier space median filter. *Signal Processing Letters, IEEE*, 12(8):573–576, 2005.

D. C. Hunt, O. Tousignant, and J. A. Rowlands. Evaluation of the imaging properties of an amorphous selenium-based flat panel detector for digital fluoroscopy. *Medical physics*, 31(5):1166–1175, 2004. URL `http://europepmc.org/abstract/med/15191306`.

E. M. A. Hussein and E. J. Walker. Review of one-side approaches to radiographic images for the detection of explosives and narcotics. *Radiation Measures*, 29(6):581–591, 1999.

IATA. IATA Annual Review 2013, June 2013.

ICA. Coming of Age, scaling new heights. The ICA journey, 2012.

ICRU. *Medical Imaging: The Assessment of Image Quality*. International commission on radiation units and measurements, 1996.

IEC. Medical electrical equipment - Characteristics of digital x-ray imaging devices–Part 1: Determination of the detective quantum efficiency. International Electrotechnical Commission (IEC). *Geneva, Switzerland*, 62220–1, 2003.

Hartmut Illers, Dirk Vandenbroucke, and Egbert Buhr. Measurement of correlated noise in images of computed radiography systems and its influence on the detective quantum efficiency. In *Medical Imaging 2004*, pages 639–647. International Society for Optics and Photonics, 2004.

ImageJ. ImageJ: an open source image processing program developed by Wayne Rasband at the National Institutes of Health, 2015. URL `www.imagej.net`.

IPEM. Measurement of the Performance Characteristics of Diagnostic X-Ray Systems: Digital imaging systems. Technical Report 32 part VII, 2010.

Øyvind Isaksen. A review of reconstruction techniques for capacitance tomography. *Measurement Science and Technology*, 7(3):325, March 1996. ISSN 0957-0233. doi: 10.1088/0957-0233/7/3/013. URL `http://iopscience.iop.org/0957-0233/7/3/013`.

Takayuki Ishida, Shigehiko Katsuragawa, Katsumi Nakamura, Heber MacMahon, and Kunio Doi. Iterative image warping technique for temporal subtraction of sequential chest radiographs to detect interval change. *Medical physics*, 26(7):1320–1329, 1999.

Filip Jacobs, Erik Sundermann, Bjorn De Sutter, Mark Christiaens, and Ignace Lemahieu. A fast algorithm to calculate the exact radiological path through a pixel or voxel space. *Journal of computing and information technology*, 6(1):89–94, 1998.

T. Y. Ji, Z. Lu, and Q. H. Wu. Optimal soft morphological filter for periodic noise removal using a particle swarm optimiser with passive congregation. *Signal Processing*, 87(11):2799–2809, 2007.

G. W. Johnson, S. E. Laskey, S. Robson, and M. R. Shortis. Dimensional & accuracy control automation in shipbuilding fabrication: an integration of advanced image interpretation, analysis, and visualization techniques. In *Proceedings of Analysis and Visualization Techniques, 20th Congress ISPRS, Istanbul, Turkey*, 2004.

Robert A. Jones. An automated technique for deriving MTFs from edge traces. *Photographic Science and Engineering*, 11(2):102, 1967.

Avinash C. Kak and Malcolm Slaney. *Principles of computerized tomographic imaging*. Society for Industrial and Applied Mathematics, 2001. URL `http://ieeexplore.ieee.org/iel1/36/173/x0440791.pdf`.

Takeo Kanade, Peter Rander, and P. J. Narayanan. Virtualized reality: Constructing virtual worlds from real scenes. *IEEE multimedia*, (1):34–47, 1997. URL `http://www.computer.org/csdl/mags/mu/1997/01/u1034.pdf`.

Akiko Kano, Kunio Doi, Heber MacMahon, Dayne D. Hassell, and Maryellen L. Giger. Digital image subtraction of temporally sequential chest images for detection of interval change. *Medical Physics*, 21(3):453–461, 1994.

H.M. Karara. Non-topographic photogrammetry. *American society for photogrammetry and remote sensing*, 1989.

A. Katsevich. Theoretically Exact Filtered Backprojection-Type Inversion Algorithm for Spiral CT. *SIAM Journal on Applied Mathematics*, 62(6):2012–2026, January 2002. ISSN 0036-1399. doi: 10.1137/S0036139901387186. URL `http://epubs.siam.org/doi/abs/10.1137/S0036139901387186`.

Alexander Katsevich. Image reconstruction for the circle-and-arc trajectory. *Physics in Medicine and Biology*, 50(10):2249, May 2005. ISSN 0031-9155. doi: 10.1088/0031-9155/50/10/005. URL `http://iopscience.iop.org/0031-9155/50/10/005`.

R. Kerner. A New Dimension in Diagnostics. *Medical Design Technology*, August 2013. URL `http://www.mdtmag.com/articles/`.

Rainer Kölle, Garik Markarian, and Alex Tartar. *Aviation security engineering: a holistic approach*. Artech House, 2011.

K. Kohm. Modulation transfer function measurement method and results for the Orbview-3 high resolution imaging satellite. In *Proceedings of ISPRS*, pages 12–23, 2004.

S. Kolokytha. Non-contact object localisation forautomated 'on-belt' tomosynthesis. Technical report, London, 2011.

A. Konstantinidis. *Evaluation of digital X-ray detectors for medical imaging applications*. PhD thesis, UCL (University College London), 2011. URL `http://discovery.ucl.ac.uk/1322919/`.

A. Konstantinidis. 2.02 - Physical Parameters of Image Quality. In A. Brahme, editor, *Comprehensive Biomedical Physics*, pages 49–63. Elsevier, Oxford, 2014. ISBN 978-0-444-53633-4.

A. Konstantinidis, A. Olivo, and R. D. Speller. Technical Note: Modification of the standard gain correction algorithm to compensate for the number of used reference flat frames in detector performance studies. *Medical physics*, 38(12):6683–6687, 2011.

H. A. Kramers. On the story of X-ray absorption and of the continuous X-ray spectrum. *Philos*, pages 836–871, 1923.

Kristoph D. Krug, Jay A. Stein, and Adam L. Taylor. *Device and method for inspection of baggage and other objects*. Google Patents, June 1994. US Patent 5,319,547.

Andrew Kuhls-Gilcrist, Amit Jain, Daniel R. Bednarek, Kenneth R. Hoffmann, and Stephen Rudin. Accurate MTF measurement in digital radiography using noise response. *Medical Physics*, 37:724, 2010. ISSN 0094-2405. doi: 10.1118/1.3284376.

LesNumeriques. Les Numériques - S'informer pour mieux acheter, 2015. URL `http://www.lesnumeriques.com`.

Michael S. Lewis-Beck and Andrew Skalaban. The R-squared: Some straight talk. *Political Analysis*, pages 153–171, 1990. URL `http://www.jstor.org/stable/23317769`.

F. G. Lippert and C. Hirsch. The three dimensional measurement of tibia fracture motion by photogrammetry. *Clinical orthopaedics and related research*, (105):130–43, 1974. ISSN 0009-921X.

Logitech. Products - Logitech®, 2015. URL `http://www.logitech.com`.

T. Luhmann. On the determination of object rotation and translation in 3-D space (6 DOF) by a single camera. *Proceedings of Optical 3-D Measurement Techniques VII*, 2:157–166, 2005.

T. Luhmann, S. Robson, S Kyle, and I. Harley. *Close Range Photogrammetry: Principles, Methods and Applications*. Whittles, Scotland, 2006.

Thomas Luhmann. Precision potential of photogrammetric 6dof pose estimation with a single camera. *ISPRS Journal of Photogrammetry and Remote Sensing*, 64(3):275–284, 2009.

L. W. MacDonald. Realistic Visualisation of Cultural Heritage Objects, 2014.

Albert Macovski. *Medical imaging systems*. Prentice Hall, 1983.

JB Antoine Maintz and Max A. Viergever. A survey of medical image registration. *Medical image analysis*, 2(1):1–36, 1998.

A. Malliori, K. Bliznakova, R. D. Speller, L. Rigon, G. Tromba, and N. Pallikarakis. Image quality evaluation of breast tomosynthesis with synhcrotron radiation. *Medical Physics*, 39(9):5621–5634, 2012.

N. W. Marshall. A comparison between objective and subjective image quality measurements for a full field digital mammography system. *Physics in medicine and biology*, 51(10):2441, 2006. URL `http://iopscience.iop.org/0031-9155/51/10/006`.

N. W. Marshall. Calculation of quantitative image quality parameters. *Notes Describing the Use of Obj_Iq_Reduced NHSBSP Equipment Report*, 902, 2009.

Harry E. Martz, Clint M. Logan, Daniel J. Schneberk, and Peter J. Shull. *X-ray imaging: fundamentals, industrial techniques, and applications*. CRC Press, 2013. URL `http://cds.cern.ch/record/1581539`.

Calvin R. Maurer and J. Michael Fitzpatrick. Interactive image-guided neurosurgery , in: A Review of Medical Image Registration,. *American Association of Neurological Surgeons*, pages 17–44, 1993.

A. Maydeu-Olivares and C. Garcia-Forero. Goodness-of-Fit Testing. *Int. Encycl. Educ*, 7:190–196, 2010.

Emir Medic and Maziar Soltani. Methods for characterization of digital, image-producing detectors within medical X-ray diagnostics. *University essay from Blekinge Tekniska Högskola/Sektionen för Teknik (TEK)*, 2005.

Edward M. Mikhail and Friedrich E. Ackermann. Observations and least squares. 1976. URL `http://cds.cern.ch/record/102983`.

E.M. Mikhail, J.S. Bethel, and J.C McGlone. *Introduction to modern photogrammetry*. John Wiley and Sons, Inc, 2001.

Jan Modersitzki. Image registration with local rigidity constraints. In *Bildverarbeitung für die Medizin*, pages 444–448. Springer Berlin Heidelberg, 2007. ISBN 978-3-540-71090-5 978-3-540-71091-2.

R. H. Morgan, L. M. Bates, U. V. Gopalarao, and A. Marinaro. The frequency response characteristics of x-ray films and screens. *The American journal of roentgenology, radium therapy, and nuclear medicine*, 92:426–440, 1964. URL `http://europepmc.org/abstract/med/14207592`.

Motion Analysis Cooperation. URL `http://www.motionanalysis.com/`.

Jean-Pierre Moy and B. Bosset. How does real offset and gain correction affect the DQE in images from x-ray flat detectors? In *Medical Imaging'99*, pages 90–97. International Society for Optics and Photonics, 1999.

Frank Natterer and others. *Mathematical methods in image reconstruction*. Siam, 2001.

J. A. Navvaro, D. A. Becker, B. T. Kenna, and C. F. Kossack. A general protocol for operational testing and evaluation of bulk explosive detection systems. pages 347–367, 1996.

L. T. Niklason, B. T. Christian, L. E. Niklason, D. B. Kopans, D. E. Castleberry, B. H. Opsahl-Ong, C. E. Landberg, P. J. Slanetz, A. A. Giardino, R. Moore, D. Albagli, M. C. DeJule, P. F. Fitzgerald, D. F. Fobare, B. W. Giambattista, R. F. Kwasnick, J. Liu, S. J. Lubowski, G. E. Possin, J. F. Richotte, C. Y. Wei, and R. F. Wirth. Digital tomosynthesis in breast imaging. *Radiology*, 205(2):399–406, November 1997. ISSN 0033-8419. doi: 10.1148/radiology.205.2.9356620.

Nikon. D100 from Nikon Inc. ©, 2015. URL `http://www.nikonusa.com/en/Nikon-Products/Product-Archive/`.

NPL. Modelling for non-contacting CMMs. Project 2.3.1/2/3 - large scale metrology. Ref. MPU 8/6.1.1 - 09121999. Technical report, University College London, National Physical Laboratory Leica UK,, 2001.

J.M. Park, Jr. E. A. Franken, M. Garg, L.L. Fajardo, and L.T. Niklason. Breat tomosynthesis: Present considerations and future applications. *RadioGraphics*, 27(1):231–240, 2007.

G. N. Peggs, Paul G. Maropoulos, E. B. Hughes, A. B. Forbes, S. Robson, M. Ziebart, and B. Muralikrishnan. Recent developments in large-scale

dimensional metrology. *Proceedings of the Institution of Mechanical Engineers, Part B: Journal of Engineering Manufacture*, 223(6):571–595, 2009. URL `http://pib.sagepub.com/content/223/6/571.short`.

Juergen Peipe. High-resolution CCD area array sensors in digital close range photogrammetry. In *Optical Science, Engineering and Instrumentation'97*, pages 153–156. International Society for Optics and Photonics, 1997.

Photometrix. Products © 2015 Photometrix, 2015. URL `http://www.photometrix.com.au/products/`.

Brian W. Pogue and Michael S. Patterson. Review of tissue simulating phantoms for optical spectroscopy, imaging and dosimetry. *Journal of Biomedical Optics*, 11(4):041102–041102–16, 2006. ISSN 1083-3668. doi: 10.1117/1.2335429.

Satish C. Prasad, William R. Hendee, and Paul L. Carson. Intensity distribution, modulation transfer function, and the effective dimension of a line-focus x-ray focal spot. *Medical physics*, 3(4):217–223, 1976.

William K. Pratt. *Digital image processing : PIKS Scientific inside /William K. Pratt.* Wiley-Interscience, Hoboken, NJ, 4th ed., newly updated and rev. ed. edition, 2007. ISBN 0-471-76777-8.

Prohardver. PROHARDVER! - Az Online PC Magazin, 2015. URL `http://prohardver.hu/`.

T. Rayner, B. Thorson, S. Beevor, and R. West. Explosives detection using quadrupole resonance analysis. pages 275–280, 1996.

Stephen E. Reichenbach, Stephen K. Park, and Ramkumar Narayanswamy. Characterizing digital image acquisition devices. *Optical Engineering*, 30 (2):170–177, 1991.

C. B. Reid, M. M. Betcke, D. Chana, and R. D. Speller. The development of a pseudo-3d imaging system (tomosynthesis) for security screening of passenger baggage. *Nuclear Instruments and Methods in Physics Research Section A: Accelerators, Spectrometers, Detectors and Associated Equipment*, 652(1):108–111, October 2011a. ISSN 0168-9002. doi: 10.1016/j.nima.2010.08.081.

C. B. Reid, B.T. Cox, J.A. Horrocks, and R. Speller. A pseudo-3d X-ray imaging system (tomosynthesis) for real-time industrial non-destructive screening applications. *Journal of Instrumentation*, 2011b.

I. Reiser and Nishikawa. Task-based assessment of breast tomosynthesis effect of acquisition parameters and quantum noise. *Medical Physics*, 37(4): 1591–1600, 2010.

B. R. Ren, T. Wu, A. Smith, C. Ruth, L. Niklason, Z. X. Jing, and J. Stein. The Dependence of Tomosynthesis Imaging Performance on the Number of Scan Projections. volume 4046, pages 517–524. Springer-Verlag, 2006.

S. Robson. Introduction to Photogrammetry, 2005.

S. Robson, L. W. MacDonald, S Kyle, and M. Shortis. Effect of illumination wavelength on optimizing multi-camera location systems in a factory environment. Seville, 2015.

Stuart Robson, Timothy A. Clarke, and Jin Chen. Suitability of the Pulnix TM6cn CCD camera for photogrammetric measurement. volume 2067, pages 66–77, 1993. doi: 10.1117/12.162137. URL `http://dx.doi.org/10.1117/12.162137`.

Stuart Robson, Lindsay MacDonald, Stephen Kyle, and Mark Shortis. Multispectral calibration to enhance the metrology performance of C-mount camera systems. *ISPRS-International Archives of the Photogrammetry, Remote Sensing and Spatial Information Sciences*, 1:517–521, 2014.

F. L. Roder. The evolution of computed tomography (CT) as an explosives detection modality. pages 297–308, 1991.

F.L. Roder and B.G. Stebler. Image processing requirements for computed tomographic explosives detection. pages 30–38, 1992.

Frank Rogge, Dirk A. Vandenbroucke, Luc Struye, Hilde Bosmans, Peter Willems, and Guy Marchal. Practical method for detected quantum efficiency (DQE) assessment of digital mammography systems in the radiological environment. In *Medical Imaging 2002*, pages 645–655. International Society for Optics and Photonics, 2002.

Albert Rose. The sensitivity performance of the human eye on an absolute scale. *JOSA*, 38(2):196–208, 1948.

R. D. Rosenberg, J. F. Lando, W. C. Hunt, R. R. Darling, M. R. Williamson, M. N. Linver, F. D. Gilliland, and C. R. Key. The New Mexico Mammography Project. Screening mammography performance in Albuquerque, New Mexico, 1991 to 1993. *Cancer*, 78(8):1731–9, 1996. ISSN 0008-543X.

Kurt Rossmann. Point Spread-Function, Line Spread-Function, and Modulation Transfer Function: Tools for the Study of Imaging Systems 1. *Radiology*, 93(2):257–272, 1969. URL `http://pubs.rsna.org/doi/pdf/10.1148/93.2.257`.

Margarita Rova. *Affine multi-view modelling for close range object measurement*. PhD thesis, UCL (University College London), 2010. URL `http://discovery.ucl.ac.uk/20004/`.

Detlef Ruprecht and Heinrich Müller. Deformed crossdissolves for image interpolation in scientific visualization. *Journal of Visualization and Computer Animation*, 5(3):167–181, 1994. ISSN 1049-8907. doi: 10.1002/vis.4340050304.

Detlef Ruprecht and Heinrich Müller. Image warping with scattered data interpolation. *IEEE Computer Graphics and Applications*, (2):37–43, 1995. URL `http://www.computer.org/csdl/mags/cg/1995/02/mcg1995020037.pdf`.

John C. Russ. *The image processing handbook*. CRC press, 2006.

Ehsan Samei. Image quality in two phosphor-based flat panel digital radiographic detectors. *Medical physics*, 30(7):1747–1757, 2003.

Ehsan Samei, Michael J. Flynn, and David A. Reimann. A method for measuring the presampled MTF of digital radiographic systems using an edge test device. *Medical physics*, 25(1):102–113, 1998.

Michael Sandborg, David R. Dance, and Gudrun Alm Carlsson. Calculation of contrast and signal-to-noise degradation factors for digital detectors in chest and breast imaging. 2003. URL `http://www.diva-portal.org/smash/record.jsf?pid=diva2:328134`.

D. Schafer, M. Annis, and M. Hacker. New X-ray technology for the detection of explosives. pages 269–281, 1991.

T. Schenk. Introduction to photogrammetry. *The Ohio State University, Columbus*, 2005.

I. Sechopoulos and C. Ghetti. Optimization of the acquisition geometry in digital tomosynthesis of the breast. *Medical Physics*, 36(4):1199–1207, 2009.

Jeremy M. Sharp. *Yemen: Background and US relations*. DIANE Publishing, 2010.

Mark R. Shortis, Timothy A. Clarke, and Tim Short. Comparison of some techniques for the subpixel location of discrete target images, 1994.

Mark R. Shortis, James W. Seager, Stuart Robson, and Euan S. Harvey. Automatic recognition of coded targets based on a Hough transform and segment matching. volume 5013, pages 202–208, 2003. doi: 10.1117/12.476172. URL `http://dx.doi.org/10.1117/12.476172`.

Robert L. Siddon. Fast calculation of the exact radiological path for a three-dimensional CT array. *Medical Physics*, 12:252–255, March 1985. ISSN 0094-2405. doi: 10.1118/1.595715. URL `http://adsabs.harvard.edu/abs/1985MedPh..12..252S`.

Sameer Singh and Maneesha Singh. Explosives detection systems (EDS) for aviation security. *Signal Processing*, 83(1):31–55, January 2003. ISSN 0165-1684. doi: 10.1016/S0165-1684(02)00391-2.

Sarabjeet Singh, Mannudeep K. Kalra, Jiang Hsieh, Paul E. Licato, Synho Do, Homer H. Pien, and Michael A. Blake. Abdominal CT: Comparison of Adaptive Statistical Iterative and Filtered Back Projection Reconstruction Techniques. *Radiology*, 257(2):373–383, November 2010. ISSN 0033-8419. doi: 10.1148/radiol.10092212. URL `http://pubs.rsna.org/doi/full/10.1148/radiol.10092212`.

M. J. Smith and E. Cope. The effects of temperature variation on single-lens-reflex digital camera calibration parameters. *International Archives of Photogrammetry, Remote Sensing and Spatial Information Sciences*, 28, 2010. URL `http://www.isprs.org/proceedings/Xxxviii/part5/papers/158.pdf`.

R.C. Smith and P.R. Krall. Full volume dual-energy high speed computed tomography (CT) explosives detection system. pages 260–263, 1996.

Robert Speller. Radiation-based security. *Radiation Physics and Chemistry*, 61(3–6):293–300, June 2001. ISSN 0969-806X. doi: 10.1016/S0969-806X(01)00252-3.

Spiegel. Foiled Parcel Plot: World Scrambles to Tighten Air Cargo Security. November 2010.

G.M. Stevens, Birdwell R. L., Beaulieu C. F., Ikeda D. M., and Pelc. N. J. Circular tomosynthesis: Potential in imaging of breast and upper cervical spine-preliminary phantom and in vitro study. *Radiology*, 228(2):569–575, 2003.

Grant M. Stevens, Rebecca Fahrig, and Norbert J. Pelc. Filtered backprojection for modifying the impulse response of circular tomosynthesis. *Medical Physics*, 28:372, 2001. ISSN 0094-2405. doi: 10.1118/1.1350588.

Harry L. Stiltz. *Aerospace telemetry*, volume 1. Prentice-Hall Englewood Cliffs, NJ, 1961.

H. Strecker. Automatic detection of explosives in airline baggage using elastic x-ray scatter. *Medicamundi*, 42(2):30–33, 1998.

Student. The probable error of a mean. *Biometrika*, pages 1–25, 1908. URL `http://www.jstor.org/stable/2331554`.

Rahul Swaminathan and Shree K. Nayar. Nonmetric calibration of wide-angle lenses and polycameras. *Pattern Analysis and Machine Intelligence, IEEE Transactions on*, 22(10):1172–1178, 2000.

Alan O. Sykes. An introduction to regression analysis, 1993.

M. B. Szafraniec. *Coded Aperture Phase Contrast Tomosynthesis*. Doctoral, UCL (University College London), February 2013. URL `http://discovery.ucl.ac.uk/1383234/`.

Laszlo Tabar, Gunnar Fagerberg, Hsiu-hsi Chen, Stephen W. Duffy, Charles R. Smart, Adel Gad, and Robert A. Smith. Efficacy of breast cancer screening by age. New results swedish twocounty trial. *Cancer*, 75(10):2507–2517, 1995. ISSN 0008-543X. doi: 10.1002/1097-0142(19950515)75:10¡2507::AID-CNCR2820751017¿3.0.CO;2-H.

Donald O. Thompson and Dale E. Chimenti. *Review of progress in quantitative nondestructive evaluation*, volume 18. Springer Science & Business Media, 2012.

Anders Tingberg. *Quantifying the quality of medical x-ray images. An evaluation based on normal anatomy for lumbar spine and chest radiography.* Lund University, 2000. URL `http://lup.lub.lu.se/record/40610`.

Meritxell Tortajada, Robert Martí, Jordi Freixenet, Josep Fernández, and Melcior Sentís. Image Correction and Reconstruction for Breast Biopsy. In *Digital Mammography*, pages 545–552. Springer, 2008.

Bill Triggs, Philip F. McLauchlan, Richard I. Hartley, and Andrew W. Fitzgibbon. Bundle Adjustment — A Modern Synthesis. In Bill Triggs, Andrew Zisserman, and Richard Szeliski, editors, *Vision Algorithms: Theory and Practice*, pages 298–372. Springer Berlin Heidelberg, 2000. ISBN 978-3-540-67973-8 978-3-540-44480-0.

Henrik Turbell. Cone-beam reconstruction using filtered backprojection. 2001.

D. Van de Sompel, S. M. Brady, and J. Boone. Task-based performance analysis of FBP, SART, and ML for digital breast tomosynthesis using signal CNR and Channelised Hotelling Observers. *Medical Image Analysis*, 15(1): 53–70, 2011.

Petra Van den Elsen, Evert-Jan D. Pol, Max Viergever, and others. Medical image matching-a review with classification. *Engineering in Medicine and Biology Magazine, IEEE*, 12(1):26–39, 1993.

Srinivasan Vedantham, Andrew Karellas, Sankararaman Suryanarayanan, Douglas Albagli, Sung Han, Eric J. Tkaczyk, Cynthia E. Landberg, Beale Opsahl-Ong, Paul R. Granfors, Ilias Levis, and others. Full breast digital mammography with an amorphous silicon-based flat panel detector: physical characteristics of a clinical prototype. *Medical Physics*, 27(3):558–567, 2000.

S. A. Veress, F. G. Lippert, M. C. Y. Hou, and T. Takamoto. Patellar tracking patterns measurement by analytical x-ray photogrammetry. *Journal of biomechanics*, 12(9):639–650, 1979.

Vicon Motion Systems. URL `http://www.vicon.com/`.

G. Welch. SCAAT: Incremental Tracking with Incomplete Information, 1996.

Greg Welch, Gary Bishop, Leandra Vicci, Stephen Brumback, Kurtis Keller, and others. The HiBall tracker: High-performance wide-area tracking for virtual and augmented environments. In *Proceedings of the ACM symposium on Virtual reality software and technology*, pages 1–ff. ACM, 1999. URL `http://dl.acm.org/citation.cfm?id=323664`.

Greg Welch, Gary Bishop, Leandra Vicci, Stephen Brumback, Kurtis Keller, and D'nardo Colucci. High-performance wide-area optical tracking: The hiball tracking system. *presence: teleoperators and virtual environments*, 10 (1):1–21, 2001.

K. Wells and D. A. Bradley. A review of X-ray explosives detection techniques for checked baggage. *Applied Radiation and Isotopes*, 70(8):1729–1746, August 2012. ISSN 0969-8043. doi: 10.1016/j.apradiso.2012.01.011.

Mark B. Williams, Peter A. Mangiafico, and Piero U. Simoni. Noise power spectra of images from digital mammography detectors. *Medical physics*, 26 (7):1279–1293, 1999.

Thomas Williams. *The optical transfer function of imaging systems*. CRC Press, 1998.

P. R. Wolf and B. A. Dewitt. *Elements of Photogrammetry: with applications in GIS*, volume 3. McGraw-Hill New York, 2000.

S. Wong, S. Robson, A.P. Gibson, and J.C. Hebden. Low cost real-time webcam photogrammetry to determine the locations of optical topography sensors located on the human head. Remote Sensing and Photogrammetry Society Annual Conference, 2009.

Sen Wong. *A fast webcam photogrammetric system to support optical imaging of brain activity*. PhD thesis, UCL (University College London), 2012. URL `http://discovery.ucl.ac.uk/1344106/`.

A. Workman and A. R. Cowen. Signal, noise and SNR transfer properties of computed radiography. *Physics in Medicine and Biology*, 38(12):1789, 1993. URL `http://iopscience.iop.org/0031-9155/38/12/007`.

Tao Wu, Alexander Stewart, Martin Stanton, Thomas McCauley, Walter Phillips, Daniel B. Kopans, Richard H. Moore, Jeffrey W. Eberhard, Beale Opsahl-Ong, Loren Niklason, and Mark B. Williams. Tomographic mammography using a limited number of low-dose cone-beam projection images. *Medical Physics*, 30:365, 2003. ISSN 0094-2405. doi: 10.1118/1.1543934.

Tao Wu, Richard H. Moore, Elizabeth A. Rafferty, and Daniel B. Kopans. A comparison of reconstruction algorithms for breast tomosynthesis. *Medical physics*, 31(9):2636–47, 2004a. ISSN 0094-2405.

Tao Wu, Juemin Zhang, Richard Moore, Elizabeth Rafferty, Daniel Kopans, Waleed Meleis, and David Kaeli. Digital tomosynthesis mammography using a parallel maximum-likelihood reconstruction method, 2004b.

Martin J. Yaffe. Digital mammography. *Handbook of medical imaging*, 1: 329–372, 2000.

Yale. Statistical Topics: Test of Significance, 1998. URL `http://statistics.yale.edu/`.

S. L. Zabell. On Student's 1908 Article "The Probable Error of a Mean". *Journal of the American Statistical Association*, 103(481):1–7, 2008. URL `http://amstat.tandfonline.com/doi/abs/10.1198/016214508000000030`.

B. Zhao, J. Zhou, Y. H. Hu, T. Mertelmeier, J. Ludwig, and W. Zhao. Experimental validation of a three-dimensional linear system model for breast tomosynthesis. *Medical Physics*, 36(1):240–251, 2009.

J. Zhou, B. Zhao, and W. Zhao. A computer simulation platform for the optimization of a breast tomosynthesis system. *Medical Physics*, 34(3): 1098–1109, 2007.

Hafiz M. Zin, Anastasios C. Konstantinidis, Emma J. Harris, John PF Osmond, Alesandro Olivo, Sarah E. Bohndiek, Andy T. Clark, Renato Turchetta, Nicola Guerrini, Jamie Crooks, and others. Characterisation of regional variations in a stitched CMOS active pixel sensor. *Nuclear Instruments and Methods in Physics Research Section A: Accelerators, Spectrometers, Detectors and Associated Equipment*, 620(2):540–548, 2010.

# Appendices

## Appendix A: Matlab code developed for plotting profile lines

```
% Matlab code developed for plotting profile lines
% by Selina Kolokytha, 2012
close all; clear all; clc; close all; clear all; clc;
% Specify location of the Images
path1='C:\Documents and Settings\skolokyt\Images\';
% Specify x coordinate of Line
x1=141
x2=215
x3=327
% For x=x1
% read in Image a
I = imread('0.jpg');
% plot profile line of Image a
ROI1=I(:,x1);
figure
plot(ROI1,'–b')
hold on
% read in Image b
I = imread('100.jpg');
% plot profile line of Image b in the same graph
ROI2=I(:,x1);
plot (ROI2,'r-')
hold off
% Title graph and label axis
title('Profile line plot 1')
xlabel('pixel number')
ylabel('grayscale')
% Insert a graph legend outside the graph
hleg = legend('Image a','Image b',...
'Location','EastOutside')
% For x=x2
% read in Image a
```

```
I = imread('0.jpg');
% plot profile line of Image a
ROI1=I(:,x2);
figure
plot(ROI1,'–b')
hold on
% read in Image b
I = imread('100.jpg');
% plot profile line of Image b in the same graph
ROI2=I(:,x2);
plot (ROI2,'r-')
hold off
% Title graph and label axis
title('Profile line plot 2')
xlabel('pixel number')
ylabel('grayscale')
% Insert a graph legend outside the graph
hleg = legend('Image a','Image b',...
'Location','EastOutside')
% read in Image a
I = imread('0.jpg');
% For x=x3
% plot profile line of Image a
ROI1=I(:,x3);
figure
plot(ROI1,'–b')
hold on
% read in Image b
I = imread('100.jpg');
% plot profile line of Image b in the same graph
ROI2=I(:,x3);
plot (ROI2,'r-')
hold off
% Title graph and label axis
title('Profile line plot 3')
xlabel('pixel number')
ylabel('grayscale')
% Insert a graph legend outside the graph
hleg = legend('Image a','Image b',...
'Location','EastOutside')
% END of code
```

# Appendix B. Configuration of Network and Ethernet Adapter

The various discovery protocols that Windows 7 uses can cause disruption to the operation of the control card used in the camera. Thus the following configuration changes are recommended.
It is strongly recommended that a system Restore Point should be generated prior to making any modifications.
You can create a restore point manually at any time by following the steps below
1. In the Control Panel, click to open System.
2. In the left pane, click System protection. If you're prompted for an administrator password or confirmation, type the password or provide confirmation.
3. Click the System Protection tab, and then click Create.
4. In the System Protection dialog box, type a description, and then click Create.

5.1 Configuring the Wired Ethernet Adapter
5.1.1 Select only TCP/IPv4 protocol only
1. Start -¿ Control Panel -¿ Network Connections
2. Right Click 'Local Area Connetion'
3. Open Properties dialog for the adapter connected to the camera (see below).
4. Uncheck all options except 'Internet Protocol Version 4 (TCP/IPv4)'.

5.1.2 Assign IPv4 Settings
1. Select Internet Protocol Version 4 and click 'Properties' to open the dialog that is shown right.
2. Enter IP Address of the Adapter.
3. Clear any Default Gateway settings

5.1.3 advanced setting
Assigning a metric to persuade Windows not to use it
1. Click 'IP Settings' tab
2. Uncheck the 'Automatic Metric' box.
3. Enter an 'Interface Metric' of 100.
4. Clear any Default Gateway settings

Prevent the adapters addresses being registered in the DNS.
5. Click 'DNS' tab.
6. Uncheck the 'Register this connection's addresses in the DNS' box.

Configure the WINS settings.
9. Click 'WINS' tab
10. Uncheck the 'Enable LMHOSTS lookup' box.

11. Select radio button option ‘Disable NetBIOS over TCP/IP’.
12. Click ‘OK’ to exit ‘Advanced Settings’
13. Click ‘OK’ to exit the IPv4 properties.
14. Click ‘OK’ to exit the Adapter properties.

5.2 Stop the SSDP M-SEARCH * HTTP/1.1 packets
5.2.1 Stop the SSDP Discovery Service
1. Start -¿ Control Panel -¿ System and Security -¿ Administrative Tools
2. Open ‘Services’
3. Scroll to the service ‘SSDP Discovery’ and open the Properties dialog
4. Click ‘Stop’
5. Click ‘OK’

5.2.2 Stop UPnP Device Host Service
1. Start -¿ Control Panel -¿ Administrative Tools
2. Open ‘Services’
3. Scroll to the service ‘UPnP Device Host’ and open the Properties dialog
4. Click ‘Stop’ 10. Click ‘OK’

5.2.3 Configure Live Messenger Live Messenger may continue to send data after these services have been stopped. Refer to the Knowledge Base article http://support.microsoft.com/kb/317843. To shut this down use the Registry Editor to perform the following:
1. Start Registry Editor (Regedt32.exe).
2. Locate and click the following key in the registry:
HKEY_LOCAL_MACHINE\Software\Microsoft\DirectPlayNATHelp\DPNHUPnP
3. On the menubar click Edit-¿ New -¿ DWORD (32bit) Value
4. Enter UPnpMode as the ‘Name’
5. On the menubar click ‘Edit-¿Modify. . . ’
6. Enter a value of 2
7. Click ‘OK’
8. Quit Registry Editor

5.3 Configure Profile’s Sharing Options In Network and Sharing Center select the Change Advanced sharing settings and turn off everything for the profile being used.
These should include:
1. Network Discovery
2. File and Printer sharing
3. Public folder sharing
If you see UDP packets with a destination port sentinelsrm then go to Services and stop the Sentinel HASP License Manager service.

5.4 Disable IGMP

1. Start Registry Editor (Regedt32.exe).
2. Locate and click the following key in the registry:
HKEY_LOCAL_MACHINE\System\CurrentControlSet\Services\Tcpip\Parameters
3. On the menubar click Edit-¿ New -¿ DWORD (32bit) Value
4. Enter IGMPVersion as the 'Name'
5. On the menubar click 'Edit-¿Modify. . . '
6. Enter a value of 0
7. Click 'OK'
8. On the menubar click Edit-¿ New -¿ DWORD (32bit) Value
9. Enter IGMPLevel as the 'Name'
10. On the menu bar click 'Edit-¿Modify. . . '
11. Enter a value of 0 12. Click 'OK' 13. Quit Registry Editor

5.5 Add static route for Camera Add a static route to the Routing Table to get rid of/reduce the ARP protocol packets.
1. Open a DOS Prompt
2. Type the command:
route –p ADD ¡Camera Address ¿ MASK 255.255.255.255 ¡NIC Address¿
Where:
–p flag makes the entry persistent
¡Camera Address¿ is the IP address of the Camera (10.0.0.1)
¡NIC Address¿ is the IP Address of the NIC to which the camera is connected (198. . . )
3. Close the DOS Prompt

## Appendix C. Screenshot of the LabVIEW Block Diagram developed.

A screenshot of the Block Diagram of the LabVIEW code developed is shown below, rotated by 90° clockwise for better visualisation.

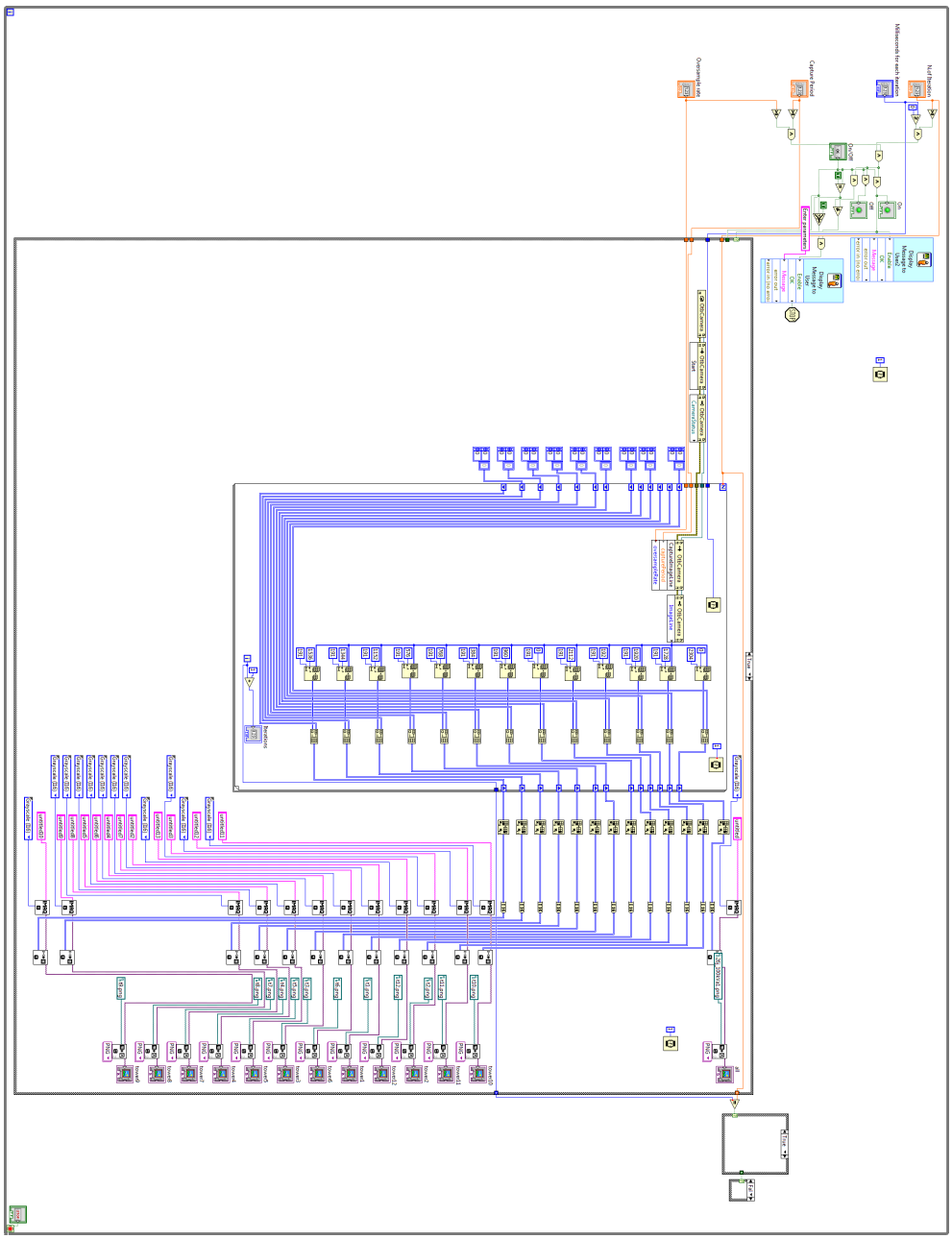

## Appendix D: Matlab code developed for measuring the warping effect in ObT

```
% Matlab code for estimate warping effect

% Import x-ray projection image and convert to normal double matrix
cdata=imread('C:\Users\Turbo-X\Dropbox\PhD work May 15\Image Quality Analysis\warping\12J\12Jwarp100b_calib_crop.png');
%cdata=imcrop(cdata, [1 576 499 191]);
projim0 = double(cdata(:,:,1));
projim= projim0; %flipdim(projim0,1);
I= image (projim0), hold on; colormap('parula'); colorbar; hold on
title('A2');
```

```
xlabel('Iterations');
ylabel('Pixels');
peakloc = zeros(size(projim,2),3);

% Subtract the baseline from the image
for i = 1:size(projim,2);projim(:,i) = projim(:,i) - mean(projim(1:20,i));
end

% Find location of the peak of each the lines in the image
for i = 1:size(cdata,2);
[peaks,loc] = findpeaks(projim(:,i));
l = find(peaks >10 & loc >20 & loc < 30);
peakloc(i,1) = mean(loc(l));
l = find(peaks >10 & loc >45 & loc < 55);
peakloc(i,2) = mean(loc(l));
l = find(peaks >10 & loc >72 & loc < 80);
peakloc(i,3) = mean(loc(l));
end
%peakloc(isnan(peakloc)) = 0; %Comment out if zeros not wanted
%
% Plot line profiles in orange,red,black
plot(peakloc(:,1),'black')
hold on
plot(peakloc(:,2),'r')
plot(peakloc(:,3),'b')
legend('R1','R2','R3','Location','southeast')
%
% Distinguish the three lines so as to choose relative plots
R1 = peakloc(:,1);
R2 = peakloc(:,2);
R3 = peakloc(:,3);
%
% Open Curve Fitting Tool App % Choose: Y=pi, Poly, Degree=1
cftool (peakloc)

%END
```

## Appendix E. Example VMS project, calibration and target files

Example VMS project, calibration and target files (used in section....)

**VMS project file:**

#

```
#
# Vision Measurement System
# Project Information File
d100_end
#
C:\Users\Turbo-X\Desktop\Selina\MasterOBTSystemCoordinationWithNikon
#
# Project Type
NETWORK
#
# Image acquisition mode
FRAME
#
# Project measurement units
units millimetres
#
# Target data filename
nikon3feb15output.tar
#
# Calibration data filename
nikon_output.cal
#
# Photo orientation data filename
d100_end.pho
#
# Image measurement data filename
d100_end.obs
#
# Survey data filename
scalebars3.sur
#
# Number of active images
14
#
1000 .\images\dsc_4541.jpg
1001 .\images\dsc_4543.jpg
1002 .\images\dsc_4550.jpg
1003 .\images\dsc_4551.jpg
1004 .\images\dsc_4552.jpg
1005 .\images\dsc_4556.jpg
1006 .\images\dsc_4557.jpg
1007 .\images\dsc_4561.jpg
1008 .\images\dsc_4564.jpg
1009 .\images\dsc_4565.jpg
```

1010 .\images\dsc_4568.jpg
1011 .\images\dsc_4570.jpg
1012 .\images\dsc_4575.jpg
1013 .\images\dsc_4581.jpg
#
# End of VMS project file
#

**VMS calibration file:**

# VMS Project: Camera data
# This file contains information on 1 cameras
# Parameters : 1=PPx,2=PPy,3=PD,4-6=radial,7-8=decentring,9=orthogonality,10=affinity
1
#
# Calibration parameters for camera 1
1 0.0780 0.0047
2 -0.0929 0.0050
3 28.8987 0.0069
4 -1.4675e-004 1.6118e-006
5 2.3860e-007 1.9366e-008
6 -1.6287e-010 6.9764e-011
7 2.3003e-006 1.9901e-006
8 9.2839e-006 1.9800e-006
9 -4.7286e-005 1.8703e-005
10 3.3373e-005 2.0306e-005
#
# x and y pixel size in mm and x, y image size in pixels
0.00780 0.00780 3008 2000
#
#
# Fiducial Mark Data
# Camera Point Ref X Ref Y Std X Std Y Obs X Obs Y Std X Std Y
#
# No fiducial information for this camera
#
# End of file
#

**VMS target file:**

# VMS Project: Target data output
# 60 Targets
# Targets in millimetres, precisions in 1000*millimetres
#

| # Target | X | Y | Z | flag | sdx | sdy | sdz |
|---|---|---|---|---|---|---|---|
| # | | | | | | | |
| 700 | 64.9992 | 140 | -899.2321 | 6 | 11.8032 | 13.4949 | 254.0125 |
| 701 | 65.0182 | -322.9415 | -856.2499 | 4 | 10.1358 | 194.3599 | 185.4173 |
| 702 | 64.982 | -339.5903 | -856.2024 | 4 | 10.5253 | 201.2449 | 185.3994 |
| 703 | 64.9952 | -345.2383 | -503.0235 | 4 | 24.5715 | 238.2587 | 71.8191 |
| 12 | -105.4029 | -402.5703 | -500.0048 | 1 | 79.4614 | 260.4311 | 17.6163 |
| 23 | -615.4789 | -101.2102 | -500.0028 | 1 | 282.6667 | 192.8386 | 18.4699 |
| 24 | -389.9911 | -297.7682 | -499.9962 | 1 | 191.8252 | 232.8601 | 12.583 |
| 608 | 4.536 | 399.5397 | -867.4656 | 0 | 68.1014 | 125.4194 | 312.2819 |
| 607 | 63.259 | 365.7929 | -906.5691 | 0 | 57.4792 | 110.1295 | 312.6423 |
| 606 | 133.1458 | 328.3978 | -863.7342 | 0 | 74.9072 | 106.6325 | 312.1751 |
| 605 | 134.2612 | 330.3895 | -777.2586 | 0 | 68.8117 | 107.6791 | 284.703 |
| 604 | 68.3964 | 368.1323 | -734.0601 | 0 | 65.2995 | 121.7115 | 277.3275 |
| 6 | -581.0167 | 34.5021 | -923.6879 | 0 | 267.5433 | 91.4639 | 222.1056 |
| 7 | 227.747 | -283.0937 | -860.0114 | 0 | 75.866 | 177.793 | 199.2913 |
| 8 | -174.403 | 187.5412 | -899.4001 | 0 | 105.3686 | 51.3633 | 246.0396 |
| 10 | -82.8116 | 139.3835 | -898.7538 | 0 | 71.7383 | 44.714 | 242.4498 |
| 400 | 82.405 | -346.23 | -500.2844 | 0 | 38.3894 | 238.9166 | 73.4631 |
| 401 | 83.7667 | -435.7595 | -501.8964 | 0 | 39.4777 | 269.3484 | 75.8725 |
| 402 | 17.85 | -347.406 | -499.6497 | 0 | 43.5498 | 240.7036 | 70.4671 |
| 403 | 20.3533 | -438.1357 | -501.315 | 0 | 42.0718 | 271.1988 | 72.662 |
| 404 | 26.6032 | -461.7997 | -497.2164 | 0 | -1 | -1 | -1 |
| 410 | -66.6552 | -365.1044 | -498.7015 | 0 | 66.1955 | 248.2594 | 63.2331 |
| 411 | -84.7263 | -452.8564 | -498.7693 | 0 | 73.2525 | 279.1521 | 78.5364 |
| 412 | -129.2791 | -351.5756 | -498.7712 | 0 | 88.2859 | 245.1464 | 62.5879 |
| 413 | -145.9542 | -440.3784 | -498.851 | 0 | 95.2304 | 276.2478 | 77.8713 |
| 414 | -139.3553 | -461.6472 | -494.5936 | 0 | -1 | -1 | -1 |
| 420 | -204.5241 | -338.9599 | -498.8543 | 0 | 117.2408 | 242.9268 | 59.0811 |
| 421 | -235.3861 | -424.7096 | -499.4603 | 0 | 129.3731 | 272.8559 | 78.1134 |
| 422 | -271.8908 | -535.6449 | -493.96 | 0 | 145.238 | 313.7981 | 109.0915 |

| | | | | | | | |
|---|---|---|---|---|---|---|---|
| 423 | -267.4256 | -318.9364 | -498.1844 | 0 | 141.3597 | 238.3363 | 55.917 |
| 424 | -294.7499 | -405.2872 | -499.0442 | 0 | 152.2701 | 267.8102 | 72.6973 |
| 425 | -332.65 | -515.005 | -493.5941 | 0 | 172.8854 | 308.183 | 124.0011 |
| 430 | -343.9431 | -283.9895 | -498.0589 | 0 | 171.6147 | 229.6689 | 54.3072 |
| 431 | -390.0051 | -362.1373 | -497.1339 | 0 | 190.182 | 256.2422 | 67.8029 |
| 432 | -450.0215 | -461.5354 | -491.399 | 0 | 215.8016 | 292.601 | 98.9947 |
| 433 | -399.1853 | -250.943 | -497.4727 | 0 | 194.1435 | 221.6048 | 53.6442 |
| 434 | -444.9622 | -330.7143 | -496.7509 | 0 | 212.3009 | 247.9764 | 65.537 |
| 435 | -505.6014 | -428.184 | -491.0946 | 0 | 243.0173 | 282.9592 | 117.2387 |
| 440 | -473.8488 | -205.4394 | -497.6883 | 0 | 224.8592 | 211.6775 | 52.9208 |
| 441 | -536.0158 | -272.1781 | -498.9757 | 0 | 249.4367 | 233.0608 | 62.0603 |
| 442 | -615.175 | -356.9293 | -494.0107 | 0 | 293.8329 | 263.7779 | 143.2113 |
| 443 | -521.1964 | -161.6648 | -497.8269 | 0 | 244.2804 | 202.0575 | 54.5764 |
| 444 | -582.5759 | -227.9737 | -499.0594 | 0 | 268.0628 | 221.9414 | 57.7707 |
| 445 | -662.1102 | -312.7506 | -494.0512 | 0 | 313.9987 | 252.2458 | 141.6755 |
| | | | | | | | |
| 450 | -569.633 | -100.0132 | -498.0315 | 0 | 264.2636 | 189.6883 | 60.5965 |
| 451 | -637.3681 | -159.5529 | -499.074 | 0 | 290.6547 | 206.2545 | 57.1623 |
| 453 | -611.7694 | -52.2044 | -497.7871 | 0 | 281.3225 | 182.5252 | 69.4999 |
| 454 | -678.5752 | -111.63 | -498.8579 | 0 | 308.0663 | 197.378 | 60.4683 |
| 460 | 10.5547 | -335.3533 | -855.8413 | 0 | 41.1705 | 199.1909 | 177.5406 |
| 461 | -157.9078 | -330.3362 | -855.3807 | 0 | 97.3577 | 199.7349 | 178.1932 |
| 462 | -266.8185 | -304.1878 | -854.5252 | 0 | 138.6412 | 190.4147 | 172.7501 |
| 463 | -457.0939 | -196.5373 | -854.1475 | 0 | 215.4774 | 156.2894 | 183.465 |
| 600 | 22.0331 | 404.3264 | -966.1457 | 0 | 62.2658 | 133.9375 | 343.2851 |
| 601 | 120.839 | 350.2313 | -965.7352 | 0 | 63.6392 | 115.2698 | 337.5606 |
| 609 | 2.6817 | 403.0874 | -777.3326 | 0 | 71.1412 | 130.8645 | 291.9188 |
| 22 | -241.5053 | -39.4343 | -582.2247 | 0 | 131.3829 | 140.0709 | 98.1083 |
| 5 | -174.8277 | -167.7304 | -580.5927 | 0 | 103.8701 | 172.1325 | 77.8871 |
| 9 | -366.464 | -77.0781 | -578.1539 | 0 | 180.5173 | 154.5342 | 80.0436 |
| 11 | -109.8802 | -21.0387 | -586.6063 | 0 | 82.2289 | 131.5055 | 118.7192 |
| 21 | -294.1818 | 68.4662 | -584.7789 | 0 | 154.0068 | 124.4291 | 124.307 |

#
# End of file
#

## Appendix F: 'Shapes' 3D circle fit output

Instability in direction cosines
Rotating Primary Data
OMEGA: 0.5236 PHI: 0.5236 KAPPA: 0.5236
Elapsed time in Seconds 3.36311631E-044
RESULTS OF CIRCLE FITTING.

---

The circle fitted to the data set provided lies in the plane
of which the equation is :
(-0.001976)X + ( 0.002058)Y + (-0.999996)Z + ( 582.789521) = 0.
The coordinates of its centre are :
X = -62.94485 ; Y = 292.41753 ; Z =-582.06561
Its radius is : 381.83834
The RMS of the residuals, normal to the Plane of the circle is: 0.000000
and the RMS of the radial residuals in the plane are: 0.001759
The residuals normal to the plane of the circle, and the radial
residuals in the plane, are :

| | Normal | Radial |
|---|---|---|
| 1 | 0.00000 | 0.00165 |
| 2 | 0.00000 | -0.00244 |
| 3 | 0.00000 | 0.00078 |

* THESE VALUES ARE IN THE SAME UNITS AS THE DATA.

## Appendix G: Table of the critical values of *t* for a statistic *t-test*

Below is the table of the critical values of $t$ for a statistic *t-test* reproduced from Dougherty [1992]. The critical value of $t$ for a specific test is determined by the degrees of freedom N-1 and the significance level $\alpha$, for a one-tailed test or $\frac{a}{2}$ for a two-tailed test (ie. $t_{N-1,\frac{a}{2}}$ ).

**t Distribution: Critical Values of t**

| | | *Significance level* | | | | | |
|---|---|---|---|---|---|---|---|
| *Degrees of freedom* | *Two-tailed test:* | 10% | 5% | 2% | 1% | 0.2% | 0.1% |
| | *One-tailed test:* | 5% | 2.5% | 1% | 0.5% | 0.1% | 0.05% |
| **1** | | 6.314 | 12.706 | 31.821 | 63.657 | 318.309 | 636.619 |
| **2** | | 2.920 | 4.303 | 6.965 | 9.925 | 22.327 | 31.599 |
| **3** | | 2.353 | 3.182 | 4.541 | 5.841 | 10.215 | 12.924 |
| **4** | | 2.132 | 2.776 | 3.747 | 4.604 | 7.173 | 8.610 |
| **5** | | 2.015 | 2.571 | 3.365 | 4.032 | 5.893 | 6.869 |
| **6** | | 1.943 | 2.447 | 3.143 | 3.707 | 5.208 | 5.959 |
| **7** | | 1.894 | 2.365 | 2.998 | 3.499 | 4.785 | 5.408 |
| **8** | | 1.860 | 2.306 | 2.896 | 3.355 | 4.501 | 5.041 |
| **9** | | 1.833 | 2.262 | 2.821 | 3.250 | 4.297 | 4.781 |
| **10** | | 1.812 | 2.228 | 2.764 | 3.169 | 4.144 | 4.587 |
| **11** | | 1.796 | 2.201 | 2.718 | 3.106 | 4.025 | 4.437 |
| **12** | | 1.782 | 2.179 | 2.681 | 3.055 | 3.930 | 4.318 |
| **13** | | 1.771 | 2.160 | 2.650 | 3.012 | 3.852 | 4.221 |
| **14** | | 1.761 | 2.145 | 2.624 | 2.977 | 3.787 | 4.140 |
| **15** | | 1.753 | 2.131 | 2.602 | 2.947 | 3.733 | 4.073 |
| **16** | | 1.746 | 2.120 | 2.583 | 2.921 | 3.686 | 4.015 |
| **17** | | 1.740 | 2.110 | 2.567 | 2.898 | 3.646 | 3.965 |
| **18** | | 1.734 | 2.101 | 2.552 | 2.878 | 3.610 | 3.922 |
| **19** | | 1.729 | 2.093 | 2.539 | 2.861 | 3.579 | 3.883 |
| **20** | | 1.725 | 2.086 | 2.528 | 2.845 | 3.552 | 3.850 |

## Appendix H: VMS bundle adjustment execution steps

VMS can perform photogrammetric computations for up to 8 cameras simultaneously. The specifics steps for creating a global project for up to 8 cameras simultaneously and computing a bundle adjustment to provide coordinate estimates and simultaneous camera calibration are given below:

• Create a new "calibration" file merging all four individual "calibration" files.

• Create a new "photograph orientation" file merging all four individual "photograph orientation" files, making sure the individual cameras are numbered (1 to 8) as well as their respective images (1000 to 1015, 2000 to 2015 and so on).

• Create a new "observation" file merging all four individual "observation" files globally correcting the photograph names so that they match the "photograph orientation" file and matching the new name to the "project" file.

• Create a new network project in VMS, using all created files above.

- Once the project is loaded, identify targets in FOV- either automatically using targets codes, or manually by identifying and numbering target locations - and then compute a resection for each image in the network.
- Identify any new targets to be coordinated in 3D, which are visible in in 2 or more images, and then compute an intersection to generate their XYZ coordinates.
- Use the new targets to automatically find corresponding targets in other images.
- Execute a bundle adjustment of the 1 or 8 camera(s).
- Perform analysis of output log files.

More details can be found online at: www.geomsoft.com/VMS/index.shtml. Two example screenshots of VMS projects are shown in Figures 5.11 and 5.19.